TECHNISCHE UNIVERSITÄT MÜNCHEN

Lehrstuhl für Luftfahrtsysteme

Hybrid-Electric Propulsion Systems for Small Unmanned Aircraft

Joachim Schömann

Vollständiger Abdruck der von der Fakultät für Maschinenwesen der Technischen Universität München zur Erlangung des akademischen Grades eines

Doktor-Ingenieurs (Dr.-Ing.)

genehmigten Dissertation.

Vorsitzender:		Univ.-Prof. Dr.-Ing. Florian Holzapfel
Prüfer der Dissertation:	1.	Univ.-Prof. Dr.-Ing. Mirko Hornung
	2.	Univ.-Prof. Dr.-Ing. Horst Baier

Die Dissertation wurde am 12.12.2013 bei der Technischen Universität München eingereicht und durch die Fakultät für Maschinenwesen am 11.07.2014 angenommen.

ABSTRACT

One of the primary applications of unmanned aerial vehicles is surveillance. A low altitude surveillance aircraft allows the use of light sensor payloads in a small airframe. This reduces operational cost. As surveillance often needs to be conducted covertly, the capability of silent flight enables the use of low altitude aircraft. Electric propulsion systems operate significantly more silent than combustion engines. Due to the low specific energy of batteries they are limited in performance and endurance. Hybrid-electric propulsion systems combine the advantages of both systems by enabling a high performance and long endurance aircraft to fly electrically and thus more silently. They are therefore very well suited for surveillance missions.

Existing methods for the design of aircraft with hybrid-electric propulsion system do not satisfy the three basic requirements for preliminary design methods: accuracy, high computational efficiency and generic applicability. Therefore, the first objective of this study is to introduce a method for the design of small unmanned hybrid-electric aircraft that does comply with the demands. The method's core is a propulsion system design procedure. It is embedded in an aircraft design scaling process. The integrated propulsion system component models ensure accuracy by the use of power state variables. State variables allow a more accurate prediction of energy converters' efficiency than with power-based approaches. In addition, the method makes use of surrogate models for the propulsion components. These surrogate models are derived from commercial product databases with emphasis on a computationally efficient formulation. This means that regression functions are preferred over interpolation. The surrogate models are formulated continuous and the underlying databases cover the complete requirement space. This contributes to their generality. A full factorial optimization scheme is applied to the propulsion system design procedure.

The second objective of this study is the analysis of hybrid-electric propulsion systems. The identification of basic characteristics can be used for the reasonable consideration of hybrid-electric aircraft in the design process. The strongest mass driver is the battery. The higher the mission's electric flight time ratio is, the heavier the aircraft gets. For short flight times, hybrid-electric offer advantages in fuel and energy consumption due to the more efficient use of the internal combustion engine and its shorter use. The higher efficiency is caused by the combined use of engine and electric motor at maximum power demand and the resulting better balanced torque demand between the flight phases. For longer flight times the increased takeoff mass and the resulting power demand outbalance the efficiency advantages of hybrid-electric aircraft.

KURZFASSUNG

Eines der Hauptanwendungsgebiete von unbemannten Fluggeräten sind Beobachtungsmissionen. Um die Betriebskosten zu minimieren, sollen diese Missionen oft in geringer Flughöhe durchgeführt werden. Dies ermöglicht die Nutzung leichterer Sensorik und somit auch kleiner Fluggeräte. Eine weitere Anforderung kann die unbemerkte Beobachtungsmission sein. Eine niedrige Flughöhe erfordert dann ein hinreichend leises Fluggerät. Elektrische Antriebssysteme arbeiten deutlich leiser als Verbrennungsmotoren. Da Batterien aber eine wesentlich geringere Energiedichte aufweisen als fossile Kraftstoffe, sind elektrische Fluggeräte in Leistung und Flugdauer beschränkt. Hybridantriebe kombinieren die Vorteile beider Antriebssysteme und ermöglichen so leistungsfähige Fluggeräte, die lange Missionen absolvieren, aber auch elektrisch und damit leise fliegen können. Deshalb sind sie für Überwachungsmissionen besonders gut geeignet.

Flugzeugentwurfsmethoden werden nach drei elementaren Anforderungen bewertet: Genauigkeit, effiziente Umsetzbarkeit und generische Anwendbarkeit. Diese Kriterien werden von gegenwärtigen Entwurfsmethoden für Flugzeuge mit hybridem Antriebssystem nicht erfüllt. Deshalb ist das erste Ziel dieser Arbeit die Einführung einer Entwurfsmethode für kleine unbemannte Fluggeräte mit hybriden Antriebssystemen, die diesen drei Anforderungen gerecht wird. Die Kernfunktionalität der Methode ist die Auslegung des Antriebssystems. Die dabei verwendeten Modelle der Antriebskomponenten erreichen hohe Genauigkeit durch die Nutzung von Zustandsvariablen. Die Zustandsvariablen ermöglichen eine genauere Bestimmung der Wirkungsgrade von Energiewandlern als leistungsbasierte Ansätze. Im Hinblick auf eine effiziente Umsetzung werden Ersatzmodelle der Antriebskomponenten erstellt. Die Ableitung stetiger Regressionsfunktionen aus Datenbanken kommerzieller Produkte wird dabei Interpolationen vorgezogen. Ein vollfaktorieller Optimierungsansatz wird in die Antriebsauslegung integriert. Das zweite Ziel dieser Arbeit ist die Analyse hybrider Antriebssysteme. Die Identifizierung der grundlegenden Leistungsmerkmale ermöglicht eine sinnvolle Berücksichtigung im Entwurfsprozess. Die Batterie ist die größte Einzelmasse des Systems. Je höher der Anteil elektrischer Flugzeit an der Gesamtflugzeit ist, desto schwerer wird das Fluggerät. Für kurze Flugdauern zeigt sich beim Hybridantrieb ein im Vergleich zum konventionellen Antrieb geringerer Kraftstoff- und Energieverbrauch durch die kürzere und effizientere Nutzung des Verbrennungsmotors. Der höhere Wirkungsgrad ist bedingt durch die gleichzeitige Nutzung von Elektro- und Verbrennungsmotor bei maximalem Leistungsbedarf und die damit gleichmäßigere Drehmomentanforderung. Für längere Flugzeiten wird dieser Vorteil durch die höhere Masse und den daraus resultierenden höheren Leistungsbedarf aufgehoben.

ACKNOWLEDGEMENTS

This thesis resulted from my work as research scientist with the Institute of Aircraft Design (Lehrstuhl für Luftfahrtsysteme) of Technische Universität München. It bases on knowledge I gained from several research projects. Parts of the method presented in this thesis were developed by me in the project DemUEB Phase 3 (Demonstration of the use of unmanned aircraft in Bavaria) funded by the Bavarian Ministry of Economic Affairs, Infrastructure, Transport and Technology, in which the Institute of Aircraft Design participated as sub-contractor of Cassidian (Airbus Defence and Space).

In the creation of this thesis I was supported by several people, to who I want to express my gratitude. Especially to Mirko Hornung, who supervised this thesis and gave valuable advice. Moreover I want to thank Horst Baier for the evaluation of the thesis as second supervisor and Florian Holzapfel for chairing the examination board.

In my time at the university I had the great pleasure to work next door to my close friends Bastian Figlar and Benedikt Mohr. Their presence not only resulted in an enjoyable workplace atmosphere, but also ensured me support, for which I am very grateful. The same applies to Sebastian Speck and Daniel Paulus with who I cooperated in several projects and who also under high work load were ideal work mates and became good friends. Discussions with Peter Phleps and Philipp Böck combined constructiveness and cheerfulness. Christian Rößler and I cooperated in several unmanned aircraft projects, in which I learned to know him as a very reliable and dedicated colleague and an outstanding expert in unmanned aircraft and electric propulsion.

There are several persons I want to thank outside the university. Daniel Meindl and Alvaro Carrera Acosta supported me with their optimistic non-engineering view on my research activities. Andrea Eltahir challenged me not to be satisfied with the achieved, while Philippe let me participate in his enormous excitement for aviation and his already impressive technical knowledge. The thesis defense was largely eased for me by the care of Katrin Käppner.

I want to use the prominent position of the last paragraph to thank my family. My parents not only enabled me to receive the education leading to this thesis but also supported me at all times. Their vita and that of my brother Stefan always was an inspiring example of dedication and how to reach personal goals sincerely.

Munich, 22nd October 2014

CONTENT

1 INTRODUCTION

1.1 Hybrid-Electric Propulsion Systems as a Transition Technology

Today's mobility is based on fossil fuels and on the assumption that their supply will be continuing. As forecasts show this assumption is false, new ideas are needed for the mobility of tomorrow. One of those is electric propulsion. While used for decades in railroads, its use in transportation systems with mobile power storages was enabled by batteries with increasing specific energy only in the recent past. From an ecological view, electric propulsion systems do not generate emissions at the vehicle itself. The emissions created during the conversion of the energy used for charging of electric energy storages depend on the prevailing energy mix. For aircraft, electric propulsion systems have further specific advantages: They almost eliminate all propulsion system noise emissions except for the propeller noise. In addition they are more reliable, cleaner, easier in handling and do not require inflammable agents. Disadvantages are the significantly lower specific energy compared to fossil fuels and the sensitivity of new battery technologies to physical impacts and atmospheric conditions. From a certain scale on, the high mass of the battery-electric propulsion systems make them impractical. Intensive research is done on alternative power sources to the battery, such as the photovoltaic cell and the hydrogen fuel cell, and their application in aircraft. A more quickly applicable approach is the hybrid-electric propulsion system. A hybrid propulsion system (from Latin hybrida) combines two or more different power converters or energy sources. A hybrid-electric propulsion system within this work is defined as a combination of a battery-powered electric motor and an internal combustion engine and can be seen as a transition technology from fossil fuel to electric propulsion. Hybrid-electric propulsion systems moved into the public focus in the late nineteen-nineties, when they were first used in series production automobiles. There, the objective is to lower fuel consumption. Three advantageous effects in the interaction of electric motor and combustion engine contribute to the hybrid-electric system's efficiency:

- The combustion engine almost always runs in its most efficient operating point, additionally converted energy is stored in the battery, at low speeds and at rest it is turned off.
- The electric motor propels the vehicle at low speeds and assists the internal combustion at high power commands.
- Braking energy is recovered by a generator and stored in the battery

Although the given effects allow a downsizing of the engine, a hybrid-electric propulsion system is generally heavier than a conventional one due to the additional

electric components. The given advantages cannot be transferred to aircraft applications one-by-one, because an automotive driving cycle differs essentially from an aircraft's mission profile. The aircraft mission contains significantly less load changes, so that energy recuperation and low speed phases may not relevantly contribute to fuel efficiency.

The missions performed by unmanned aerial vehicles (UAV) mainly have the objective to gather and distribute information. The applications and payloads are manifold with new concepts emerging constantly. The society benefits from the use of UAVs especially by excluding the pilot from the immanent danger of being airborne. Furthermore UAVs may carry out a mission with a smaller vehicle compared to manned aircraft. This allows better cost and energy efficiency. The smaller size of UAVs combined with the reduction of possible harm to human life makes them a very suitable platform to introduce new aircraft technologies.

1.2 Motivation and Objective

Unmanned aerial vehicles can be advantageously employed for aerial surveillance, which makes it one of their major applications (GUNDLACH, 2012). For certain missions it is necessary to conduct the surveillance undetectably. A small, low-altitude UAV offers advantages in cost with both, the airframe itself and a less sophisticated close-range sensor payload. To use such an aircraft for clandestine surveillance, it is mandatory to keep its acoustic signature as low as possible. An electric propulsion system is the best choice for this objective, but strongly limits the endurance and range due to the low specific energy.

An aircraft mission consists of several functional flight phases with different requirements. A surveillance mission is composed of the eponymous phase, take-off and climb, the cruise flight to and from the surveillance area and descent and landing. The central issue in designing a conventional aircraft propulsion system is the sizing of the power plant to the maximum power phase, take-off and climb. During the cruise and surveillance phases, which usually occupy a much longer portion of the mission time, the power demand is lower and the plant runs in partial power. This goes along with energy losses and unsatisfactory efficiency for most systems, explicitly for the internal combustion engine.

Surveillance missions are therefore carried out more advantageously by hybrid-electric aircraft. They allow the combination of different energy converters or storages to optimize efficiency and capabilities in each flight phase. For a surveillance mission, this means that the surveillance phase is operated with silent electric propulsion only, whereas the internal combustion engine allows a fast or long-enduring cruise to and

from the surveillance area. Maximum power may be provided by the electric motor and the internal combustion engine together in dual-mode, so that both power units can be downsized compared to a conventional system. The challenge in designing a hybrid-electric aircraft is to outbalance the increased mass resulting from electric propulsion with increased efficiency as far as possible.

The first objective of this study is the development of a preliminary design method for small unmanned hybrid-electric aircraft. The key element of the method is the propulsion system design. The second objective is the quantitative assessment of hybrid-electric aircraft in terms of takeoff mass, fuel and energy consumption using the design method. The results allow a first insight into hybrid-electric aircraft design trends. This enables the aircraft designer to identify for which mission and which requirements hybrid-electric aircraft should be considered as a design alternative.

Preliminary design methods are demanded to be accurate, as generic as possible and to require as little computation time as possible, so that a large design space can be explored quickly. For hybrid-electric propulsion systems, only power-based design methods are available. A power-based model describes an energy converter's operation based on its output or input power. Power-based models do not allow an accurate determination of an energy converter's efficiency, as power alone does not sufficiently describe the state the converter is in. For more precise performance estimation, the developed design method is composed of models based on state variables. State variables within this study are defined as the factors of power. In the mechanical domain these are velocity and force or rotational velocity and torque. For electrical power, current and voltage are the state variables, and in the chemical domain mass flow and lower heating value. A more figurative formulation used by RIZZONI, GUZELLA & BAUMANN (1999) names the first variable in the above pairs the flow variable and the second the effort variable.

Models based on state variables exist for battery-electric or fuel cell systems. They are either generic, but derived too globally for the specific use case of unmanned aircraft with highly efficient components, or discrete. Discrete models access existing propulsion system component look-up tables. This increases computation time to a value impractical for preliminary design and violates the demand for generality. Suitable models for internal combustion engines are neither available. This study therefore introduces continuous state variable models and integrates them to a hybrid-electric aircraft design method that complies with the three demands of high accuracy, generality and low computational time.

1.3 Scope

A hybrid-electric propulsion system is applicable as primary propulsion system to configurations that are conventionally powered by internal combustion engines or electric motors. Those configurations include unmanned, ultralight and general aviation aircraft. In this study only fixed-wing unmanned aircraft up to 150 kg takeoff mass are regarded. This limit is set by German regulations (DEUTSCHER BUNDESTAG, 2011; HIRLING & HOLZAPFEL, 2012).

Unmanned aircraft with surveillance missions are a promising field of application for hybrid-electric propulsion systems for the reasons described above. Also, they allow showing basic effects of the hybridization, as certification regulations are less restrictive than for manned aircraft.

1.4 Organization of Thesis

Following this introduction, chapter 2 summarizes fundamentals of hybrid-electric propulsion system components and their combination within the different possible architectures. Furthermore, the state-of-the-art of each component is described. Research projects focusing on hybrid-electric propulsion systems and existing aircraft are briefly introduced.

In chapter 3, the design method is developed. The first part describes the propulsion system design procedure and its integration into an aircraft design process based on scaling a baseline configuration. The second part introduces the component models used in the propulsion system design procedure. The models' capabilities commonly include determination of the efficiency and mass estimation. Mass prediction models are developed for the propeller, the internal combustion engine, the fuel tank, the electric motor, the electronic speed controller and the battery. Efficiency estimation is introduced for the propeller, the internal combustion engine and the electric components: electric motor, electronic speed controller and battery.

The developed method is used to design, analyze and discuss hybrid-electric aircraft in chapter 4. The first part is the exploration of a requirement space defined by varying payload and flight time. Takeoff mass, energy and fuel consumption of hybrid-electric aircraft are analyzed and set in relation to battery-electric and internal combustion engine aircraft. The second part describes hybrid-electric aircraft's sensitivity to variation of the parameters electric flight time ratio, battery specific energy and additional mass. Furthermore, challenges in the computational implementation of the method and their implications are discussed.

Chapter 5 summarizes and evaluates the achievements of this study. The first section recaptures capabilities and limitations of the design method and its integrated models and indicates possible future improvements. The second section recapitulates the analysis of hybrid-electric aircraft and provides an outlook on their potential future development.

2 FUNDAMENTALS OF HYBRID-ELECTRIC PROPULSION SYSTEMS

The term hybrid propulsion system is used for manifold technologies and systems. This chapter aims to constrain it and to present systems relevant for the application in unmanned aerial vehicles and their components. In chapter 2.1, the propulsion configurations mostly used in automotive or aircraft systems are described, assessed and compared. In chapter 2.2, the description of the components necessary for these configurations follows. The components include the propeller, the electric motor with controller, the battery, the internal combustion engine and fossil fuels. For each component, the principle of operation is explained and which specific technology might be most suitable for the use in unmanned aircraft. Furthermore, the state-of-the-art and a technology forecast are given. Chapter 2.3 contains realizations of hybrid-electric propulsion systems or projects working on their design for both unmanned and manned aircraft.

2.1 Hybrid-Electric Configurations

The hybrid-electric propulsion system is here defined as the combination of an electric motor and an internal combustion engine within one power plant. There are several possibilities of combining the components. The three configurations mainly used in the automotive sector are described in the next sections: the series configuration, the parallel configuration and the series-parallel configuration. In the series configuration, one power unit propels the aircraft and the energy storage is hybridized. In the parallel configuration, two power units, fed by one power source each may drive the propeller. The series-parallel configuration is a combination of both.

2.1.1 Series Hybrid Configuration

In a series hybrid configuration, as shown in Figure 1, the propeller is only driven by the electric motor. The internal combustion engine's mechanical power is converted into electric power by a generator. It is used either to directly provide power to the electric motor or to charge the battery.

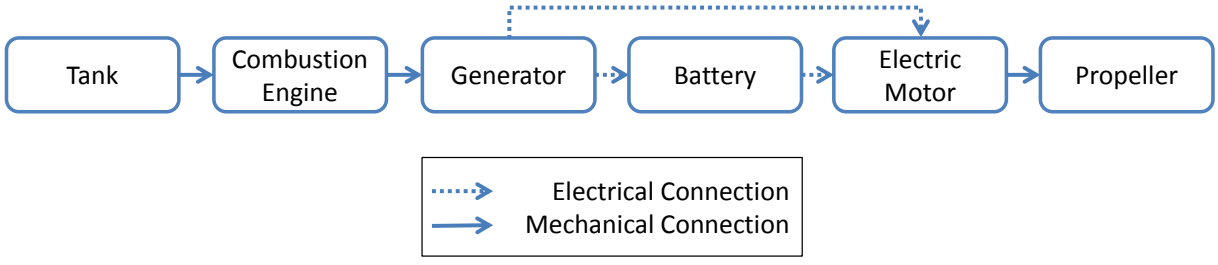

Figure 1: The series hybrid-electric configuration (modified from SCHOEMANN & HORNUNG (2012))

The advantage of the series configuration is that the combustion engine is completely decoupled from thrust generation and can hence constantly run in its optimum operating point. Furthermore, the simplicity of the concept allows an easy propulsion control. As a disadvantage, the electric motor needs to provide the complete propulsion power alone, so that it needs to be dimensioned for the maximum power phase and thus is heavy. The inclusion of a generator adds further mass to the configuration. Regarding the efficiency of the configuration, only a small portion of the fossil fuel's energy is used for propulsion, as mechanical power is converted to electrical and back instead of being used to drive the propeller directly.

2.1.2 Parallel Hybrid Configuration

The parallel hybrid configuration, depicted schematically in Figure 2, is characterized by two parallel propulsion paths, combustion and electric, which are coupled mechanically. The electric motor and the combustion engine may both drive the propeller alone. Furthermore, they may drive it in combination. Torque of both power units is added using torque coupling. The parallel configuration also allows charging the batteries, when the internal combustion engine drives the propeller and the electric motor, which is then used as a generator. It is reasonable to provide a mechanical disconnection device in both propulsion paths. Otherwise, when running isolated, the additional torque of driving the inactive power unit must be provided by the active machine.

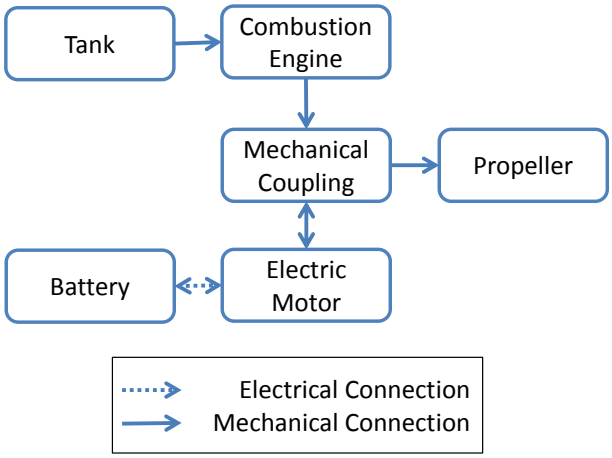

Figure 2: The parallel hybrid-electric configuration (modified from SCHOEMANN & HORNUNG (2012))

As the maximum power is provided by motor and engine together, both may be sized smaller than in isolated systems. With the possibility of both power units individually driving the propeller, the parallel configuration may provide full propulsion redundancy. The disadvantages of this configuration are the extra mass of a mechanical coupling and a more sophisticated propulsion control system. Furthermore the internal combustion engine's operation may be less optimal than in a series

configuration, as it is involved in thrust generation and consequently used more dynamically. Disconnecting the engine from the power train may be done with an electromagnetic clutch or a free wheel. An electromagnetic clutch adds complexity and mass. A free wheel however only transfers power from the engine, so that it does not allow starting the engine with the primary electric motor and hence makes a starter motor and additional mass necessary. The only quantitative comparison of series and parallel configuration for UAV was done by HARMON (2005). For a 13.6 kg takeoff mass system, the parallel configuration is 8 % lighter.

A special case of the parallel configuration is an innovative concept with aerodynamic coupling presented by HISEROTE & HARMON (2010). There, the aircraft is equipped with two propellers aligned on the longitudinal axis. One is driven by a battery-electric system, the other one by the combustion engine. Charging the batteries is achieved by using the propeller as a windmill when the aircraft is propelled by the combustion engine. Although both of the systems may operate autonomously in their most efficient state of operation, the low efficiency of the aerodynamic coupling makes this concept disadvantageous.

2.1.3 Series-Parallel Configuration

The series-parallel configuration, also known as power-split configuration, is a combination of the two configurations described above. As depicted in Figure 3, propeller, internal combustion engine, electric motor and generator are connected to a planetary gear. It makes load distribution more flexible and allows the engine to operate in its most efficient rotational velocity range more independently from the current thrust requirement.

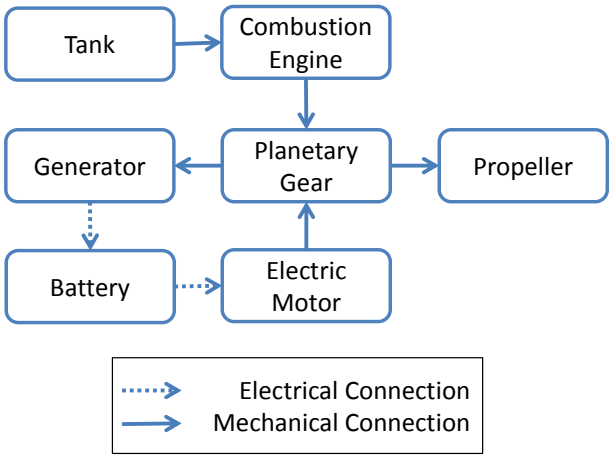

Figure 3: The series-parallel hybrid-electric configuration (modified from SCHOEMANN (2011))

A further advantage of the series-parallel configuration is the possibility to disable the combustion engine without mechanically disconnecting it from the power train. The

planetary gear makes the series-parallel configuration the most in design and control. In terms of mass, the planetary gear and additional generator make a series-parallel system heavier than a parallel one.

2.2 Components of Hybrid-Electric Propulsion Systems

The five fundamental propulsion components arranged in Figure 4 are typical elements of a hybrid-electric propulsion system: the propeller as thrust generator, two energy converters, the internal combustion engine and the electric motor as well as two power sources, the battery and fossil fuel. The battery is here categorized as energy storage, although it combines energy storage and conversion of chemical energy into electric energy. Auxiliary components, necessary to integrate the formerly mentioned into a working system, are the electric motor controller, a fuel tank and a coupling.

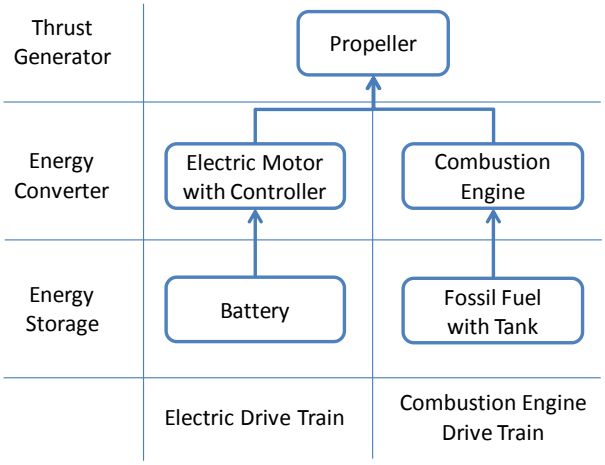

Figure 4: Fundamental components of a hybrid-electric propulsion system

In the following chapters the basic function and state-of-the-art of the five main components are described. The figures of merit regarded for an energy converter are its efficiency and specific power. Efficiency is the ratio of output power to input power. It is a dimensionless indicator for energy losses in the converter. Specific power is the ratio of the output power to the mass of the converter.

Energy storages are evaluated primarily by their energy content. The key properties are specific energy and energy density. The former, also denominated as lower heating value (LHV) for fuels, relates energy to mass, the latter to volume. For fuels, the power output is defined by the supplied machine. Electrochemical energy storages in contrast may have a limited power output. Analog to the energy content, the evaluation parameters are specific power and power density, related to mass and volume, respectively.

2.2.1 Propeller

The propeller converts rotational mechanical energy into translational mechanical energy. The application of torque at a rotational velocity results in the generation of thrust that causes the air vehicle to move at a translational velocity. Aerodynamically, the propeller blade may be seen as a rotating wing. The blades generate lift, when in motion through the air. A portion of this lift, depending on the angle of attack and the blade twist angle, contributes to the propeller thrust. The drag implied in the thrust generation defines the necessary torque to rotate the propeller. As a propeller blade, which is moved at constant rotational velocity, experiences varying local velocities, the propeller has a varying distribution of chord and twist over its radius. Furthermore, the blade may be swept and various airfoils may be used for the different blade sections. Propeller losses are caused by its drag. The drag types regarded are, analog to the wing, friction drag, form drag, induced drag and wave drag.

The propeller geometry and the relative wind at the blades, defined by the free-stream and the rotational velocity, are the drivers of the generated thrust and the propeller efficiency. In terms of thrust, a higher value may be obtained with an increased rotational velocity, an increase in propeller disc diameter or an increased number of propeller blades. Generally a bigger diameter propeller at low rotational velocity works more efficient than a small diameter propeller at high rotational velocity (ANDERSON, 1999). Both, thrust and efficiency are highly dependent on the blade airfoil and twist, as may be read in detail in PHILIPS (2009) and WALD (2006).

Main design restrictions for a propeller are its tip Mach number and ground clearance. The relative velocity of the propeller is largest at its tip. There, the critical Mach number should not be exceeded in order to avoid a significant drop in efficiency and increased noise. A reduction of the tip Mach number can be achieved by either reducing the propeller diameter or its rotational velocity. Ground clearance of a propeller may be secured either with a high enough mounting position, a small diameter or foldable blades. For the propeller sizes suitable for small unmanned aircraft, commercial models made of carbon fiber reinforced plastics (CFRP) are widely available. They are more lightweight and more rigid than wooden propellers.

In electric propulsion systems the propeller is a main source of noise. For the reduction of its acoustic signature operational approaches (SPECK, WILBERG & HORNUNG, 2013), dedicated aircraft configurations and the optimization of the propeller geometry (SPECK, PFEFFERKORN, KICKER & HORNUNG, 2013) are promising approaches.

2.2.2 Electric Motor

The electric motor is a machine that converts electrical energy into mechanical energy. The motor consists of a moving part, the rotor, and a static part, the stator. Magnets are mounted on both parts. As the magnets on the stator attract and repel those on the rotor, the latter spins. In order to keep the movement ongoing, the polarity of the magnets has to be changed constantly. In a direct-current (DC) electric motor, electromagnetic coils are placed on the rotor. They are connected to a commutator ring switch on the shaft, which runs by carbon brushes connected to the input voltage. Reversing polarity as described comprises several disadvantages. The sliding contact of the brushes and the commutator causes friction, noise, sparking, and heat dissipation.

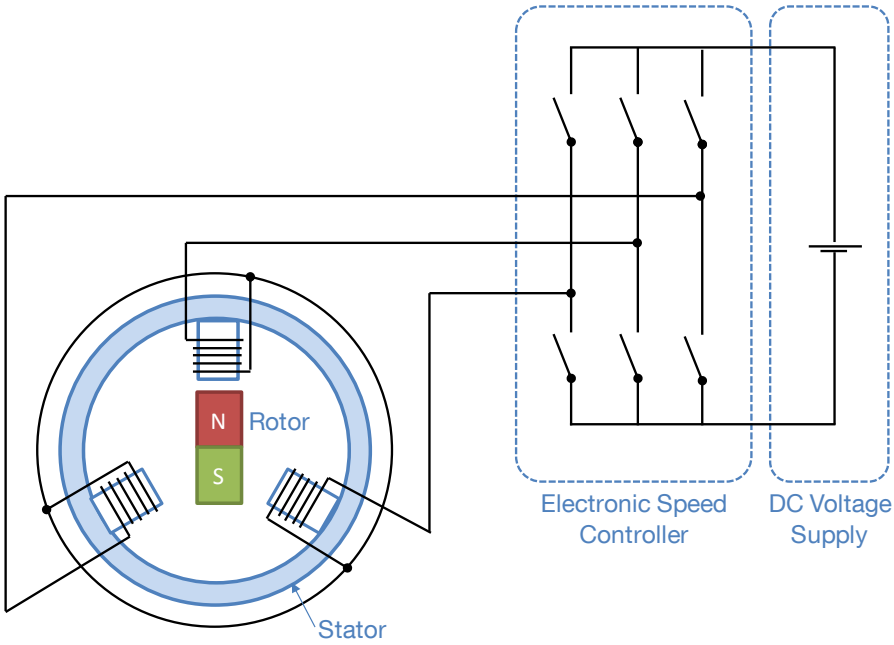

Figure 5: Schematic design of a brushless DC motor with electronic speed controller (modified from RÖßLER (2011) and RETZBACH (n.d.))

The concept of a brushless direct-current electric motor (BLDC) is based on the electronic phase commutation. Permanent magnets are placed on the rotor, electromagnetic coils on the stator. The brushless DC motor alone is not a DC motor, as it is three-phased. For its operation an electronic speed controller (ESC) is mandatory. The electronic speed controller converts the direct-current input into an approximated sinusoidal three-phase current using transistors. The schematic concept is illustrated in Figure 5. The information on the rotor's current position is obtained using either Hall Effect sensors or sensors measuring the back electromotive force. The back electromotive force (back-EMF) is induced into the coil by the change of magnetic flux. When a coil is located directly opposite of a rotor permanent magnet pole, no voltage is induced. This information can be used to determine the rotor

position. The BLDC motor's disadvantage of requiring a controller is largely outbalanced by its advantages. The elimination of the brushes reduces friction and heat dissipation. Both contribute to a higher motor efficiency. The reduction in heat dissipation allows the motor to accept higher current before reaching its critical temperature. Consequently it has a higher specific power than the brushed motor. The spark-free commutation increases the electromagnetic compatibility (EMC) of the brushless motor and reduces maintenance requirements.

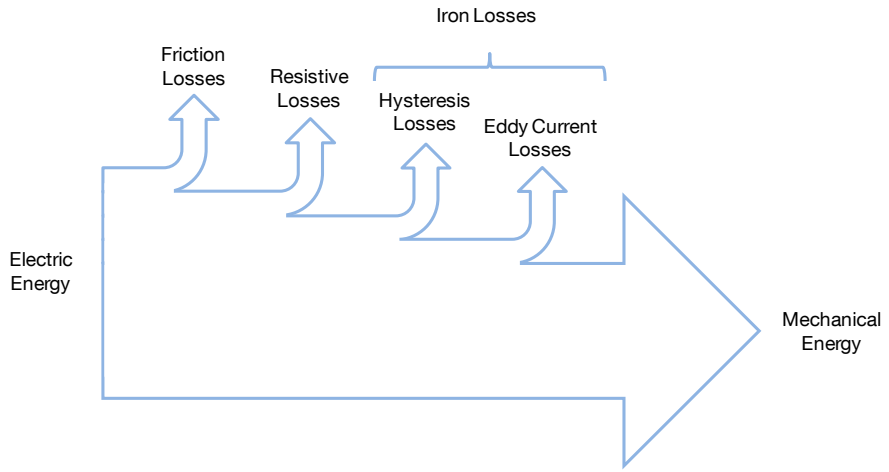

Figure 6: Energy balance of an electric motor (arrow sizes not to scale) (SCHOEMANN, 2011)

The energy balance of the brushless DC electric motor is shown in Figure 6. In the figure, the arrows are not drawn proportionally to the quantities of losses. Maximum efficiencies of brushless machines may range up to well above 90 %. Three types of losses occur in an electric motor: friction losses, resistive losses and iron losses. Friction losses comprise friction at the bearings and the drag caused by the rotor moving through air. Resistive losses describe the heat dissipation occurring for currents flowing through conductors, here especially the coil wires. The iron losses contain loss types that are mainly located in the stator iron core, notably hysteresis and eddy current losses. Hysteresis losses describe the energy losses through alternating magnetization of the iron core. Eddy currents are caused by the induced back-EMF. The flow of eddy currents through the iron core results in resistive losses, named eddy current losses.

In the electronic speed controller, further losses occur due to the heat dissipation caused by the switching processes. In part load operation, these losses are significant, because each phase signal is pulse-width modulated in high frequency in order to reduce the effective voltage applied.

There are two main types of BLDC motors distinguished by their rotor location. In an outrunner arrangement, the rotor runs around the stator, whereas in an inrunner arrangement it runs within the stator. Performance characteristics vary between the

two types. The bigger diameter of the rotor allows outrunner motors to build up bigger torque, whereas the higher inertia leads to lower rotational velocities. Inrunner motors respectively create lower torque at higher rotational velocities. The position of the electromagnetic coils outside at the casing allows easier heat management of the inrunner motor. This contributes to a typically higher efficiency when compared to the outrunner. As a consequence of the high rotational velocity, inrunner motors are often used with gearboxes. In that case, the implicated additional energy loss and mass needs to be weighed with the lower motor efficiency of the outrunner.

Another possibility to vary the relationship of torque and rotational velocity of a BLDC motor is the wiring of the three phases. Wired in a star connection the motor provides more torque at lower rotational velocity, whereas in a delta connection it is the other way round (RÖßLER, 2011, p. 24)

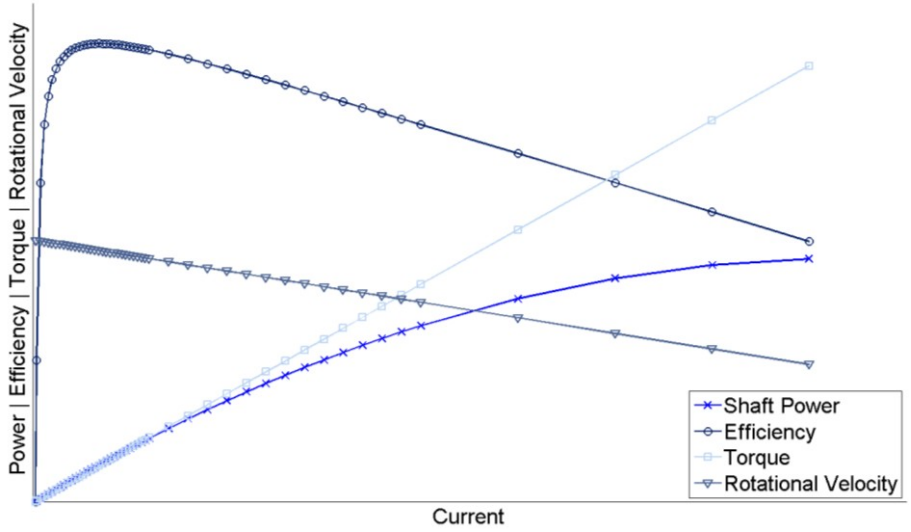

Figure 7: Operational characteristics of a BLDC electric motor

The qualitative operational characteristics of a BLDC motor are shown in Figure 7. The exemplary data given assumes a constant voltage supply and the motor running at full load. As it can be seen there, the electric motor provides maximum rotational speed in no-load condition. An increase in load leads to a linear increase of the torque provided. The maximum torque is limited by the maximum current the motor can bear before reaching it critical temperature.

The basic description of the brushless electric motor in this chapter is based on HANSELMANN (2006), in which the interested reader may find more detailed information about operation and design of this engine type.

An analysis of high-altitude operation of a commercial UAV electric motor was done by MCELROY & LANDRUM (2012). In a vacuum chamber, in which pressure was reduced while temperature was kept constant, a significant decrease in thrust and

power was observed for one combination of electric motor, electronic speed controller and propeller. The electric motor performance is limited at higher altitudes due to a decreased air convective heat transfer coefficient and the resulting reduction in cooling.

A future technology for electric motors is the high temperature superconducting (HTS) machine. The non-existing ohmic resistance of superconductors and strong magnetic fields allow the realization of lighter and more efficient machines. A use for manned aircraft is envisaged (SIEMENS, 2013), whereas no declaration of intent to downsize the technology to a size suitable for UAV has been published yet.

2.2.3 Battery

A battery is an electrochemical device that provides electrical voltage and may be used as storage for electric energy. The battery as a system consists of one or several cells connected in parallel or series. Each cell is composed of two electrodes in an electrolyte. The positive electrode, the cathode, is commonly a metal oxide, its negative counterpart, the anode, a metal. During discharge, voltage is generated in a redox reaction. When the electrodes are introduced into the electrolyte both experience oxidation. The less noble the electrode material is, the higher is the rate of oxidation. This creates an electric potential between the electrodes. When an electric consumer load is connected to the battery, a continuous electron flow from anode to cathode is established. The anode is oxidized, whereas the cathode material is reduced. The electric circuit is closed by the ion flow through the electrolyte. Cations flow from anode to cathode, whereas anions flow from cathode to anode. Certain cell types require a separator within the electrolyte that is only permeable for ions and prevents an internal short-circuit fault. The theoretical voltage, the battery can provide, depends on the potential difference of the two electrodes, which is defined by the chosen materials' standard reduction potentials. Anode materials have negative standard reduction potentials, for cathode materials they are positive. The energy content of a cell is governed by the electrochemical equivalent of a material. An overview of electrode materials pairs and their theoretical values for both standard reduction potential and electrochemical equivalent is given by LINDEN (2001, p. 1.11 ff.).

Battery cells can be divided into primary and secondary cells. Primary cells are intended for single use, whereas secondary cells may be re-charged. Primary cells may provide higher energy content, but for transportation applications cost and the imperative of sustainability dictate the use of secondary cells.

The basic requirement for a transportation battery is low weight. This led to research into Lithium based batteries. Lithium is the most lightweight metal on earth and has a

very low negative standard reduction potential and a high electrochemical equivalent. The use of pure Lithium as anode material resulted in instable cells. During the charging process the solute Lithium re-attaches in incontrollable structures called dendrites, which, by growing to the cathode, may cause a short-circuit fault and lead to fire or explosion (RETZBACH, 2008). As a consequence, Lithium was intercalated in more stable electrode materials. The applicable technology that emerged is the Lithium-ion battery that uses a Lithium metal oxide as cathode material and a carbon anode, commonly graphite.

The most widespread Lithium-ion battery type for aircraft models and unmanned aircraft is the Lithium-polymer battery, which uses a polymer as electrolyte. The abstinence of a liquid electrolyte in this battery type allows reducing the casing to a minimum and consequently leads to a low battery mass.

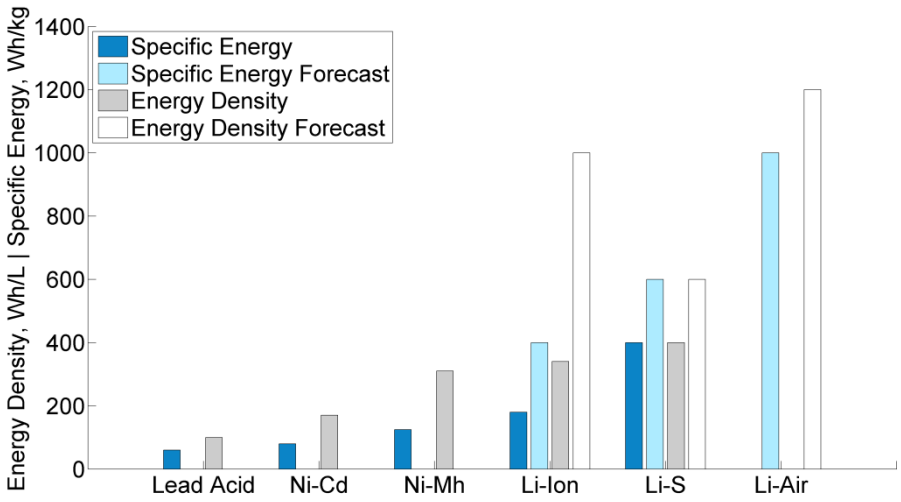

Figure 8: Energy properties of different battery types (Data from LINDEN (2001), SION POWER (n.d.) and CHRISTENSEN ET AL. (2012))

The Lithium-ion battery in comparison with other battery types has a very high specific energy. This can be seen graphically in Figure 8, where also the values for Lead-Acid, Nickel-cadmium (Ni-Cd), Nickel-metal hydride (Ni-Mh), Lithium-sulfur (Li-S) and Lithium-air (Li-Air) batteries are indicated. The value of 200 Wh/kg for current Lithium-ion batteries is not valid for every application. It may be reached in small cells for consumer electronics. A state-of-the art value derived from a database of Lithium-polymer batteries is 168 Wh/kg. For automotive application a lower value may be caused by a crash approved casing and monitoring electronics. The battery types with higher specific energy are not yet commercially available and discussed later in this chapter.

The Ragone plot in Figure 9 sets specific power in relation to specific energy for different battery types and super capacitors. In terms of specific power, the Lithium-ion battery is superior to other battery types. The Lithium-polymer battery is indicated

with a maximum specific power of below 1000 W/kg in Figure 9. A state-of-the-art value, derived from a database of commercial models is around 9000 W/kg, which in Figure 9 is indicated for very high power Lithium-ion batteries.

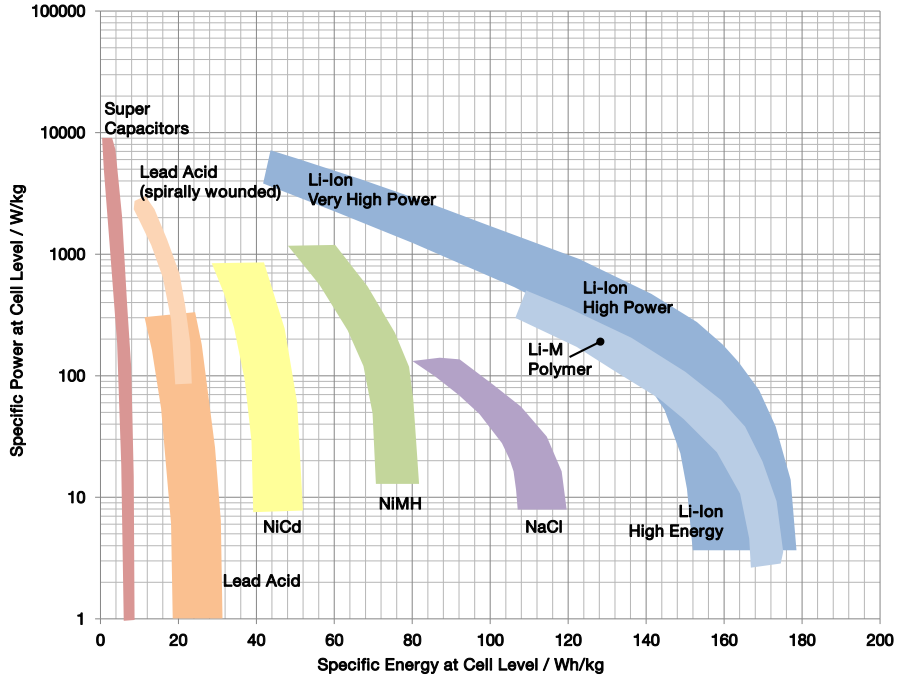

Figure 9: Ragone chart relating specific power and specific energy for different battery types (KUHN & SIZMANN (2012), with data from KÖHLER (2008))

Lithium-polymer batteries offer the advantages of high specific energy and power as well as the high number of possible charge and discharge cycles. There is no memory effect, i.e. the reduction of capacity due to incomplete discharge. The self-discharge rate can be neglected. According to RETZBACH (2008, p. 148) it is around 2–3 % per month. The disadvantages of Lithium-polymer batteries are mostly related to safety and may be controlled by proper handling. Excess charge or exceeding of the maximum operational temperatures can cause the decomposition of the electrodes or the electrolyte. This may result in the release of gases which may overstretch the casing and inflame when escaping. For the same reason, the battery is sensitive to physical impact. During the charging process care has to be taken that all cells of a battery are equally charged. Cells denying charge may lead to an excess charge of other cells. The common method to avoid this is a cell voltage monitoring and balancing system. Differences in charging capacities of cells may be production or wear characteristics. Another mistreatment to be avoided is depth discharge, the extraction of too much of the stored energy, which may lead to irreversible damage. A rule of thumb for the minimum voltage of a cell is 3.0 V or 20 % of the capacity to be left unused.

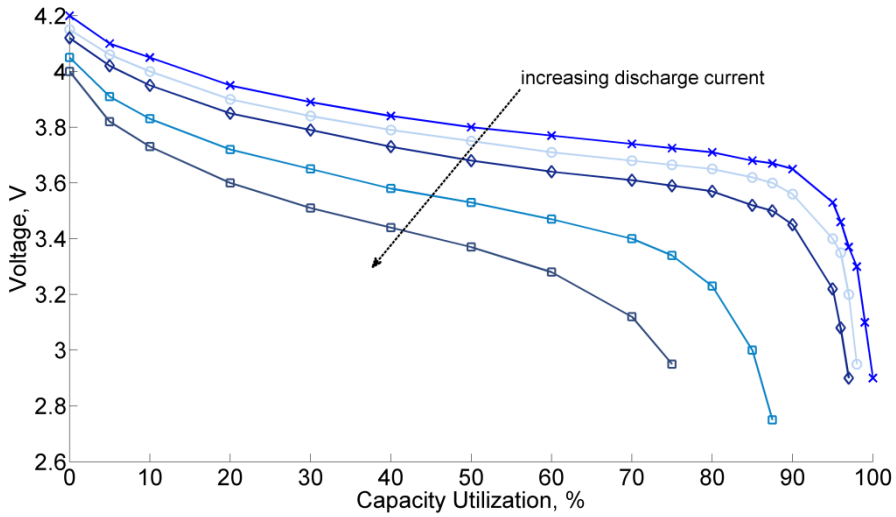

Figure 10: Discharge curves of a Lithium-polymer battery for various discharge currents (Data from LINDEN (2001, p. 35-77))

The discharge characteristics of a Lithium-polymer battery are shown in Figure 10. It can be seen, that there is voltage drop with extracted capacity and drawn current. The lower the drawn current is, the shallower is the drop in voltage over extracted capacity.

Energy cannot be ideally discharged from a Lithium-polymer battery. The main loss mechanisms according to SAHA & GOEBEL (2009) and RETZBACH (n.d.) are summarized in Figure 11. Resistive losses are most relevant for Lithium-polymer batteries.

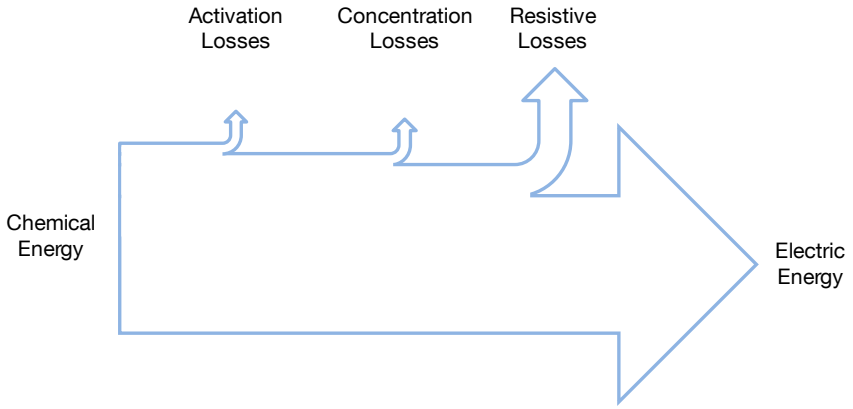

Figure 11: Energy balance of a Lithium-polymer battery (arrows not to scale)

The resistive losses result from the battery's internal resistance. Activation losses are mainly caused by the chemical reaction at the junction of electric and ionic conduction. Concentration losses refer to the losses caused by a difference in ion concentration within the electrolyte. The losses practically occur in a difference between the open-circuit voltage (OCV) of the battery and the terminal voltage.

A performance reduction may occur for low ambient temperatures. One main effect contributing to this is that ohmic resistances increase at low temperatures. As an

experience value, temperatures of below 15 °C may cause a notable impairment. The influence on specific energy is given in Figure 12. A further drop in available energy comes with battery age.

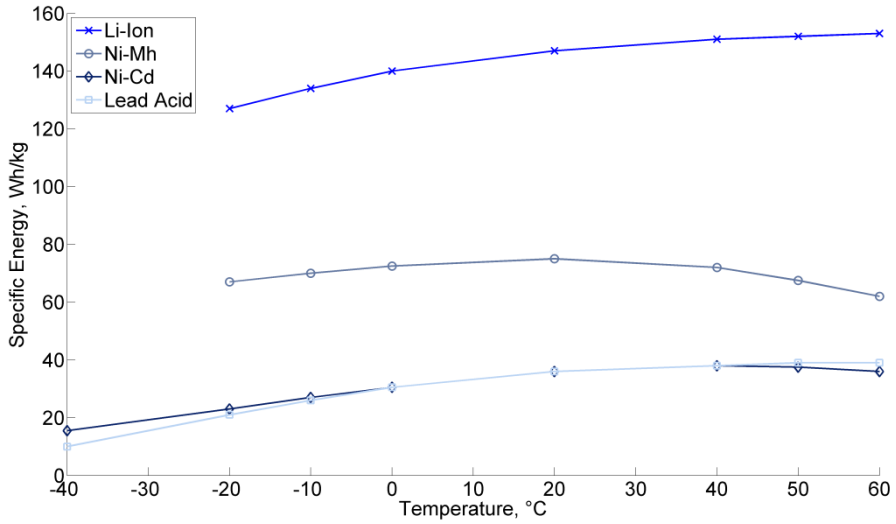

Figure 12: Influence of temperature on the specific energy of batteries (Data from LINDEN (2001, p. 22.5))

The specific energy of batteries is far below the values of fossil fuels, although having experienced a constant increase over the last twenty years (see chapter 2.2.5). For their wider application in transport it is mandatory to increase this value. The energy density of Lithium-ion batteries is expected to increase up to a value of 400 Wh/kg (CHRISTENSEN ET AL., 2012). Research into Lithium-based batteries with higher energy densities is ongoing. Two promising models are the Lithium-sulfur and the Lithium-air battery. Both do not use Lithium in intercalation material but enable its stable use as anode.

In Lithium-Sulfur batteries, the Lithium anode is combined with a carbon and Sulfur cathode. The energy density of current models reaches 350 Wh/kg, whereas for the future values of 600 Wh/kg are advertised (SION POWER, n.d.). Lithium-sulfur cells have been used in the unmanned endurance world record aircraft Qinetiq Zephyr (QINETIQ, n.d.).

The Lithium-air battery uses a Lithium anode and the oxygen of the ambient air or from a tank. In a review by CHRISTENSEN ET AL. (2012) a possible energy density of 1000 Wh/kg or more is expected. In a prediction on market entry by the same author it is assumed that the battery will remain in research for the next five years. Other experts foresee a market readiness of Lithium-Sulfur and Lithium-air batteries for electromobility in 2025 (THIELMANN, SAUER, ISENMANN, WIETSCHEL & PLÖTZ, 2012).

2.2.4 Internal Combustion Engine

The internal combustion engine converts the chemical energy stored in fuels into mechanical energy. The engine is kept in motion by the pressure rise caused by the combustion of fuel. Engine types may be distinguished by the number of strokes per work cycle and the method of ignition. In terms of the ignition method, either spark-ignition (SI) or compression-ignition (CI) is used. An SI engine is commonly known as petrol or Otto engine, whereas the CI engine is often referred to as Diesel engine, with both alternative terms referring to the fuel used in the engine or its inventor. The difference between SI and CI engine is, as implied in the names, that the air-fuel mixture in a SI engine is ignited using a spark plug, whereas in CI engine it is compressed to such an extent that it ignites itself. In CI engines the fuel is injected into the cylinder, whereas in basic SI engines fuel and air are mixed in the carburetor prior to entering the cylinder. Both engine types can be designed as two-stroke or as four-stroke engine. A four-stroke engine requires four strokes and two crankshaft revolutions per work cycle, a two-stroke engine only needs two strokes and one crankshaft revolution. The description of the engine types and their properties in this chapter is based on the text books by HEYWOOD (1988) and GSCHEIDLE (1994). In both detailed information on the different engine's design and operation may be found.

In CI engines the air-fuel mixture is compressed to higher pressures, which goes along with reinforced structure. In comparison with the SI engine it is heavier and has a higher moment of inertia. The higher pressure and mass result in higher torque at lower rotational velocities. Fuel injection leads to heterogeneous air-fuel mixture and combustion, perceivable in a louder and rougher operation. Combustion takes longer than in an SI engines, which contributes to the lower rotational velocity. The wide use of CI engines results from its higher efficiency. Thermal efficiency is increased because the air-fuel mixture is leaner and combustion takes place at higher pressure and higher temperature than in SI engines. The absence of a carburetor with a throttle plate increases the volumetric efficiency.

Four-stroke engines are used in the majority of automobiles, so that intensive research was done on the increase of efficiency and specific power of this engine type. Modern SI engines use electronic direct-injection systems instead of a carburetor. This allows more exact control of the air-fuel mixture and consequently more efficient operation. For modern automotive CI engines charging is common. Chargers compress the air going into the engine and allow increasing power without increasing the engine's displacement volume. Furthermore, pollutant emission is reduced and in some rotational velocity ranges and the efficiency is enhanced. The turbocharger as one common device is driven by an exhaust gas turbine. With the current effort to reduce

CO_2 emissions, one approach is to downsize the engine's displacement volume while keeping its power constant using charging (HUSS, HÜBNER & WACHTMEISTER, 2010). A light modification of the four-stroke cycle used with some combustion engines in hybrid-electric vehicles is the Atkinson cycle. In an Atkinson cycle the pressure in the combustion chamber is reduced to exhaust pressure. Using more energy released in the combustion process allows higher efficiencies but reduces the engine's power density (HEYWOOD, 1988, p.185).

The design of the two-stroke spark-ignition engine is simpler than that of the four-stroke version. The simplified scavenging process however may allow fresh charge with unburned fuel to escape as well as burnt mixture to remain in the cylinder. The unused fuel causes a low efficiency of the two-stroke engine and high emissions compared to four-stroke models. Fuel for two-stroke engines requires a lubricant additive, because the crankcase is used for compression and the crankshaft must be lubricated. The lubricant is not or only partly combusted in the process so that it contributes to the high emissions of the engine. The simplicity of the two-stroke engine is also its key advantage. It is low-priced and lightweight. The low mass together with its characteristic to execute a power stroke twice as often as a four-stroke engine gives it a higher specific power. Recent advances in combustion engine technology were not primarily applied to the two-stroke engine, because it serves niche markets. The users of motor scooters, snowmobiles or gardening tools are not as sensitive to optimized fuel efficiency as drivers of automobiles or managers of commercial road vehicle fleets. Nevertheless research was done on direct injection, turbo chargers and compression pumps and the results are promising (EHSANI, GAO, GAY & EMADI, 2005).

The Wankel rotary engine is a particular four-stroke SI engine in which a triangular rotor performs an eccentric rotary motion. The moving clearances between the rotor and the oval housing are used to conduct the four strokes. The Wankel engine executes one power stroke with each revolution. In addition to the low weight and volume of the engine this leads to a high specific power. The design of the engine allows a smoother run than with reciprocating piston engines. The absence of valves makes it more silent. The combustion chamber being constantly in motion may result in a slower or incomplete combustion, which is reflected in lower efficiency and more pollutant emissions. Manufacturing of a Wankel motor requires high precision and is cost intensive. High precision is especially needed for the sealing of the rotor apex. The disadvantages of the engine led to seldom use in automobiles. Recently an increased use of Wankel engines has been observed. It is for example used in a hybrid-electric vehicle concept (VOLKSWAGEN AG, 2013) and in the first manned hybrid-electric aircraft (see 2.3.2).

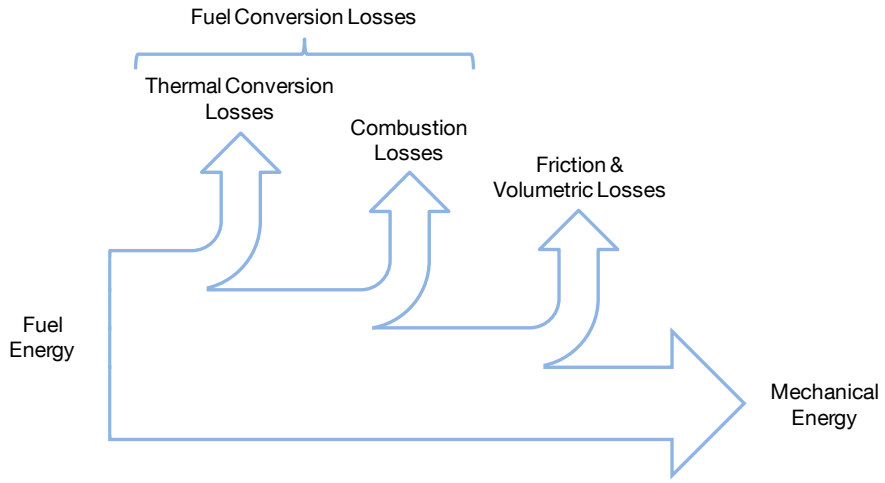

Figure 13: Energy balance of an internal combustion engine (SCHOEMANN, 2011)

The energy balance of an internal combustion engine is displayed in Figure 13. Fuel conversion losses represent the biggest part of losses. They comprise the combustion losses and the thermal conversion losses. Combustion losses stand for energy not released from the fuel due to incomplete combustion. Thermal conversion losses describe the released energy that is not converted into work, heat dissipation being the biggest part. Friction and volumetric losses occur due to the unavoidable mechanical imperfection of the engine. Volumetric losses are those that occur during the induction process. Maximum efficiencies for naturally aspirated automotive engines are 0.3 for a four-stroke SI engine, 0.42 for a four-stroke CI engine and 0.24 for a two-stroke SI engine (HEYWOOD, 1988, p. 887).

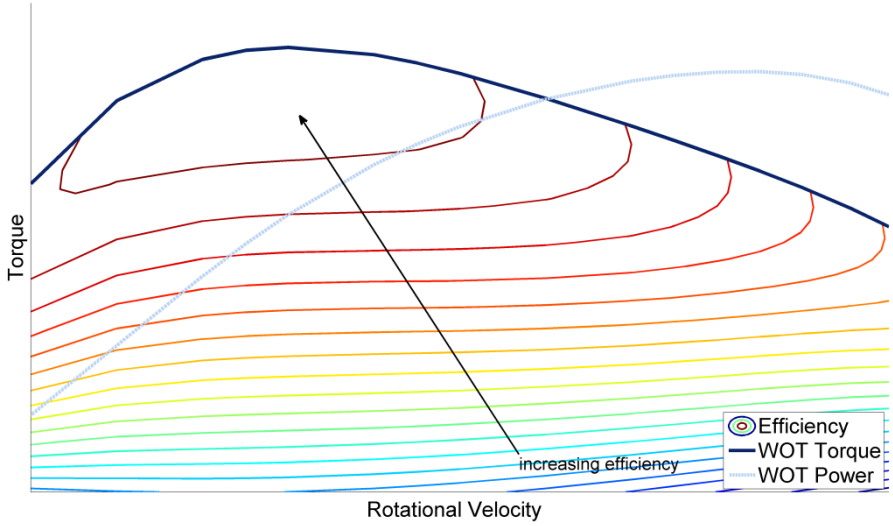

Figure 14: Torque, Power and Efficiency characteristics of an internal combustion engine (created with engine data from HENDRICKSON & MCGEER (1999))

The characteristics of an internal combustion engine's torque and power as a function of rotational velocity are given in Figure 14. Torque and power are plotted for the wide-open throttle (WOT) condition, which stands for the maximum possible torque,

and consequently power, at one rotational velocity. The engine's efficiency is depicted in form of an efficiency map. In the efficiency map lines of constant efficiency are given for the rotational velocity range and torque levels below wide-open throttle torque. Best efficiency is achieved at or slightly below WOT torque. The UAV engine with whose data Figure 14 is created achieves a maximum efficiency of 0.35 (HENDRICKSON & MCGEER, 1999). The torque curve is shallower than that of an electric engine, which is the reason for the use of a gearbox in automobiles. Another difference is the existence of an idle rotational velocity. The specific power of automotive combustion engines is between 400 W/kg for Diesel engines and 500 W/kg for SI engines (HEYWOOD, 1988, p. 58). The engines used for small UAV are significantly smaller than those in automobiles. Commercial engines with displacement volumes below 420 cm³ in a database assembled for this research (see Appendix B.2) have a specific power range of 1000 W/kg to 3500 W/kg. Inaccurate power indications by the manufacturers and the equivocality of which components are included in the motor mass indication may be reasons for the very high values. Other reasons include the simplicity of the small engines and their design for an operating life shorter than that of automotive engines.

As performance data are mainly published for automotive engines, the University of Maryland investigated small internal combustion engines with an experimental and a computational approach. The results include the statement that the performance of small engines may not be precisely predicted with common motor simulation tools (MENON & CADOU, 2007). Furthermore it was found out that the actual power output and efficiency may be significantly lower than stated by the manufacturer (CADOU & MENON, 2004). An efficiency of 8 % was measured for a 2.45 cm³ engine (MENON, MOULTON & CADOU, 2007). The bigger part of the small engines applicable for small UAVs uses carburetors. As reported by GREISER, MENGISTU, ROTRAMEL & HARMON (2011), a proper carburetor calibration may heavily influence its operational performance.

Internal combustion engines commonly cannot initiate operation without an auxiliary starter. On ground, engines may be actuated using the propeller, but in flight an aircraft engine needs a starter motor supplying sufficient torque.

2.2.5 Fossil Fuel

Fossil fuels store chemical energy that can be transformed into heat via combustion and into mechanical energy using a suitable heat engine. Transportation fuels are refined from crude petroleum oil. For internal combustion engines, there are two relevant fuel types: gasoline and Diesel.

Although small engines suitable for the use in UAV may be run with conventional automotive fuels, the focus shall be on aviation fuels, as with the professionalization of UAV operation, airfield ground infrastructure will be used.

Gasoline is the lighter of the two fuels and requires a more elaborate refining process. For aviation it is usually distributed under the name AvGas (Aviation Gasoline). Diesel is heavier than gasoline. In its properties it is very similar to kerosene that is used also for jet aviation. For both, the collective term heavy fuel is used. The most common standards for kerosene are Jet-A1 for civil aviation and JP-8 (Jet Propellant 8) in the military domain.

Table 1: Properties of fossil fuels (HEMIGHAUS ET AL., 2006)

	Aviation Gasoline	**Kerosene**
Gravimetric Density [g/L]	0.715	0.81
Specific Energy [MJ / kg]	43.71	43.28
Specific Energy [kWh / kg]	12.14	12.02
Energy Density [MJ / L]	31	35.06
Energy Density [kWh / L]	8.61	9.74

The most important properties of both fuels are given in Table 1. Diesel fuel has a significantly higher energy density, but due to the higher gravimetric density the specific energy of both fuels is similar. Heavy fuels are considered safer, because their flash point is at higher temperature. The flash point is the lowest temperature at which the fuel can be ignited. For kerosene the flash point is at 38°C, whereas that of gasoline is far below at -37 °C.

As described in chapter 2.2.4, a mixture of gasoline and lubricant is used as fuel for two-stroke engines. The volume ratio is commonly between 25:1 and 100:1.

2.3 Hybrid-Electric Aircraft

The description of the components' properties in 2.2 allows a comparison of electric propulsion and internal combustion engine propulsion from an energetic viewpoint: In terms of efficiency, electric motors are clearly advantageous over internal combustion engines with values of over 0.90 compared to a maximum of 0.42. The significant advantage of the internal combustion engine however is the specific energy of fossil fuels, which is about 60 times higher than that of state-of-the-art batteries, according to Table 1, Figure 8 and Figure 9. Both figures of merit may be consolidated by the

analysis of exergy, the energy available for propulsion (SEITZ, SCHMITZ, ISIKVEREN & HORNUNG, 2012). In a comparison of the specific exergy available at the power unit shaft, the internal combustion engine system achieves around 24 times the value of a battery-electric system with state-of-the-art Lithium-polymer batteries. The ratio is reduced to 12 with the forecasted Lithium-polymer battery specific energy of 400 Wh/kg and to 5 with a value of 1000 Wh/kg, as expected for Lithium-air batteries. For the application of the two systems in aircraft, this has significant consequences: The lower specific exergy of battery-electric propulsion systems results in a significantly steeper increase of mass with flight time. Therefore battery-electric aircraft are clearly less suitable for long endurance missions.

Hybrid-electric aircraft combine a battery-electric drive train with an internal combustion engine and combine their capabilities. Hybrid-electric propulsion enables an aircraft to fly long endurances using the internal combustion engine and more silently, when propelled by the electric motor. Contrary to the automotive industry, where hybrid-electric propulsion was incorporated into series production vehicles, there are neither manned nor unmanned commercial hybrid-electric aircraft on the market now. The aircraft that were flown are technology demonstrators.

2.3.1 Unmanned Aircraft Projects

One of the earliest published reports on hybrid-electric UAV is about the hybridization of an internal combustion engine with an electric motor, batteries and a photovoltaic system (HARMATS & WEIHS, 1999). As a main result, it is summarized that the parallel configuration proves to be more efficient than the series configuration.

The only prototype of an unmanned aircraft with hybrid-electric propulsion system to the author's knowledge was built at the Air Force Institute of Technology. The project is headed by Frederick Harmon, a pioneer in the application of this type of propulsion system in UAV. After initial work on conceptual design and simulation of hybrid-electric UAV (HARMON, FRANK & CHATTOT, 2006) as well as control (HARMON, 2005; HARMON, FRANK & JOSHI, 2005), the cornerstone for the current project named Condor, was laid with the refinement of the conceptual design method (HISEROTE & HARMON, 2010). The result is a power based preliminary design method in which efficiencies have to be estimated from case to case. In the use case of a 13.6 kg (30 lb) aircraft, a reduction in fuel mass was achieved, but the additional propulsion system mass was balanced with reduced payload in order to keep the take-off mass equal to that of a reference configuration with combustion engine. In further publications the testing (GREISER, MENGISTU, ROTRAMEL & HARMON, 2011) and integration in the aircraft (AUSSERER & HARMON, 2012) is described. Despite its lower efficiency, a brushed DC motor was chosen for easier torque control and generator use. During the

testing of the system a main problem was the restart of the combustion engine with the propulsion electric motor. Furthermore, one of the engines chosen for testing did not provide the advertised performance and caused a failure of the belt system due to its rough run.

A team of the Australian Research Centre for Aerospace Automation and the Queensland University of Technology realized a prototype of a parallel hybrid-electric propulsion system and derived performance prediction rules from the experimental results (GLASSOCK, HUNG, GONZALEZ & WALKER 2007, 2009). In further work, possible reductions in fuel consumption when using an ideal operating line strategy were investigated using a simulation environment for hybrid-electric UAV (HUNG & GONZALEZ 2012a, b).

In the recent past, several university projects treated the design or construction of hybrid-electric propulsion systems or hybrid-electric unmanned aircraft (BAGASSI, BERTINI, FRANCIA & PERSIANI, 2012; DESCHENES, BROWN, SOBIN & WEST, 2011; LIEH, SPAHR, BEHBAHANI & HOYING, 2011; KOSTER ET AL., 2011).

2.3.2 Manned Aircraft Projects

The title of the world's first series hybrid-electric aircraft is claimed by Siemens AG, Diamond Aircraft and EADS, for the modified DA36 E-star motor glider presented at the Paris Air Show in 2011. The propulsion system of this aircraft is shown in Figure 15b. It consists of a 70 kW electric motor by Siemens and an Austro Engines Wankel engine providing 30 kW continuous power (SIEMENS, 2011). The next generation aircraft DA 36 E-star 2 uses a 100 kg lighter propulsion system than its predecessor. According to SIEMENS (2013), the aircraft offers the payload capacity and range of a conventional utility aircraft, whereas fuel consumption and CO_2 emission are reduced by 25 %. The aircraft had its maiden flight in June 2013.

The Embry-Riddle Aeronautical University Eco-Eagle participated in the 2011 Green Flight Challenge. The aircraft is a modified Stemme S10 with roughly 1100 kg takeoff mass and a wing span of 22.8 m. The parallel hybrid-electric system uses a 75 kW Rotax 912 combustion engine and a 30 kW electric motor by Flight Design. A CAD model of the system is provided in Figure 15a. The machines are connected with a belt system. An overrunning clutch system allows disconnecting both the combustion engine and the electric motor (EAGLE FLIGHT RESEARCH CENTER, 2011).

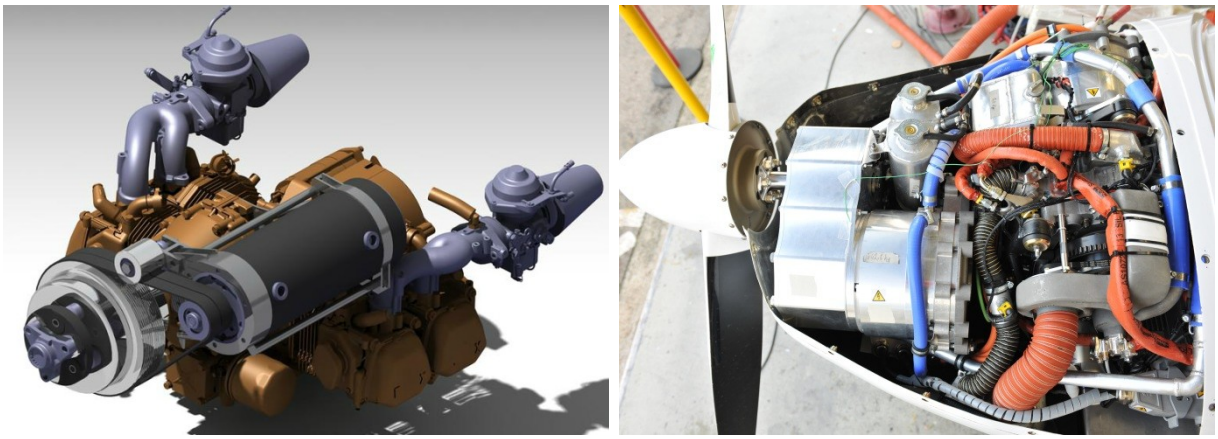

a) b)

Figure 15: a) Parallel hybrid-electric system of the Eco Eagle (EAGLE FLIGHT RESEARCH CENTER, 2011) b) series hybrid-electric system of the DA36 e-star (SIEMENS, 2011)

The company Flight Design that supports the development of the Eco-Eagle also offers a standalone parallel hybrid-electric propulsion system. It combines an 85 kW combustion engine with a 30 kW electric motor. A Lithium iron phosphate battery is used as energy storage. The system is advertised as power boost for take-off and climb with a reduction of the fuel consumption from original 35 L/h to a range from 25 L/h to 28 L/h (FLIGHT DESIGN, 2010).

The Volta Volaré GT4 is a four-seater aircraft with around 1725 kg take-off mass. It is equipped with a hybrid-electric power plant, for which no technical details are publically available. The aircraft was announced to go into series production in 2012 (VOLTA VOLARÉ, 2012), but by September 2013 no information about a first flight was available.

3 MODELING AND DESIGN OF HYBRID-ELECTRIC AIRCRAFT

In order to quantify the capabilities of the propulsion components described in the previous chapter, their behavior needs to be modeled. In preliminary aircraft design, three principal demands are posed to a model: high generality, low computational effort and high accuracy. The demand for high accuracy is an end in itself and helps reducing cost of the design process. An exact as possible prediction of capabilities and limitations in the preliminary stage reduces expensive system modifications in the detailed design stage. High generality and low computational effort both enable a model to quickly explore a wide design space and to create reasonably comparable results. The demands for high accuracy and low computational effort may oppose each other, so that a satisfying compromise needs to be found.

In this chapter, a method to design aircraft with hybrid-electric propulsion system is presented. In chapter 3.1 the aircraft design process is regarded with focus on propulsion system design. In the following chapter 3.2, models for the single components of the hybrid-electric propulsion system are developed in detail. Throughout the chapter it will be highlighted how various aspects of the modeling contribute to the fulfillment of the three demands.

3.1 Aircraft Design Process

Generally, an aircraft propulsion technology should not be regarded singularly, but within a suiting aircraft, in order to properly describe the interdependency of propulsion system and aircraft (GUR & ROSEN, 2009; RÖßLER, 2012). The reason becomes clear, when analyzing a typical aircraft design process, as displayed in Figure 16.

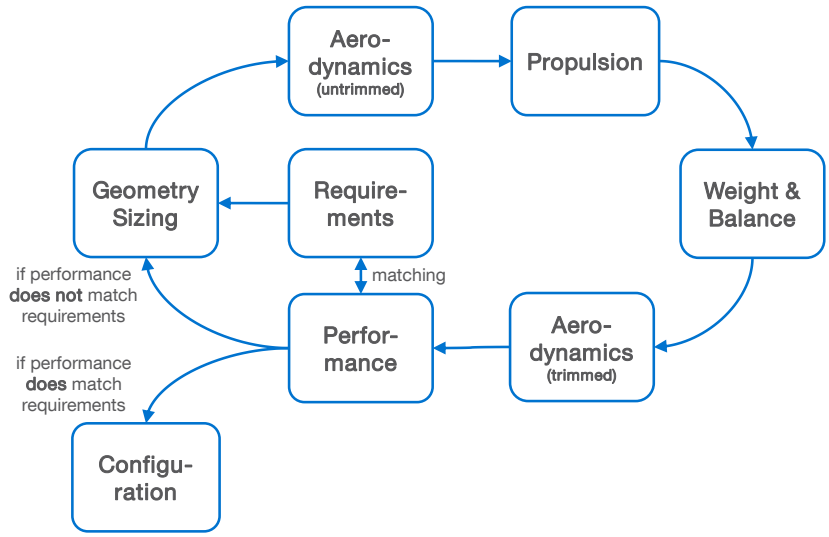

Figure 16: Typical aircraft design process (modified from SCHOEMANN & HORNUNG (2012))

From a specified set of requirements an initial geometry is estimated using empirical values. In a first prediction of aerodynamics for the untrimmed aircraft the power requirement is determined. The power requirement is the input of the propulsion module. Its output is the mass of the system providing this power. Propulsion system mass is then used to compute the aircraft's overall mass and balance. After predicting aerodynamics for the trimmed aircraft, the performance is analyzed and matched with the requirements. If the performance does not match the requirements, the aircraft geometry is modified and further iterations are run until an acceptable compliance is reached.

This recapturing of basic aircraft design concepts shows that the output of a propulsion design module influences the input. The power demand changes with propulsion system mass. A cascade process results in the aircraft design iteration: If an initial propulsion power assumption leads to a heavier propulsion system than expected, the assumed power will not be sufficient and the power demand computed in the next iteration loop increases. This again leads to a higher propulsion system mass, and so forth. This effect evolutes until the process reaches convergence. In any aircraft, in which the conversion of stored energy into motion correlates with fuel burn, mass and consequently the power demand constantly changes. This is the case for all systems based on fossil fuel, thus also the hybrid-electric system.

In the next two chapters, first the propulsion system design module, as process core, is introduced detachedly from the aircraft design process. Chapter 3.1.2 then describes the module's integration into a design process based on scaling a reference aircraft and the application of an optimization scheme to it.

3.1.1 Propulsion System Design

In chapter 2.1, the three most common hybrid-electric configurations are introduced. Out of the parallel, the series and the series-parallel configuration, the first has the highest potential for high efficiency. It is affirmed in HARMON (2005) and HARMATS & WEIHS (1999) that the parallel configuration is best suited for unmanned hybrid-electric aircraft. It is therefore used as the reference to present the design process in this chapter.

Surveillance missions, as schematically outlined in Figure 17, are one of the main applications of UAVs (GUNDLACH, 2012). In this mission type hybrid-electric aircraft are expected to be advantageous over conventional aircraft due to the combination of flight phases with differing requirements. The mission in Figure 17 is chosen as reference mission in this study. For the surveillance over the target area, the ability to operate covertly and hence silent is advantageous. Flying with small acoustic footprint

is enabled by electric propulsion. If the target area is at long distance from the airfield or needs to be reached quickly, then high velocity or long endurance capability is necessary. An electric propulsion system is not suitable for this due to the low specific energy. An internal combustion engine system is favorable for these mission phases. The hybrid-electric propulsion combines these power units and capabilities.

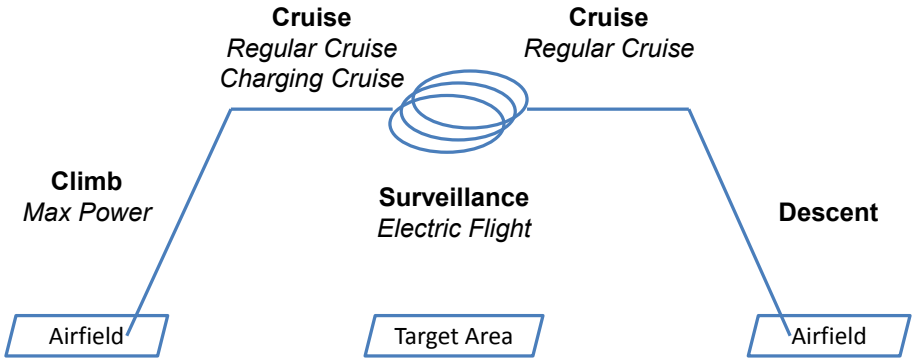

Figure 17: Exemplary hybrid-electric surveillance mission with flight phases and design points (SCHOEMANN & HORNUNG, 2013)

In the mission schematic in Figure 17, takeoff and climb are merged into one climb phase. Takeoff is not regarded in more detail, because small unmanned aircraft commonly use auxiliary takeoff systems like winches or catapults. A first cruise phase brings the aircraft to its target area, where the surveillance is started. Surveillance is conducted silently using the propulsion system's electric flight capability. The assumption that electric flight is silent is not questioned within the scope of this study. An approach to quantify the acoustic footprint of battery-electric low altitude UAVs was conducted parallel to this study by SPECK, WILBERG & HORNUNG (2013). After the electric flight phase, the aircraft returns to an airfield in a second cruise phase. Descent and landing are neglected, as they may be operated unpowered. A mission may also be composed of several cruise and electric flight phases. A reasonable modification of the mission could include several target areas or multiple surveillance phases over one area and cruise phases in between, in which the batteries are recharged.

In order to properly design the propulsion system, the flight mission needs to be translated into requirements for the propulsion system. As explained earlier, the constantly changing mass of a system with fuel consumption implies constant variations in thrust demand. Exactly determining the mass of such propulsion system requires the inclusion of a mission simulation into the propulsion system design module. This anyhow would significantly increase computation time. The integration of the mission simulation and associated computation time issues are resumed in chapter 3.1.2. As an alternative which requires significantly less computational effort, the mission is reduced to a set of points, each representative for one characteristic

mission phase and the related propulsion demands and activity. These points are further denoted as design points. From the given surveillance mission, four design points are identified:

- *Regular Cruise* (RC): The propeller is driven by the internal combustion engine
- *Electric Flight* (EF): The propeller is driven by the electric motor
- *Charging Cruise* (CC): The internal combustion engine drives the propeller and uses the electric motor as a generator to charge the battery
- *Maximum Power* (MP): The internal combustion engine and the electric motor both drive the propeller

The points are associated to the mission in Figure 17. *Maximum Power* defines the climb phase. The flights to and from the target area are defined in the design point *Regular Cruise*. If the batteries are charged during the flight to the target area *Charging Cruise* is applicable. The requirements for the electric flight phase are summarized in the design point *Electric Flight*. At points *Regular Cruise* and *Electric Flight*, one of the propulsion power units of the system works in single-mode. At points *Charging Cruise* and *Maximum Power* both work in dual mode. A parameter to characterize the interaction between the electric and the combustion system is the degree of hybridization *DoH*. The *DoH* is the electric power fraction of the propeller shaft power. In Figure 18 all four points are shown with their *DoH* and the power distribution. The top bar shows the power P_{prop} fed to the propeller shaft, the middle one the power P_{ICE} delivered from the internal combustion engine and the bottom bar the power P_{EM} delivered by the electric motor.

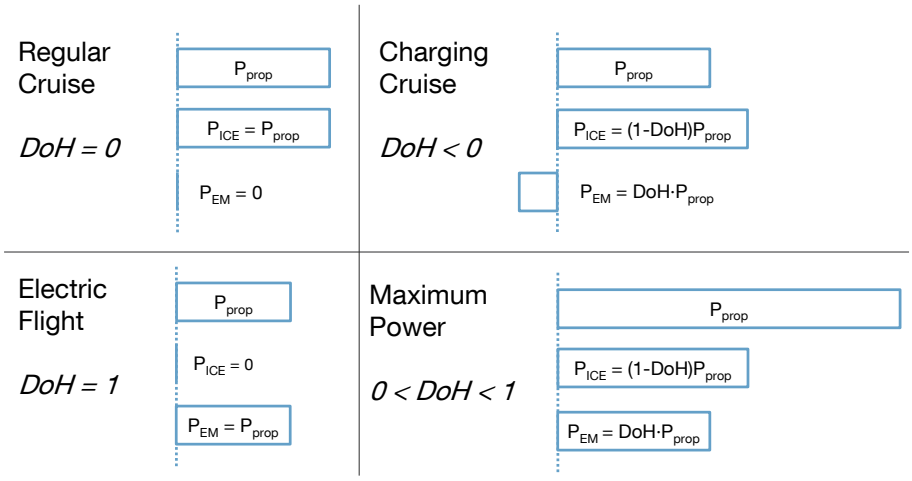

Figure 18: Power distribution and degree of hybridization at the design points (modified from SCHOEMANN & HORNUNG (2012))

At design point *Regular Cruise*, with the electric motor stopped *DoH* is equal to zero, whereas during *Electric Flight* all propulsion power is delivered by the electric motor and *DoH* takes the value one. If energy is fed to the electric system, as during

Charging Cruise, *DoH* falls below zero, because formally, a negative power is delivered. In order to propel the aircraft with *Maximum Power* the electric motor contributes a portion of the overall power and *DoH* hence is between zero and one.

The mission requirements, formulated as the four design points, are the input for the design procedure. An important prerequisite for the procedure's definition is the knowledge of the type of models used. The published models for the design of hybrid-electric propulsion systems are power based (HARMON, FRANK & CHATTOT, 2006; BAGASSI, BERTINI, FRANCIA & PERSIANI, 2012). This means that in the interaction of two propulsion components in line, only the power transmitted between the two is regarded and components are sized based on the power input or output only. Designing a system with such models ignores operational characteristics of the components. For example, a power demand of an internal combustion engine could be fulfilled with a slow-turning high torque engine or a faster-turning engine with lower torque, if the product was equal. Furthermore, no reasonable power based estimation of energy converters' efficiencies, such as the electric motor and the internal combustion engine efficiency, is known to the author. Therefore here, the operation of the components is described by their state variables. State variables are the factors of power. A denotation by RIZZONI, GUZELLA & BAUMANN (1999), distinguishing the two factors into one flow variable and one effort variable is resumed. The relevant state variables for the described task of modeling a hybrid-electric propulsion system are summarized in Table 2 for the mechanical, the electrical and the chemical domain. It is also indicated for which components the state variables are applicable. Input and output in this case are to be seen in the direction of energy flow from storage to propeller.

Table 2: State variables used in the design of hybrid-electric propulsion systems (based on RIZZONI, GUZELLA AND BAUMANN (1999))

Domain	Flow Variable	Effort Variable	Application
Mechanical	Rotational Velocity	Torque	Propeller Input, Electric Motor Output, Internal Combustion Engine Output
	Translational Velocity	Force	Propeller Output
Electrical	Current	Voltage	Electric Motor Input ESC Input and Output Battery Output
Chemical	Mass Flow	Lower Heating Value	Internal Combustion Engine Input Fuel Output

Models are commonly formulated in state variables within simulations of hybrid-electric propulsion systems with defined components (HARMON, 2005; HUNG &

GONZALEZ, 2012a). Their use allows a differentiation of the various states of operation of a system. This increases the accuracy of the models, because the energy converters' efficiencies may be soundly estimated at every design point instead of being globally approximated with empirical values. Including those models in the preliminary design phase of an aircraft increases the prediction accuracy and hence saves time and cost. Furthermore, the design of small UAV propulsion systems is usually based on commercial off-the-shelf (COTS) components. This state variable approach allows a close prediction which components may be used, as the data sheets of COTS components refer to state variables as well.

There are two principal types of building up a design procedure integrating the component models: forward-facing or backward-facing. A forward-facing procedure follows the energy flow, which means that it starts at the energy source and ends with the generated propulsive performance the propeller provides. It requires initial assumptions for the power converter efficiencies in order to size the energy storage. The process is then run in iterations until the computed performance reaches the requirements and a defined criterion of convergence for the energy converters' efficiencies is met. The backward-facing procedure starts at the propeller output and sizes energy converters and storages so that the requirements are fulfilled. In comparison, the backward-facing process runs faster, as it runs straight, without iterations. In a backwards-facing process, one component model passes the requirements for both state variables to the next model in line. This means that a possible relation between the two state variables within the following component may not be considered. Electrochemical energy storages commonly have such characteristic dependencies of their state variables voltage and current, so called polarization curves. The battery, which is used in a hybrid-electric system, has a relatively shallow polarization curve, so that voltage may be assumed to be constant. Propulsion systems with electric energy storages characterized by steeper polarization curves, for example fuel cell systems, are better designed with forward facing procedures. Due to the advantages in computation time, here the backward-facing process is selected for realization.

The propulsion system design procedure is depicted in Figure 19. Generally each of the component modules computes the indicated output from the module input and the design variables. The design variables are geometric or operational properties of the components. The modules' objectives in almost every case comprise the estimation of the component's mass and efficiency. Exceptions are the coupling and the fuel tank. Both components are assumed to have no power dissipation. For the coupling, also mass is neglected, as the detailed mechanical concept is not specified in preliminary design. The general effect of additional mass on the aircraft is nevertheless quantified

in chapter 4.3.3 and may be used for the evaluation of coupling concepts in a later design phase.

The input of the procedure consists of the mission requirements and the design variables. The mission is defined, in terms of the propulsion system, by the state variables for propulsive power, thrust and velocity, and flight time for each of the four design points. The requirements for *Charging Cruise* are driven by a charging strategy. Possible strategies are to operate at *Regular Cruise* thrust and velocity and to prescribe a constant charging current or the time for a complete charge. Alternatively the adaption of velocity within a defined range may be allowed, so that the most efficient possible engine operating point is selected. The output of the process is the overall propulsion system mass. It is required for the determination of the takeoff mass in the aircraft design process introduced in detail in chapter 3.1.2. Further auxiliary outputs may of course be defined.

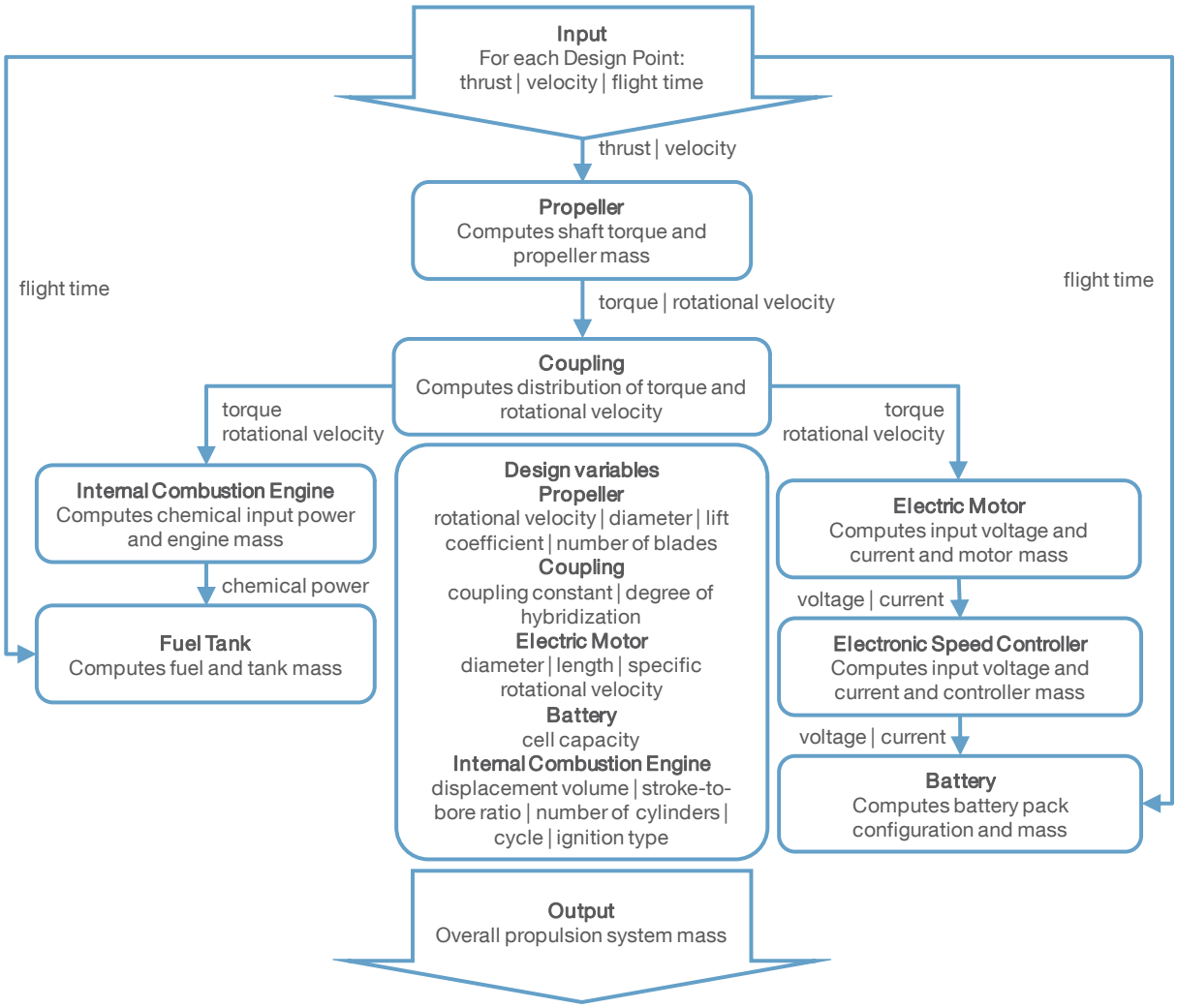

Figure 19: Propulsion system design procedure (modified from SCHOEMANN & HORNUNG (2012))

The propeller module is the first in the design procedure. It computes propeller mass, torque and rotational velocity. Its input is thrust and velocity as well as the design

variables, rotational velocity, diameter, lift coefficient and number of blades. The relation between the design variable rotational velocity and the rotational velocity output is clarified in chapter 3.2.6. A simple coupling module distributes torque and rotational velocity to the electric motor and the combustion engine. The coupling design variables are the coupling constant and the degree of hybridization. The electric motor module determines the motor mass and the required input voltage and current from the demand in torque and rotational velocity and the design variables diameter, length and specific rotational velocity. The electronic speed controller computes the component mass and the voltage drop caused by the controller. In the battery module, the battery efficiency and the resulting required electric energy for all flight phases is determined. The battery pack configuration in terms of cells in series and parallel is then identified and the mass computed. The combustion engine module returns engine mass and required chemical power for an input of torque and rotational velocity demand. The design variables are the displacement volume, the stroke-to-bore ratio, the number of cylinders, the ignition method and the operating cycle. From the required chemical power and the flight time the fuel tank module determines the mass of the fuel required for all flight phases and the mass of a tank to contain it. The fuel tank module does not use state variables, as it is assumed to be without loss, and no design of the tubing is done. The masses of all components are added to the overall propulsion system mass.

3.1.2 Overall Aircraft Design

The aircraft design process is set-up with regard to its application within this study. The objective, besides the development of the method, is to show general trends caused by hybrid-electric propulsion systems. Therefore the process is focused on propulsion system design and the framework is kept simple with a scaling approach. Two advantages are implied: First, computation time is kept small compared to a full-scale design process. Second, scaling an aircraft generally means that its planform shape is not modified. The non-dimensional aerodynamics of the reference aircraft hence are kept untouched. This means that the influence of varying geometry or aerodynamics is eliminated from the results and a clear emphasis is put on the effects caused by propulsion system modifications.

The basic sequence of the process is outlined in Figure 20. After the following overview of the modules' functions, each is described in detail. The inputs consist of the reference aircraft data and aircraft requirements. From both an initial sizing of the aircraft is conducted. With the initial data, a hybrid-electric propulsion system is designed within an optimization framework. The aircraft constantly changes mass when the internal combustion engine is active and burns fuel. In the propulsion system

design procedure a constant thrust is input for each design point. As necessary thrust is dependent on aircraft mass, the assumption of a constant thrust level leads to slight inaccuracies in the determination of the required energy for the design points *Regular Cruise* and *Maximum Power*. Therefore a more detailed estimation of the necessary fuel mass and battery capacity in the form of a mission simulation follows the propulsion system design. The aircraft is adapted to the resulting fuel and battery mass in a scaled sizing process following the simulation. Furthermore the thrust levels yielded by the simulation are evaluated and used as an input for the next run of the propulsion system design procedure. Propulsion system optimization, mission simulation and scaled sizing are run in iteration loops, until takeoff mass convergence is reached.

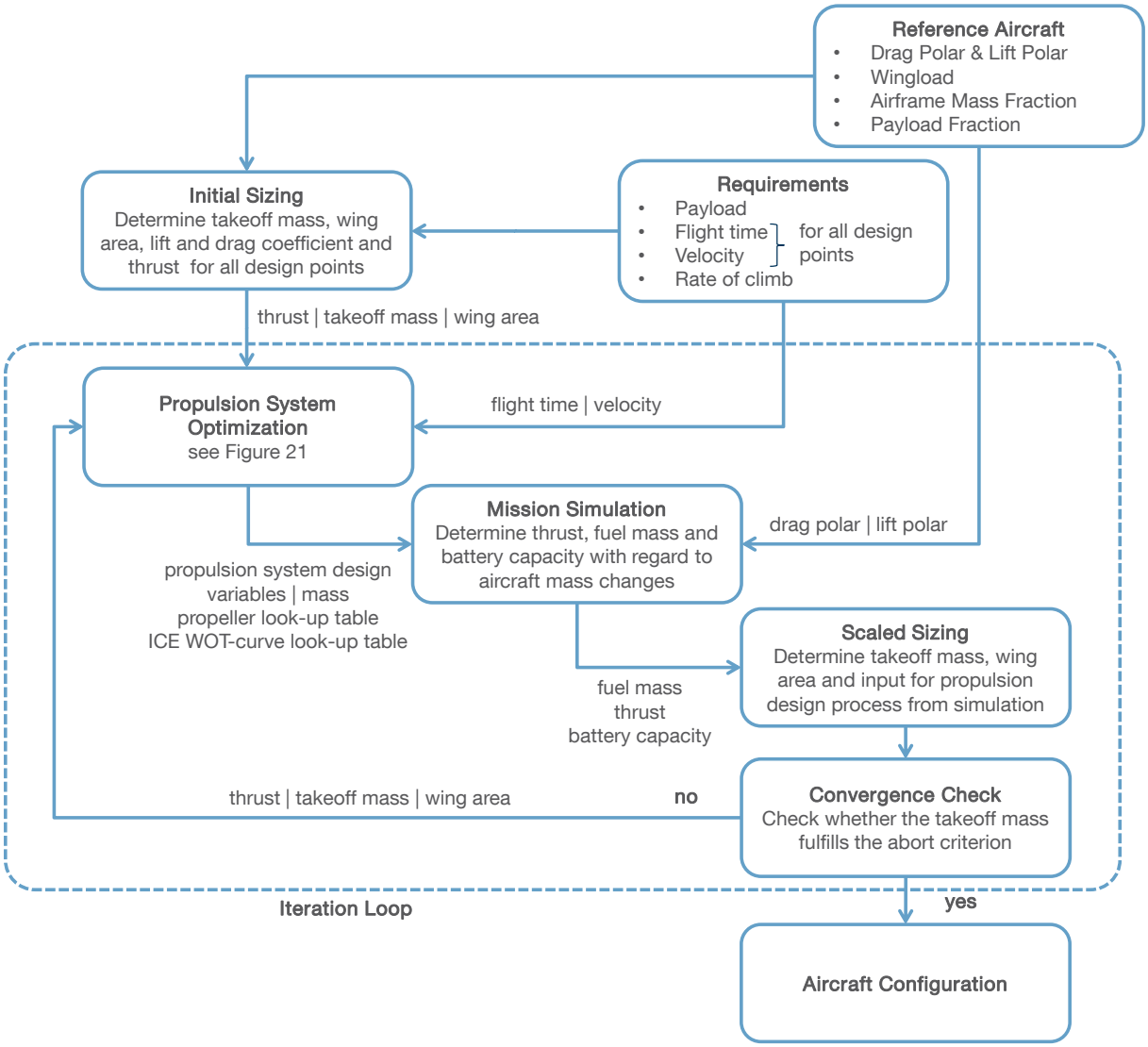

Figure 20: Aircraft Design Process based on reference aircraft scaling

The reference aircraft data set contains the lift and drag polar in dimensionless form and three structural key characteristics. The wing load is defined as the ratio of maximum takeoff weight (MTOW) to wing area. Airframe mass fraction and payload

fraction are the ratios of the respective mass to the maximum takeoff mass. The aircraft requirements include the payload and the necessary information to define the flight mission outlined in Figure 17: flight time and velocity for each design point and the rate of climb *RoC*.

Initial Sizing

In the next step, an initial aircraft sizing is performed and the input for the propulsion system design module and the mission simulation is determined. The propulsion system design procedure input according to Figure 19 is included in the requirements except for the thrust demand. The wing area is a necessary input for the mission simulation. The missing data are determined from the requirements and the reference aircraft data in an initial sizing process. First, the takeoff mass is computed from payload m_{PL} and the reference payload fraction $(m_{PL} / m_{TO})_{ref}$ according to (1).

$$m_{TO} = \frac{m_{PL}}{\left(\frac{m_{PL}}{m_{TO}}\right)_{ref}} \tag{1}$$

The fitness of the reference payload fraction is the main driver for the number of iteration loops necessary until convergence of the takeoff mass. The wing area is computed from the fraction of takeoff mass m_{TO} and the reference wing load $(m_{TO} / S)_{ref}$. The lift coefficient for *Regular Cruise* $c_{L,RC}$ is then identified in (2) from the assumption of horizontal flight and the resulting equalization of lift and weight.

$$c_{L,RC} = \frac{2g}{\rho v_{RC}^2}\left(\frac{m_{TO}}{S}\right)_{ref} \tag{2}$$

The corresponding drag coefficient $c_{D,RC}$ is interpolated from the drag polar of the reference aircraft. The lift-to-drag ratio or aerodynamic efficiency E_{RC} is the fraction of $c_{L,RC}$ and $c_{D,RC}$. In horizontal flight, *Regular Cruise* thrust T_{RC} may be set equal to drag and is computed as given in (3).

$$T_{RC} = \frac{m_{TO} g}{E_{RC}} \tag{3}$$

It is assumed, that the drag polar of the reference aircraft is also valid for climb. The *Maximum Power* thrust T_{MP} may then be computed according to (4).

$$T_{MP} = T_{RC}\left(\left(\frac{v_{MP}}{v_{RC}}\right)^2 + E_{RC}\frac{RoC}{v_{MP}}\right) \tag{4}$$

The thrust for *Electric Flight* T_{EF} is determined analogously to that for cruise flight, using (2) with the electric flight velocity v_{EF} and (3) with the according lift-to-drag ratio E_{EF}. The drag polar is left unchanged also for *Electric Flight*. The thrust demand for *Charging Cruise* is equal to *Regular Cruise* thrust if not defined otherwise by the charging strategy.

Propulsion System Optimization

With thrust, velocity and flight time known for each design point, the propulsion system design module is executed. The propulsion system design block in Figure 20 is the propulsion system design procedure described in 3.1.1 within an optimization framework. The optimization's objective is to determine the design variables, so that the cost function is minimized. Propulsion system mass is chosen as cost function. The reasons for this choice are better comprehensible if the implementation of the optimization is explained prior. The process in Figure 21 is the content of the propulsion system optimization block in Figure 20. Its core is the propulsion system design procedure presented in chapter 3.1.1, which is provided with its operational input and design variables.

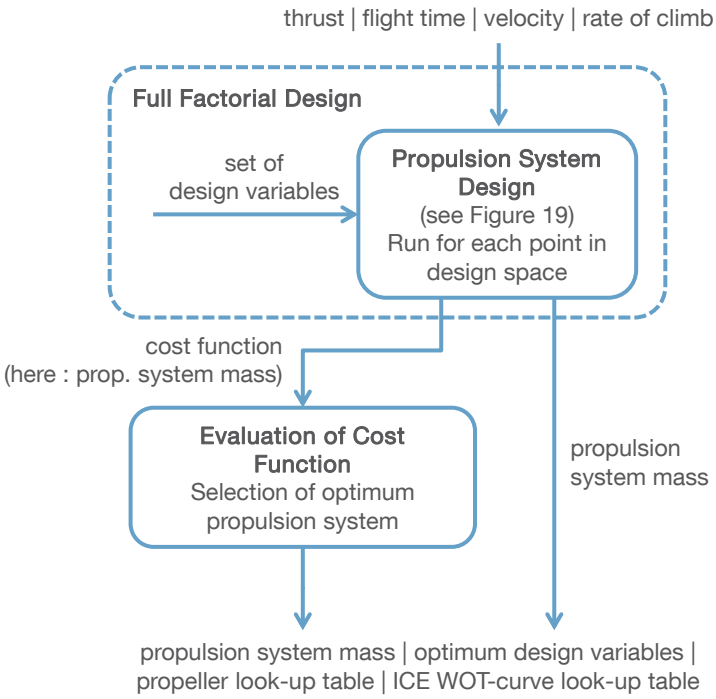

Figure 21: Propulsion system design optimization framework

The applied optimization scheme is a full-factorial optimization. This means that the design space's dimensionality is defined by the number of design variables and the size in each dimension by the discretization of the respective design variable. The propulsion system design procedure is executed at each point in the design space. The models integrated in the propulsion system design procedures are formulated

continuously in order to allow a generic applicability. Within the full-factorial optimization however they are discretely called for each combination of design variables and consequently provide a discrete output. The cost function results are then evaluated and the design variables are selected that define the design point with minimum propulsion system mass. They are output together with the propulsion system mass value and performance data required for the mission simulation. For the selected propeller these are torque and rotational velocity look-up tables over thrust and velocity. For the internal combustion engine, the course of the wide-open throttle curve (see chapter 3.2.4) is provided as look-up table.

Although full factorial optimization is a relatively time consuming optimization method, it is chosen due to its simplicity. For a first requirement space exploration, as performed in this study, it allows to get full overview of the design space and to easily analyze the design method. Further development of the design method could include a more efficient algorithm. The mix of continuous and discrete variables is properly addressed with stochastic methods.

The optimization scheme is only applied to the propulsion system design procedure, and not the complete aircraft design process. The unacceptably high computation times for the latter solution are causal for this setting. This statement may be clarified with a brief quantitative assessment of the time required for optimization. The propulsion system design procedure in Figure 19 uses 15 design variables. Several of those may only take few values. The internal combustion engine cycle may only have two strokes or four strokes. Similar limitations apply for the engine's number of cylinders and the ignition type or the number of propeller blades. If each of the remaining 11 design variables was discretized with 5 support points, this would result in 5^{11} design points. Consequently the design procedure would be executed over 48 Million times. If the procedure runtime was one tenth of a second, the full factorial optimization still would require over 56 days. Applying the optimization scheme to the complete aircraft design process would require running the iteration process in Figure 20 including the mission simulation for every design point. This would increase overall runtime to impractical values. The capsulated optimization has two major drawbacks. First, the choice of the optimum propulsion system is based on imperfect fuel and battery mass estimation, as the mission simulation is conducted after the optimization. This inaccuracy is of little relevance, as the fuel mass fraction of the propulsion system mass of hybrid-electric aircraft is quantified in chapter 4.2 to be fairly low. The differences in battery mass are negligibly low as the inaccuracies only apply for the short *Maximum Cruise* design point. Second, the cost function has no access to the final aircraft properties. In each iteration step the propulsion system is optimized independently of the previous or following iterations. Within the optimization the mass

cascade effect of a selected system through the following iteration steps cannot be foreseen.

Having identified this optimization process' peculiarity, the choice of the cost function is explained. Reasonable cost functions are aircraft takeoff mass, fuel mass and on-board energy consumption. Optimizing for minimum takeoff mass returns the aircraft with the easiest handling. At the limit of 150 kg takeoff mass, the process determines the maximum feasible requirements in this class. Furthermore, in *Regular Cruise* and *Electric Flight*, minimum mass leads to minimum propulsion energy: Energy is the product of aircraft weight, velocity and time divided by aerodynamic efficiency. Aerodynamic efficiency in this design process is determined as function of the lift coefficient. The lift coefficient is independent of mass for constant wing loads according to (2). As velocity and flight time are defined by the requirements and constant, a minimum mass aircraft minimizes the energy demand. The actual energy consumption however is also driven by the propulsion system components. The implementation of the takeoff mass cost function is not possible, as takeoff mass is computed after the propulsion system design and because in the optimization its converged value cannot be foreseen. The propulsion system resulting in minimum takeoff mass may nevertheless be identified by minimizing the propulsion system mass. Propulsion system mass is the only portion of takeoff mass that is affected by the optimization. Minimizing it in every iteration loop hence results in minimum takeoff mass. The applicability of the consumed energy and fuel mass cost functions is complicated by the interaction of optimization and design procedure. A most energy or most fuel efficient system may have a higher than minimum system mass. This may cause further iterations of the aircraft design procedure and, due to the cascade effect, result in a further increase of takeoff mass and significantly higher power demand. The optimization then selects the most energy or fuel efficient configuration for the power demand in each iteration, as it is only applied to the propulsion system design. If the process converges at significantly higher than minimum takeoff mass, the result is only the optimum for the last iteration, but not the globally most energy or fuel efficient system. Energy or fuel consumption then may be considerably higher than for the minimum propulsion system mass results.

Furthermore, using the fuel mass cost function requires a secondary cost function for the electric components. Otherwise they could be freely chosen, because they have no direct influence on fuel mass in the propulsion system design procedure. Their influence only takes effect in the mass cascade. The three optimization strategies are quantitatively compared in 4.3.1.

Mission Simulation

The mission simulation model is run with the optimum propulsion system selected in the propulsion system design module. It is a dynamic point mass model, which only allows longitudinal motion. It was originally developed by HOLZAPFEL[1] and refined by MÜLLER (2006). For the use within the presented design framework, the propulsion module was modified from turbofan jet engines to hybrid-electric power plants. The simulation's input in this hybrid-electric version is the flight trajectory, defined by altitude and velocity, and the degree of hybridization at discrete points. The simulation furthermore accesses the reference aircraft's drag polar, lift polar and requires the aircraft wing area and specified limits for the flight performance parameters climb and sink rate, acceleration, climb angle and altitude. The sequence of the simulation here is described with focus on the propulsion system. A basic schematic is provided in Figure 22, further details on the other modules may be found in MÜLLER (2006).

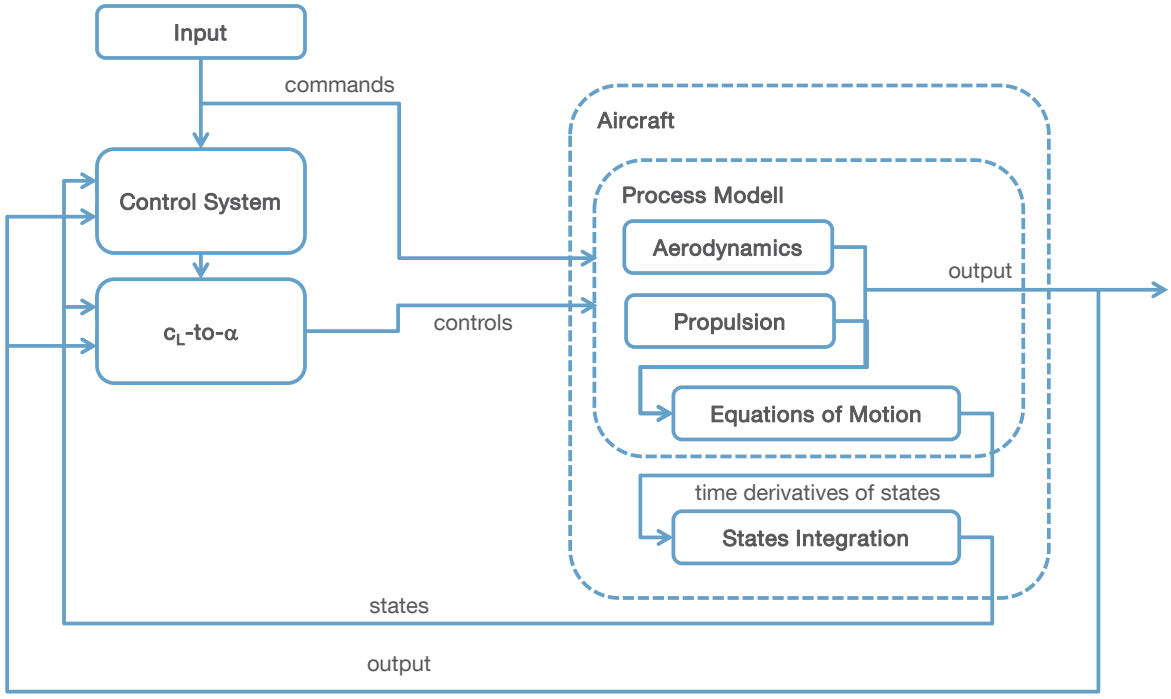

Figure 22: Schematic of the mission simulation

The input commands, altitude, velocity and *DoH*, are fed into a control system module. There they are transformed into a reference system using a first-order lag element and thrust and lift coefficient commands are determined by comparison of the reference values with the aircraft states. In the second module, the lift coefficient command is transformed into an angle of attack command using the reference aircraft's lift polar. In the first two modules, all commands are constrained with the provided performance limitations. The following aircraft module yields the time

[1] HOLZAPFEL, FLORIAN, Institute of Flight System Dynamics, Technische Universität München

derivatives of the aircrafts states, velocity, path angle, downrange, altitude and mass. For this purpose propulsion and aerodynamics are evaluated. The aerodynamics module returns lift and drag utilizing the provided lift and drag polar. The propulsion modules' main output for this application is the fuel mass flow. With the propulsion and aerodynamics outputs and the aircraft states of the previous time step the aircraft's equations of motion return the states' time derivatives. The states may be obtained by integration of the time derivatives and are fed back into the aircraft model and the control system.

The propulsion module of the simulation is set up similarly to the design process in Figure 19. The propeller module interpolates rotational velocity and torque for the thrust command at the current velocity from the look-up table generated by the propulsion system design module. The coupling block distributes torque and rotational velocity to the internal combustion engine and electric motor, governed by the degree of hybridization command. The *DoH* command furthermore disables the electric or combustion engine blocks when not used. The electric motor block is an implementation of the electric model developed in chapter 3.2.1. The following battery block returns the used energy, the used capacity and the state of charge. In the internal combustion engine block, the fuel mass flow is determined by computation of the engine efficiency. The process uses the baseline efficiency map and the wide-open throttle curve generated by the propulsion system design module for normalization according to chapter 3.2.4.

The mission simulation returns the course of mission thrust profile, the consumed fuel mass and the required battery capacity.

Scaled Sizing

The fuel mass and the required battery capacity returned by the mission simulation are used to conduct a scaled sizing of the aircraft. First the propulsion system mass $m_{\text{propulsion}}$ computed in the propulsion system design module is adapted with the changes in fuel, tank and battery mass according to (5). Therefore the difference of the fuel mass from design module and simulation Δm_{fuel} is computed. Then the difference in fuel tank mass Δm_{tank} is identified using the mass estimation model presented in chapter 3.2.5. The difference in battery mass $\Delta m_{\text{battery}}$ is determined using the battery mass estimation model in 3.2.3 with the required capacity predicted by the mission simulation.

$$\mathrm{m}_{\text{propulsion}_{\text{new}}} = \mathrm{m}_{\text{propulsion}} + \Delta\mathrm{m}_{\text{fuel}} + \Delta\mathrm{m}_{\text{tank}} + \Delta\mathrm{m}_{\text{battery}} \tag{5}$$

With the new propulsion mass $m_{\text{propulsion,new}}$, a new takeoff mass $m_{\text{TO,new}}$ is determined as the sum of the airframe mass, the payload and the adapted propulsion system mass according to (6). The airframe mass is determined by multiplying the reference airframe-to-MTOM ratio with the takeoff mass of the current iteration loop.

$$\mathrm{m_{TO,new}} = \mathrm{m_{airframe}} + \mathrm{m_{PL}} + \mathrm{m_{propulsion,new}} = \left(\frac{\mathrm{m_{airframe}}}{\mathrm{m_{TO}}} \right)_{\mathrm{ref}} \mathrm{m_{TO}} + \mathrm{m_{PL}} + \mathrm{m_{propulsion,new}} \tag{6}$$

The new takeoff mass and the thrust demand derived from the mission simulation are then fed back into the propulsion system design module. For design points *Regular Cruise* and *Electric Flight*, the thrust is averaged from the according flight phase. For the *Maximum Power* design point, the maximum value during climb is set. The propulsion system design module, the mission simulation and the scaled sizing are run in an iteration loop until the abort criterion is fulfilled. The abort criterion for the iteration loop is the convergence of the takeoff mass. Depending on the desired accuracy and constraints in terms of computation time, the relative deviation ε in (7) may be set more or less strict.

$$\varepsilon = \frac{\mathrm{m_{TO,new}} + \mathrm{m_{TO}}}{\mathrm{m_{TO}}} \tag{7}$$

3.2 Propulsion System Component Models

This chapter introduces the models integrated in the propulsion system design procedure. The principles for their creation are equal to those for the design method: high accuracy, generality and low computational effort. High accuracy requires a careful validation of all computed data with validated models or experimental data. The design of small unmanned aerial vehicles is almost always driven by the objective of low cost, so that the use of COTS components is common. Therefore, for every component involved, a database of suitable COTS products and its relevant data was created. Where mathematical models were unavailable the databases were used to derive surrogate models. The required accuracy is furthermore obtained by formulating the models in state variables, as explained in 3.1.1.

The imperative of short computation times demands mathematical surrogate models rather than interpolation from look-up tables. It may generally be said, and is quantified in the following chapters, that interpolation causes higher computational effort, than evaluating a surrogate equation. Although interpolation may return results of higher accuracy, the disadvantage of high computation times weighs heavier, as it

may make the models inapplicable for preliminary design. One exception is the propeller model described in chapter 3.2.6.

For the sake of generality, the models are not formulated discretely. Discrete modeling, as done by RÖßLER (2011) and NOTH (2008), uses only COTS components and their data. This allows very accurate results and simplifies a realization of the designed aircraft. Nevertheless, for analyzing trends, it is not desirable to be bound to a product range, but to include virtual products, that should be developed in order to improve the system. Furthermore, continuous models allow extrapolation and the modification of certain key values in order to indicate the influence of future technologies or improvements.

In the following chapters the component modules used in the design procedure for hybrid-electric propulsion systems are described. First the electric components, with electric motor, electronic speed controller and battery, and then the combustion engine components with the engine itself and the fuel system. The last chapters contain the propeller and coupling modules. All modules except for the coupling include mass estimation models. The energy converter modules and the battery module also contain efficiency prediction models.

3.2.1 Electric Motor

The task of the electric motor module in the propulsion system design process is to determine the required input voltage and current for a demand in torque and rotational velocity. Additionally, motor mass is computed. The central element of the module is the electric model. Comprehension of the electric motor design process is simplified by primarily examining this electric model. It bases on a simplified equivalent circuit for the electric motor depicted in Figure 23. The model was originally developed for DC motors (DRELA, 2007). Within the analysis here, due to the advantages described in chapter 2.2.2, only brushless DC motors are considered. The model is used to describe BLDC motors in several previous publications (LUNDSTRÖM, AMADORI & KRUS, 2010; GUR & ROSEN, 2009B). RÖßLER (2011) compared the computed performance data with manufacturer validation data and found acceptable accordance.

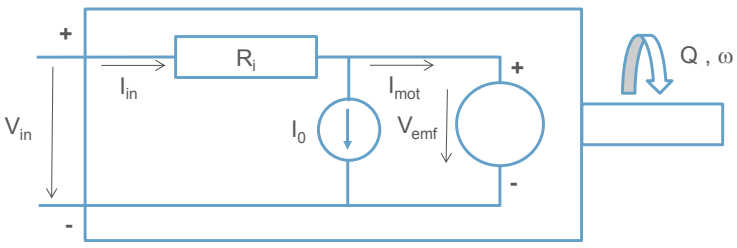

Figure 23: Equivalent circuit for the electric motor (SCHOEMANN & HORNUNG, 2012)

The loss mechanisms included in this model are resistive losses, represented by the internal resistance R_i and friction and iron losses, represented by the no-load current I_0. In more practical terms, the no-load current is the current the electric motor draws when no load is connected. The following two equations, (8) for the useable voltage V_{emf}, also called the electromotive force (EMF) and (9) for the motor current I_{mot} may be derived from the circuit using Kirchhoff's circuit laws.

$$V_{emf} = V_{in} - R_i I_{in} \tag{8}$$

$$I_{mot} = I_{in} - I_0 \tag{9}$$

In (8) and (9), V_{in} is the voltage supplied to the motor and I_{in} is the current it draws from the energy storage. The input power P_{in} in (10) is defined as the product of the two.

$$P_{in} = V_{in} I_{in} \tag{10}$$

In terms of the output power, it is assumed, that the product of voltage V_{emf} and current I_{mot} may be converted into mechanical power without further losses. Their product is then equal to the product of shaft torque Q and rotational velocity ω, as given in (11).

$$P_{out} = V_{emf} I_{mot} = Q\omega \tag{11}$$

The electric model is based on the assumption that the motor runs at full throttle. In this state, the rotor cannot further accelerate and equilibrium between the electromotive force and the back-electromotive force is reached. The relation between the back-electromotive force and the rotational speed, called back-emf constant or specific rotational velocity K_v, may hence be applied to the electromotive force as in (12).

$$K_v = \frac{N}{V_{emf}} = \frac{\omega \frac{30}{\pi}}{V_{emf}} \tag{12}$$

From equations (8) to (12) the expressions for the model outputs I_{in} and V_{in} may be formulated in (13) and (14).

$$I_{in}(Q,\omega) = QK_v \tfrac{\pi}{30} + I_0 \tag{13}$$

$$V_{in}(Q,\omega) = \frac{\omega}{K_v \frac{\pi}{30}} + \left(QK_v \tfrac{\pi}{30} + I_0\right) R_i \tag{14}$$

It can be noted from (13) and (14), that besides the input variables torque Q and rotational velocity ω, knowledge of the so-called motor characteristics, internal resistance R_i, no-load current I_0 and specific velocity K_v is required. All three are not constant over the operational range of the electric motor. The internal resistance and the specific rotational velocity decrease with an increase in motor current. For the internal resistance a modeling approach is available (DRELA, 2006). The no-load current increases with increasing rotational velocity, as hysteresis losses increase linearly and eddy-current losses proportional to its square (HANSELMANN, 2006, pp. 32-33). In the model used in this study, all three values are kept constant. This simplification leads to acceptable inaccuracies, as proven in a validation effort with manufacturer data done by RÖßLER (2011, pp. 59-60).

The electric model and a mass prediction model are the main elements of the electric motor design process in Figure 24.

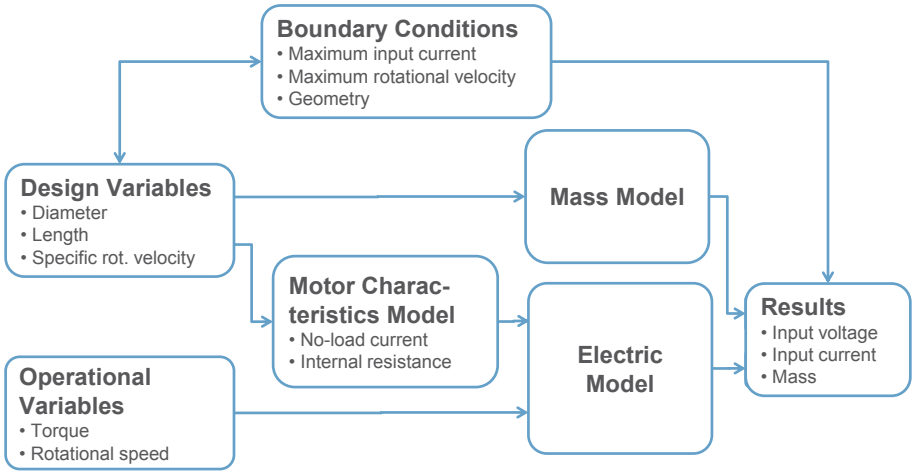

Figure 24: Electric motor design process (SCHOEMANN & HORNUNG, 2013)

The process inputs are the operational variables, torque and rotational velocity, and the design variables. From the design variables the motor mass and the motor characteristics are computed. As previously described, the input voltage and current are determined from the operational variables and the motor characteristics using the electric model.

Parameters with major influence on the electric motor's performance are the motor diameter and length, the number of coil windings, the number of stator teeth, the number of magnet poles and the wire gauge. Diameter, length and specific rotational velocity were chosen as design variables. This choice was driven by their public availability within regression and validation data, and their suitability for the creation of a motor characteristic surrogate model and a mass prediction model. Both models are presented in the following.

As stated above, the three motor characteristics internal resistance, no-load current and specific rotational velocity need to be determined in order to use the electric model. In previous work, this was done either discretely by utilizing a list of existing motors and their characteristics (RÖßLER, 2011; NOTH, 2008) or with a surrogate model based on regression (GUR & ROSEN, 2009). The former approach is very accurate, but requires high computation time and does not allow extrapolation. The latter commonly shows less accurate results, but significantly reduced computation time. The regression model from the quoted work in particular derives one-dimensional equations for a wide range of electric motors of varying quality. This makes its application very time efficient and suitable for the given use case of an optimization routine to show general trends, but too imprecise for the use in preliminary design of high performance UAV. An approach to the modeling of the motor characteristics using textbook methods (HANSELMANN, 2006) led either to detailed models inadequate for preliminary design or to idealized models that could not be validated with the data of commercial motors. Consequently an approach to create a surrogate model from commercial motor data using regression was conducted. A motor database was created, which contains over 700 different brushless DC motors (see Appendix B.1). The manufacturer data not always contain the full range of potential design variables. Commonly published data include internal resistance, no-load current and specific rotational velocity as well as motor diameter, length and the number of windings. From the analysis of the data, it became apparent, that equations derived for motors from one manufacturer may not be applied to those of another one without a significant loss in accuracy. Important data, like the number of magnet poles, the number of stator teeth or the wire gauge, are not published. Thus differences in motor architecture may not be represented in the model. It was hence decided to use one representative manufacturer for each of the two main motor types, inrunner and outrunner. As representative for the inrunner motors, manufacturer Lehner[2] was chosen. Its product range contains motors in exceptionally fine increments. For the outrunner motors, Scorpion[3] was chosen out of the same reason, although the product range is significantly smaller. The approximate power range covered with the inrunner motors is 250 W to 4000 W, whereas the outrunners range from 70 W to 2800 W. The inrunner range is wider than the outrunner range and allows deriving more accurate models. In order to show the trends more clearly, figures in this chapter are exclusively for inrunner motors if not denoted otherwise.

The investigation on how the three motor characteristics may be formulated best as a function of the design variables led to the curves for internal resistance and no-load current over specific rotational velocity plotted in Figure 25 and Figure 26. The data are arranged as follows: Each curve represents one motor series. In a motor series all

[2] Data available at: http://www.lehner-motoren.com/motors/ [Accessed 13 August 2012]
[3] Data available at: http://www.scorpionsystem.com/catalog/motors/ [Accessed 13 August 2012]

motors have the same diameter and length but varying specific rotational velocities. Curves of the same color represent motors with equal diameters but different lengths. The directions of increasing diameter and length are indicated in Figure 25.

The internal resistance decreases for increasing length and diameter. The definition of a conducting wire's resistance as function of its length l_{wire}, its gauge A_{wire} and its resistivity ρ_{wire} is given in (15). Increasing motor case dimensions allow the use of big wire gauges, which according to the definition reduces the wire resistance.

$$R = \rho_{wire} \frac{l_{\text{wire}}}{A_{\text{wire}}} \tag{15}$$

Equation (15) may also be used to explain the decrease of internal resistance with increasing specific rotational velocity. The increase of specific rotational velocity is obtained with a reduction of coil windings. The resulting shorter wire length causes a decrease in resistance.

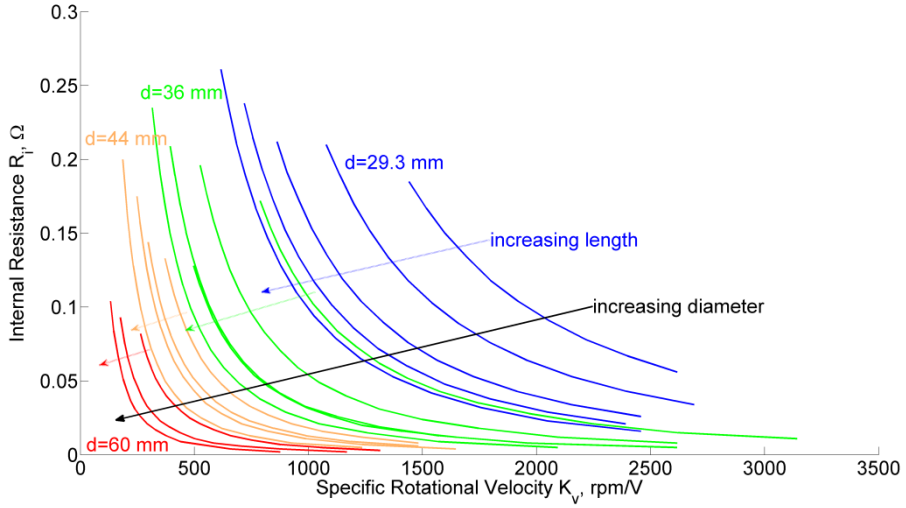

Figure 25: Behavior of electric motor internal resistance over specific rotational velocity (modified from SCHOEMANN & HORNUNG (2012))

The data for the no-load current in Figure 26 are arranged in the same way as for the internal resistance. No-load current increases with increasing diameter, length and specific rotational velocity. With bigger motor sizes air drag increases as well as the eddy-current losses. Furthermore additional bearings may be necessary. The rising no-load current for higher specific rotational velocities may be explained with the simultaneous decrease in internal resistance. According to Ohm's law low resistances lead to high currents. Additionally, higher specific rotational velocities result in higher no-load rotational velocities under the assumption that the supplied voltage remains unchanged. Higher rotational velocities lead to an increase in friction losses, hysteresis and eddy current losses (HANSELMANN, 2006, pp. 32-33).

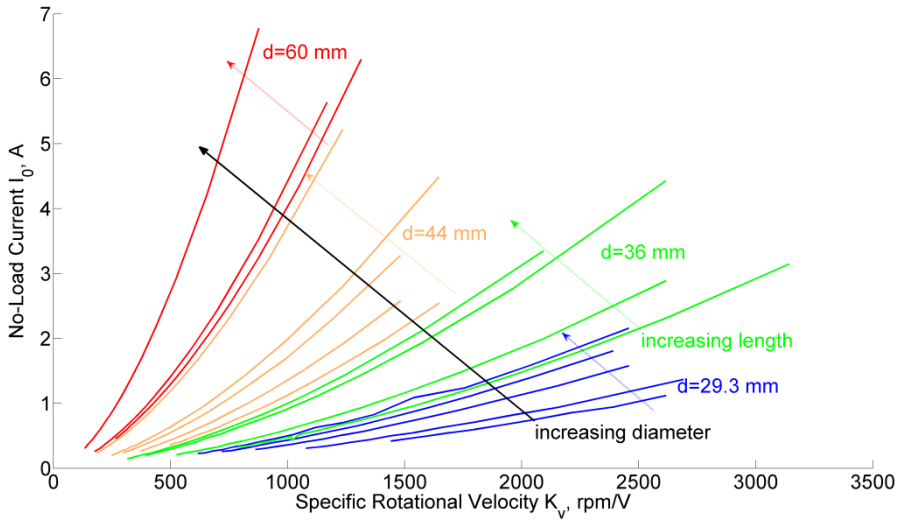

Figure 26: Behavior of electric motor no-load current over specific rotational velocity (modified from SCHOEMANN & HORNUNG (2012))

Internal resistance and no-load current may be modeled as functions of the motor diameter, length and specific rotational velocity. Internal resistance, no-load current and the specific rotational velocity may just as well be modeled as function of diameter, length and the number of windings. The specific rotational velocity is a relative value and one of the main motor characteristics. Therefore it is a more significant variable than the absolute number of windings, which alone does not sufficiently allow a statement on motor performance. It was hence decided to use the specific rotational velocity as design variable.

A regression analysis was conducted to create surrogate models for a quick and accurate computation of the internal resistance and no-load current from the design variables. The curves in Figure 25 and Figure 26 may be accurately fitted with power functions. For each of the two characteristics, the exponents of K_v in these functions differ so little, that they may be assumed to be equal. Three approaches to find the most accurate power function regression model are compared in the following:

1. Power function regression over the product of motor diameter and length and specific rotational velocity
2. Normalization of the curves with their respective minimum or maximum, on both ordinate and abscissa. Regression of both the normalized curves and the extreme values used for normalization
3. Power function regression for each single curve and regression of the coefficients over the product of diameter and length.

The first approach, as described in SCHOEMANN & HORNUNG (2012), results in the following two equations (16) and (17).

$$\begin{aligned} R_i[\Omega] = {} & 0.834 \cdot 10^{-3} \left(dl[mm^2]\right)^{0.5876} K_v[rpm/V]^{0.3791} - 3.937(dl)^{0.0896} \\ & + 8.414\, K_v^{-0.1213} - 3.965 \cdot 10^{-6}(dl) - 3.086 \cdot 10^{-8}\, K_v - 3.427 \cdot 10^{-8}(dl) K_v \\ & + 3.289 \end{aligned} \tag{16}$$

$$\begin{aligned} I_0[A] = {} & -0.1053 \cdot 10^{-3} \left(dl[mm^2]\right)^{0.7564} K_v[rpm/V]^{0.8308} + 4.35 \cdot 10^{-3}(dl)^{0.8386} \\ & + 0.04637\, K_v^{0.5622} - 8.978 \cdot 10^{-4}(dl) - 2.1 \cdot 10^{-4}\, K_v + 4.298 \cdot 10^{-6}(dl) K_v \\ & - 0.4844 \end{aligned} \tag{17}$$

The second approach is previously described in SCHOEMANN (2012). For each motor series (i.e. one single curve in Figure 25 and Figure 26), the values for the specific rotational velocity are normalized by the series' minima $K_{v,min}$, the internal resistance by the series' maxima $R_{i,max}$ and the no-load current by the series' minima $I_{0,min}$ respectively. The resulting curves in Figure 27 are quasi-concurrent.

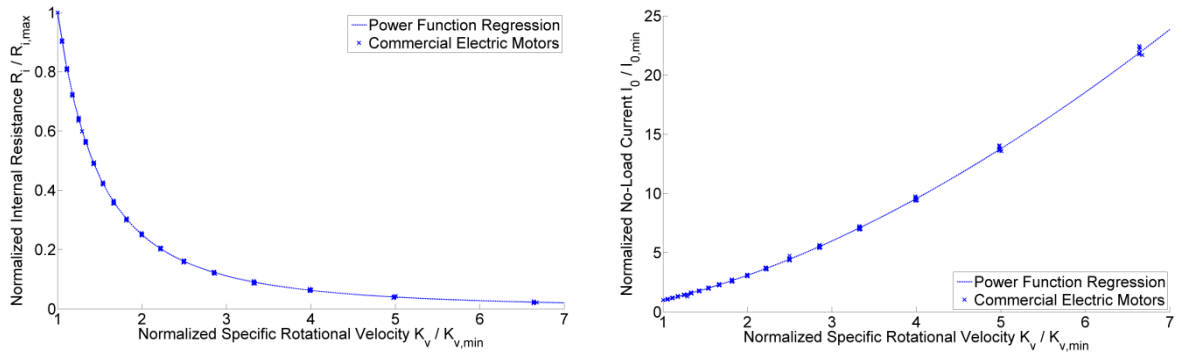

a) b)

Figure 27: Normalized curves a) of the internal resistance and b) the no-load current for inrunner motors

It can be seen in Figure 27 that the power function regression is in very good accordance with the normalized values of commercial motors. The equations are formulated in (18) and (19).

$$\frac{R_i}{R_{i,max}} = \left(\frac{K_v}{K_{v,min}}\right)^{-2} \tag{18}$$

$$\frac{I_0}{I_{0,min}} = \left(\frac{K_v}{K_{v,min}}\right)^{1.63} \tag{19}$$

In order to determine the absolute values of R_i and I_0, regression functions for the minimum specific rotational velocity $K_{v,min}$, the minimum no-load current $I_{0,min}$ and the maximum internal resistance $R_{i,max}$ for each motor series are derived. The minimum specific rotational velocity may be formulated as power function of the product of motor diameter and length. The maximum internal resistance can be accurately modeled as function of the diameter and length as independent variables. The

minimum no-load current may not at all be fitted accurately, so that approach two may only be used for the internal resistance.

In the third approach, described by SCHOEMANN & HORNUNG (2013), each single curve of the families shown in Figure 25 and Figure 26 is fitted individually. As stated before, all curves may be approximated with power functions in the form given in (20) and (21) below.

$$R_i[\Omega] = c_{Ri} K_v[\mathrm{rpm/V}]^{-2} \tag{20}$$

$$I_0[\mathrm{A}] = c_{I0} K_v[\mathrm{rpm/V}]^{1.63} \tag{21}$$

The gathered coefficients c_{Ri} and c_{I0} are formulated as regression functions of the product of diameter and length in (22) and (23).

$$c_{Ri} = 1.5 \cdot 10^{13} \left(dl[\mathrm{mm}^2]\right)^{-2.55} + 650 \tag{22}$$

$$c_{I0} = 1.631 \cdot 10^{-11} \left(dl[\mathrm{mm}^2]\right)^{1.735} \tag{23}$$

Both functions are visualized with the original coefficients in Figure 28.

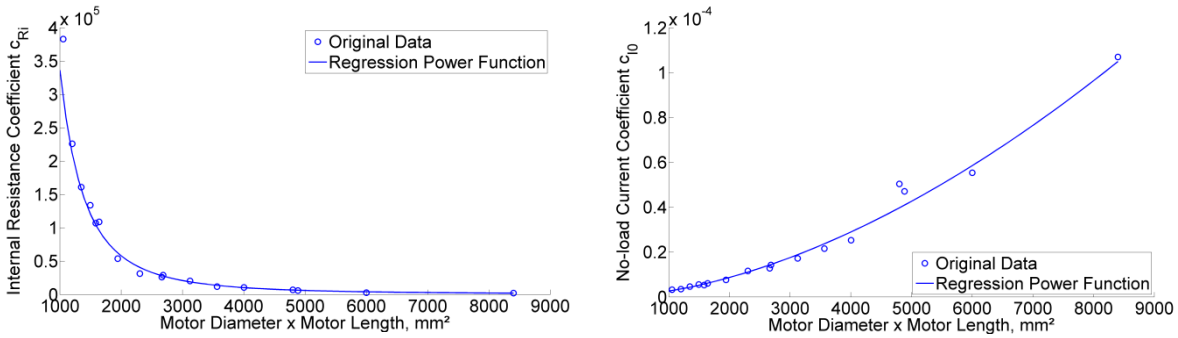

a) b)

Figure 28: Regression power functions for the coefficients of the a) internal resistance and b) no-load current power functions (SCHOEMANN & HORNUNG, 2013)

Approach one and three require only two design variables, the product of motor diameter and length *dl* and the specific rotational velocity K_v, whereas approach two requires K_v and both, diameter *d* and length *l*. The three approaches are compared in terms of accuracy using the commercial inrunner motors the regression is based on. The relative residuals are plotted in Figure 29 for the internal resistance and in Figure 30 for the no-load current.

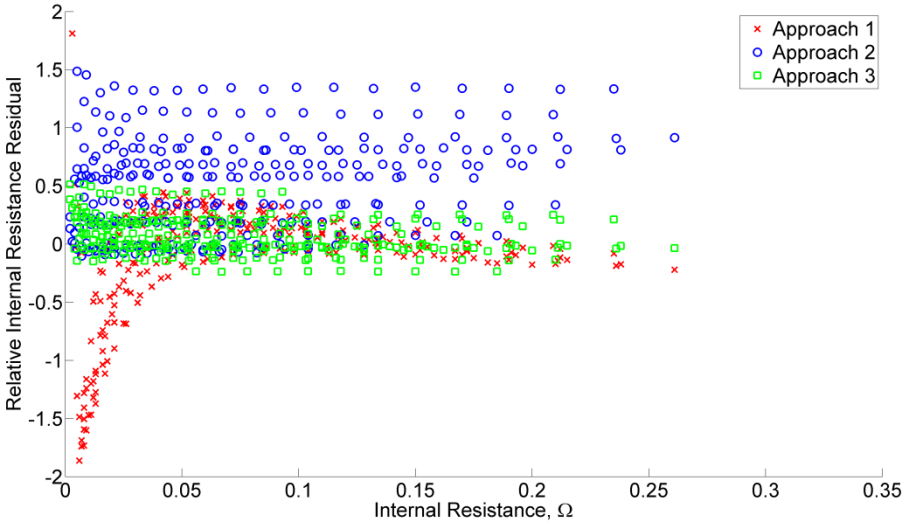

Figure 29: Relative residuals for the electric motor internal resistance prediction

The internal resistance prediction using approach two is significantly less accurate than the other two. Approach one computes too low values at low internal resistances, which correlate with motors with big dimensions. The implied disadvantage of a strong design space restraint is discussed later in this chapter. Approach three shows slightly higher residuals at high internal resistances (small motors) than approach two, but predicts low R_i much more accurate. The coefficient of determination is a figure of merit for the correlation between model results and true values. It is compiled for the three approaches in Table 3. Approach three leads to a slightly higher value than approach one.

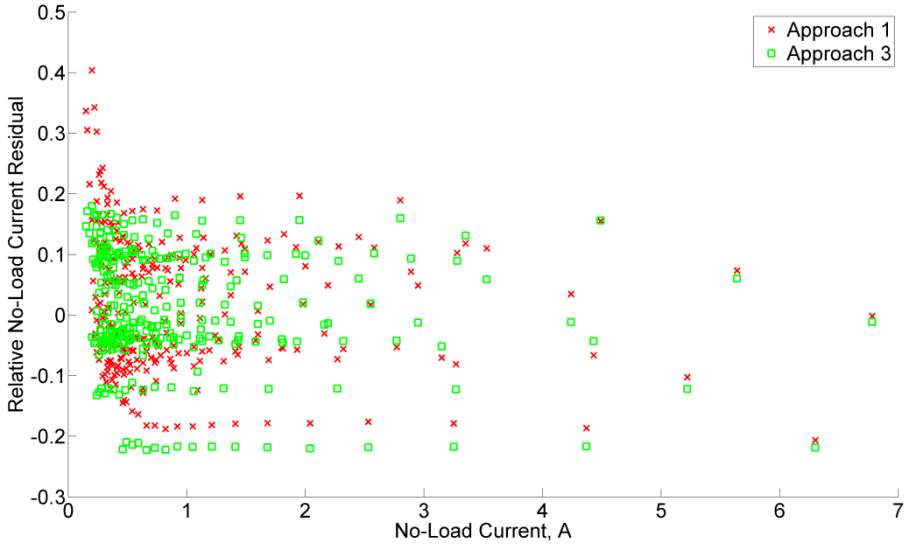

Figure 30: Relative residual for the electric motor no-load current prediction

In terms of the no-load current prediction, approach one and three show very similar accuracy. Generally, approach one provides slightly higher results. The coefficients of determination in Table 3 show a slightly higher value for approach one.

Table 3: Coefficients of determination for the prediction of electric motor internal resistance and no-load current

	Internal Resistance	**No-Load Current**
Approach 1	0.9366	0.9754
Approach 2	0.8942	-
Approach 3	0.9500	0.9741

The computation times required for the three approaches are compared to an interpolation procedure in Table 4. As the no-load current prediction of approach two was too inaccurate to be considered, computation time of approach two contains the I_0 prediction of approach one. Each of the three regression approaches requires around 2.4 ‰ of the average computation time of an interpolation for the determination of one pair of internal resistance and no-load current.

Table 4: Computation time of the three approaches to electric motor characteristic prediction in comparison with interpolation

	Normalized Computation Time	**Mean Computation Time per Run [s]**
Interpolation	1	0.0126
Approach 1	0.0024	$3.0482 \cdot 10^{-5}$
Approach 2	0.0023	$2.9505 \cdot 10^{-5}$
Approach 3	0.0023	$2.8604 \cdot 10^{-5}$

In order to generically use the equations a careful restraint of the design space is necessary, which means the establishment of boundary conditions for the association between the design variables. In case of the motor characteristics surrogate model, a relationship between the product of diameter and length and the specific rotational velocity is required. If both, *d* and *l*, are used as design variables singularly, as necessary for the mass estimation described in the further course of this chapter, a relation between the two geometric variables is needed. Equations (24) and (25) describe the minimum and maximum length as function of the diameter. The relations are derived from the database of commercial motors for a diameter range of 29 mm to 60 mm.

$$l_{min}\,[\mathrm{mm}] = 1.465\,d[\mathrm{mm}] - 6.76 \tag{24}$$

$$l_{max}\,[\mathrm{mm}] = 2.787\,d[\mathrm{mm}] - 22.72 \tag{25}$$

The following regression power equations (26) and (27) for the minimum and maximum K_v as function of *dl* are also derived from the motor database.

$$K_{v,min}\,[\mathrm{rpm/V}] = 1.38 \cdot 10^{7} \left(dl[\mathrm{mm}^2]\right)^{-1.332} \tag{26}$$

$$K_{v,max}\,[\mathrm{rpm/V}] = -1752\left(dl[\mathrm{mm}^2]\right)^{0.1611} + 8243 \tag{27}$$

Figure 31 graphically shows the resulting restraint of the electric motor design space. Each horizontal line of markers represents one motor series from the database. Equation (26) is a fit of the very left point of each series, whereas (27) is a fit of the very right points.

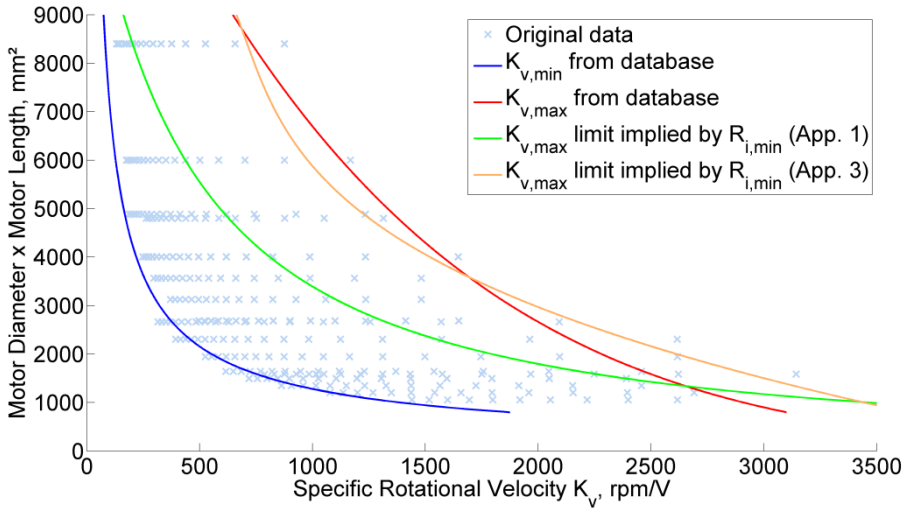

Figure 31: Restraint of the inrunner electric motor design space for the determination of internal resistance and no-load current (modified from SCHOEMANN & HORNUNG (2012))

A further limit included in Figure 31 is the maximum K_v implied by the self-imposed prerequisite not to underrun the minimum internal resistance of each series. In order to create this limit, the regression function (28) is created from the minimum R_i of each series. It is plotted with the database values in Figure 32.

$$R_{i,min}\,[\Omega] = 7.895 \cdot 10^{9} \left(dl[\mathrm{mm}^2]\right)^{-3.701} + 4.19 \cdot 10^{-3} \tag{28}$$

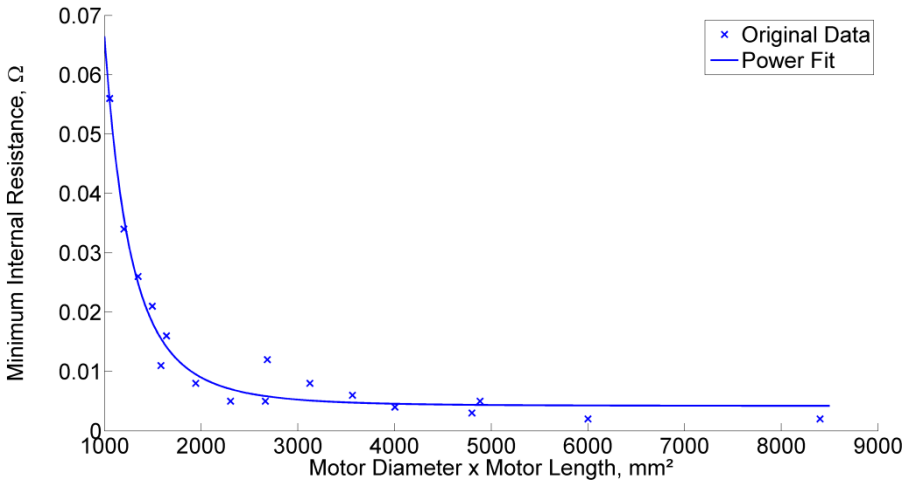

Figure 32: Minimum internal resistance per motor series as function of the product of motor diameter and length (SCHOEMANN & HORNUNG, 2012)

An equation for $K_{v,max}$ is derived from the values of K_v, for which the R_i provided by approaches one and three are equal to the $R_{i,min}$ computed with (28). Approach two is not applicable because it is based on a three-dimensional design space defined by d, l and K_v. As internal resistance decreases with increasing size of the motor, this restraint excludes big motors from the design space. Of the two limits for $K_{v,max}$ the smaller at each product of d and l defines the design space. In Figure 31 it can be noted that the boundary condition for approach one restrains the design space significantly more than the one for approach three. This is due to the earlier mentioned tendency of the equations resulting from approach one to determine low internal resistance too optimistic, as shown in Figure 29.

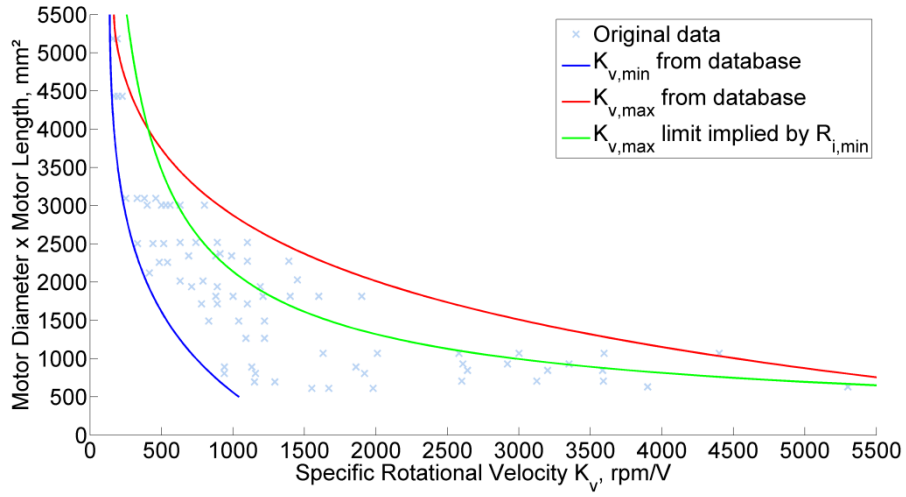

Figure 33: Restraint of the outrunner electric motor design space for the determination of internal resistance and no-load current (modified from SCHOEMANN & HORNUNG (2012))

The derivation of equations for the outrunner motors is significantly more challenging than for the inrunner motors, as every series contains less motors than it is the case for the inrunners. The overall number of motors is one third of the inrunners. This only allows the use of approach one to model the internal resistance and no-load current.

The accuracy of the R_i prediction is satisfactory with a coefficient of determination of 0.9491, whereas for the I_0 prediction only an unacceptable value of 0.6822 may be reached. As described for the inrunner motors, the equations resulting from approach one here also return too optimistic internal resistances for big motors. In the design space restraint plot in Figure 33 it can be seen that the feasible range of K_v is very narrow at high *dl*.

The inrunner motor characteristics surrogate model bases on commercial motors with a *dl* range of 1000 mm² to 8400 mm². Within this range no discontinuities in the behavior of internal resistance and no-load current is noted. For a further increase in motor size, no step change, neither in technology nor in the used motor architecture is required. Based on this information it is assumed that both motor characteristics also behave continuously in an extrapolation up to 16,000 mm². The limits derived for the minimum and maximum specific rotational velocities in (26) and (27) are not applicable for extrapolation as they run to negative values. For values bigger than 8400 mm² they are replaced with constant values of 82 rpm/V and 700 rpm/V. These values correlate with the values of $K_{v,min}$ and $K_{v,max}$ at a *dl* of 8400 mm².

Besides the restraints for the design variables, a reliable model also requires restraint functions for the operational variables. The limit for the input voltage is driven by the electric speed controller and discussed in the respective chapter 3.2.2. The electric motor limits the maximum rotational velocity ω_{max} and the maximum input current I_{max}. Data not available by the manufacturer were determined by RÖßLER (2011) using the manufacturer's motor diagrams. Only approach one leads to an acceptable accuracy in a regression of the obtained data for I_{max}.

$$\begin{aligned} I_{max}\left[A\right] = {} & 1.98\left(dl\left[mm^2\right]\right)^{-0.0979} K_v\left[rpm/V\right]^{0.9603} + 0.2335\left(dl\right)^{0.8978} - 13.4\,K_v{}^{0.3} \\ & - 0.091\left(dl\right) - 0.7446\,K_v + 6.197\cdot 10^{-5}\left(dl\right)K_v + 3.654 \end{aligned} \tag{29}$$

The maximum current modeled by (29) is the maximum continuous current. Electric motors are commonly able to bear a higher current for a short period of several minutes. Very few data are published on the maximum current behavior or the ratio of maximum current to maximum continuous current. HISEROTE (2010) classifies a ratio of 1.75 as conservative, whereas the only manufacturer[4] in the motor database with specifications on maximum power reports a ratio of 2. The peak maximum current is therefore set to the double value of the continuous maximum current I_{max}. For the maximum rotational velocity a plain value of N_{max} = 85.000 rpm is given by the manufacturer. This corresponds to a ω_{max} of 8900 1/s.

[4] Data available at: http://www.neumotors.com/Site/Motors.html [Accessed 13 August 2012]

In a comparison of the three approaches to create a surrogate model for the prediction of the electric motor characteristics internal resistance and no-load current, approach two may be discarded. The predicted internal resistances are significantly more inaccurate than with the other two approaches, whereas the prediction of no-load current is impractical due to the impossibility of setting up a regression function for the minimum no-load current per motor series. The decision between approach one and three is mainly driven by their capability to predict internal resistance as differences in the accuracy of the I_0 prediction are marginal. The impreciseness of approach one for big motors has, as it was shown, significant effect on the design space and practically limits the applicability of the model to electric motors with low K_v below a certain size. Therefore, approach three is chosen. In comparison to the interpolation procedure it offers the advantage of an easier extrapolation and shorter computation times. The resulting restrained internal resistance and no-load current maps are given in Figure 34.

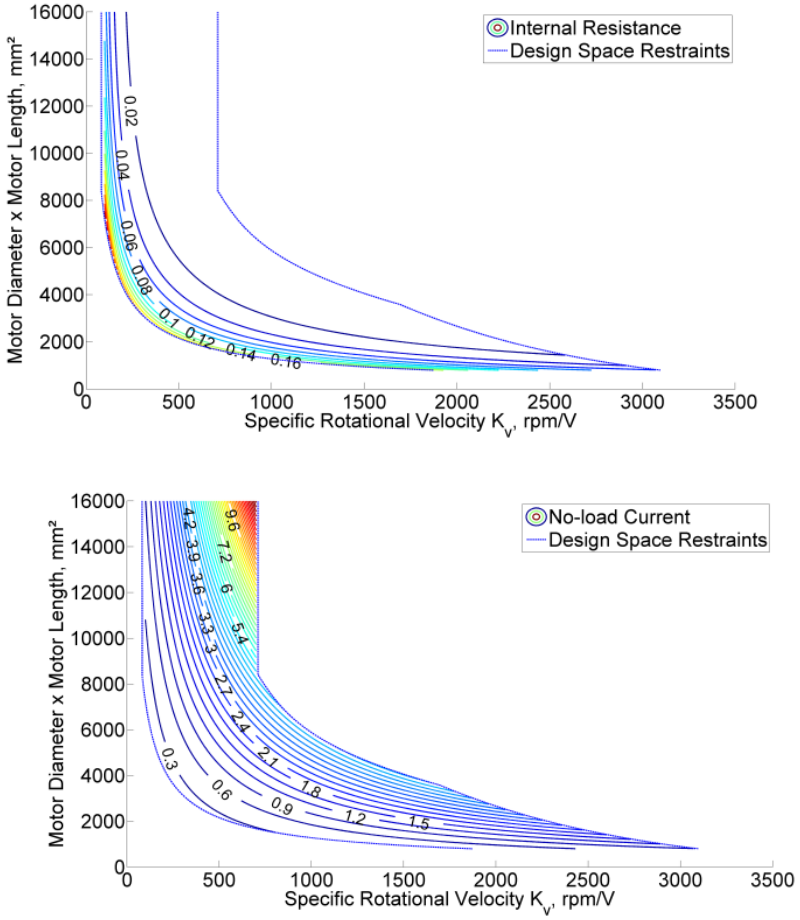

Figure 34: Internal resistance (top) and no-load current (bottom) maps for inrunner motors

Besides the electric properties and efficiency of an electric motor, its mass is a decisive factor for the decision whether it is suitable. The electric motor has elements whose mass is depending on its surface, on its volume and on its length. Nevertheless, simpler regression functions of the product of motor diameter and length *dl* or the

product of diameter squared and length d^2l are linear and provide high accuracy. Using the function (30) of dl reduces the number of design variables to two, dl and K_v, whereas the function (31) of d^2l returns more accurate results with a coefficient of determination of 0.984 compared to 0.979.

$$m_{EM}\,[g](dl) = 0.2232\,dl\,[mm^2] - 193.1 \tag{30}$$

$$m_{EM}\,[g](d^2l) = 3.365 \cdot 10^{-3}\,d\,[mm]^2\,l\,[mm] + 16.36 \tag{31}$$

Both inrunner functions (30) and (31) are plotted with the original data from the motor database in Figure 35, including the outrunners. The choice of the mass estimation function (30) is quantitatively justified in chapter 4.1.

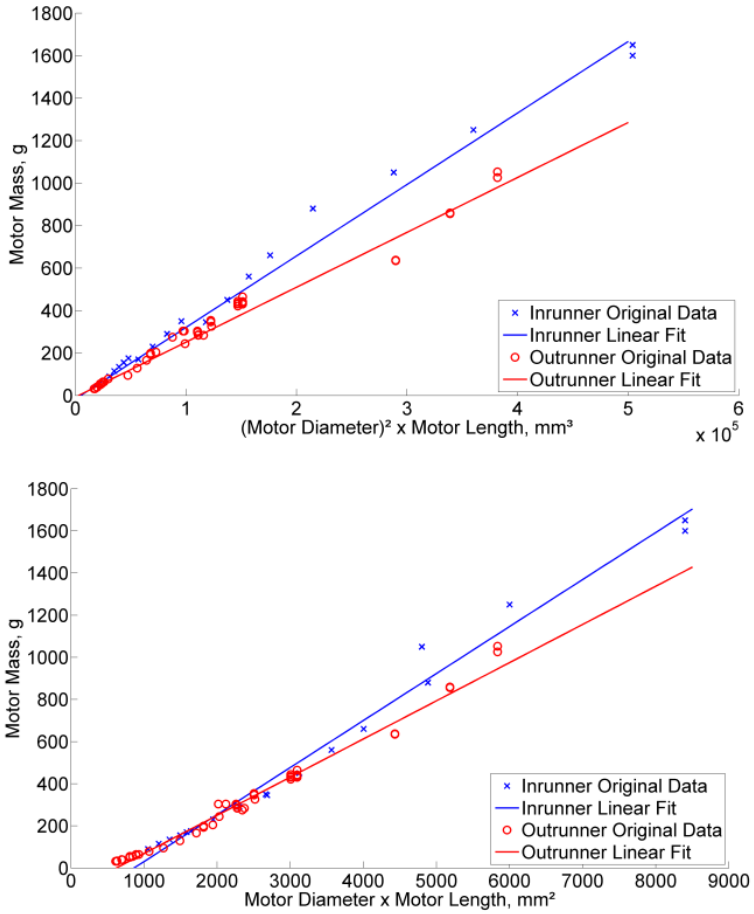

Figure 35: Mass prediction for inrunner and outrunner electric motors as function of a) d^2l and b) dl (modified from a) SCHOEMANN & HORNUNG (2012) and b) SCHOEMANN & HORNUNG (2013))

In summary, the described electric motor design process allows determining a motor's required input voltage and current as well as its mass for a given set of design variables, torque demand and rotational velocity. Two central elements of the process are regression-based: the mass estimation model and the prediction model for the motor characteristics internal resistance and no-load current. These surrogate models may only capture the design space defined by the underlying data base. For the

inrunner motor model an extrapolation is considered justifiable to overcome this limitation. For the outrunners the limited published regression data leads to more inaccurate equations and a smaller design space. This might be changed with a more extensive data set that includes potential design variables that manufacturers commonly do not publish, as the number of magnet poles, the number of stator teeth or the wire gauge.

3.2.2 Electronic Speed Controller

The electronic speed controller (ESC) module provides the component's input voltage and current as well as its mass. The inputs consist of the electric motor input voltage and current.

The energy dissipation in the ESC causes a voltage drop, which is quantified by the ESC efficiency. It was described in chapter 2.2.2, that the electronic speed controller's efficiency may be significantly lower in part load operation than in full load operation. In a conventional electric propulsion system this is decisive, as the system only bears full load during a short phase at takeoff and climb, whereas the biggest flight phase commonly is in part load conditions. In parallel hybrid-electric systems, the electric propulsion path may be designed to always run at maximum continuous power, as it runs in dual mode with the internal combustion engine during takeoff and climb. Nevertheless, only very few investigations on ESC efficiency are published. LUNDSTRÖM, AMADORI & KRUS (2010) gathered some experimental data, whereas RÖßLER (2011) derived the only estimation method known to the author. Its central equation is given in (32).

$$\eta_{ESC} = \frac{V_{in,ESC} - R_{i,ESC} I_{in,ESC}}{V_{in,ESC}} - \frac{k_{PTF}}{V_{in,ESC}} \left(1 - \frac{P_{in,ESC}}{P_{max,ESC}} \right) \tag{32}$$

The first term represents full load efficiency, which is fully dependent on the ESC's internal resistance $R_{i,ESC}$. The second term is equal to zero when the input power $P_{in,ESC}$ is equal to the maximum input power $P_{max,ESC}$. It represents the efficiency change in part load. The figure of merit for part load efficiency is the part-throttle factor k_{PTF}. It was experimentally determined by RÖßLER (2011) for three commercial ESC. The values differ strongly from 200 V to 400 V, and no rule might be derived. Furthermore the internal resistance is not a parameter commonly published by the manufacturers. The absence of estimation rules for $R_{i,ESC}$ and k_{PTF} thus prevents the generic use of (32). In the original application by RÖßLER (2011), $R_{i,ESC}$ and k_{PTF} of the most efficient controller are globally integrated into the equation. Until further experimental data is available, this is assumed to be more reasonable than neglecting ESC efficiency. For the use in the backward-facing design procedure, equation (32) is formulated in terms

of the output voltage, instead of the input voltage. The original equation is visualized in Figure 36 in the form of an efficiency map. The values clearly underline the importance of ESC efficiency estimation for part load. Efficiency decreases with sinking load and input voltage. The COTS controller for which the part-throttle factor and internal resistance were measured is the Kontronik Jive 80 HV[5]. It has an input voltage range of 16 V to 50 V.

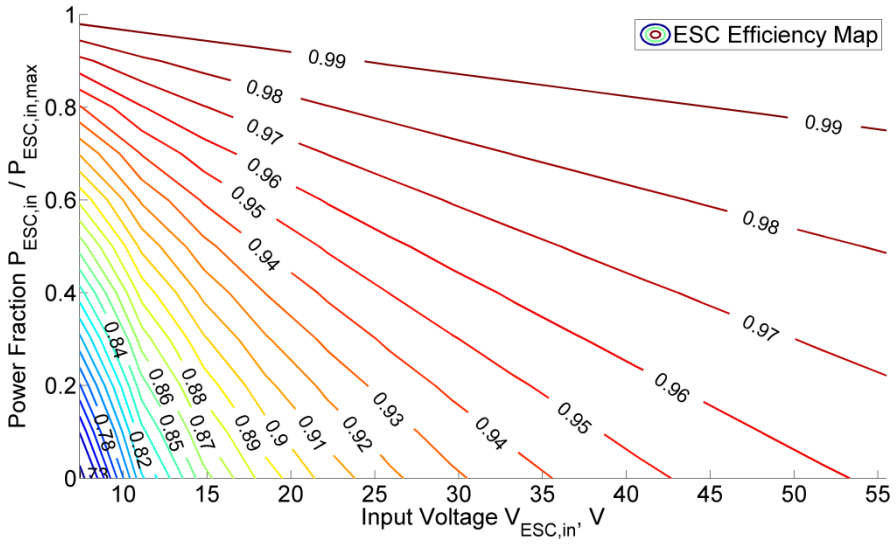

Figure 36: Electronic speed controller efficiency map for the Kontronik Jive 80 HV (SCHOEMANN & HORNUNG (2013), generated with model from RÖßLER (2011))

One important restraint implied in the use of COTS electronic speed controllers is their voltage limitation. State-of-the-art controllers do not allow an input higher than 15 Lithium-polymer cells in series, which corresponds to a nominal voltage of 55.5 V. This value was taken from a database of commercial ESC in which data of 50 models were collected (see Appendix B.3). The database was further used to derive a prediction rule for controllers mass. The scatter in the mass data is significant although the controllers in the database are in a comparable price range and have comparable capabilities. When regarded as function of input current, linear functions with high accuracy may be derived for each single manufacturer product line, but no reasonable overall function. A general prediction rule (33) may be formulated as a function of input power. The original data and a derived linear fit are plotted in Figure 37. The linear fit has a fair coefficient of determination of 0.8020.

$$m_{ESC}\,[g] = 0.026\, P_{ESC,cont,max}\,[W] + 5.747 \tag{33}$$

Equation (33) is in good accordance with other regression function predicting the mass of electronic speed controllers, as for example in NOTH (2008).

[5] Data available at: http://www.kontronik.com/index2.php?option=com_content&task=view&id=37&Itemid=1 [Accessed 23 April 2013]

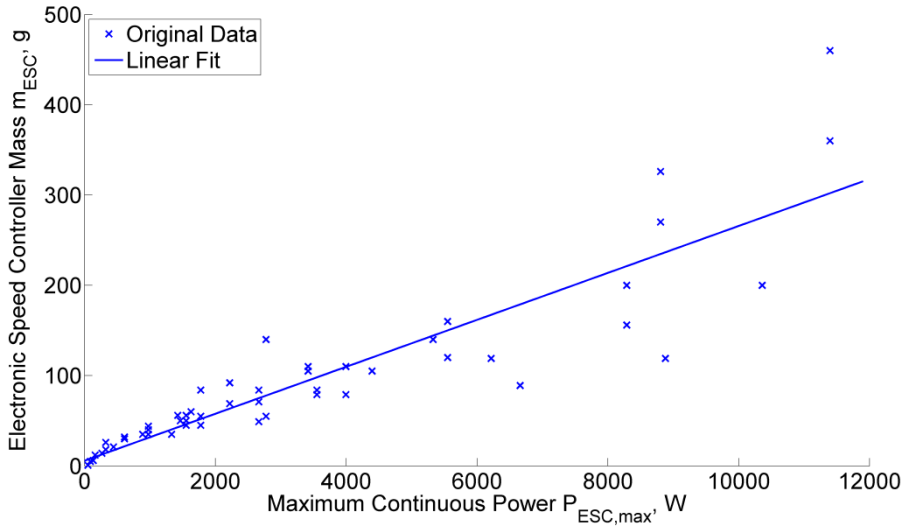

Figure 37: Mass prediction for electronic speed controllers (SCHOEMANN & HORNUNG, 2012)

In a parallel hybrid-electric propulsion system, the electric motor is supposed to work as a generator as well. It is not common for COTS electronic speed controllers to include a generator capability. Enabling the transformation of rotary-current into direct-current may result in a mass penalty compared to the database values.

3.2.3 Battery

The objective of the battery module is the determination of the component mass. A common way to determine the mass of a Lithium-polymer battery is to assume a constant value for the specific energy and size it according to the required energy. A shortcoming of this method is the missing consideration of battery voltage, drawn current and efficiency. Furthermore, the assumption that a battery pack is available in arbitrary energy packages is not true if COTS components are used. Therefore, a new method is introduced, that includes the computation of the number of cells in parallel and series as well as the battery efficiency. Input parameters of the module are input voltage and current of the electronic speed controller. The capacity of one battery cell is the design variable of this model.

An estimation function for the mass of battery cells was derived from the database of over 400 Lithium-polymer batteries (see Appendix B.4). A fit over cell energy E_{cell} and maximum continuous discharge current $I_{max,cell}$ showed very good compliance. The original data and the double linear fit are plotted in Figure 38. Furthermore, the minimum and maximum limits for $I_{max,cell}$ as function of E_{cell} are derived from the database and included in Figure 38.

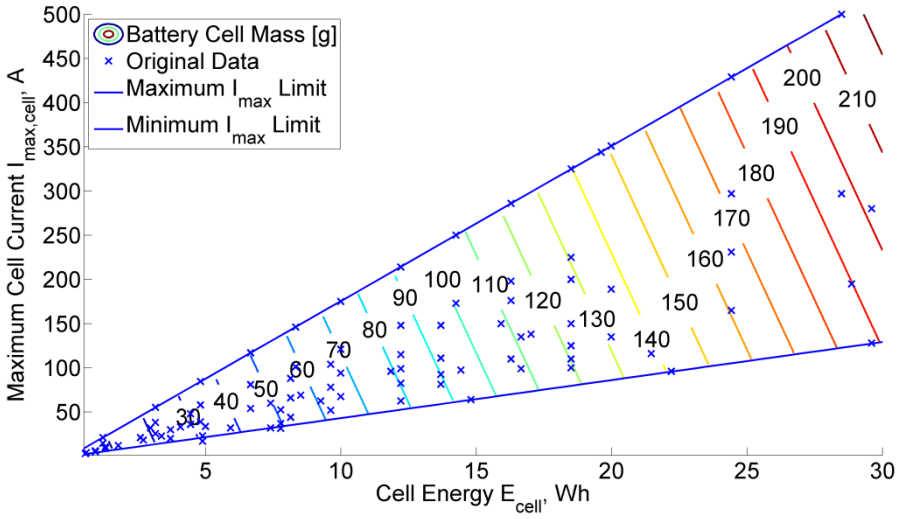

Figure 38: Mass prediction for batteries at cell level (SCHOEMANN & HORNUNG. 2012)

The fitted function (34) includes values for the specific energy and specific current of the battery in the denominator of first term and the second term, respectively. They may be adapted with technology factors for parameter studies. The equation indicates a much higher sensitivity of battery mass to energy than to the discharge current. The battery database that it was derived from mainly consists of batteries intended for aircraft models. This type of battery is commonly designed for a high discharge current.

$$m_{cell}[g] = \frac{E_{cell}[Wh]}{0.168} + \frac{I_{max,cell}[A]}{11.06} \tag{34}$$

The fitted specific energy of 168 Wh/kg is relatively conservative, especially when associated with the outlook in chapter 2.2.3. The cell energy E_{cell} in (34) is the product of the cell capacity C_{cell} and the nominal cell voltage V_{cell}. The maximum continuous discharge current $I_{max,cell}$ is the maximum drawn current divided by the number of cells in parallel.

$$I_{max,cell} = \frac{I_{in,ESC,max}}{n_p} \tag{35}$$

The number of cells in parallel is computed as the rounded up the fraction of the capacity required and the capacity available per cell, according to (36).

$$n_p = \left\lceil \frac{C_{req}}{C_{cell}} \right\rceil = \left\lceil \frac{\left(1.25 \sum \frac{I_{ESC,in,i}\, t_i}{\eta_{battery,i}} \right)}{C_{cell}} \right\rceil \tag{36}$$

The capacity C_{req} required to fulfill a flight mission is the sum of the products of the currents drawn I_i and the time t_i they are drawn for each design point i, divided by the battery efficiency $\eta_{battery,i}$. As explained in chapter 2.2.3, only 80 % of the capacity of a Lithium-polymer battery should be discharged. The required capacity then results in 1.25 times the nominally required capacity.

The efficiency of a battery is mainly driven by the resistive losses inside the component (SAHA & GOEBEL, 2009). At constant discharge current it is perceivable as a voltage drop from the internal, open-circuit voltage (OCV) to that available on the terminals. A model to predict the internal resistance of a battery is presented by RÖßLER (2011). The regression equation (37) allows the determination of the internal resistance $R_{i,batt}$ from the capacity of the battery cell C_{cell} and the maximum continuous C-rate r_c. The C-rate is the fraction of discharge current and capacity, and the reciprocal value of the time necessary to completely discharge the battery at this current.

$$R_{i,batt} = n_S \frac{3.367\, r_{c,max} + 409.7}{r_{c,max}\, C_{cell}} \tag{37}$$

The estimation is not applicable in this form, as the maximum C-rate of a battery cell would need to be included as battery design variable, resulting in an increase in computational time. Therefore equation (37) was applied to the Lithium-polymer battery database in order to derive an estimation model more compatible with the design procedure (SCHOEMANN & HORNUNG, 2013). In Figure 39, the results are plotted over cell capacity, the battery design variable, which proofed to be suitable for a one-dimensional prediction of internal resistance. It can be seen there, that internal resistance decreases with increasing cell capacity. This may be explained with the bigger size of high capacity batteries, which allows the use of thicker, lower resistance wiring, according to (15). A further explanation is that low capacity batteries commonly are not designed for high discharge currents and therefore higher resistance is accepted for the sake of lower cost.

The equation derived using a power fit is (38).

$$R_{i,cell}[\Omega] = 0.01162\, C_{cell}^{2.245}[\mathrm{Ah}] + 0.0015 \tag{38}$$

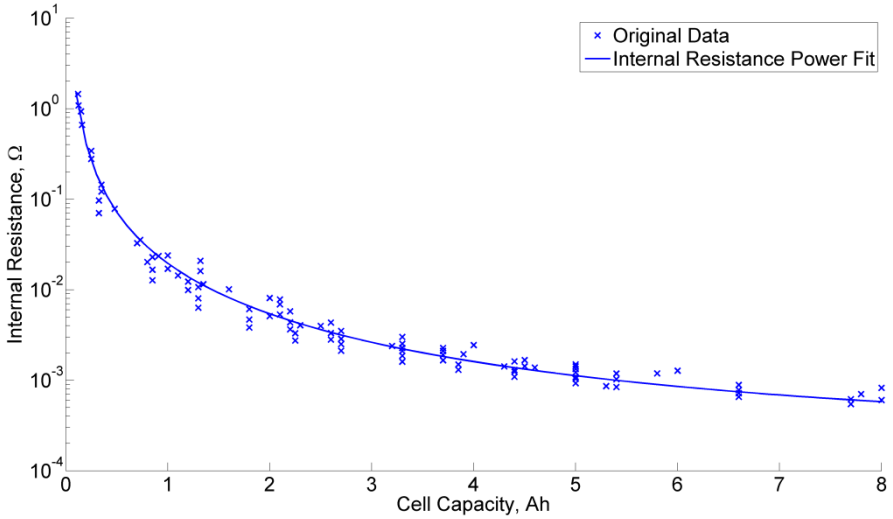

Figure 39: Battery internal resistance estimation (SCHOEMANN & HORNUNG, 2013)

The battery resistance is the product of the cell resistance and the number of cells in series, which is computed from the maximum ESC input voltage $V_{\text{in,ESC,max}}$ and the cell voltage V_{cell}. As only an integer number of cells may be connected, the ratio is rounded up according to (39).

$$n_s = \left\lceil \frac{V_{\text{in,ESC,max}}}{V_{\text{cell}}} \right\rceil \tag{39}$$

The voltage per cell V_{cell} may be set to the nominal 3.7 V for Lithium-polymer batteries. With knowledge of the internal resistance, the open-circuit voltage may be computed from the ESC input voltage and current using Ohm's law. The battery efficiency is the ratio of output voltage, here equal to the ESC input voltage, to the open-circuit voltage.

The mass of the battery is then computed according to (40) as the product of the number of cells in series and parallel and the mass of one cell.

$$m_{\text{battery}} = m_{\text{cell}} n_p n_s \tag{40}$$

3.2.4 Internal Combustion Engine

The internal combustion engine module determines the required chemical input power and engine mass. Its inputs are the shaft torque and rotational velocity as well as the design variables. The engine input power is not formulated in its state variables mass flow and lower heating value. Accuracy is not compromised, as the lower heating value may reasonably be assumed constant for each fuel type. The required mass flow may be used to size a fuel tube system, which is excluded from this design method due to the low impact on overall mass.

In order to determine the engine input power, the identification of its efficiency is necessary. Dynamic modeling of the processes within the internal combustion engine requires extensive computation time, due to the necessary combustion simulation. Simple surrogate models are not available. A quicker alternative in terms of computation time is the scaling of engine performance.

A common formulation of the efficiency of an internal combustion engine is the efficiency map. In an efficiency map, lines of constant efficiency are plotted for varying torque demands and rotational velocities. Efficiency maps are widely available for automotive engines (HEYWOOD, 1988; GUZELLA & ONDER, 2010). For smaller engines suitable for the use in unmanned aerial vehicles they are very seldom published, as this class of engines is only used in niche markets such as gardening tools, recreational vehicles or model aircraft. In these areas, fuel consumption is negligible or a global statement on efficiency is accepted by the customer and consequently no data dependent on state variables is available. Manufacturers of small engines commonly provide no efficiency data, but either just gross power or a so-called wide-open throttle (WOT) curve, which contains the maximum torque for each rotational velocity.

The engine design procedure is shown in Figure 40. Its main elements are a mass model and an efficiency scaling model. The mass model consists of a regression function with which the engine mass may be computed from the design variables. For the efficiency scaling model, a baseline efficiency map is chosen based on the design variables. The map is formulated in mean-value variables, mean efficient pressure (MEP) instead of torque, and mean piston speed instead of rotational velocity. These variables are explained in the next paragraph. The operational input to the model, torque demand and rotational velocity, are converted into the mean value variables using the design variables. The efficiency is obtained by scaling the baseline efficiency using the design variables and the mean-value variables as input. The design variables are the displacement volume V_d, the stroke-to-bore ratio S/B, the number of cylinders n_{cyl}, the number of strokes per work cycle n_{stroke} and the ignition method. The latter

two are only required for the choice of a suiting baseline efficiency map, whereas the other three are used to determine the mean-value variables and for the sizing process in the way described.

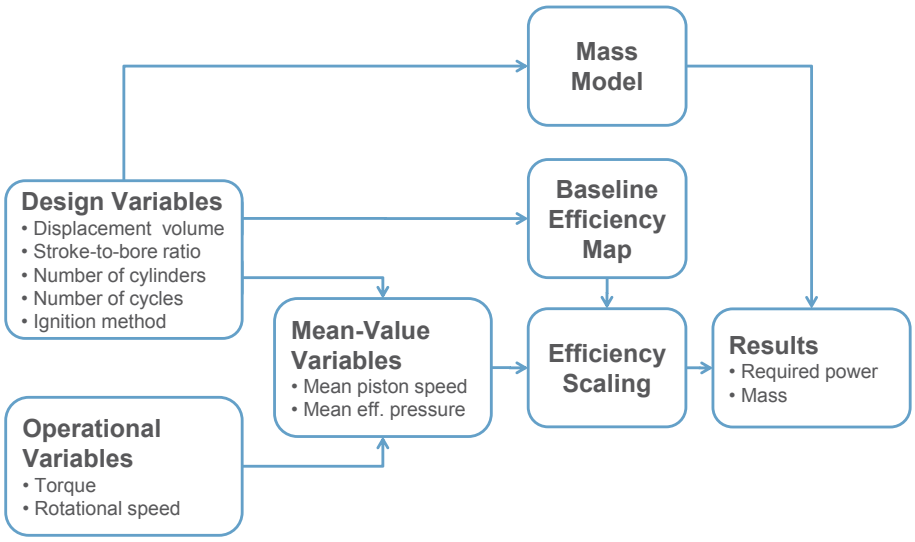

Figure 40: Internal combustion engine design process (SCHOEMANN & HORNUNG, 2013)

Mean-value variables are formulated with respect to geometric properties of the engine. This allows an easier comparison and scaling of the properties and performance of engines of different sizes (GUZELLA & ONDER, 2010). The rotational velocity ω is converted into the mean piston speed c_m, using the stroke S.

$$c_m = \frac{S}{\pi}\omega \tag{41}$$

The stroke S may be determined from the displacement volume V_d, the stroke-to-bore ratio S/B and the number of cylinders n_{cyl} as given in (42).

$$S = \sqrt[3]{\frac{4V_d}{\pi n_{cyl}}\left(\frac{S}{B}\right)^2} \tag{42}$$

The mean-value variable to specify the engine load is the mean effective pressure p_{me}. It is defined by associating the torque demand Q to the engine displacement volume V_d.

$$p_{me} = Q\left(\frac{4\pi}{V_d}\right) \tag{43}$$

Two scaling procedures were considered for this work. The Willans-Line approximation is presented in several authors' works on automotive engines (RIZZONI & GUZELLA, 1999; RAJAGOPALAN, WASHINGTON, RIZZONI & GUEZENNEC, 2003;

WEI, 2004; GUZELLA & ONDER, 2010). As explained in SCHOEMANN & HORNUNG (2012), it is considered not to be perfectly suitable for the task and a new scaling method was developed.

The Willans-Line model assumes the quasi-linear relation between input power and output power of an engine given in (44).

$$P_{out} = eP_{in} - P_{loss} = e\left(\dot{m}_{fuel} H_{LV}\right) - P_{loss} \tag{44}$$

Two of the loss mechanisms, described in chapter 2.2.4, are incorporated in (44): The thermal losses are represented by the thermal efficiency e and the friction and volumetric losses by the power loss P_{loss}. The input power of the engine is equal to the product of fuel mass flow $\dot{m}_{fuel}$ and the fuel's lower heating value H_{LV}. The power formulation in (44) may easily be converted into the torque formulation in (45) with a division by the rotational velocity. Equation (46) is the mean-value formulation of (45). The available mean efficient pressure p_{ma} and the mean effective pressure loss p_{mloss} are computed from the right-hand terms of (45) analogous to equation (43).

$$Q_{out} = e\frac{\dot{m}_{fuel} H_{LV}}{\omega} - Q_{loss} \tag{45}$$

$$p_{me} = ep_{ma} - p_{mloss} \tag{46}$$

The variables representing loss, e and p_{mloss}, are calibrated from existing efficiency maps. RIZZONI & GUZELLA (1999) proposed the polynomial equations (47) for e and (48) for p_{mloss}.

$$e = \left(e_{00} + e_{01} c_m + e_{02} c_m^2\right) - \left(e_{10} + e_{11} c_m\right) p_{ma} \tag{47}$$

$$p_{mloss} = p_{mloss,0} + p_{mloss,2} c_m^2 \tag{48}$$

Both equations show dependency on the mean piston speed. The definition of e furthermore includes a term that is linearly dependent on p_{ma}. Equations (47) and (48) clarify that equations (44) to (46) do not describe a linear relation and why they are referred to as quasi-linear above. From equation (44) and (46) to (48), the definition of the engines efficiency in (49) may be derived.

$$\eta = \frac{P_{out}}{P_{in}} = \frac{eP_{in} - P_{loss}}{P_{in}} = \frac{p_{me}}{p_{ma}}$$
$$= \frac{p_{me}}{\frac{\left(e_{00} + e_{01}c_m + e_{02}c_m^2\right)}{2\left(e_{10} + e_{11}c_m\right)} \pm \sqrt{\frac{\left(e_{00} + e_{01}c_m + e_{02}c_m^2\right)}{2\left(e_{10} + e_{11}c_m\right)} - \frac{p_{me} + p_{mloss,0} + p_{mloss,2}c_m^2}{e_{10} + e_{11}c_m}}} \tag{49}$$

With the lack of published data on small engines described above, data on thermal efficiency e or the other losses p_{mloss} are not available. Furthermore, no published Willans-Line coefficients for other than automotive engines are known to the author. Thus, for the calibration of the model with an existing efficiency map, equation (49) would have to be used. It is obvious from the structure of the equation, that both, determining the coefficients and using the equation within the design process will require high effort in computational time. This disadvantage of the method is not adressed in the publications describing it, as it is used in a forward-facing process there. In a forward-facing process, contrary to the backward-facing process described here, the engine's shaft torque is computed from the available fuel mass flow and lower heating value.

An alternative engine performance scaling method was presented in SCHOEMANN & HORNUNG (2012) and SCHOEMANN (2012). It is characterized by a more direct scaling of a baseline efficiency map. The default baseline map for four-stroke SI engines is compiled from the data on an engine development specifically for UAVs (HENDRICKSON & MCGEER, 1999). The efficiency map of the 28.3 cm³ engine is plotted in Figure 41.

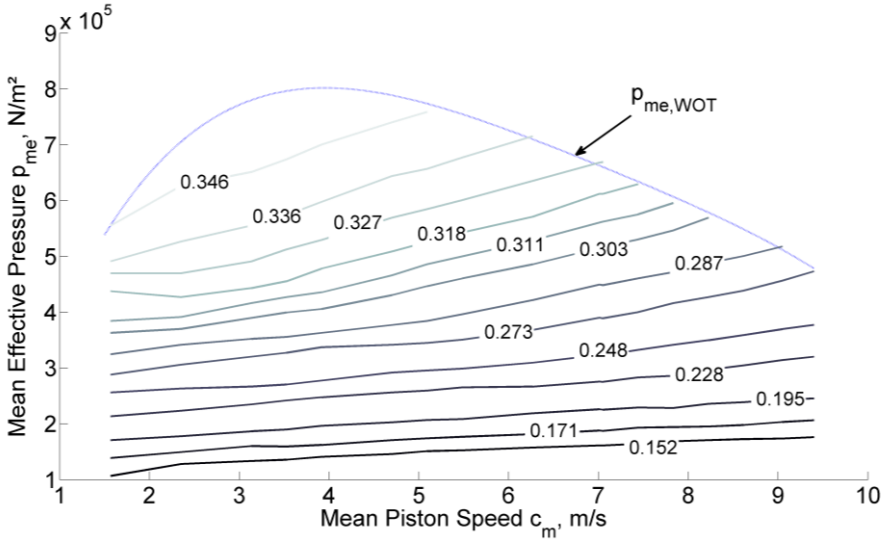

Figure 41: Baseline internal combustion engine efficiency map (data taken from HENDRICKSON & MCGEER (1999))

The engine achieves highest efficiencies at wide-open throttle. Automotive engines commonly show a slightly different characteristic with the most efficient operation

points slightly below WOT (GUZELLA & ONDER, 2010). For two-stroke engines, efficiency maps are only available from outdated agricultural or marine engines (HEYWOOD, 1988).

The baseline efficiency map is normalized twofold in order to enable easier scaling with relative values.

1. The WOT-curve $p_{\mathrm{me,WOT}}$ (see Figure 41) is normalized by its absolute maximum $p_{\mathrm{me,max}}$

$$\overline{\mathrm{p}_{\mathrm{me,WOT}}}(\mathrm{c}_{\mathrm{m}}) = \frac{\mathrm{p}_{\mathrm{me,WOT}}(\mathrm{c}_{\mathrm{m}})}{\mathrm{p}_{\mathrm{me,max}}} \tag{50}$$

   The resulting curve is shown in Figure 42. There, also the course of the product of c_{m} and p_{me} is plotted as it is proportional to engine shaft power. The mean piston speed at which it reaches its maximum is equal to the mean piston speed $c_{\mathrm{m,Pmax}}$ at which maximum power is reached. The reason for the normalization of the WOT-curve is to allow the determination of its course if only one WOT point of operation is known.

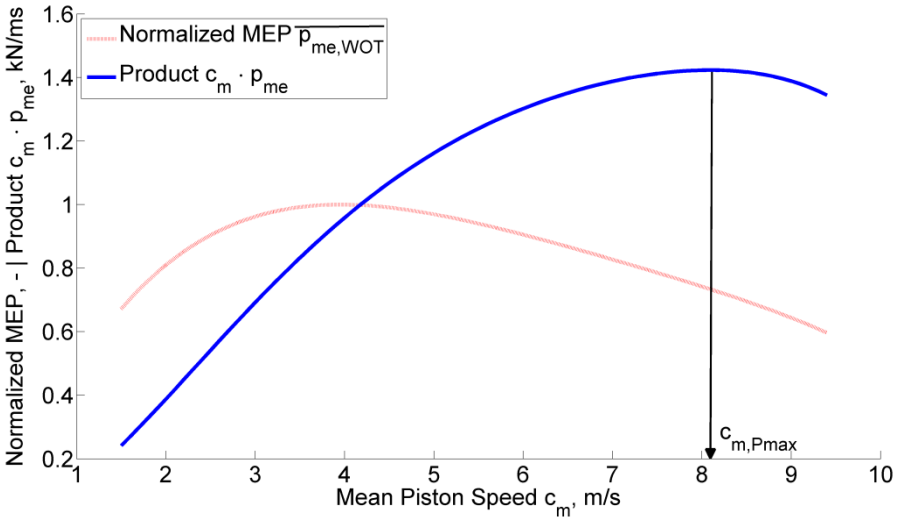

Figure 42: Normalized wide-open throttle mean effective pressure (MEP) and product of c_m and p_{me}

2. The effective mean pressures p_{me} at a certain mean piston speed are normalized by the value $p_{\mathrm{me,WOT}}$ of the WOT-curve at the c_{m} value.

$$\overline{\mathrm{p}_{\mathrm{me}}}(\mathrm{c}_{\mathrm{m}}) = \frac{\mathrm{p}_{\mathrm{me}}(\mathrm{c}_{\mathrm{m}})}{\mathrm{p}_{\mathrm{me,WOT}}(\mathrm{c}_{\mathrm{m}})} \tag{51}$$

   The normalized efficiency map is provided in Figure 43. The purpose of this normalization is to transform the baseline efficiency map into a relative and scalable formulation, independent of the course of the WOT-curve.

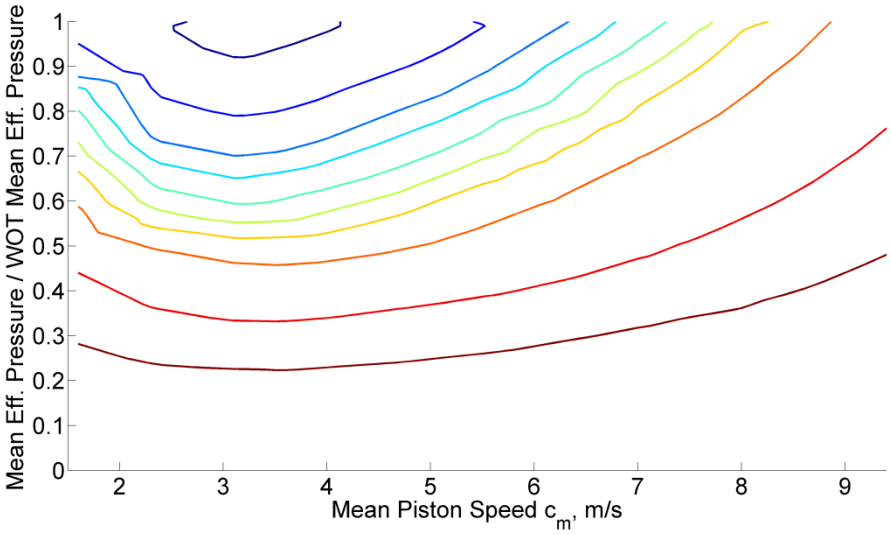

Figure 43: Normalized baseline efficiency map

Scaling the efficiency from the baseline efficiency map in the form described above to engines of varying size implies two assumptions analog to the normalizations.

1. The course of the normalized WOT curve is independent of engine size
2. The efficiency at an operational point defined by the mean piston speed c_m and the normalized mean effective pressure $\overline{p_{me}}$ is independent of engine size

The successful validation of the two assumptions is addressed after the complete derivation of the method. In order to determine engine efficiency from a normalized efficiency map in the form of Figure 43, knowledge of the mean piston speed c_m and the normalized mean effective pressure $\overline{p_{me}}$ is required. A target engine with the same stroke number and ignition method as the baseline engine is defined by its design variables V_d, S/B and n_{cyl}. The mean piston speed may be computed from them according to (41). In order to determine the normalized mean effective pressure according to (51), $p_{me,WOT}$ at this mean piston speed is necessary. It can be computed from $\overline{p_{me,WOT}}$ and $p_{me,max}$ by re-arrangement of (50). The former value is included in the baseline engine data, whereas the latter must be computed from the target engine's design variables. In order to do so, (50) is solved for $p_{me,max}$ and formulated for the point of maximum power P_{max}. Then, (41) and (43) are used to associate $p_{me,max}$ to the maximum power.

$$p_{me,max} = \frac{p_{me,WOT}(c_{m,Pmax})}{\overline{p_{me,WOT}(c_{m,Pmax})}} = \frac{Q_{Pmax}\left(\frac{4\pi}{V_d}\right)}{\overline{p_{me,WOT}(c_{m,Pmax})}} = \frac{\frac{P_{max}}{c_{m,Pmax}}\left(\frac{4S}{V_d}\right)}{\overline{p_{me,WOT}(c_{m,Pmax})}} \tag{52}$$

The mean piston speed $c_{m,Pmax}$ at which maximum power is reached can be taken from the baseline engine data as indicated in Figure 42. The maximum power is determined using functions derived from a database of 250 small internal combustion engines with

displacement volumes from 10 cm³ to 420 cm³ (see Appendix B.2). Maximum power is one of the properties commonly provided by the manufacturers. Setting P_{max} in combination with the engine displacement volume leads to linear functions for the two-stroke (2S) engine (53) and for the four-stroke (4S) engine (54).

$$P_{maxICE,2S}[W] = 70.39\,V_d[cm^3] + 454.9 \tag{53}$$

$$P_{maxICE,4S}[W] = 64.81\,V_d[cm^3] + 119.2 \tag{54}$$

Both functions, and the original data, are visualized in Figure 44. For the four-stroke equation a coefficient of determination of 0.9956 is obtained, whereas the value for the two-stroke fit is slightly lower at 0.9709.

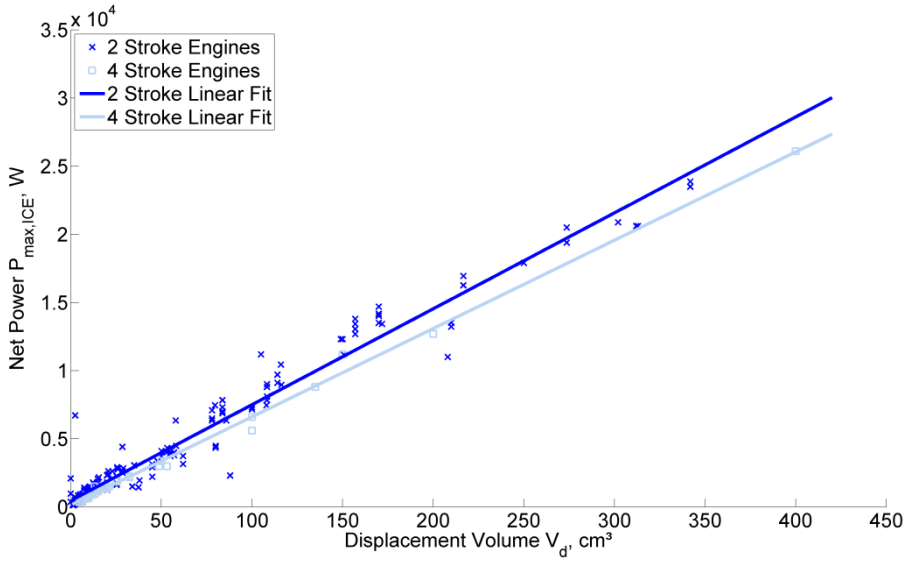

Figure 44: Internal combustion engine net power as function of the displacement volume (SCHOEMANN AND HORNUNG, 2012))

The efficiency then may be interpolated from the normalized efficiency map in Figure 43. Alternatively and faster in terms of computation time, it may be computed using (55). The second degree polynomial fit of the normalized efficiency map has a coefficient of determination of 0.9865.

$$\begin{aligned}\eta = {} & 0.03034 + 0.01901\,c_m + 0.6152\,\overline{p_{me}} - 0.002927\,c_m^2 \\ & + 0.003281\,c_m\,\overline{p_{me}} - 0.3383\,\overline{p_{me}}^2\end{aligned} \tag{55}$$

One boundary condition needs to be defined for the areas of very low $\overline{p_{me}}$ for which no data is available.

$$\overline{p_{me,min}} = 0.0051\,c_m^2 - 0.034\,c_m + 0.2313 \tag{56}$$

This restraint, which was derived from the baseline efficiency map data, is of little practical relevance, as the objective of the engine sizing process is to keep any points of operation out of this low efficiency zone.

When scaling engine efficiency, the importance of varying stroke-to-bore ratios must not be neglected. It defines the basic geometry of the cylinder and hence has a significant influence on the combustion process and efficiency accordingly (HUß, HÜBNER & WACHTMEISTER, 2010; WEINOWSKI ET AL., 2009; FILIPI & ASSANIS, 2000). Quantitative information for the change in overall efficiency resulting from a modification of the stroke-to-bore ratio is provided by FILIPI & ASSANIS (2000). For two absolute values of p_{me} (2.62 bar and 5 bar), relative changes in efficiency at various rotational velocities are determined for engines with S/B of 1.0 and 1.3 relative to the reference engine with an S/B of 0.7. Generally it can be noted, that efficiency increases with higher stroke-to-bore ratio up to a certain rotational velocity. Higher increases are notable for small rotational velocities, as an increase in friction losses due to the rise in stroke-to-bore ratio is more dominant at high rotational velocities. From the given data, a prediction model was derived to determine the efficiency normalized by the efficiency of a reference engine with a stroke-to-bore ratio of 0.7. The data is visualized in Figure 45 for a mean efficient pressure of 2.62 bar.

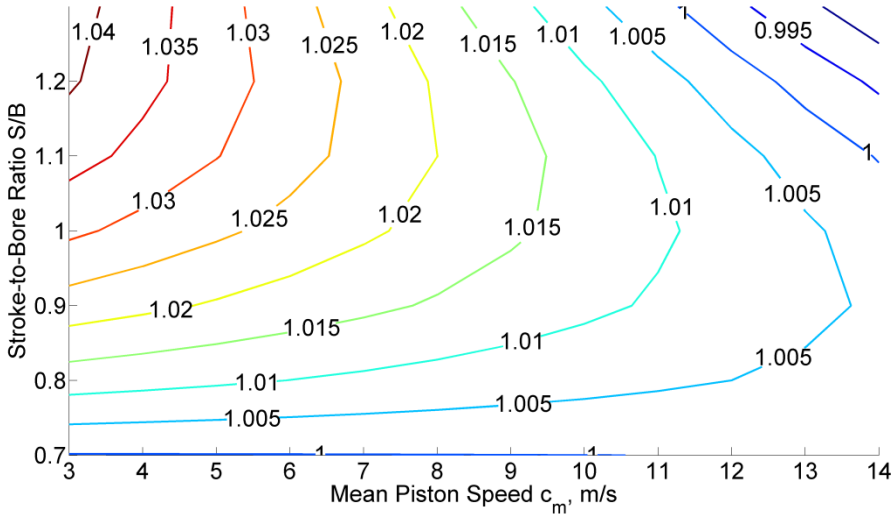

Figure 45: Normalized efficiency change due to the variation of the stroke-to-bore ratio at varying rotational velocities (SCHOEMANN & HORNUNG, 2012))

The mentioned trend of lower normalized efficiencies, even below unity, is stronger for the other investigated case of p_{me} equal to 5 bar. Due to only two points of support for the mean efficient pressure, the applicability of the prediction model is very limited without further data. An example to illustrate this strong limitation is that even very small engines with a displacement volume of 25 cm³ reach a maximum p_{me} of over 5 bar. The influence of stroke-to-bore ratio variations on efficiency may therefore not be implemented into the method, until further data is available.

As stated above, the scaling method is based on two assumptions. The first one, on the scaling of WOT curves may easily be validated, as those curves are available for several commercial engines. For validation the Honda GX series[6] of engines was chosen. The four-stroke engines are available from 25 cm³ to 390 cm³. As a test case for the validation, the WOT curve of the 160 cm³ model was scaled to all other displacement volumes of the series. The relative deviations at the target engine displacement volumes and varying mean piston speeds are plotted in Figure 46. Deviations exceeding 0.1 are reached for mean pistons speeds around 4 m/s and 8 m/s when downscaling. The deviations are considered acceptable for preliminary design.

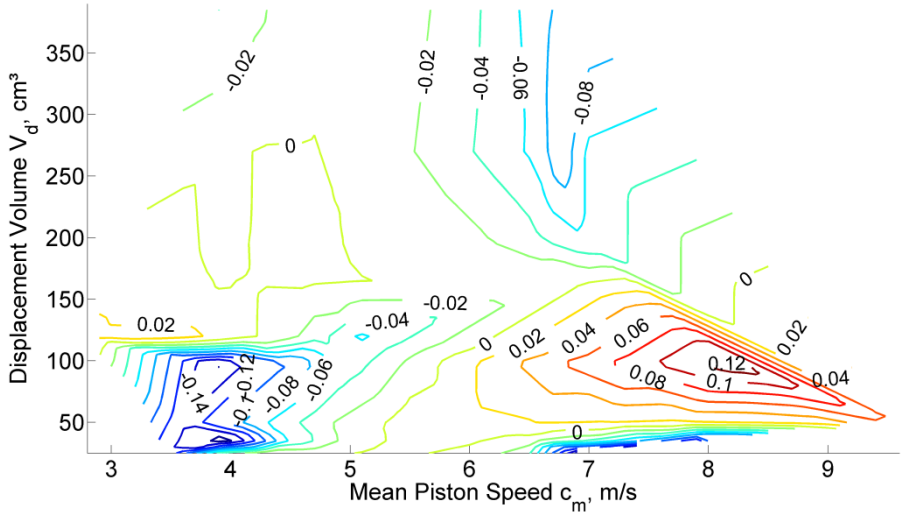

Figure 46: Relative deviation in scaling the wide-open throttle-curve of the Honda GX series (SCHOEMANN & HORNUNG, 2012)

Assumption two may be rephrased to the statement, that the normalized efficiency map, as plotted in Figure 43, is equal for engines of varying displacement volume. This statement of course needs to be limited to similar engines, which means to the same number of strokes and the same ignition method. Furthermore, the operational range of mean piston speeds needs to be similar. Validating this assumption is complicated by the low number of published efficiency maps with sufficient data. As two similar engines are needed, a 2.0L SI engine (GUZELLA & ONDER, 2010, pp. 66) is compared to a 1.9L SI engine included in the tool ADVISOR 2003[7] and originally presented in REILLY, ANDERSEN, CASPARIAN & DUGDALE (1991). The relative deviations of the two normalized efficiency maps are visualized in Figure 47. Critical deviations of above 0.1 occur only in the boundary regions, especially for low $\overline{p_{me}}$ and high c_m. The objective in the choice of an internal combustion engine for a propulsion system is however to avoid operation in these areas of low efficiency, so that these deviations are of little practical importance.

[6] Data available at: http://engines.honda.com/models/series/gx [Accessed 04 August 2012]
[7] Available at: http://bigladdersoftware.com/advisor/ [Accessed 15 February 2013]

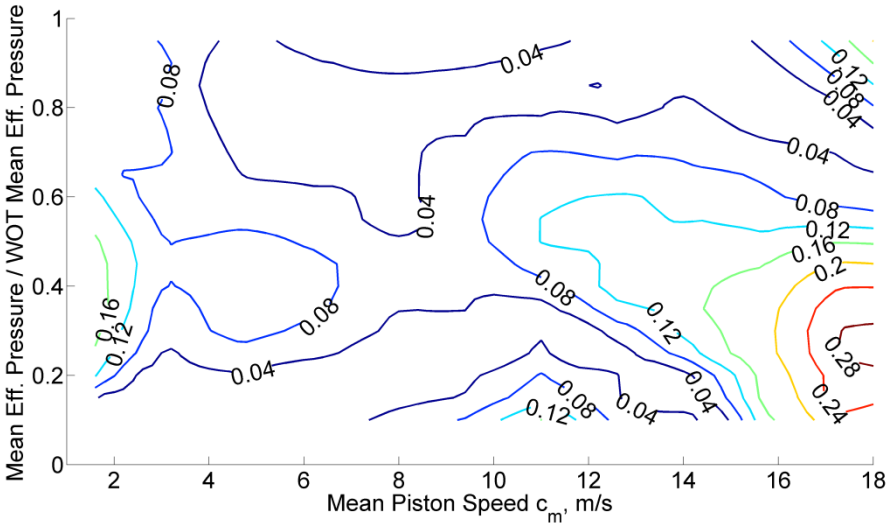

Figure 47: Relative deviation in comparison of the normalized efficiency maps of a 1.9 L and a 2.0 L automotive engine

The displacement volume is a main driver for the size of an internal combustion engine. Compared to automotive engines, the small commercial engines included in database are relatively simple, with almost no electronic components. The only relevant auxiliary components are the carburetor, the exhaust system and optionally a starter. In terms of the manufacturer specification of mass, it is not always clear which of these auxiliary components are included in the given value, which may lead to scatter in the mass data of the database of commercial motors. Nevertheless the database engines' mass may be determined from their displacement volume with acceptable accuracy. In Figure 48, the original data is plotted for two-stroke, four-stroke and Wankel engines. The figure proofs the statement made in chapter 2.2.2 that two-stroke engines are more lightweight than the four-stroke models with the same displacement volume due to their simplicity. For the four-stroke engines the linear function (58) is derived with a coefficient of determination of 0.9672. The mass of the two-stroke engines may be predicted with a linear regression function as well, but the power function (57) models the mass of very small engines with higher accuracy. The coefficient of determination of the power function is 0.9503. The number of Wankel engines is too low to derive a serious mass prediction function.

$$m_{ICE,2S}[g] = 40.15\, V_d\left[cm^3\right]^{0.9046} + 192.5 \tag{57}$$

$$m_{ICE,4S}[g] = 37.53\, V_d\left[cm^3\right] + 60 \tag{58}$$

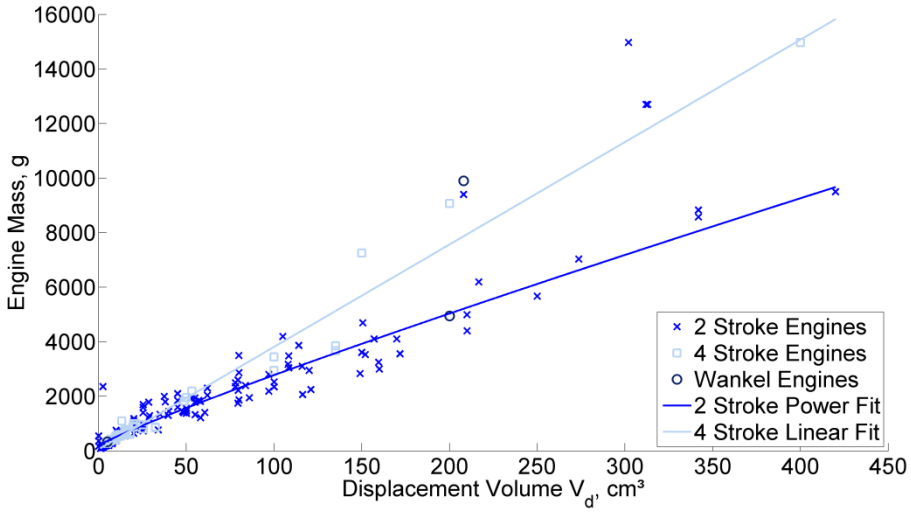

Figure 48: Mass prediction for internal combustion engines (SCHOEMANN & HORNUNG, 2012)

The presented method allows the determination of the mass and fuel chemical power demand of an internal combustion engine for points of operation defined by torque and rotational velocity. Two assumptions for the behavior of engine efficiency over varying size are presumed and validated as applicable with acceptable accuracy. The method is highly dependent of the quality of the scaled baseline data. Currently, only very few engine efficiency maps are available. With a denser database of efficiency maps, the starting point of the scaling process could be chosen closer to the target point, resulting in higher accuracy. An alternative way to obtain efficiency maps is to compute them using numerical simulations. Available software is commonly used for automotive engines and does not correctly model the behavior of small engines (MENON & CADOU, 2007). The influence of stroke-to-bore ratio on engine efficiency was identified as a decisive factor but may not be modeled appropriately due to the lack of data. The presented approach would be enhanced into an applicable model if data for a wider range of mean efficient pressures were available.

3.2.5 Fuel System

The term fuel system includes the fuel itself and the fuel tank. It is assumed that no relevant energy loss occurs in the fuel system, so that its efficiency is set to unity. The fuel system module hence determines only the mass of both, fuel and tank. The fuel mass is driven by the chemical energy required by the internal combustion engine. It is obtained for each design point i from the multiplication of the chemical engine input power $P_{\mathrm{ICE,in,i}}$ and the flight time t_{i}. The energies required for all design points are summed and divided by the lower heating value H_{LV}, the specific energy of the fuel, as in (59).The H_{LV} for common fuels are summarized in Table 1.

$$m_{fuel} = \frac{\sum P_{ICE,in,i}\, t_i}{H_{LV}} \tag{59}$$

In order to estimate the mass of fuel tanks, a database of commercial plastic tanks has been created (see Appendix B.5). Two main types of tanks have to be distinguished, as their mass differs significantly. Both are displayed in Figure 49. The transport canister in Figure 49a is a more robust model. The industrial canister in Figure 49b is more lightweight. Both are certified for road transport of dangerous goods.

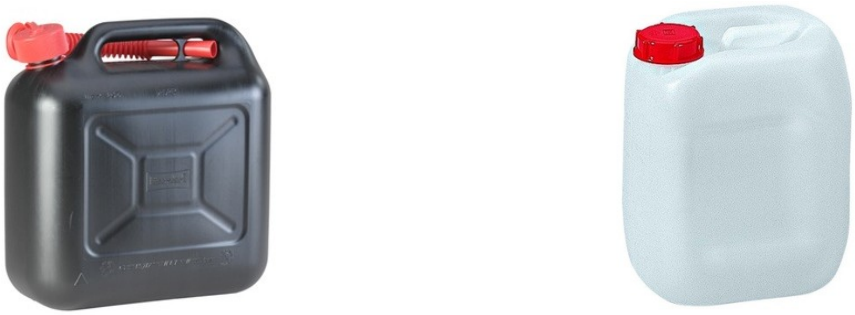

a) b)

Figure 49: Fuel tank types a) transport canister b) industrial canister (HÜNERSDORFF GMBH, n.d.)

The distribution of tank mass over fuel volume is plotted in Figure 50. Fuel volume may is fuel mass divided by fuel density (see Table 1) according to (60).

$$V_{fuel} = \frac{m_{fuel}}{\rho_{fuel}} \tag{60}$$

In Figure 50, the original data is shown as well as two regression functions, derived for the transport and industrial canisters each. The mass of the industrial canisters is approximated well with the linear function (62) and a coefficient of determination of 0.9952.

$$m_{tank,industrial}[g] = 42.72\, V_{fuel}[L] + 30.65 \tag{61}$$

The transport canisters' mass may be estimated with the cubic function (62) and a coefficient of determination of 0.9923

$$m_{tank,transport}[g] = 6.43 \cdot 10^{-2}\, V_{fuel}[L]^3 - 4.87\, V_{fuel}[L]^2 + 137\, V_{fuel}[L] + 24.4 \tag{62}$$

It is unclear and against obvious presumptions, why the difference between the two types is biggest for medium volumes. If both functions were extrapolated to bigger volumes, the curve for the transport canisters grows unrealistically steep. Therefore a linear function seems to be more reasonable. Furthermore, in conventional aircraft designs, the fuel tanks will be inside a load bearing airframe and do not need to be as

robust as the transport canisters are. For all analyses in this study therefore (62) is used.

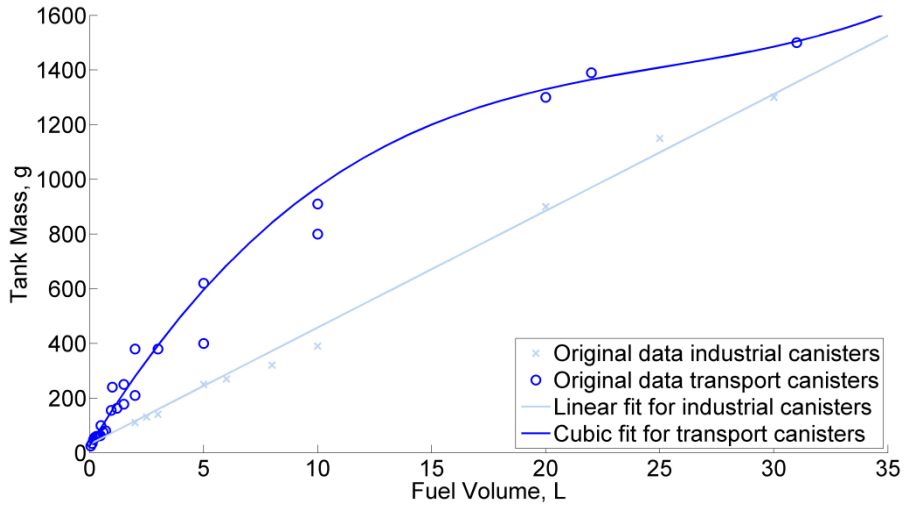

Figure 50: Mass prediction for fuel tanks (SCHOEMANN & HORNUNG, 2012)

3.2.6 Propeller

The propeller model is the first in the sequence of the design procedure. Its task is to compute the shaft power state variables, torque and rotational velocity, from the design variables and the propulsion power state variables thrust and translational velocity.

An overview of the historical development of propeller performance prediction is provided by WALD (2006). A commonly used method to predict propeller performance is the vortex theory. The vortex theory implies the use of the blade-element theory and is based on the original minimum energy condition first formulated by BETZ (1919). In its original form, and in its enhanced formulation by GOLDSTEIN (1929), the vortex theory is only applicable to propellers with low disk loading. An extension of the method to heavy loaded propellers was done by THEODORSEN (1948). Applicable design procedures using vortex theory were presented by LARRABEE & FRENCH (1983) as well as ADKINS & LIEBECK (1994).

The tool XROTOR[8] uses the procedure by LARRABEE & FRENCH (1983) with some extensions that are documented in DRELA (2006). It was chosen to use XROTOR, because it is validated and regularly updated. Furthermore XROTOR is freely available and allows to be automated within a MATLAB/SIMULINK environment. Running XROTOR or any other implementation of the vortex theory within the design process significantly extends the required computation time (MOFFIT, 2010). Consequently, XROTOR is used outside of the design process to generate propeller

[8] Available at: http://www.mit.edu/drela/Public/web/xrotor [Accessed 08 August 2012]

performance data. The integration of the data into the design process using a surrogate model or interpolation is compared in this chapter.

The basis of the propeller data, contrary to the other components, is not a propeller database. The specifications of commercial propellers do not commonly include the airfoil, twist or chord distribution of the blade. Therefore XROTOR's function to optimize the blade chord and twist distribution for a specified design point is used. The procedure is depicted in Figure 51. A similar approach was used by RÖßLER (2011) to compute two-dimensional propeller data.

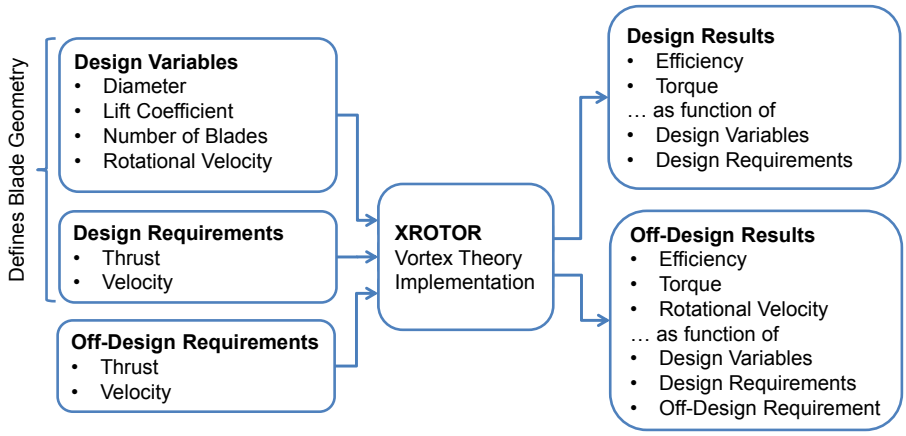

Figure 51: Propeller data computation procedure

A propeller design point, not to be confused with the propulsion system design points defined in chapter 3.1.2, is defined by requirements for thrust, velocity, rotational velocity, diameter, lift coefficient and the number of blades. The six input variables include the two operational requirements thrust and velocity. The remaining four are selected as design variables. Further parameters necessary for the program execution, as the hub radius and the hub wake displacement body radius, are kept at a default value, as they are less significant for the designer.

For a propeller design point, XROTOR optimizes the blade geometry and computes efficiency and torque. In addition to the design point, off-design performance is considered as well. An off-design point is a point at which the propeller optimized for the design point is used with different operational requirements. It is defined by the design point inputs and off-design requirements for thrust and velocity. For the off-design points, efficiency, torque and off-design rotational velocity are computed. In the design procedure, the propeller design point is assigned to a propulsion system design point, most reasonably the one with longest flight time, which commonly is *Regular Cruise*. The other propulsion design points are then treated as propeller off-design points. This procedure thus selects no globally optimized propeller. Choosing one design point for which the propeller is optimized may result in a lower efficiency than it could be achieved with a propeller that is specifically designed for the

combination of the propulsion system design points. Such a procedure, as presented by GUR & ROSEN (2009b) would nevertheless require the blade geometry to be treated as design variable, which would remarkably increase computation time.

The procedure described above and shown in Figure 51 is used to create a full factorial design of experiment consisting of six-dimensional look-up tables for the design data and eight-dimensional tables for the off-design data. The ranges of the input parameters are chosen, so that the anticipated requirements for small unmanned aircraft are covered. The first method considered for the integration of the data into the design process is interpolation from the look-up tables. The second approach, using polynomial fitting, was complicated by the high multidimensionality of the data, as visual examination is difficult for more than three dimensions. Therefore it was tried to reduce the number of variables by consolidating them in characteristic non-dimensional variables. The commonly used propeller coefficients are the advance ratio J, the thrust coefficient c_T and the torque coefficient c_Q. Their definitions as used by PHILIPS (2009) are given in (63) to (65). In these equations, v_{tip} is the blade tip velocity, ρ the air density and $d_{propeller}$ the propeller diameter.

$$J = \frac{v}{\frac{\omega}{2\pi} d_{propeller}} \tag{63}$$

$$c_T = \frac{T}{\left(\frac{\omega}{2\pi}\right)^2 \rho d_{propeller}^4} \tag{64}$$

$$c_Q = \frac{Q}{\left(\frac{\omega}{2\pi}\right)^2 \rho d_{propeller}^5} \tag{65}$$

From the design point data, polynomial fits for the efficiency and the torque coefficient may be modeled with high coefficients of determination. The equations for both, as function of the thrust coefficient and advance ratio, are given below.

$$\eta_{design} = -0.02784\, c_T^2 - 0.7796\, J^2 - 1.321\, c_T + 0.938\, J + 0.5777\, J c_T + 0.7073 \tag{66}$$

$$c_{Q,design} = 0.6193\, c_T^2 - 0.003375\, J - 0.1498\, c_T + 0.2109\, J c_T + 0.00834 \tag{67}$$

Polynomial fits for the off-design data are found as function of the thrust coefficient, the advance ratio as well as the ratios of off-design velocity and thrust to their respective design value. The equations are provided in Appendix A due to their length.

For the evaluation of the two surrogate models, accuracy and computation time are regarded. As figure of merit for accuracy, the residuals of all five modeled variables are plotted over the original values in Figure 52. Furthermore the coefficients of determination are summarized in Table 5.

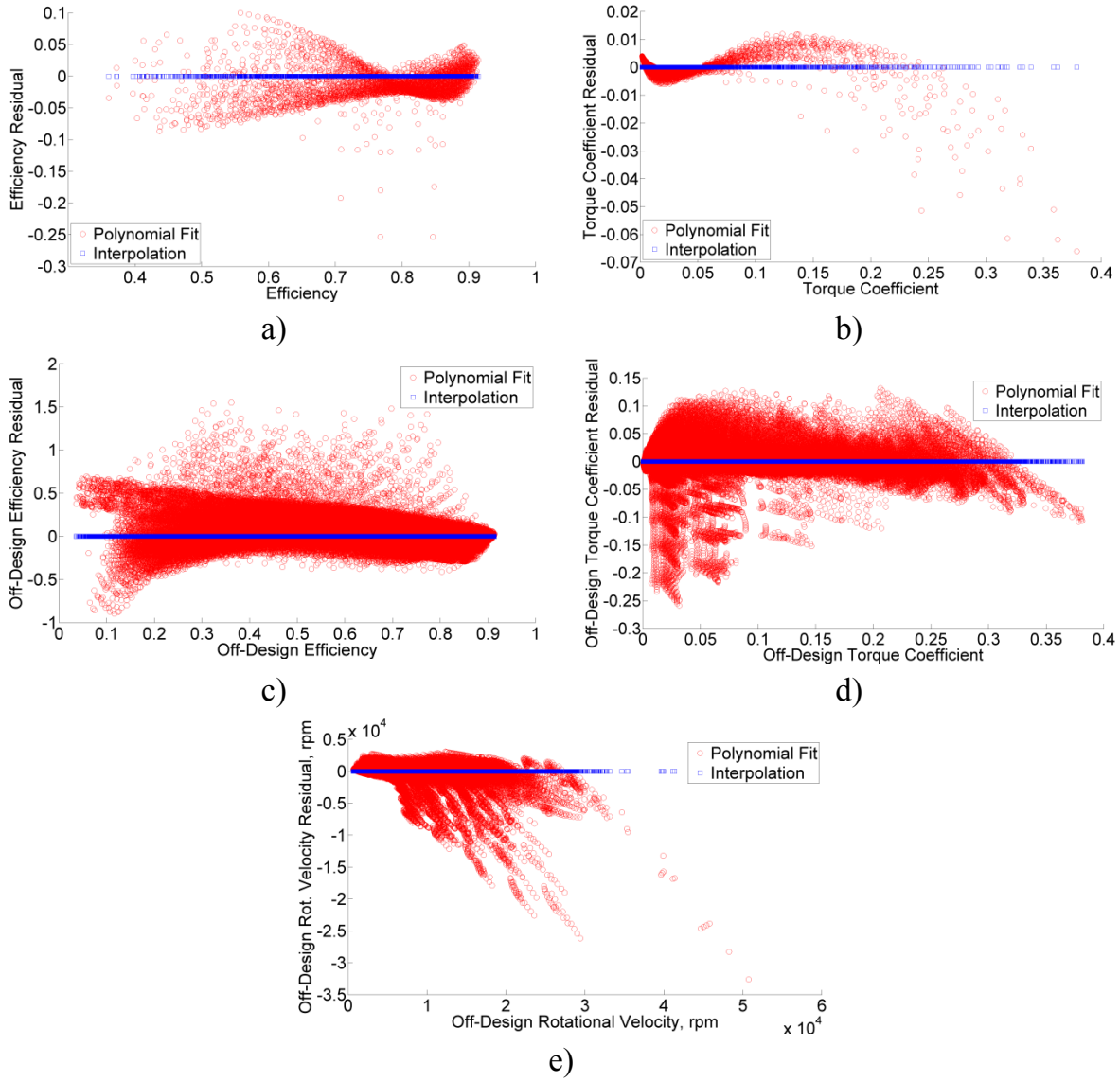

Figure 52: Residual plot for the propeller surrogate models (a) design efficiency (b) design torque coefficient (c) off-design efficiency (d) off-design torque coefficient (e) off-design rotational velocity

Table 5: Coefficients of Determination R^2 of the propeller surrogate models

	Design Torque Coefficient	**Design Efficiency**	**Off-Design Torque Coefficient**	**Off-Design Efficiency**	**Off-Design Rotational Velocity**
Interpolation	1	1	1	1	1
Polynomial Fit	0.9929	0.9289	0.9042	0.6178	0.9512

The interpolation is the more accurate method with coefficients of determination of virtually one. It has however to be considered, that accuracy is evaluated at the supporting points. The accuracy of interpolation between those points cannot be captured. The polynomial fit shows less accurate, but acceptable results for the design torque coefficient and efficiency, with more scatter for the latter. For the off-design performance, accuracy is significantly reduced. Rotational velocity may be predicted with an acceptable coefficient of determination but the residuals show that the model returns values near zero for a lot of off-design points. The R^2 for the torque coefficient is lower and the residual plot shows wide scatter. When the torque coefficient and the rotational velocity are used to determine torque using (65), an inacceptable coefficient of determination of 0.46 is reached. Off-design efficiency estimation returns values below zero and above one for an inacceptable number of off-design points. The imprecise prediction of off-design values, especially where the feasible range of efficiency is left, would require a restriction of the input values and therefore restrain the design space.

In terms of the computation effort, the time required for the computation of exemplary couples of design and off-design requirements is determined. It is given in Table 6 as a mean value of 100 runs and normalized by the time XROTOR needed for this task. Both surrogate models work faster than XROTOR. The fitted polynomial equation returns results in less than one hundred-thousandth of the original computation time, whereas the interpolation needs slightly more than a third. For the evaluation of the computation time of the interpolation it has to be noted, that it may be significantly decreased by a smart design process implementation. The eight-dimensional interpolation performed for this analysis is more time consuming than a step-wise partial interpolation (see chapter 4.1).

Table 6: Computation time required by the propeller surrogate models

	Normalized Computation Time	**Mean Computation Time per Run [s]**
XROTOR (incl. pre- and post-processor)	1	1.48
Interpolation	0.35	0.52
Polynomial Fit	$8.9 \cdot 10^{-6}$	$1.32 \cdot 10^{-5}$

Albeit interpolation requires considerably more time than the polynomial fit, it is chosen for the integration of the propeller data. The low accuracy of the fit would not only make the results doubtable but might also require a strong limitation of the design space, which is inacceptable for the task of exploration of a system's capabilities.

Interpolation is also chosen in a similar comparison of propeller surrogate models by MOFFITT (2010). There a third order response surface works fastest but least accurate, whereas a neural network returns reasonably accurate values but requires more time than the most accurate interpolation. Nevertheless a well-adjusted neural network may be a good compromise of computation time and accuracy and a future improvement of this design method.

The estimation of propeller mass is enabled with approximation (68), adapted by KEIDEL (2000) for modern propeller technology. The estimation was validated for the use with carbon fiber reinforced plastics propellers by RÖßLER (2011).

$$m_{propeller}[kg] = 0.12\, n_{blades}^{0.391} \left(d_{propeller}[m] \frac{P_{shaft}[W]}{1000} \right)^{0.782} \tag{68}$$

Mass in this equation is estimated from the number of blades n_{blades}, the propeller diameter $d_{propeller}$ and the shaft power P_{shaft}. A validation with the data of COTS propellers is impossible for the author, as commonly propeller manufacturers do not publish the mass of their products.

3.2.7 Coupling

The coupling within this preliminary design method is treated as an ideal and massless component, as the actual mechanical realization is very much dependent on the exact aircraft geometry, the mounting position of the propulsion system and further airframe conditions.

In the propulsion system design process, the coupling module's objective is to distribute torque and rotational velocity to the electric motor and the internal combustion engine. As existing parallel hybrid-electric propulsion systems have been realized with pulley or chain assemblies, such is modeled (AUSSERER & HARMON, 2012; EAGLE FLIGHT RESEARCH CENTER, 2011; GLASSOCK, HUNG, GONZALEZ & WALKER, 2007). Pulley or chain assemblies are so called torque-coupling devices, which means that the torque of the two connected power units is added. If the propeller is mounted on the engine shaft, the relation of torques is described according to (69), in which the coupling constant $k_{coupling}$ is the pulley radius ratio of the engine shaft r_{ICE} to the motor shaft $r_{EM.}$ (EHSANI, GAO, GAY & EMADI, 2005, pp.124).

$$Q_{propeller} = Q_{ICE} + k_{coupling} Q_{EM} = Q_{ICE} + \frac{r_{ICE}}{r_{EM}} Q_{EM} \tag{69}$$

For the rotational velocity equation (70) is applicable.

$$\omega_{\text{propeller}} = \omega_{\text{ICE}} = \frac{\omega_{\text{EM}}}{k_{\text{coupling}}} \tag{70}$$

With (70), the rotational velocity of motor and engine may be determined, as the coupling constant is one design variable of the coupling. In order to determine the torque of the two power units the degree of hybridization in (71) is used as the second coupling design variable.

$$\text{DoH} = \frac{P_{\text{shaft,EM}}}{P_{\text{shaft,propeller}}} = \frac{Q_{\text{EM}}\omega_{\text{EM}}}{Q_{\text{propeller}}\omega_{\text{propeller}}} \tag{71}$$

Using (70) in (71) leads to equation (72) for the electric motor torque Q_{EM} and with (69) to the internal combustion engine torque Q_{ICE} (73).

$$Q_{\text{EM}} = Q_{\text{propeller}} \frac{\text{DoH}}{k_{\text{coupling}}} \tag{72}$$

$$Q_{\text{ICE}} = Q_{\text{propeller}}(1 - \text{DoH}) \tag{73}$$

4 PROPULSION SYSTEM ANALYSIS

The design method developed in chapter 3 is applied in this chapter. The primary objectives are to identify and discuss characteristics, capabilities and limitations of hybrid-electric aircraft based on the results. It is furthermore determined for which requirements they are advantageous over aircraft with conventional propulsion systems. The results help aircraft designers to decide for which application a hybrid-electric propulsion system should be considered. Albeit the objective is to draw conclusions as general as possible, they are only valid for the use cases chosen within this study. The secondary objective of the application is the practical analysis of the method's computational efficiency and the description of measures leading to its increase.

Chapter 4.1 describes the challenges and findings of the computational implementation of the design method and their influence on the results. Chapter 4.2 compares hybrid-electric aircraft to conventionally propelled aircraft. Therefore a requirement space defined by ranges of payload and flight time requirements is explored. The effect of key influencing parameters on the hybrid-electric aircraft is analyzed in chapter 4.3. The selected parameters are the mission electric flight time ratio and the battery specific energy. Furthermore the aircraft's sensitivity to additional mass is identified. The discussion of the effect of discretization and optimization is easier accessible by means of quantitative results, so that it is integrated into chapter 4.3.1.

In the chapters 4.2 and 4.3, the aircraft are assessed in terms of takeoff mass, fuel mass and energy consumption. Aspects that cannot numerically be evaluated within this analysis are handling and ground performance. Unmanned aircraft distinguish themselves from manned aircraft by offering a clear advantage in handling qualities and cost. With increasing takeoff mass the effort in aircraft ground transportation and operation and consequently the demand in ground equipment and personnel rises. Furthermore, the heavier an aircraft, the more complex is the takeoff and landing procedure in terms of required field length or on-board equipment for an assisted takeoff or landing. The evaluation of energy consumption is limited to the on-board consumption. Any further ecological or economical investigation of the energy used for charging the aircraft on ground would require in-depth knowledge of the local energy mix and prices and may not be generalized. Additionally, the mass distributions of the aircraft and propulsion system are considered. One parameter that may be used to easily evaluate an aircraft's transport efficiency is the payload fraction of takeoff mass. The reciprocal value is an approximation for the aircraft growth factor (BALLHAUS, 1954). It is a figure of merit for the increase of takeoff weight resulting from payload carried additionally.

4.1 Computational Analysis of the Design Method

The main task of the implementation of the design method into program code was computational efficiency. The propulsion system design including the optimization is by far the most time consuming part of the design procedure. The propeller model and explicitly the interpolation require considerably more time than the other modules. The computational time therefore is highly dependent on the number of calls of the propulsion system design procedure, as well as the computational realization of the procedure and the available computer hardware. The number of calls is determined by the active design variables and their discretization. The number of executions of the propulsion system design procedure within the aircraft design process is driven by the fitness of the initial assumption for the payload fraction.

In the full factorial optimization process, the cost function results for the complete design space are gathered in a matrix. Its dimensionality is defined by the number of design variables and the size in each dimension by the discretization of the respective design variable. The size of such a matrix in a computer system is limited by the random-access-memory (RAM). For practical purposes the hardware limits were set by a commonly available COTS dual-core processor computer with 8 GB RAM and 64-bit operating system. In such a system, an empirical value of 5 GB RAM is available for all matrices. If only one matrix was necessary, its maximum number of elements then would be 6.25e8 under the assumption that each matrix element requires 8 Bytes (double precision).

The design variables are summarized in Table 7. It was already mentioned in chapter 3.1.2 that several variables may be set to constant values. The selected values either predominate in the COTS databases or are suitable for UAV. Spark-ignition was selected for the internal combustion engine, as compression-ignition is only seldom realized in small COTS engines. Furthermore, a four-stroke duty cycle was defined, albeit more COTS models are two-stroke engines. Efficiency maps for the engine efficiency scaling model however are only available for four-stroke SI engines. Additionally four-stroke engines are more efficient and this study aims at assessing state-of-the-art technology. The number of cylinders is set to two, as most small COTS engines have either one or two cylinders. A higher number of cylinders contributes to the engine's running smoothness, which may be a relevant criterion for a sensor payload. The stroke-to-bore ratio was set to 1 and not varied, since the prediction model of its influence on efficiency could not be used for the reasons described in chapter 3.2.4. Further fixed variables are the number of propeller blades and the propeller lift coefficient. The choice of two blades was driven by the much wider availability of two bladed COTS propellers than of three or more blades. The lift

coefficient was set to 0.5 based on a recommendation of the designer of the used blade airfoil[9]. Another reason for that decision is that a reasonable variation would require more insight into aerodynamics than desirable at the preliminary phase.

Table 7: Design variables and their discretization

Component	Design variable	Value range	Points
Propeller	Rotational velocity	2000 – 8000 rpm	13
	Diameter	0.05 – 0.055 m	11
	Lift coefficient	0.5	1
	Number of blades	2	1
Coupling	Coupling constant	1 – 3	5
	Degree of hybridization	0.1 – 0.7	7
Electric motor	Diameter x length	500 – 16000 mm²	11
	Specific rotational velocity	Flexible	12
Battery	Cell capacity	1 – 8 Ah	5
Internal combustion engine	Displacement Volume	Flexible	10
	Stroke-to-bore ratio	1	1
	Number of cylinders	2	1
	Cycle	Four-stroke	1
	Ignition type	Spark-ignition	1

In the process of defining the design variables, the use of the product of electric motor diameter and length *dl* or of both, diameter *d* and length *l*, was quantitatively assessed. The use of *d* and *l* allows a more accurate motor mass prediction, but increases computation time, as described in 3.2.1. One version of the propulsion system design procedure using *dl* and one using *d* and *l* were used to explore the design space defined in chapter 4.2. The average relative deviation of the propulsion system masses computed by the two procedures is below 1 %, whereas the computation time can be reduced by 93 % by the use of *dl* (SCHOEMANN & HORNUNG, 2013). In absolute values a run of the propulsion system design procedure for the hybrid-electric system with *dl*

[9] RÖßLER, CHRISTIAN, Institute of Aircraft Design, Technische Universität München

and the discretization in Table 7 takes approximately 2 min. In the version using *d* and *l* the runtime averages around 45 min.

The value ranges of the design variables in Table 7 are chosen to cover the defined requirement space. The number of support points is a compromise of computation time and accuracy. The ranges are fixed, except for the engine displacement volume and the electric motor specific rotational velocity. For both the minimum and maximum value of the range are formulated flexibly, as function of another design variable or a requirement. The functions were derived from the respective databases of commercial components. The minimum and maximum specific rotational velocity functions (26) and (27) of *dl* are plotted in Figure 31. The displacement volume range is determined by the maximum power demand through solving equation (53) or (54) for $V_{\mathrm{d,Pmax}}$ and then allowing a range of 0.5 $V_{\mathrm{d,Pmax}}$ to 1.5 $V_{\mathrm{d,Pmax}}$. The use of flexible discretization increases accuracy compared to a rigid definition. It may be applied to more design variables, when empirical relations between requirements and design variables have been derived from analyses of specific use cases. The influence of discretization on the results is discussed in chapter 4.3.1.

A further measure to reduce computation time is an efficient implementation of the method into program code. If one module detects that the component with the selected design variables does not comply with the operational requirements, the procedure is stopped and the next point in design space is attended. Furthermore the execution of modules that do not affect each other is separated, although formally the full-factorial approach means to include every possible combination of design variables. This is applied to the electric and combustion engine power trains. The output of the electric power train modules has no effect on the output of the internal combustion engine and fuel tank module, and the other way around. Therefore, not all modules must be called at every point of the design space. They are only executed when relevant design variables are changed. The computation time required by the propeller interpolation is reduced by eliminating look-up table dimensions by step-wise interpolation, whenever the respective design variable is changed. Compared to an eight-dimensional interpolation at every design point, the time-consumption may be lowered significantly by this procedure.

In the aircraft design procedure, the number of iterations may be minimized by using the payload fraction of the previous point in the requirement space as initial value. A finer requirement space discretization then possibly reduces the computation time, as less iteration loops are required per requirement point.

4.2 Requirement Space Exploration

The objective of this chapter is to show general trends of hybrid-electric aircraft. The discussion of these trends gains informative value, when set in relation to conventional propeller aircraft. In order to compare hybrid-electric aircraft to conventional aircraft, design methods for internal combustion engine (ICE) and battery-electric (BE) aircraft have been developed. Their results are used as a reference. The design procedures for the internal combustion engine and the battery-electric aircraft are based on the models described for the hybrid-electric system in chapter 3. For both systems the propulsion system design modules are re-arranged. Input and output of the procedure are equal to the hybrid-electric procedure in Figure 19. In the internal combustion engine system design procedure, the propeller module is followed by the internal combustion engine and the fuel tank module. In the design procedure for the battery-electric system a gearbox module is included, which consists of the ideal transformation of torque and rotational speed only, with the gear ratio used as the design variable. The module sequence is propeller, gearbox, electric motor, electronic speed controller and battery. The hybrid-electric aircraft design framework may be used for ICE aircraft without changes. For battery-electric aircraft it is considerably simplified because no mass changes occur and the mission simulation becomes obsolete.

The hybrid-electric aircraft design procedure depicted in Figure 20 requires two inputs: a set of mission requirements and reference aircraft data. The mission requirements consist of payload, flight time and velocity for each design point and the rate of climb. The reference aircraft parameters are wing load, payload fraction, airframe mass fraction and aerodynamic data in form of the lift and drag polar.

As reference aircraft, the institute's unmanned research aircraft IMPULLS[10] (Innovative Modular Payload UAV of TUM-LLS) is chosen, as it represents the state-of-the-art of lightweight CFRP construction and manufacturing and the data are completely available. The aircraft's relevant data are summarized in Table 8. The current battery-electric propulsion system of the aircraft is located in the tail boom with the electric motor mounted at the backmost position. This position is very sensitive to mass changes in terms of the longitudinal balance. The IMPULLS configuration hence is not the optimum for a hybrid-electric propulsion system, but the structural and aerodynamic characteristics are nevertheless applied, as they may be realized in a different aircraft configuration.

[10] Data available at: http://www.lls.mw.tum.de/index.php?id=33#c432 [Accessed 08 August 2013]

Table 8: Key data of the IMPULLS research aircraft (PAULUS, RÖßLER, SCHOEMANN, SCHWARZE & SPECK, 2010)

Masses [kg]		**Performance**		**Geometry**	
Airframe	11.4	Flight time [min]	75	Wing area [m²]	1.55
Payload	10.1	Design cruise velocity [m/s]	19	Aspect ratio [-]	16.1
Propulsion system	6.8	Rate of climb [m/s]	3		
Maximum takeoff mass	29.7	Service ceiling [m]	1000		

The generic surveillance mission schematically outlined in Figure 17 is chosen as baseline mission for the analysis. The variety of possible mission requirements is restrained in order to keep the propulsion analysis focused on the major trends. Therefore, the *Maximum Power* (MP) requirements are constant for all following analyses with a rate of climb *RoC* of 5 m/s and a flight time of 5 min, which results in a cruise altitude of 900 m. The velocity is set to 20 m/s for *Maximum Power*, and also for *Regular Cruise* (RC) and *Electric Flight* (EF). This velocity was selected because of the proximity to the reference aircraft's design cruise velocity. A similar velocity makes the use of the reference aerodynamic data and the reference airframe mass fraction more valid. Furthermore, electric propulsion systems are mainly considered for low velocities, as propulsion power is a cubic function of velocity. With the low specific energy of electric energy storages high power demands lead to heavy aircraft and the described cascade effect. Inflight charging of the batteries is not considered in the analyses in this study. Charging would allow more than one *Electric Flight* phase with battery depletion. In between, internal combustion engine powered *Charging Cruise* flight phases are conducted. The influence of inflight charging on the performance of hybrid-electric aircraft may be investigated in a future study.

The uniform velocity for cruise and surveillance phases allows a simplification of the mission for the conventional systems. From a functional viewpoint, the distinction between the *Regular Cruise* and the *Electric Flight* segment is not applicable, because the ICE system is not capable of flying electrically and the BE system conducts the complete flight electrically. With the demands in performance being equal, cruise and surveillance are therefore merged into one flight phase. The resulting mission in Figure 53 consists only of a climb and a cruise and surveillance phase. For climb the design point *Maximum Power* is applied, whereas cruise and surveillance requirements are formulated in *Regular Cruise* or *Electric Flight* for the ICE or BE aircraft, respectively.

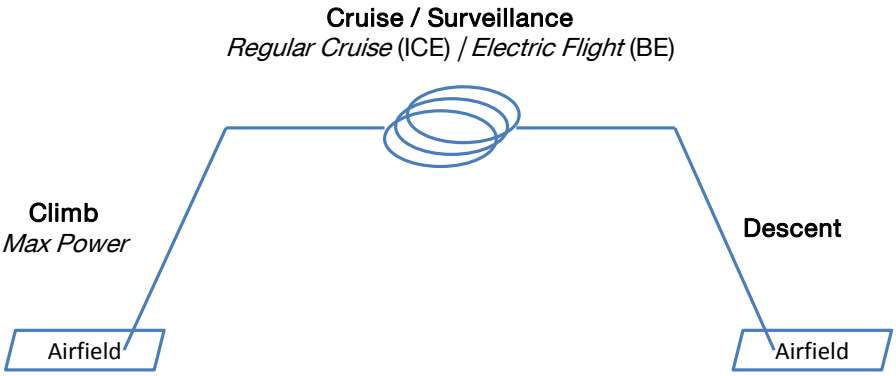

Figure 53: Exemplary conventional surveillance mission with flight phases and design points (SCHOEMANN, 2013)

The remaining requirements, payload and flight time define the requirement space in this chapter. A flight time range of 1 to 12 h with a 15 min discretization was considered. The lower limit of 1 h is set as flight times of less than 1 h may either be performed with fixed wing aircraft of a smaller category or rotorcraft. The upper limit of 12 h marks the ability to keep a system permanently airborne for 24 h per day with two aircraft and two flight legs. For hybrid-electric missions a distinction between electric and conventional flight time is necessary. The electric flight time ratio *EFTR* is therefore defined as the ratio of electric flight time t_{EF} to overall horizontal flight time according to (74). The overall horizontal flight time includes the flight times for *Electric Flight* t_{EF} and *Regular Cruise* t_{RC}.

$$EFTR = \frac{t_{EF}}{t_{EF} + t_{RC}} \tag{74}$$

The electric flight time ratios of 0 and 1 correspond to the internal combustion engine system and the battery-electric system, respectively. In the requirement space exploration hybrid electric flight time ratios of 0.25, 0.50 and 0.75 are analyzed.

A payload range of 10 kg to 70 kg is considered in the requirement space exploration. The upper limit of 70 kg is set by the maximum possible payload that can be carried in a small unmanned hybrid-electric aircraft with an electric flight time ratio of 0.25. The discretization is set to 2 kg. Table 9 summarizes the mission requirements for the requirement space exploration.

For all systems the aircraft mass and, where applicable, the consumed fuel is regarded. Furthermore, the payload and propulsion system mass fractions are analyzed, as well as the fuel and battery mass fractions of the propulsion system mass. The systems are also compared in terms of their energy consumption. The differences of hybrid-electric aircraft compared to conventional aircraft are described on system and propulsion component level for the hybrid-electric aircraft optimized for an EFTR of 0.25. A first

analysis of the selected optimization scheme is conducted on the basis of the internal combustion engine aircraft.

Table 9: Mission requirements for requirement space exploration

		ICE System	**Battery-Electric System**	**Hybrid-Electric System**
Payload		10 – 70 kg		
Flight Time	MP	5 min		
	RC	1 – 12 h	/	75 % | 50 % | 25 % of 1 – 12 h
	EF	/	1 – 12 h	25 % | 50 % | 75 % of 1 – 12 h
Velocity (MP / RC / EF)		20 m/s		
Rate of climb		5 m/s		

Generally, takeoff and required fuel mass rise with increasing payload and increasing flight time. A change of payload linearly influences the takeoff mass, driven by the aircraft growth factor. A heavier aircraft must generate more lift, which results in higher drag and an increase in required propulsion power. The product of propulsion power and flight time is the required energy. As a simplified rule, evident in the mass prediction equations in chapter 3.2, the power converters' mass depends on the required power and the energy storages' mass on the required energy. Increases in propulsion system mass drive up aircraft and fuel mass in a cascading effect.

4.2.1 Internal Combustion Engine Aircraft

The takeoff mass and fuel mass for internal combustion engine aircraft are shown in Figure 54. The diagram includes results optimized for minimum propulsion system mass in solid lines and for minimum fuel mass in thinner dashed lines. Within the takeoff mass limit of 150 kg, the complete requirement space may be realized with internal combustion engine aircraft. The takeoff mass rises approximately linearly with flight time and payload, with a steeper gradient over payload. The fuel mass gradients in Figure 54 however are steeper over flight time.

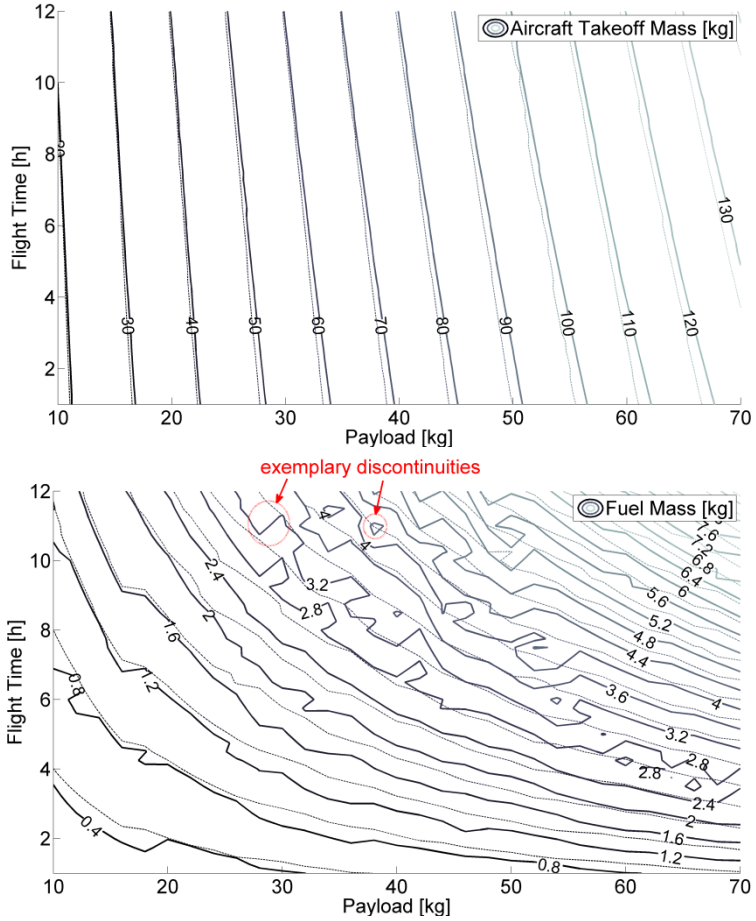

Figure 54: Takeoff mass (top) and fuel mass (bottom) for internal combustion engine aircraft

In Figure 54, and generally in the analyses in chapter 4, the fuel mass curves show more unsteadiness than the takeoff mass curves. Exemplary discontinuities are marked in the plot. The discretization of the propulsion system design variables and the use of propulsion system mass as cost function are causal for this. Generally, the longer the demanded flight time, the more important efficiency becomes. In a propeller propulsion system, efficiency may be increased by using a slow-turning high diameter propeller. In contrast to a faster-turning small diameter propeller at the same power level, the torque demand of the driving power unit increases. This results in a heavier power unit, but lighter energy storage, due to the higher efficiency. With the propulsion system mass set as cost function of the optimization, a lower efficiency fast-turning system is chosen over the more efficient slow-turning system if the resulting propulsion system mass is lower. The discontinuities in the fuel curves mark the points where the optimization changed either from a fast-turning to a slow-turning system or the other way round. The amplitudes of the deviations are influenced by the discretization of the design variables. The phenomenon will be addressed for the hybrid-electric propulsion system quantitatively in chapter 4.3.1. It is also explained there and in chapter 3.1.2, why fuel mass should not be used as cost function for the design of hybrid-electric aircraft. For internal combustion engine powered aircraft the aspect of an independently sized electric system is not applicable. Every component in

the propulsion system has influence of the fuel mass. The requirement space exploration is therefore also conducted with a modified design process, in which fuel mass is set as cost function. The results are provided in Figure 54 with dashed curves. The fuel mass curves are clearly steadier, although some smaller deviations due to the discretization remain. In the complete requirement space the fuel mass is below that of the propulsion system mass optimization. The takeoff masses however are higher than the results of the propulsion system mass optimization. The difference increases with increasing payload. The higher the flight times, the more the takeoff masses of the two optimizations converge. This is caused by the increasing importance of high efficiency for long flight times. The fuel mass optimization selects efficient slow-turning systems for the complete flight time range. The propulsion system mass optimization selects them for long flight times, when the reduction in energy storage mass outweighs the heavier power units.

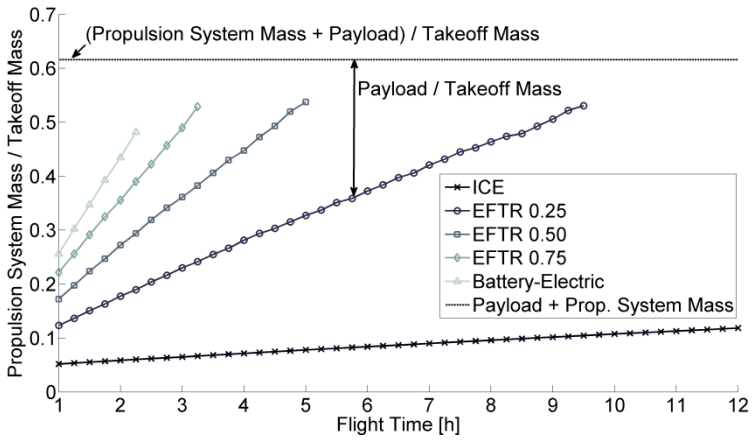

Figure 55: Payload and propulsion system mass fractions of takeoff mass. Propulsion system mass fractions are plotted; payload fractions may be read cumulatively as distance to dotted line.

In Figure 55 the mass fractions of the aircraft groups are provided for internal-combustion engine, battery-electric and hybrid-electric aircraft with EFTRs of 0.25, 0.50 and 0.75. The takeoff mass comprises of payload and the masses of the propulsion system and the airframe, according to (6). The three respective mass fractions show only small changes with varying payload. A maximum deviation of 12.5 %, which is acceptable for the discussion of trends, results from averaging the fractions over payload. The results for the propulsion system mass fractions are plotted over flight time in Figure 55. The airframe mass fraction is set constant to 0.38 from the values in Table 8, so that the sum of the normalized payload and propulsion mass also is constant at 0.62, which in Figure 55 is marked by a dashed horizontal line. The payload fractions can be read cumulatively as the distance from the curves to the horizontal line. For the internal combustion engine system, the propulsion system mass fraction increases linearly from 0.05 to a maximum of slightly above 0.11. The payload fraction consequently decreases by the same amount from 0.56 at 1 h flight

time to 0.50 at 12 h flight time. The internal combustion engine system has the highest payload fraction of all considered propulsion systems, meaning that for the transport of a certain payload the smallest aircraft is required.

The component mass fractions of the propulsion system may as well be averaged over payload with acceptable deviations. The mass of the energy storages, fuel and battery, are plotted in Figure 56 as fractions of the propulsion system mass and the takeoff mass. At the maximum flight time requirement of 12 h, fuel contributes slightly more than half of the internal combustion engine propulsion system mass or 6 % of the takeoff mass.

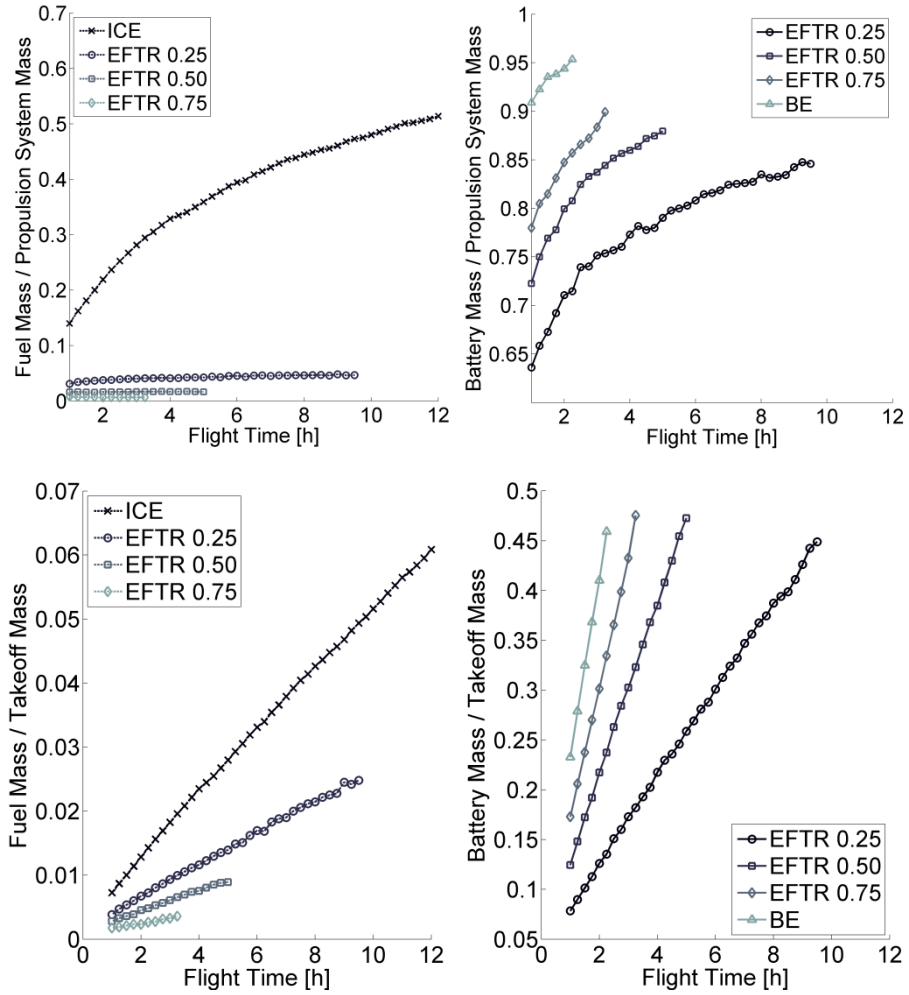

Figure 56: Energy storage mass fraction of the propulsion system mass (top) and of the takeoff mass (bottom)

4.2.2 Battery-Electric Aircraft

The takeoff mass of battery-electric aircraft is plotted in Figure 57. Battery-electric aircraft with a takeoff mass below 150 kg are not feasible for every point in the requirement space. The feasible missions are limited by the dotted curve in Figure 57. The stepped course of the feasibility curve is caused by the requirement space discretization. For 1 h flight time the payload is reduced to a maximum of 44 kg. The

maximum flight time carrying the minimum payload of 10 kg is 2 h 15 min. The influence of flight time on the aircraft takeoff mass is significantly bigger than with the internal combustion engine system. The difference is caused by the lower energy density of electric energy storage.

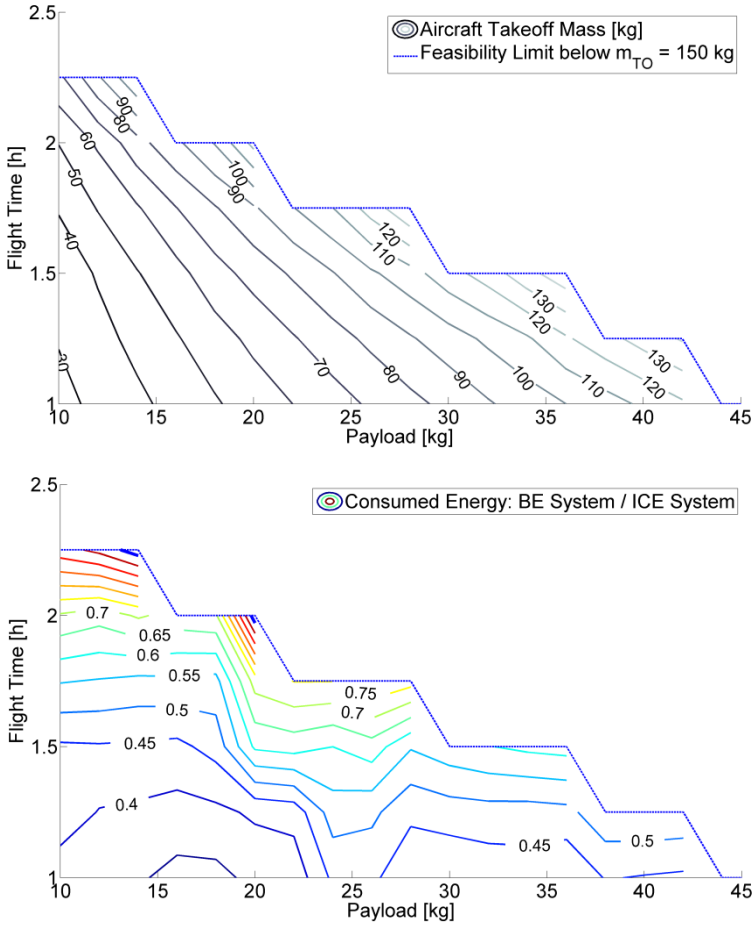

Figure 57: Takeoff mass for battery-electric aircraft (top) BE-to-ICE energy consumption ratio (bottom)

The battery-electric aircraft consume less energy than those with internal combustion engine within the requirement range they fulfill with a takeoff mass below 150 kg. The BE-to-ICE energy consumption ratio is provided in Figure 57. For 1 h flight time less than half of the energy required by an ICE aircraft is used. The consumption steeply grows with flight time and reaches the ICE level at the feasibility limit for flight times of 2 h and more. With increasing flight time the higher efficiency of the electric propulsion system is outweighed by the significantly higher mass. In comparison with the hybrid-electric and the internal combustion engine systems, the battery-electric system exhibits the highest propulsion system mass fraction in Figure 55. Consequently the payload fraction is reduced to the lowest value of all considered propulsion system types. The battery mass is the biggest position in the propulsion system mass. Its fraction, visualized in Figure 56, is above 0.9 even for the minimum flight time of 1 h. The battery mass fraction of takeoff mass exceeds 0.45 for the maximum flight time.

4.2.3 Hybrid-Electric Aircraft

The takeoff and fuel mass of hybrid-electric aircraft optimized for missions with an electric flight fraction of 0.25 are shown in Figure 58. It is noticeable that hybrid-electric aircraft with a takeoff mass below 150 kg do not fulfill the full range of requirements. The feasible requirement space is limited by the dashed line in Figure 58. The maximum payload of 70 kg is possible, but only for a maximum endurance of 1 h 15 min. Flight times over 9 h 30 min are only possible with payloads lower than the considered minimum of 10 kg. The takeoff mass of hybrid-electric aircraft as well as the mass fractions in Figure 55 and their curves' gradients are between those of the internal combustion engine and the battery-electric aircraft. The propulsion system mass fractions in Figure 56 change considerably if batteries are included. The batteries are the heaviest propulsion component. Their mass fraction rises from 0.64 at 1 h flight time to 0.85 at 12 h, whereas the fuel mass fraction's maximum value is 0.05. In relation to takeoff mass, this correlates to a maximum battery mass fraction of 0.45 and a maximum fuel mass fraction of 0.02.

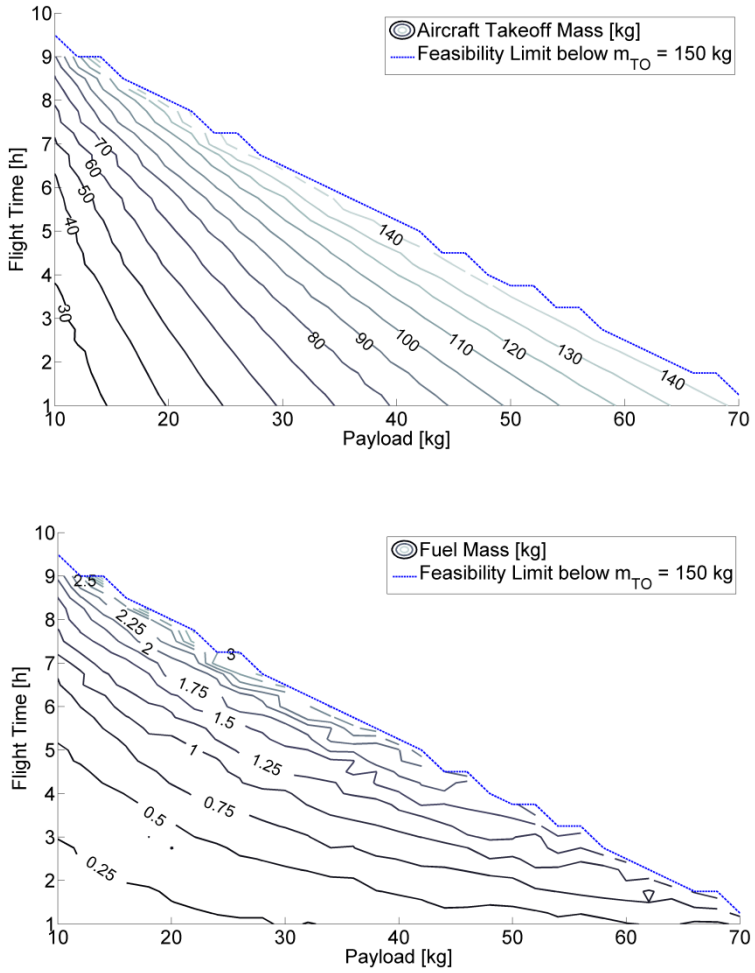

Figure 58: Takeoff mass (top) and fuel mass (bottom) for aircraft with parallel hybrid-electric propulsion system optimized for an electric flight time ratio of 0.25

The HE-to-ICE takeoff mass ratio varies only slightly with payload, whereas its growth with flight time may best be approximated with an exponential function. At the maximum hybrid-electric flight time of 9 h 30 min the maximum ratio of seven times the mass of a conventional ICE aircraft is reached.

The fuel mass consumed by the hybrid-electric system is partially lower than that required by internal combustion engine systems, as may be seen in the plot of the HE-to-ICE fuel mass ratio in Figure 59. The boundary curve is plotted in bold. Below a flight time of approximately 5 h 30 min, the hybrid-electric system consumes less fuel to perform the same mission. For 1 h flight time a minimum of 60 % of the internal combustion engine aircraft fuel mass is necessary. For flight times higher than 5 h 30 min the necessary fuel rises up to the double amount at 9 h flight time.

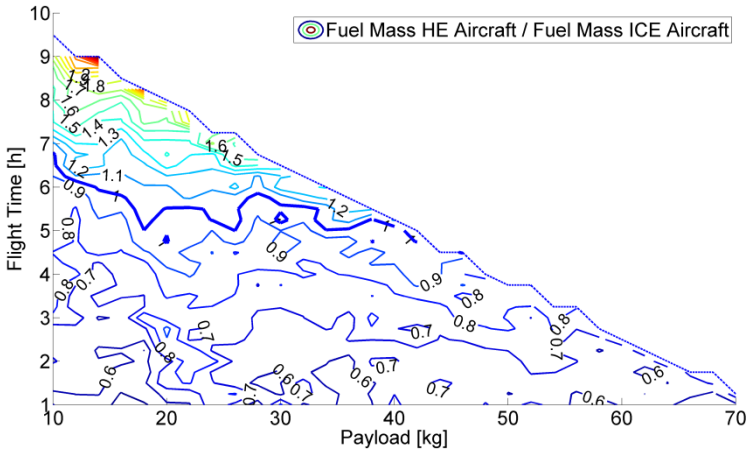

Figure 59: Ratio of the consumed fuel masses of hybrid-electric (HE) to internal combustion engine (ICE) aircraft

Three effects contribute to the fuel reduction. First, the internal combustion engine runs less time, as 25 % of the mission is conducted in electric flight. Second, for certain requirements the engine is downsized in the hybrid-electric system. During the *Maximum Power* flight phase climb, the engine and the electric motor share power generation, so that neither of the units needs to provide the amount that would have been necessary if they had been used as singular power units. This allows a reduction in size. The engine HE-to-ICE displacement volume ratio is visualized in Figure 60. The engines in the hybrid-electric system are smaller below the bold curve for a ratio of one. This correlates to a boundary flight time of 4 h, with deviations being caused by the discretization. Above this mark, the higher takeoff mass of the hybrid-electric aircraft results in a rise of the displacement volume over that of the internal combustion engine system.

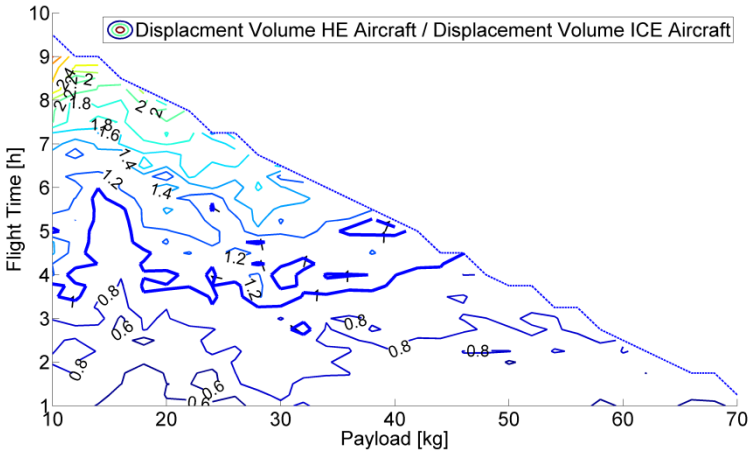

Figure 60: Ratio of the displacement volumes of hybrid-electric (HE) to internal combustion engine (ICE) aircraft

The third contributor to the reduced fuel mass of the hybrid-electric system is the higher efficiency in cruise. In the internal combustion engine aircraft, the engine is sized for its maximum power demand. The efficiency characteristics of an internal combustion engine, as shown in Figure 14, results in high efficiencies at high torque demands. As a transmission system would be impractical for unmanned aircraft, the torque demand in cruise is lower than during the *Maximum Power* phase. Therefore, the engine runs in a state of high efficiency during the short period of *Maximum Power* demand, whereas in the very much longer cruise phase only a lower efficiency may be achieved. The average torque ratio of the design points *Regular Cruise* to *Maximum Power* is 0.37 for the ICE aircraft. In hybrid-electric aircraft electric motor and internal combustion engine both drive the propeller, so that the torque load is distributed on both units. The degree of hybridization, as figure of merit for the shaft power provided by the electric motor at *Maximum Power*, reaches an average of 0.53 in the analyzed requirement space. The *DoH* values vary only in a relatively narrow range of 0.50 to 0.65. As a consequence the *Regular Cruise* to *Maximum Power* ratio of torque demand of the internal combustion engine at reaches a significantly higher average value of 0.77. The better match of torque demand allows higher efficiencies during cruise. In the considered requirement space, the cruise engine efficiency in the hybrid-electric systems averages at 0.33 and clearly exceeds the average 0.23 achieved with the internal combustion engine system.

The electric motor is similarly downsized in the hybrid-electric propulsion system. Nevertheless the downsizing is only advantageous in terms of motor mass. Figure 61 shows the HE-to-BE ratio of the factor of diameter and length. Dependent on payload and flight time variation no clear trend may be identified. Areas of increased ratios are caused by the discretization and the previously described change between fast-turning and slow-turning systems within the optimization procedure.

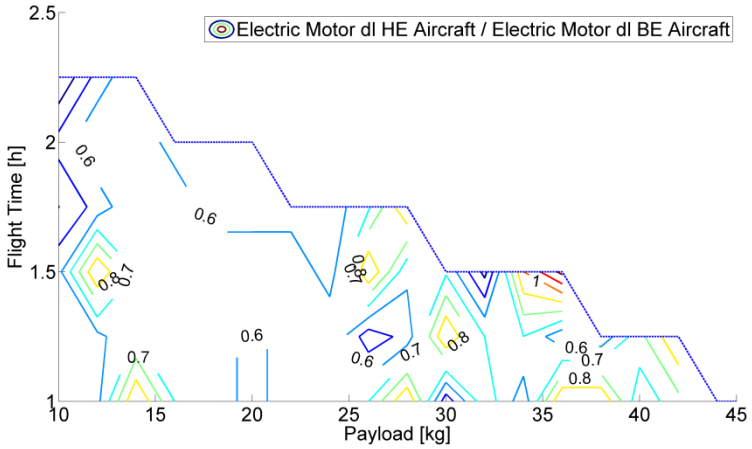

Figure 61: Ratio of the products of electric motor diameter and length of hybrid-electric (HE) to battery-electric (BE) aircraft

The reduction in motor size results in lower motor mass according to (31). Furthermore the ratio of *Electric Flight* to *Maximum Power* torque demand of the electric motor increases from 0.37 in the battery-electric system to 0.68 in the hybrid-electric system due to the shared power operation at *Maximum Power*. Contrary to the internal combustion engine, the higher relative torque demand in cruise does not result in a higher efficiency. As visible in the efficiency map for one exemplary electric motor used in a battery-electric aircraft in Figure 62, the motor efficiency is relatively stable at high values over 0.9 for a wide range of rotational velocities and torque. A significant drop occurs at very low values in both dimensions. For the example in Figure 62, an increase in torque demand for the marked *Regular Cruise* design point would result in an efficiency increase of only one percentage point.

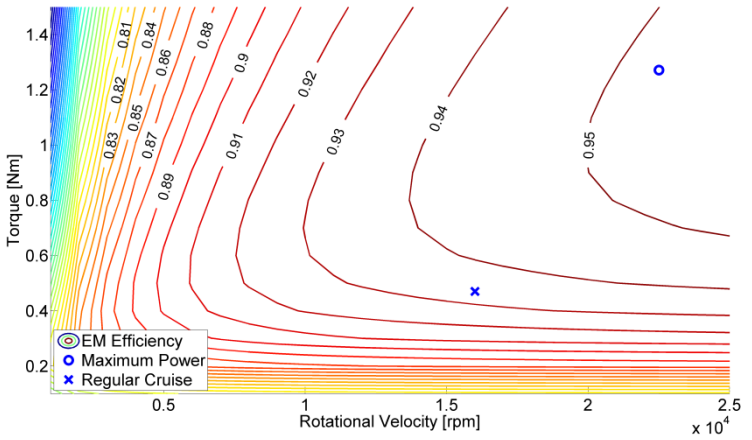

Figure 62: Efficiency map of the electric motor (*dl*=5510 and K_V=514) used in the battery-electric system for 1.25 h flight time and 19 kg payload with design points *Maximum Power* and *Regular Cruise*

In Figure 63 the HE-to-ICE ratio of consumed energy is plotted. The boundary curve, below which the hybrid-electric system is advantageous over the ICE, is plotted boldly. The corresponding flight times range between 4 h and 5 h. They are shorter than the threshold flight times in the comparison of fuel mass in Figure 59 due to the additional electric energy consumed in the hybrid-electric system. The battery-electric

system consumes less energy than both the ICE and the hybrid-electric system for flight times up to 2 h at 10 kg payload and 1 h 30 min at 35 kg payload. The most favorable aircraft in the requirement space in terms of energy consumption is indicated in the propulsion recommendation map in Figure 63.

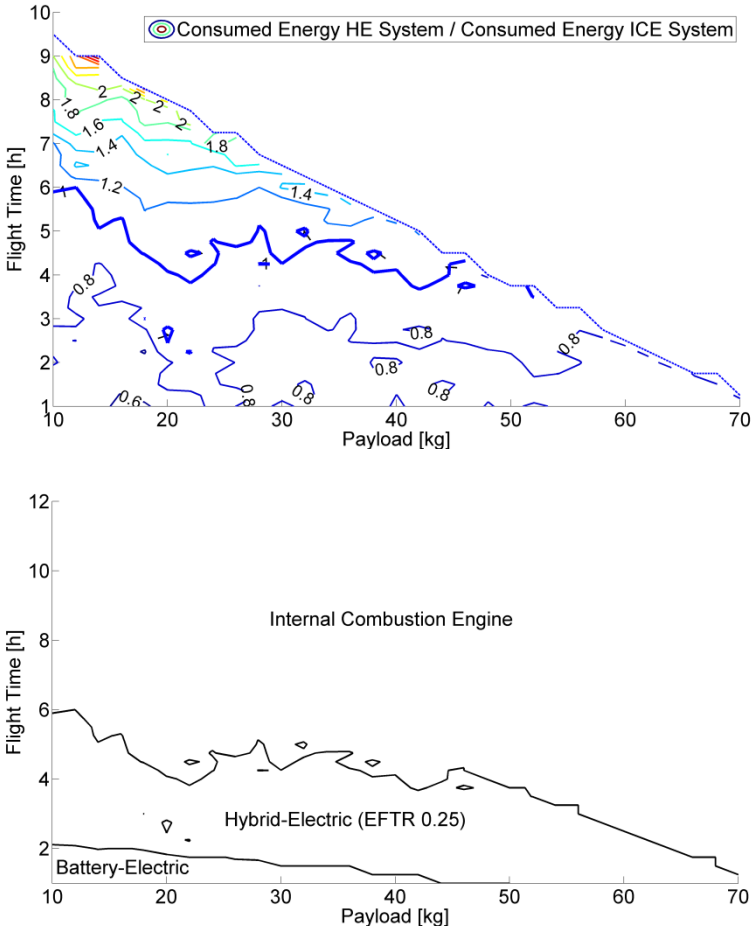

Figure 63: Ratio of the overall consumed energy of hybrid-electric and internal combustion engine systems (top) propulsion system recommendation map in terms of energy consumption (bottom)

Figure 64 provides the ratio of electric energy to total energy consumption for the hybrid-electric aircraft. The percentage varies from 11 % minimum at maximum flight time to 17 % maximum at short flight times. The decrease of the percentage with flight time can be explained with the higher influence of the *Maximum Power* design point on overall energy at shorter flight times. At *Maximum Power*, the relation of energy consumed from fuel and battery is governed by the degree of hybridization. The flight time ratio of *Regular Cruise* to *Electric Flight*, and consequently the energy type ratio for the horizontal flight phases, is defined by the EFTR. The *DoH* is higher than the EFTR, as quantified prior. Therefore, the higher the flight time ratio of *Maximum Power* to *Regular Cruise* and *Electric Flight*, the higher is the percentage of electric energy. The electric energy ratio is lower than the electric flight time ratio due to the higher efficiency of the electric propulsion system compared with the internal combustion engine

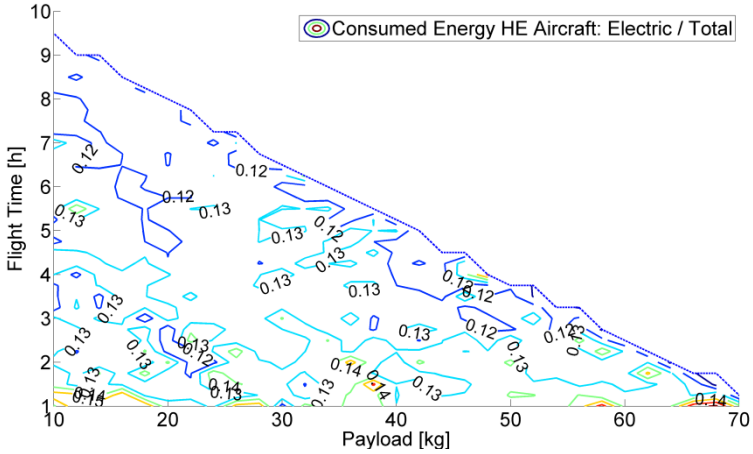

Figure 64: Percentage of electric energy in the total energy consumption of hybrid-electric (HE)aircraft

Figure 65 and Figure 66 show the takeoff mass and fuel mass of hybrid-electric aircraft optimized for missions with an electric flight time ratio of 0.50 (EFTR 0.50) and 0.75 (EFTR 0.75), respectively. The maximum flight time with 10 kg payload and below 150 kg takeoff mass is 5 h for EFTR 0.50 and 3 h 15 min for EFTR 0.75. The maximum possible payload is restricted to 64 kg for the EFTR 0.50 missions and to 54 kg for the EFTR 0.75 missions.

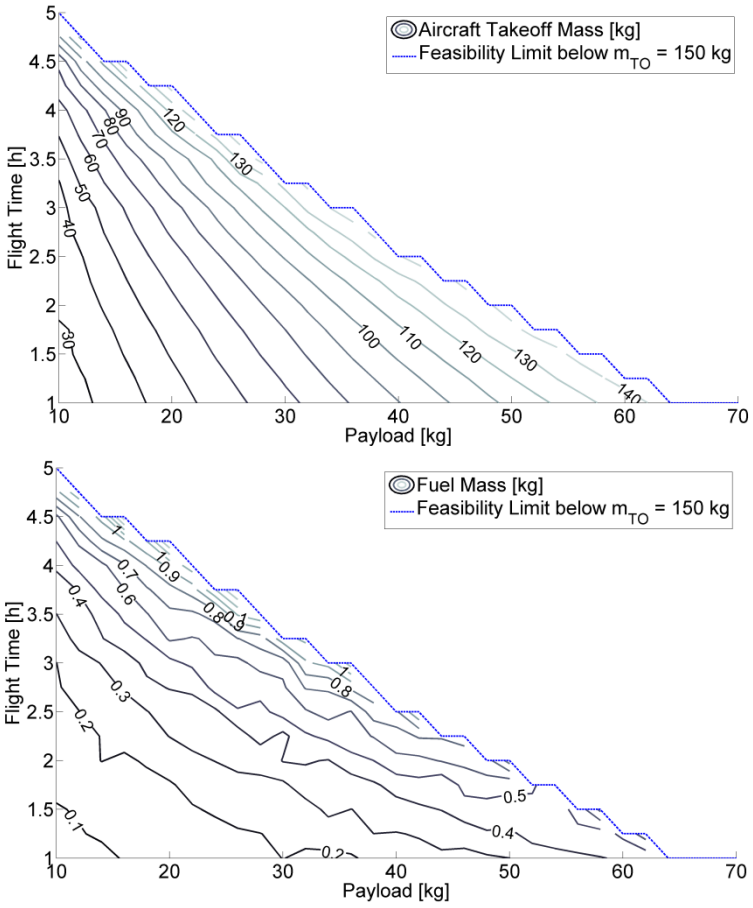

Figure 65: Takeoff mass (top) and fuel mass (bottom) for aircraft with parallel hybrid-electric propulsion system optimized for an electric flight time ratio of 0.5

The higher the electric flight time ratio, the higher is the takeoff mass. The hybrid-electric and ICE aircraft takeoff mass ratio's exponential growth with flight time increases its steepness with rising EFTR. The trends observed for the mass fractions of internal combustion engine and EFTR 0.25 hybrid-electric aircraft can be applied analogously to the higher EFTR hybrid-electric aircraft. The propulsion system mass fraction in Figure 55 and its gradient over flight time is further increased and reduces the payload fraction. The battery mass fraction of propulsion system mass in Figure 56 rises up to maximum values of 0.88 for EFTR 0.5 and 0.90 for EFTR 0.75, whereas the maximum fuel mass fraction falls below 0.02.

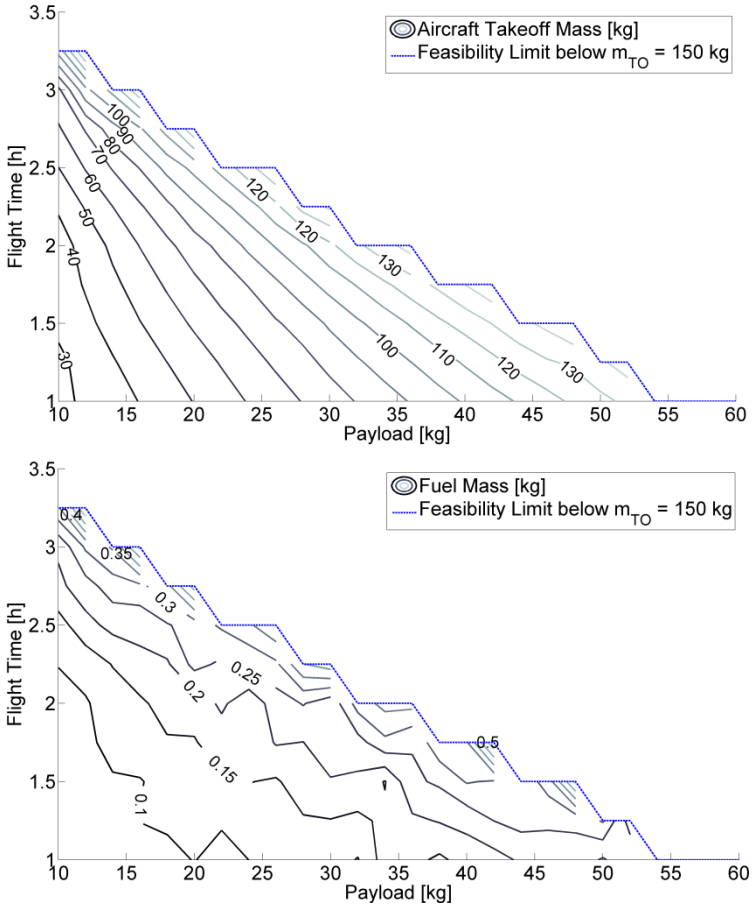

Figure 66: Takeoff mass (top) and fuel mass (bottom) for aircraft with parallel hybrid-electric propulsion system optimized for an electric flight time ratio of 0.75

The fuel consumption of EFTR 0.50 aircraft is lower than in ICE aircraft for almost the complete requirement space except for the requirements close to the 150 kg feasibility limit. The EFTR 0.75 aircraft consume less fuel within their complete feasible requirement space. Compared to the EFTR 0.25 mission, the average efficiency and the *Regular Cruise*-to-*Maximum Power* torque ratio is unchanged. The higher electric flight time ratio contributes to fuel economy, whereas the higher takeoff mass leads to a higher power and energy demand. Consequently the engine displacement volumes are bigger than in EFTR 0.25 aircraft. For the EFTR 0.50

aircraft, the displacement volumes exceed that of the ICE aircraft for flight times higher than 2 h. For the EFTR 0.75 aircraft the boundary lies between flight times of 1 h and 2 h. The ratio of electric energy to total energy rises to a range of 30 % to 38 % for EFTR 0.50 and a range of 48 % to 60 % for EFTR 0.75. The boundary flight times below which hybrid-electric aircraft are energetically advantageous over ICE aircraft fall to approximately 3 h and 2.5 h for EFTR 0.50 and EFTR 0.75, respectively. For the EFTR 0.50 aircraft, EFTR and average degree of hybridization are close, so that the distribution of electric energy percentage over flight time is reasonably steady. For EFTR 0.75, the increase of EFTR over *DoH* leads to higher electric energy percentages for increasing flight times.

4.2.4 Requirement Space Exploration Summary and Case Study

One exemplary point in requirement space is used as illustrative aid to summarize the comparison of aircraft with internal combustion engine, battery-electric and hybrid-electric propulsion systems. In the comparison, it has however to be kept in mind, that an ICE aircraft does not have the capability to fly silently. It therefore cannot carry out the surveillance mission as desired. The detail data for the three aircraft optimized for a 1 h 45 min flight time mission with 16 kg payload are gathered in Table 10. ICE aircraft are the most lightweight for the complete requirement space. The more flight time the aircraft is powered electrically, the more its takeoff mass rises. In the data in Table 10, the BE aircraft is more than twice as heavy as the ICE aircraft. Takeoff mass defines the aircraft's wing span and area and thereby heavily influences the aircraft handling qualities. For the given example the battery-electric aircraft's span exceeds 7 m so that for transport in a van, the wing might need to be divided in three sections instead of two. This leads to structural reinforcements and further mass penalties in detailed design.

The absolute fuel consumption of hybrid-electric aircraft is lower than in ICE aircraft for short missions. The boundary flight time, below which hybrid-electric aircraft are more advantageous, sinks with increasing electric flight time ratio. The lower consumption is caused by the reduced ICE-powered flight time and the combined activity of both power units at high power demands. The degree of hybridization which governs the interaction of engine and motor at Maximum Power takes values between 0.5 and 0.65. The dual use of both power units allows a downsizing of engine and motor and increased engine efficiency due to a more uniform torque demand at the design points *Regular Cruise* and *Maximum Power*. This is shown in Table 10, where the displacement volume was reduced from 30.1 cm³ in the ICE aircraft to 18.9 cm³ in hybrid-electric aircraft. The hybrid-electric *Regular Cruise* efficiency was increased to 0.33 from 0.21 for the ICE aircraft. The fuel mass is reduced by over 40 %. The electric motor is downsized to a *dl* of 3600 mm² from 5150 mm² in the BE aircraft.

Table 10: Comparison of internal combustion engine, hybrid-electric (EFTR 0.25) and battery-electric aircraft for one exemplary requirement point (16 kg payload and 1 h 45 min flight time)

	IC engine	**Hybrid-electric**	**Battery-electric**
Geometry			
Wing area [m²]	1.38	1.70	3.33
Wing span [m]	4.71	5.23	7.33
Masses [kg]			
Takeoff mass	28.82	35.49	69.62
Airframe	11.03	13.54	26.57
Payload	16	16	16
Propulsion system	1.79	5.77	27.05
- Electric motor	-	0.61	0.96
- Electronic speed controller	-	0.04	0.12
- Battery	-	3.89	25.53
- Internal combustion engine	1.19	0.77	-
- Fuel	0.37	0.21	-
- Fuel tank	0.09	0.07	-
- Propeller	0.13	0.18	0.45
Coupling			
Degree of hybridization (*MP*)	-	0.5	-
Coupling constant	-	2.5	-
Electric motor			
Diameter x length [mm²]	-	3600	5150
Specific rotational velocity [rpm/V]	-	383	586
Efficiency (*EF*/*MP*)	-	0.93 / 0.94	0.94 / 0.94
Rot. velocity [rpm] (*EF*/*MP*)	-	12500 / 18380	16000 / 22580
Torque (*EF*/*MP*)	-	0.43 / 0.60	0.59 / 1.60
Internal combustion engine			
Displacement volume [cm³]	30.1	18.9	-
Efficiency (*RC*/*MP*)	0.21 / 0.32	0.33 / 0.34	-
Rot. velocity [rpm] (*RC*/*MP*)	5000 / 7560	5000 / 7350	-
Torque [Nm] (*RC*/*MP*)	0.90 / 2.55	1.09 / 1.51	-
Propeller			
Tip radius [m]	0.2	0.25	0.5
Efficiency (*RC*/*EF*/*MP*)	0.75 / - / 0.60	0.77 / 0.77 / 0.65	- / 0.84 / 0.76
Rot. velocity [rpm] (*RC*/*EF*/*MP*)	5000 / - / 7560	5000 / 5000 / 7350	- / 2000 / 2820
Torque [Nm] (*RC*/*EF*/*MP*)	0.90 / - / 2.55	1.08 / 1.08 / 3.00	- / 4.75 / 12.79
Electric energy consumption [Wh]	-	374	2456
Fuel energy consumption [Wh]	4550	2608	-

In terms of energy consumption, the hybrid-electric aircrafts' advantage in fuel consumption and integration of more efficient electric propulsion makes them advantageous over ICE aircraft for short flight times. The additional consumption of electrical energy nevertheless reduces the boundary flight time to lower values than for fuel consumption. The battery-electric aircraft is most economical in its energy consumption for very short flight times from 1h to 2 h. In the example case, the energy consumption of the hybrid-electric and battery-electric aircraft are roughly equal, whereas the ICE aircraft consumes almost 50 % more. It is noticeable in Table 10 that the battery-electric aircraft uses a much slower-turning system with a bigger propeller than the ICE and the hybrid-electric aircraft. This results in a higher efficiency, which is more important than for the other two aircraft because of the distinctive high battery mass fraction. The higher the electric flight time ratio, the higher grows the propulsion system fraction. Furthermore, an increasing EFTR results in a steeper growth of the propulsion system fraction with flight time. This implies that the payload fraction decreases and its reciprocal, the aircraft growth factor increases. The aircraft hence becomes more sensitive to mass changes. For the battery-electric and hybrid-electric aircraft, the battery is the biggest contributor to the propulsion system mass. An increase in energy storage mass also occurs for increasing flight times. The energy demand rises and consequently the importance of efficiency grows.

4.3 Sensitivity Studies

The sensitivity studies in this chapter show the effect of aircraft design, technology or requirement parameter variations. A mission requirement only applicable for hybrid-electric aircraft is the electric flight time ratio, which is varied in chapter 4.3.1. The chapter is furthermore used to describe how the optimization scheme implemented in the design process and the choice of its cost function influence the results. The effect of the design space discretization in interaction with optimization is demonstrated with the help of a case study. Specific energy of the battery is selected as a main technology parameter impacting hybrid-electric aircraft. The influence of its variation on hybrid-electric and battery-electric aircraft in comparison to internal combustion engine aircraft is analyzed in chapter 4.3.2. Chapter 4.3.3 describes the effect of mass changes by means of payload variation. Knowledge of the aircraft's sensitivity to varying mass is crucial for the assessment of design alternatives in preliminary aircraft design.

The setup of the design procedure for the parameter variation is as described in chapter 4.2, with the following differences: For the parameter variation, only selected flight times are regarded. Flight times of 1 h, 2 h and 3 h represent the current capabilities of battery-electric propulsion systems, 6 h and 8 h are target times for improving battery technology and 12 h due to the ability to keep a system permanently airborne for 24 h

per day with two aircraft and two flight legs. The baseline payload is 10 kg, the payload requirement of the IMPULLS. Table 11 contains the mission requirements for the sensitivity studies. The varied parameter is highlighted.

Table 11: Mission requirements for parameter variation

		Electric Flight Time Ratio	**Additional Mass**	**Battery Specific Energy**
Payload		10 kg	10 – 15 kg	10 kg
Flight Time	MP	5 min		
	RC	99 % – 1 % of 1, 2, 3, 6, 8 & 12 h	75 % of 1, 2, 3, 6, 8 & 12 h	
	EF	1 % - 99 % of 1, 2, 3, 6, 8 & 12 h	25 % of 1, 2, 3, 6, 8 & 12 h	
Velocity (MP / RC / EF)		20 m/s		
Rate of climb		5 m/s		
Battery Specific Energy		168 Wh/kg, see (34)		120 – 1000 Wh/kg

4.3.1 Variation of the Electric Flight Time Ratio

The electric flight time ratio's influence on the aircraft mass, fuel mass and energy consumption has been identified in the requirement space exploration on the basis of aircraft optimized for EFTRs of 0.25, 0.50 and 0.75. This chapter investigates the full EFTR spectrum, discretized in steps of 0.01. Where applicable, the analysis contains ICE aircraft (EFTR 0) and battery-electric aircraft (EFTR 1). In order to allow a clear and comprehensible arrangement of the results, only one payload requirement and six flight time levels are considered.

Takeoff mass is the first evaluated aircraft property and plotted in Figure 67. It rises with the EFTR, with increasing gradients for increasing flight times. Incomplete curves would exceed the 150 kg limit at the next higher EFTR. Step changes occur at the transition from ICE (EFTR 0) to hybrid-electric system (EFTR 0.01) and from hybrid-electric (EFTR 0.99) to battery-electric system (EFTR 1). They are caused by the additional mass of a second power unit, which the hybrid-electric system per definition includes, although at the boundary EFTR it is only used for 1 % of the flight time. Battery-electric aircraft below 150 kg takeoff mass are feasible only for flight times of 1 h and 2h. For the 1 h mission the battery-electric aircraft is more lightweight

than hybrid-electric aircraft optimized for EFTR higher than 0.85. For the 2 h mission the hybrid-electric boundary EFTR is 0.94. ICE aircraft are the most lightweight for every considered flight time. The highest considered flight time of 12 h is feasible for hybrid-electric aircraft with EFTR below 0.2.

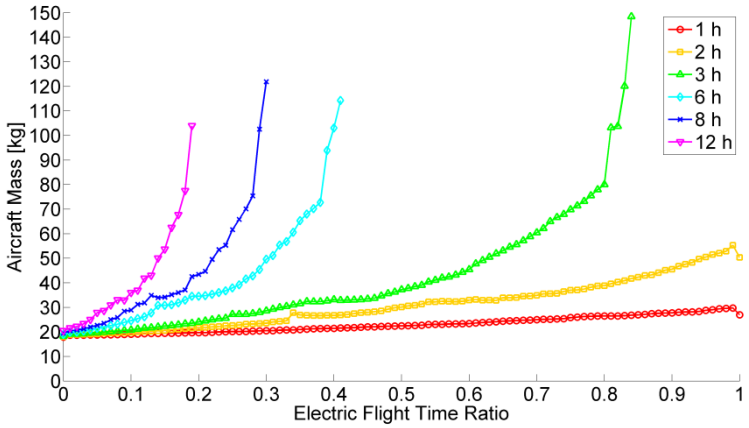

Figure 67: Hybrid-electric aircraft takeoff mass over varying electric flight time ratio

The propulsion system mass fractions are plotted in Figure 68. As in Figure 55, the dotted line marks the constant combined fraction of propulsion system and payload, so that the payload fraction may be read as the distance from the dotted line to the curve. With increasing electric flight time, the propulsion system mass fraction rises, because the specific energy of batteries is lower than that of fuel. Consequently the payload fraction decreases and the aircraft growth factor increases.

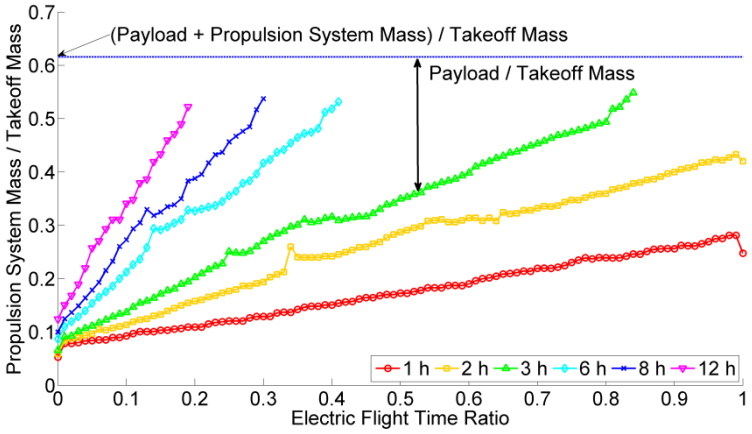

Figure 68: Propulsion system mass fractions over varying electric flight time ratio

The fuel consumption for varying EFTR is given in absolute values and relative to the ICE aircraft with equal requirements in Figure 69. For all considered flight times fuel mass decreases in a step change at the transition from ICE to hybrid-electric aircraft. The reason is the more efficient use of the engine in *Regular Cruise* due to the shared load at *Maximum Power* and the resulting, more balanced torque demand. The degree of hybridization, as the driver for the power units' interaction at *Maximum Power* ranges between 0.50 and 0.65 also for the EFTR variation. The hybrid-electric aircraft

fuel mass behavior with EFTR is dependent on the flight time. Fuel mass decreases with EFTR for the 1 h and 2 h missions, whereas for the 3 h mission it stays approximately constant up to an EFTR of 0.8 and then rises. For the higher flight time missions the fuel mass increases.

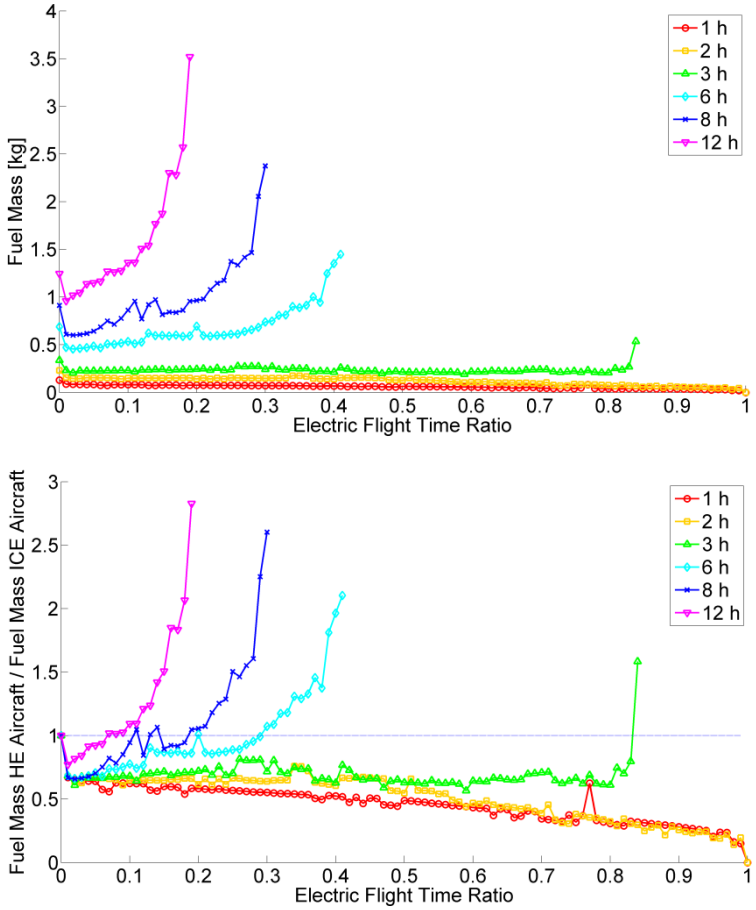

Figure 69: Absolute fuel mass of HE aircraft (top) and fuel mass ratio of HE to ICE aircraft fuel mass (bottom) over varying electric flight time ratio

In comparison to the ICE aircraft, hybrid-electric propulsion systems consume less fuel over the whole EFTR range for the 1 h and 2 h missions. The 3 h mission is conducted more economically below a threshold EFTR of 0.84. The threshold EFTR then sinks with increasing flight time according to Table 12.

Table 12: EFTR thresholds, below which a HE aircraft is more fuel efficient or energy efficient than an ICE aircraft

Flight Time [h]	Fuel Consumption	Energy Consumption
3	0.84	0.60
6	0.30	0.24
8	0.19	0.11
12	0.07	0.07

The decreasing time of ICE use with increasing EFTR contributes to a fuel mass reduction. On the other hand, takeoff mass increases with EFTR and that drives up the power and energy demand. The takeoff mass gradients increase with flight time, so that the higher energy demand predominates the effect of reduced *Regular Cruise* flight time for flight times exceeding 3 h. The most fuel efficient hybridization for flight times longer than 3 h is a use of the electric motor only for the *Maximum Power* design point, as a booster for climb. For flight times below 3 h, the reverse concept is most fuel efficient: All horizontal flight phases are conducted electrically and the internal combustion engine is used as a climb booster.

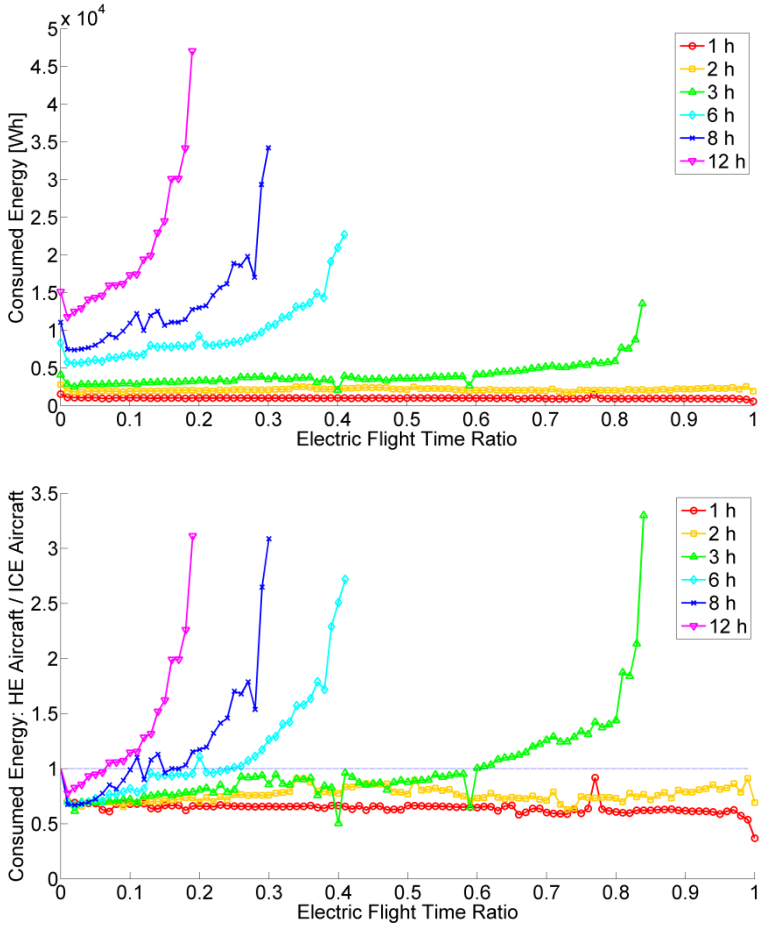

Figure 70: Absolute consumed energy of HE aircraft (top) and consumed energy ratio of HE to ICE aircraft fuel mass (bottom) over varying electric flight time ratio

Figure 70 shows the overall consumed energy of the aircraft. The fuel mass step change at the transition from ICE to hybrid-electric aircraft is visible in the energy curves as well. For the hybrid-electric EFTR, the consumed energy shows only small changes for the 1 h mission and increases with EFTR for flight times of 2 h and longer. Higher gradients are obtained for longer flight times. Where battery-electric aircraft are feasible, the energy decreases significantly compared to EFTR 0.99. Figure 70 also sets the energy in relation to the energy consumed by the respective ICE aircraft. The thresholds, below which the hybrid-electric system is advantageous, decrease in

relation to the fuel consumption due to the additional electric energy consumption. The values are summarized in Table 12. The battery-electric aircraft is most energetically economical for the 1 h mission. For 2 h flight time hybrid-electric systems with EFTR below 0.75 are more favorable. The lowest energy consumption for the 2 h and longer missions is however obtained with a use of the electric motor only for *Maximum Power*.

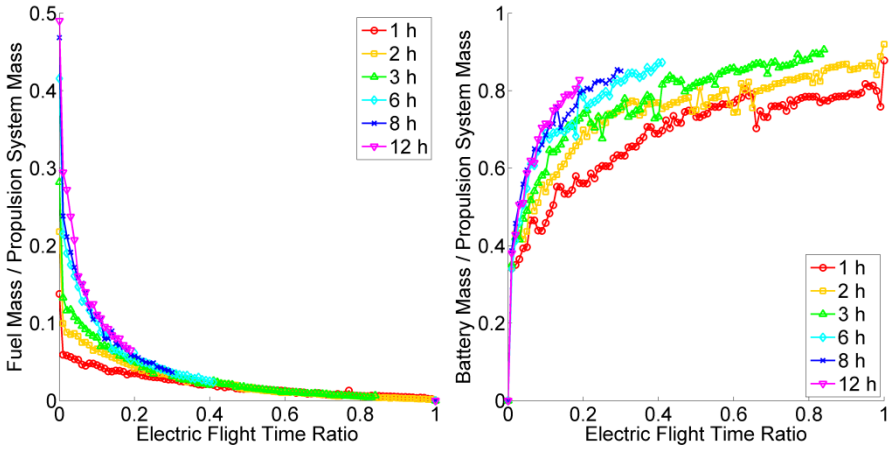

Figure 71: Energy storage mass fractions of propulsion system mass over varying electric flight time ratio

The electric energy percentage of total energy grows approximately linearly with EFTR. For all hybrid-electric aircraft the percentage is lower than the EFTR due to the higher efficiency of the electric propulsion system. The relation of the two on-board energy storages is displayed in Figure 71 in the form of battery and fuel mass fractions of the propulsion system. Increasing electric flight time ratios cause a shift of the energy demand from fuel to battery, so that the mass of the latter increases and that of the former decreases. The fuel mass fraction falls below 5 % at EFTR 0.25 for all flight times. The battery mass is the main contributor to propulsion system mass for all EFTR higher than zero.

Influence of the Design Space Discretization

Generally in chapter 4, the plots showing fuel or energy consumption are less smooth than the takeoff mass plots. The fuel mass for the 6 h mission with EFTR 0.20 in Figure 69 is a prominent example of an outlier. The cause of the unsteadiness can be explained by exemplary analyzing this point and the surrounding EFTRs. Table 13 shows detailed characteristics of the aircraft and the propulsion system optimized for the 6 h mission with EFTRs of 0.19, 0.20 and 0.21. In the comparison of EFTRs 0.19 and 0.20 it is obvious, that the power demand increases for the latter aircraft as the longer electric flight time results in a heavier aircraft. Apart from this, the optimization process reduces the *DoH* from 0.6 for EFTR 0.19 to 0.5 for EFTR 0.20, which leads to a higher *Maximum Power* torque demand of the internal combustion engine. As a consequence, the engine displacement volume is increased from 16.5 cm³ to 19.2 cm³

and the ratio of *Maximum Power* to *Regular Cruise* torque demand rises. This results in a reduction of the *Regular Cruise* engine efficiency from 0.35 to 0.32 and a significantly higher fuel mass.

Table 13: Comparison of aircraft with electric flight time ratio 0.12, 0.13 and 0.14 for requirements of 10 kg payload and 6 h flight time

	EFTR 0.19	**EFTR 0.20**	**EFTR 0.21**
Masses [kg]			
Takeoff mass	34.56	34.57	34.78
Airframe	13.19	13.27	13.28
Payload	10	10	10
Propulsion system	11.37	11.30	11.50
- Electric motor	0.61	0.61	0.96
- Electronic speed controller	0.04	0.04	0.04
- Battery	9.14	8.86	8.71
- Internal combustion engine	0.68	0.78	0.88
- Fuel	0.59	0.70	0.60
- Fuel tank	0.13	0.15	0.14
- Propeller	0.17	0.17	0.18
Coupling			
Degree of hybridization (*MP*)	0.6	0.5	0.6
Coupling constant	2.5	3	3
Electric Motor			
Diameter x length [mm²]	3600	3600	5150
Specific rot. velocity [rpm/V]	383.4	644.3	338.9
Efficiency (*EF*/*MP*)	0.92 / 0.92	0.93 / 0.94	0.93 / 0.94
Rot. velocity [rpm] (*EF*/*MP*)	9850 / 14120	15000 / 21890	9000 / 12840
Torque (*EF*/*MP*)	0.47 / 0.76	0.34 / 0.47	0.54 / 0.90
Internal Combustion Engine			
Displacement volume [cm³]	16.5	19.2	21.8
Efficiency (*RC*/*MP*)	0.35 / 0.35	0.32 / 0.34	0.35 / 0.35
Rot. velocity [rpm] (*RC*/*MP*)	4000 / 5650	5000 / 7300	3000 / 4280
Torque [Nm] (*RC*/*MP*)	1.18 / 1.27	1.03 / 1.42	1.64 / 1.81
Propeller			
Tip radius [m]	0.3	0.25	0.3
Efficiency (*RC*/*EF*/*MP*)	0.79 / 0.79 / 0.71	0.77 / 0.77 / 0.66	0.81 / 0.81 / 0.70
Rot. velocity [rpm] (*RC*/*EF*/*MP*)	4000 / 3940 / 5650	5000 / 5000 / 7300	3000 / 3000 / 4280
Torque [Nm] (*RC*/*EF*/*MP*)	1.18 / 1.17 / 3.17	1.03 / 1.03 / 2.84	1.64 / 1.63 / 4.52
Battery energy consumption [Wh]	772	838	842
Fuel energy consumption [Wh]	7206	8441	7239

The EFTR 0.20 aircraft uses a faster-turning lower diameter propeller than the EFTR 0.19 aircraft. Consequently propeller efficiency decreases. Both aircraft use an electric motor with the same *dl*, whereas the higher rotational velocity of the EFTR 0.20 aircraft leads to an increased K_v. The reduction in *Maximum Power* torque demand of the electric motor, due to the reduced *DoH,* and the higher K_v result in an *Electric Flight* efficiency increase by one percentage point. The EFTR 0.21 aircraft's propeller diameter is equal to the EFTR 0.19, but turns with 3000 rpm instead of 5000 rpm for EFTR 0.20 and 4000 rpm for EFTR 0.19. A significant increase in torque and efficiency is the consequence. Both power units in the EFTR 0.21 aircraft are therefore augmented to bear the higher torque load. The electric motor *dl* is increased from 3600 mm² to 5150 mm² and the specific rotational velocity is lowered to 338.9 rpm/V. This leads to electric motor efficiency equal to EFTR 0.20. The EFTR 0.21 internal combustion engine has a displacement volume of 21.8 m³ at which an efficiency of 0.35 is feasible for *Regular Cruise* and *Maximum Power*. The increase of the *DoH* to 0.6 and the resulting reduction in the engine *Maximum Power* to *Regular Cruise* torque ratio contributes to that. Higher engine and propeller efficiency makes the EFTR 0.21 fuel mass fall below that required for EFTR 0.20. The fuel mass for EFTR 0.20 strikes as outlier, because it marks the point before a slower-turning bigger diameter propeller outweighs a faster-turning model in terms of propulsion system mass - the cost function. The slower propeller is more efficient and consequently reduces the mass of energy storages. Reduced rotational velocity however results in higher torque, which drives the mass of the power units. In the energy storage mass curves these propeller modifications appear as step changes. The design method's high computational effort results in the relatively coarse and rigid discretization of the design variables. If they were discretized finer, the transition between fast-turning and slow-turning systems would be realized with smaller changes. This would result in a reduction of the amplitude of the outliers. Alternatively, the results of this first analysis may be used to derive rules for the flexible discretization of design variables depending on the requirements. This would allow a finer discretization without an increase of support points.

Optimization Scheme Analysis

The optimization process strictly choses the configuration returning the lowest cost function values. The above results were created using propulsion system mass as cost function. This means, that the significant value of consumed fuel only affects the decision making in terms of its contribution to the system mass. If a less efficient system is more lightweight, it is chosen over a more efficient one. In a practical, less automated approach, the designer would presumably include efficiency in the decision making criteria, if no considerable takeoff mass disadvantages resulted from it. The

propulsion system mass nevertheless is the overall most reasonable cost function, as will be shown in the following. Reasonable alternatives for a single-goal cost function are fuel mass and consumed energy. These three cost functions are applied to the design process described in chapter 3.1 and the EFTR variation for the 6 h mission is computed with each. The results for takeoff mass and fuel mass are plotted in Figure 72. The energy cost function curves show a stepped characteristic. This is due to steps in the count of battery cells in parallel according to (36). In one step, the required electric energy and capacity continuously grow with EFTR, but the battery mass is constant due to the rounding. The fuel mass simultaneously decreases, as the *Regular Cruise* flight time decreases.

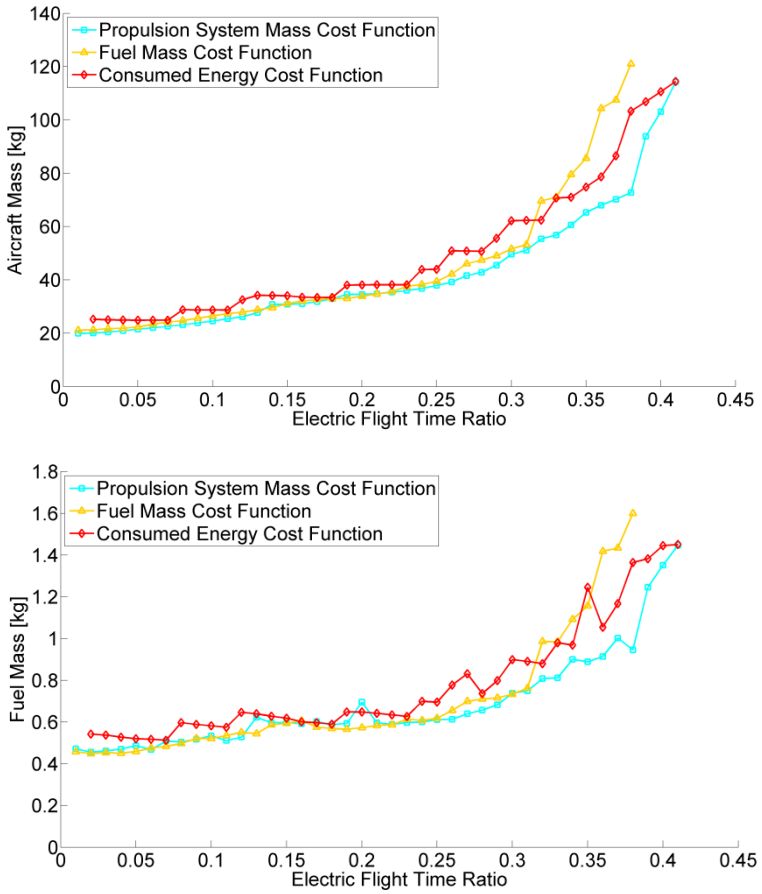

Figure 72: Hybrid-electric aircraft takeoff mass (top) and fuel mass (bottom) generated by processes with different cost functions over varying EFTR (6 h flight time)

Minimum takeoff mass is returned by the propulsion system mass cost function process. Energy consumption and fuel mass cost functions lead to mostly higher, at some EFTRs to equal masses. At low electric flight time ratios the energy consumption cost function process returns the highest values, whereas from EFTR 0.33 the fuel mass cost function process results exceed them. Generally the results diverge with increasing EFTR. The fuel mass curves show similar behavior. At several EFTRs below 0.25 the fuel mass cost function results fall below the propulsion system mass cost function fuel mass. The curves for the energy consumption show analogous

behavior. Neither fuel mass nor energy consumption may be effectively minimized using the respective parameter as cost function, due to the aircraft design process. The optimization is conducted within the propulsion system design module for the reasons described in chapter 3.1.2. The aircraft design process runs in iterations, until takeoff mass converges. The optimization is re-run in every iteration loop, but does not incorporate the mass cascade effect its output has. Choosing a configuration by minimum fuel or energy may result in a higher than minimum takeoff mass. In the next iteration loop again the minimum fuel or energy configuration is chosen for the adapted requirements. The minimum fuel mass or consumed energy may then be higher than in the respective iteration loop with the minimum propulsion system mass cost function, because the latter leads to a lower takeoff mass and consequently lower power and energy demands.

The use of fuel mass as cost function is specifically problematic due to the propulsion design process setup. As the isolated optimization process is not foreseeing the mass cascade effect, the electric drive train and the ICE drive train are not influencing each other within the propulsion system design procedure. Therefore, by secondary cost function, the most lightweight electric system is chosen. Nevertheless, selecting propeller, coupling and internal combustion engine, so that the fuel mass is minimized may result in a significantly higher than minimum propulsion system mass. In the next iteration loop this may cause fuel mass to significantly rise. In Figure 72, the results returned by the three processes differ most for EFTR 0.38. This point is therefore taken as an example to gain more insight on how the different results are obtained. In the first iteration run, starting with equal initial payload fractions, the same propeller is selected for all three systems. The propulsion system mass minimizing process selects the smallest electric motor of the three and yields the lowest electric energy requirement. Consequently the battery is the lightest of the three. The energy minimizing process selects a higher *DoH* which leads to an increased torque demand of the electric motor, a heavy motor and slightly more required energy compared to the minimum propulsion mass system. The rounding of the number of battery cells in parallel however results in a significantly heavier battery. The minimum fuel mass system has a lower coupling constant than the other two, which results in a higher electric motor torque demand. The resulting motor and battery mass is equal to the minimum energy case. The processes for minimum fuel mass and energy also select the same internal combustion engine. The minimum propulsion mass process selects a smaller, slightly less efficient model, which results in a fuel mass increase of 10 g, whereas 200 g are saved with the engine. The takeoff mass penalty of the minimum fuel and energy aircraft against the minimum propulsion system aircraft is 3 kg in the first iteration loop. In further iteration runs, the mass cascade effect increases the difference in takeoff mass and drives the final energy and fuel consumptions of the

aircraft designed with the energy and fuel cost functions over those of the minimum propulsion system mass aircraft.

Electric Flight Time Ratio Variation and Optimization Analysis Summary

Summarizing the optimization analysis, propulsion system mass as cost function is the most reasonable choice. The lower fuel mass computed by the fuel mass cost function process for some EFTRs however advises additional use of other cost functions in certain cases. An enhancement of the optimization process beyond single-goal cost functions may further improve the design process and the results.

Summarizing the effects of the EFTR variation on the aircraft, it has been shown, that takeoff mass rises with growing electric flight time. In terms of fuel and energy consumption, the shift of flight time from the less efficient ICE to the more efficient electric propulsion system with increasing EFTR is advantageous. The increasing takeoff mass and the resulting energy demand however oppose this effect and predominate for long flight times. The fuel mass rises over EFTR for flight times of 6 h and higher. For those flight times the most fuel efficient hybridization is the use of the electric motor as climb booster. For flight times shorter than 3 h applying the ICE as climb booster is most fuel efficient. The battery-electric aircraft consumes minimum energy for the 1 h mission. For longer flight times energy consumption rises with EFTR and the use of the electric motor as climb booster is most energy economical.

4.3.2 Variation of the Battery Specific Energy

The battery is identified as the main contributor to propulsion system mass in chapters 4.2 and 4.3.1. Consequently, it is a primary target for improvement. The most relevant improvement is the increase of its specific energy. In the outlook in chapter 2.2.3, future values of up to 1000 Wh/kg are envisaged. Therefore, the range of specific energy was set from a slightly lower than state-of-the-art value of 120 Wh/kg to 1000 Wh/kg with 40 Wh/kg increments. The values were applied to the denominator of the energy term in (34), instead of the 168 Wh/kg derived from the battery data base. The current term in (34) is not modified. The electric flight time ratio in this sensitivity study is set to 0.25.

Takeoff mass is plotted over the varying specific energy in Figure 73. With increasing specific energy, takeoff mass decreases. The curves' gradients decrease as well, as the battery mass fraction sinks and therefore the cascading influence of battery mass reduction on takeoff mass, quantified in the aircraft growth factor, becomes smaller. As the payload is constant with 10 kg, the aircraft growth factor here easily may be read from Figure 73 by dividing the takeoff mass by 10. At the highest specific energy,

the relative takeoff mass difference to the corresponding ICE aircraft is reduced to a range from 1.5 % for the 1 h mission to 12 % for the 12 h mission. The mass of the hybrid-electric aircraft is increased by the electric components, whereas the fuel mass is reduced in comparison to the ICE aircraft. Battery-electric aircraft equipped with 1000 Wh/kg batteries, for comparison, have relative takeoff mass differences to the ICE aircraft from 1 % for the 1 h mission to 106 % for 12 h flight time. For the 1 h mission, the battery-electric aircraft is lighter than the hybrid-electric aircraft.

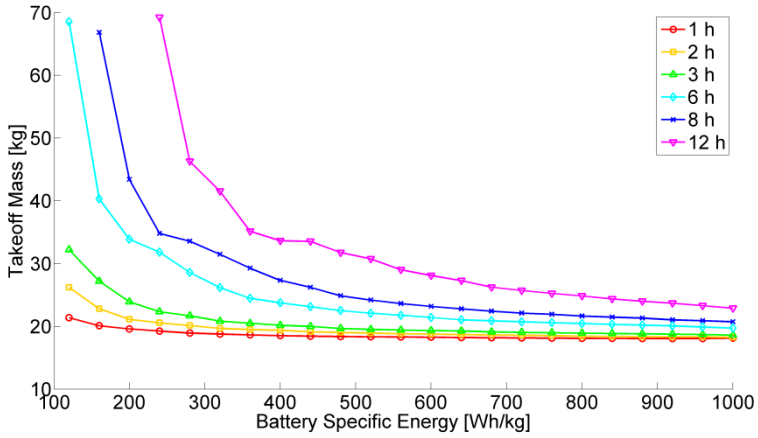

Figure 73: Hybrid-electric aircraft takeoff mass over varying battery specific energy

The fuel mass in absolute values and relative to the ICE system is provided in Figure 74. The 1 h, 2 h and 3 h flight time missions may be conducted more fuel efficient, even with the lowest specific energy considered. In a 6 h mission 160 Wh/kg are required for hybrid-electric to be more fuel efficient. The threshold value rises to 200 Wh/kg for the 8 h mission and 360 Wh/kg for the 12 h mission. The increase of specific energy has no significant effect on the degree of hybridization. The value range is slightly widened to 0.50 to 0.70 in comparison to the analyses with state-of-the-art battery technology. Nevertheless, the distribution of *DoH* over the specific energy is relatively arbitrary, as it is primarily driven by its high impact on the internal combustion engine. The dual-use of electric motor and internal combustion engine in the *Maximum Power* phase allows a significant increase in *Regular Cruise* ICE efficiency, whereas the potential to increase the already high electric motor efficiency is comparably low.

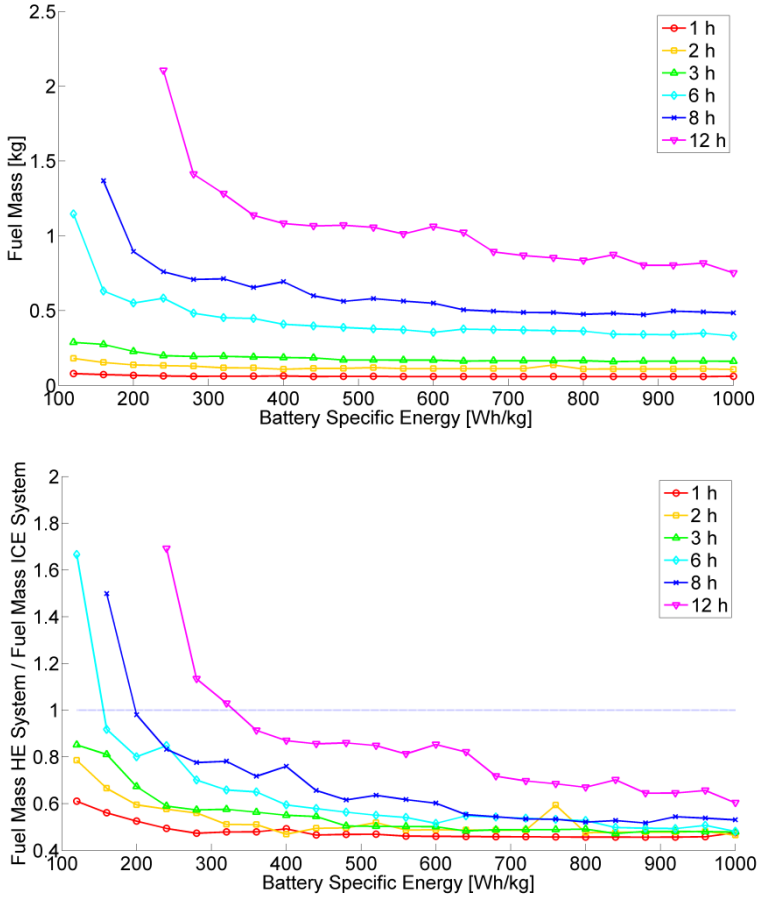

Figure 74: Absolute fuel mass of hybrid-electric aircraft (top) and fuel mass ratio of HE to ICE aircraft (bottom) over varying battery specific energy

In terms of the energy consumption, the comparison of hybrid-electric and ICE aircraft yields similar results to the fuel consumption, except for the hybrid-electric system requiring higher battery specific energies to be more economic than the ICE system due to the additional electric energy consumption. In Figure 75, the energy consumption of hybrid-electric aircraft is therefore given absolutely and as ratio of the corresponding battery-electric aircraft energy consumption. The higher flight time curves in the relative plot are limited by the feasibility of the battery-electric system within the 150 kg takeoff mass limit. Within these restrictions, the battery-electric aircraft is more energy efficient for the 1 h mission. For the longer missions, Table 14 summarizes the threshold values. The energetic advantage of the battery-electric system is the use of only an electric motor, which is significantly more efficient than the internal combustion engine included in the hybrid-electric system and the decrease of the aircraft growth factor as discussed above.

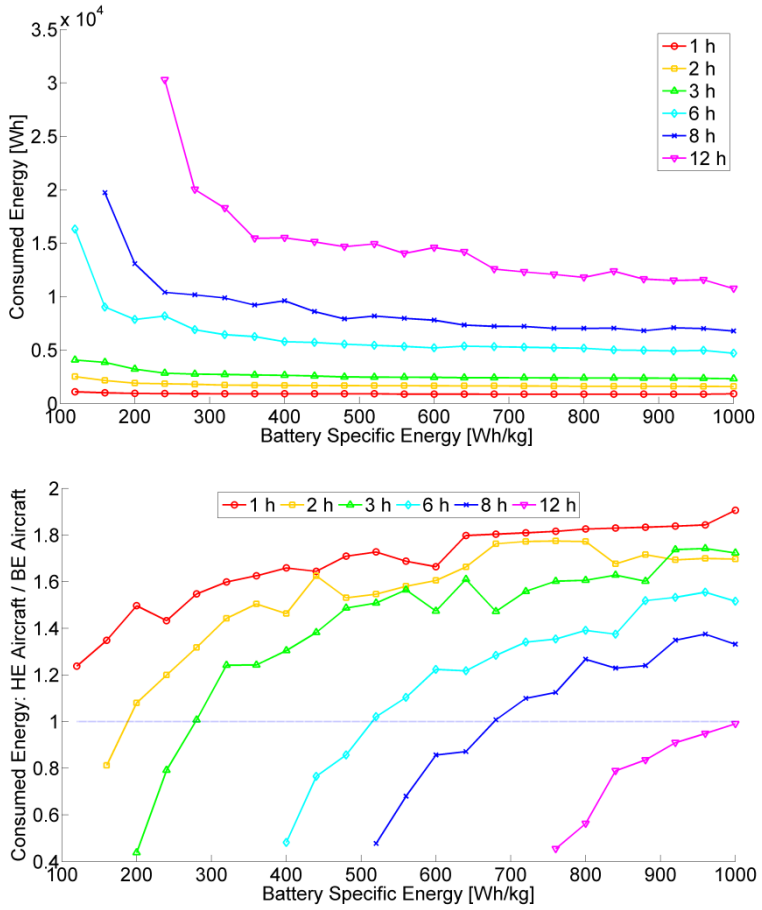

Figure 75: Absolute consumed energy of hybrid-electric aircraft (top) and consumed energy ratio of HE to BE aircraft (bottom) over varying battery specific energy

Table 14: Threshold specific energies, above which BE aircraft are more energetically efficient that HE aircraft

Flight Time [h]	Threshold Specific Energy [Wh/kg]
1	< 100
2	200
3	280
6	520
8	680
12	1000

4.3.3 Variation of the Mass

Analyzing the effect of mass changes on an aircraft is relevant in preliminary design, as it enables quick assessment of mass variations in the airframe or system components. For the analysis presented here, payload was varied, but the results may

be applied to other elements, as for example the coupling, for which no mass prediction method is included in the design method. A payload delta range of 0 kg to 5 kg in 0.5 kg increments was added to the 10 kg baseline payload. The electric flight time ratio is set to 0.25.

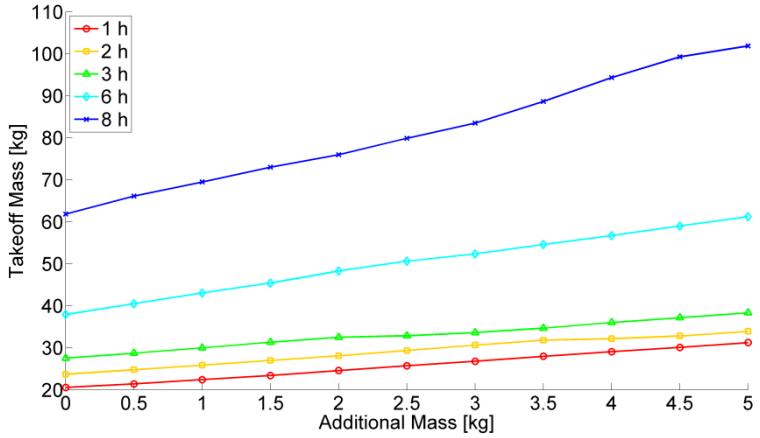

Figure 76: Hybrid-electric aircraft takeoff mass over varying additional mass

The takeoff mass resulting from the additional payload is plotted in Figure 76. A hybrid-electric aircraft is not capable of flying a 12 h mission with electric flight time ratio of 0.25 under the takeoff mass restriction of 150 kg. Therefore only flight times of 1 h, 2 h, 3h, 6 h and 8 h are considered. Takeoff mass rises approximately linearly with the increase in additional mass. The ratio of the takeoff mass increment to the additional mass increment, visible as the curves' gradients in Figure 76, is the aircraft growth factor. The aircraft growth factors increase with flight time.

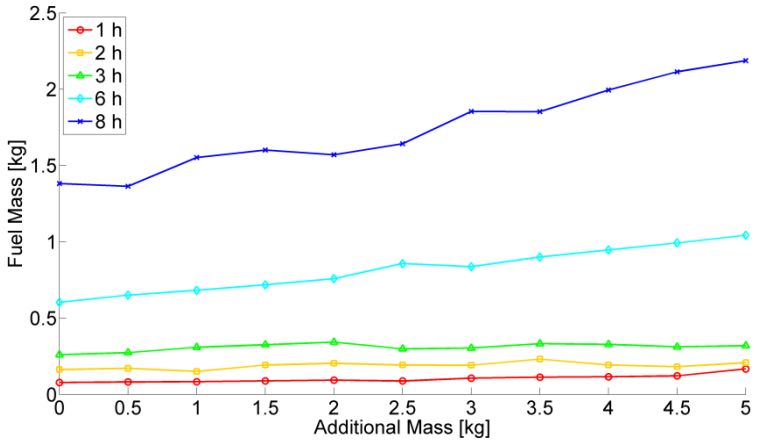

Figure 77: Fuel mass of hybrid-electric aircraft over varying additional mass

The necessary fuel mass in Figure 77 rises approximately linearly, but not monotonously. For the 6 h flight time mission a relatively linear curve is computed, whereas those for the other flight times show the ripples observed in fuel mass curves throughout this chapter. Decrease in fuel mass with increasing additional mass, for example visible for the 3 h flight time mission at the change from 2 kg to 2.5 kg, are

caused by the change from a fast-turning system to slow-turning, more efficient system with heavier power converters.

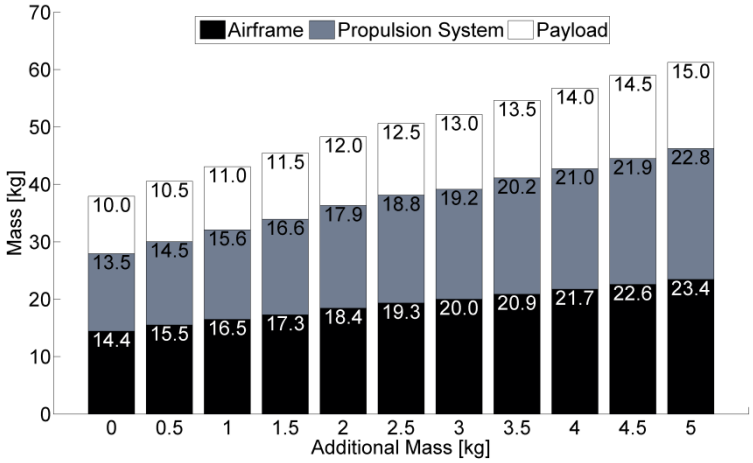

Figure 78: Mass distribution of hybrid-electric aircraft over varying additional mass (6 h mission)

The effect of the additional mass on the aircraft mass distribution is shown in Figure 78 for the 6 h mission. The 6 h mission is chosen due to its linear fuel mass curve. The aircraft optimized for a 6 h mission hence may be discussed with less distracting influence of the propulsion system rotational velocity changes. The three groups that contribute to takeoff mass according to (6) are the airframe, payload and the propulsion system. Their takeoff mass fractions stay unchanged for the mass increase, so that each group's mass increases uniformly.

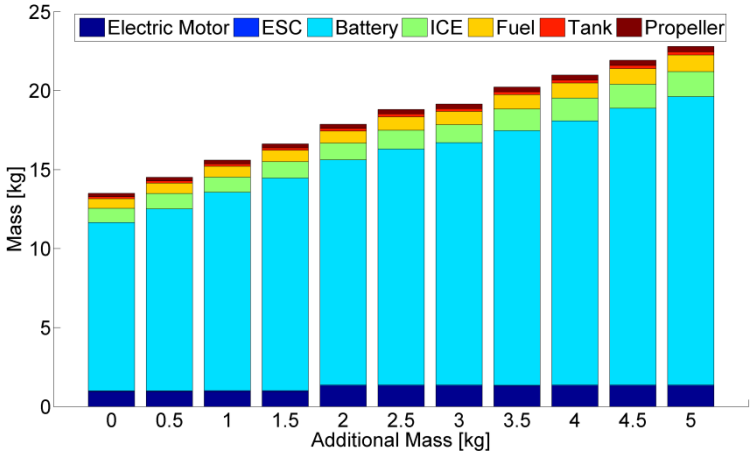

Figure 79: Propulsion system mass distribution of hybrid-electric aircraft over varying additional mass (6 h mission)

For the airframe, a constant mass fraction is immanent in the design method. Payload is directly defined by the additional mass. The effect on the third group, the propulsion system and its components is shown in the mass distribution in Figure 79. The corresponding values are provided in Table 15. The increments of discrete changes, clearly visible for example for the electric motor mass, are governed by the discretization. The component mass fractions of the propulsion system mass

nevertheless are reasonably constant with mass increase. Relative deviations from the average fraction value stay below 13 %.

Table 15: Propulsion system component masses for the 6h mission in [kg]

Additional Mass	Electric Motor	ESC	Battery	ICE	Fuel	Tank	Propeller
0	0.96	0.04	10.66	0.90	0.60	0.14	0.21
0.5	0.96	0.04	11.51	0.98	0.65	0.15	0.22
1.0	0.96	0.05	12.55	0.97	0.68	0.15	0.24
1.5	0.96	0.05	13.46	1.04	0.72	0.16	0.25
2.0	1.30	0.06	14.26	1.06	0.76	0.16	0.27
2.5	1.30	0.06	14.95	1.18	0.86	0.18	0.28
3.0	1.30	0.06	15.35	1.14	0.84	0.18	0.29
3.5	1.30	0.05	16.11	1.38	0.90	0.19	0.30
4.0	1.30	0.05	16.73	1.45	0.95	0.20	0.31
4.5	1.30	0.06	17.53	1.51	0.99	0.21	0.32
5.0	1.30	0.06	18.26	1.59	1.04	0.21	0.33

From the change of the component masses, a component growth factor may be determined analogously to the aircraft growth factor. It quantifies the mass increment of this component per increase of the payload. Figure 80 shows the aircraft growth factor, the airframe and propulsion system growth factor as well as those for each propulsion system component. Every growth factor increases with flight time. For flight times of 8 h and higher, the propulsion system growth factor exceeds that of the airframe. The propulsion system mass hence has increasing influence on the aircraft takeoff mass over flight time. Of the propulsion system growth factors, that of the battery significantly exceeds the others, coinciding with the prior insight of the battery being the main contributor to propulsion system mass. Electric motor, internal combustion engine and fuel are identified as further components with high growth factors. The fuel growth factor grows quicker over flight time than that of the power converters, which confirms the increasing contribution of energy storages with flight time in comparison to energy converters.

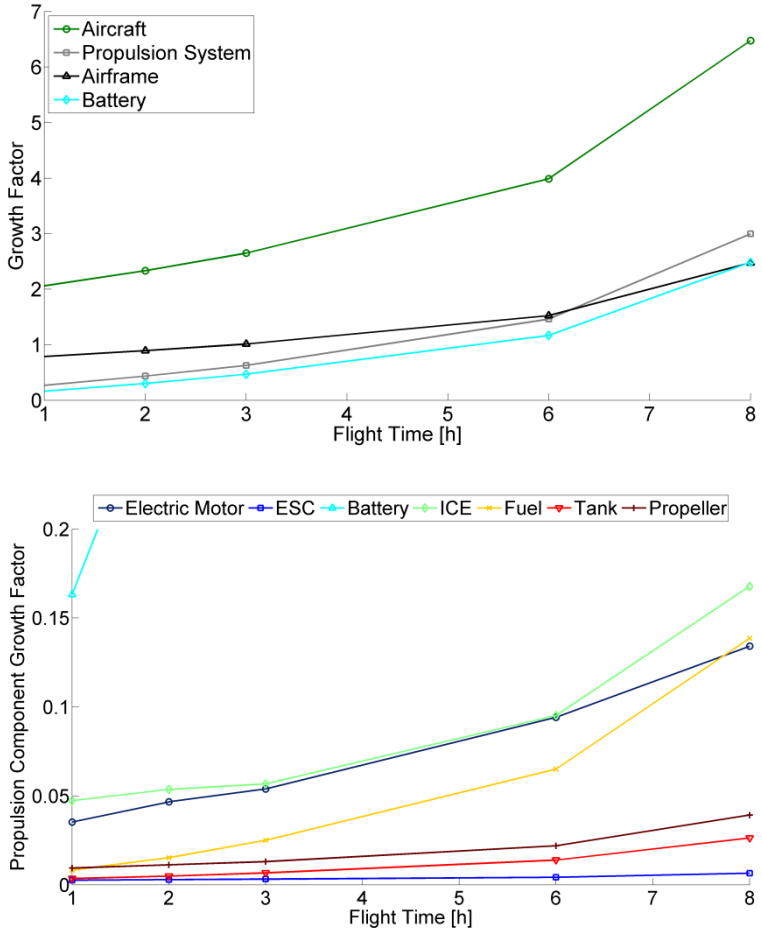

Figure 80: Growth factors of the main aircraft groups (top) and the propulsion groups (bottom)

5 SUMMARY AND OUTLOOK

5.1 Capabilities and Limitations of the Design Method

In this study, a design method for small unmanned aerial vehicles with hybrid-electric propulsion system is developed. The method's core functionality is a propulsion system design procedure, which allows the design and optimization of the propulsion system for prescribed operational requirements. It has been integrated into an aircraft design process based on the scaling of an existing reference aircraft.

The method fulfills three main demands: high accuracy, generality and low computational time consumption. Accuracy is improved, in comparison to existing power-based design methods, by developing models based on state variables. They allow the assessment of a propulsion component's state of operation. Based on that, a more valid estimation of efficiency is possible. The computation time required by the method is kept low with the wide use of surrogate models instead of time-consuming computational operations such as interpolations or file handling. The surrogate models in most cases are created with the help of regression functions from databases of commercial-off-the-shelf components. The databases do not only contribute to the validity of the models, but also to generality, as they were selected to cover the complete anticipated requirement space. In order to satisfy both aspects, generality and low computational time, a discrete use of the databases was discarded in favor of continuous surrogate models. The models used in the design procedure are limited to the class of small unmanned aerial vehicles with takeoff masses of below 150 kg.

The propulsion system design procedure is composed of component modules. A module contains a mass prediction model and, where applicable, an efficiency estimation model. The models applied were either developed in this study or integrated from other publications. The propeller module combines an existing mass prediction with a performance model. The performance model interpolates data from look-up tables, which are created outside of the design process in a design of experiment using XROTOR, an implementation of the vortex theory. A surrogate model based on polynomial fits does not return sufficiently accurate results and is therefore discarded in favor of interpolation. The propeller performance model is by far the most time-consuming model in the propulsion system design procedure. Consequently it offers the biggest potential for acceleration. One future option might be a neural network model. The coupling is treated as an ideal distributor of torque and rotational velocity. Thus the coupling module could reasonably be enhanced with mass and efficiency estimation models in the future. The internal combustion engine module consists of a mass model derived from a database of commercial engines and an efficiency

estimation model. The latter scales a normalized baseline efficiency map. The scaling model is based on the perquisites that the wide-open throttle curve and the efficiency at a point of operation defined by the normalized mean-value variables for torque and rotational velocity is unchanged by the variation of engine size. Both assumptions are proven to be acceptably valid with operational data of commercial engines. Nevertheless, the model could be significantly improved if more data on small engine efficiency was available. The engine design variables could then be used to select the most suitable baseline efficiency map for each application.

In the electric motor module an existing electric model is augmented with a newly developed motor characteristics estimation model. The motor characteristics model computes the figures of merit for the electric motor loss mechanisms from the design variables. It was derived from a database of commercial electric motors. The employed formulation of the loss mechanisms is valid only for aircraft model motors and small industrial motors. The model therefore must be extrapolated to higher power levels. The extrapolation however is reasonable, as no step changes occur in the database and as there is no technological obstacle for the motors to be scaled bigger. Although the model was derived with high coefficients of determination, an even more accurate formulation may be possible if more data on commercial electric motors were published, namely the wire gauges and the number of pole pairs and stator teeth. The electric motor module also contains a mass prediction model derived from the motor database. A mass estimation model for electronic speed controllers is derived from a database of commercial controllers. Additionally, a previously published efficiency model is reformulated. Its formulation is based on internal resistances and part-load factors determined experimentally. For both parameters no prediction rules can be derived due to the limited number of units measured in experiments. Therefore the data of one widely applicable controller is used globally. The model would gain validity if in a future work prediction functions for the part-load factor and internal resistance were derived from further experimental data. The battery mass prediction model developed in this study incorporates the influence of maximum discharge current on battery mass. An according mass law is derived from a database of commercial Lithium-polymer batteries. The battery module furthermore considers battery efficiency and the practical aspect that only an integer number of battery cells may be combined to a battery pack. For efficiency estimation, an existing two-dimensional model is applied to the battery database and re-formulated in a one-dimensional function.

The propulsion system design procedure is integrated into an aircraft design framework. In the design framework the aircraft is not designed from scratch, but a reference aircraft is scaled. The design process runs in iterations until the computed

takeoff mass converges. The concept of scaling an aircraft is primarily motivated by the emphasis of this study on propulsion system trends. Scaling an aircraft eliminates the influence of varying geometry and aerodynamics on the results and allows a clearer view on the propulsion system's impact, capabilities and limits. Nevertheless, scaling is a source for inaccuracies, especially when the scaling reference and the requirements for the new aircraft vary strongly. This could be improved by integrating the propulsion system design process into an advanced unmanned aircraft design environment, as for example developed by RÖßLER (2011) for fuel cell and battery-electric aircraft.

The design process includes the determination of an optimum propulsion system. The optimization scheme is only applied to the propulsion system design procedure. This set-up evolved from the imperative of short computational time, which prohibits an inclusion of the time-consuming mission simulation into the full-factorial optimization process. Two issues are implied: First, the fuel mass evaluated by the optimization process is computed without consideration of the aircraft mass change caused by fuel burn. Second, optimization does not foresee the effect of its selection on any aircraft property. The mass cascade effect that the selected propulsion system has on takeoff mass and the power requirement in the next iteration loop of the design process is not incorporated. The optimization therefore does not result in a global minimization of the cost function, but only in a minimization for the current iteration loop. It was identified that propulsion system mass as cost function returns the minimum takeoff mass. The alternatively analyzed fuel mass cost function optimization returns slightly lower fuel masses for some requirements, but for high electric flight times the results cascade to significantly higher takeoff and fuel masses. Possible improvements may consist of a multiple-objective optimization in its current capsulated form or a reduction of computation time to such extent that an optimization algorithm may be applied to the complete aircraft design process.

The propulsion system mass as cost function and the relatively coarse discretization of the design variables result in unsmooth curves for the energy storage masses. This is especially visible where the optimizer changes from a fast-turning system with low efficiency to a slow-turning system with higher efficiency and consequently lighter energy storages. These changes occur when the lighter energy storages of a slow-turning system contribute more to a low propulsion system mass than the lighter power units of a fast-turning system with low torque demand.

5.2 Assessment of the Hybrid-Electric Propulsion System

The developed design method was applied to compare aircraft with hybrid-electric, battery-electric and internal combustion engine propulsion systems. An evaluation was

conducted analyzing aircraft takeoff mass, fuel and energy consumption, and the mass distribution for an exemplary surveillance mission. The requirement space for the analysis is defined by a payload range of 10 kg to 70 kg and a flight time range of 1 h to 12 h, whereas the velocity is kept constant at 20 m/s. For an analysis of hybrid-electric aircraft's sensitivity to varying electric flight time ratio, battery specific energy and additional mass a payload of 10 kg and flight times of 1 h, 2 h, 3 h, 6 h, 8 h and 12 h have been considered.

In the defined requirement space, takeoff mass increases with the electric flight time ratio. It is consequently highest for battery-electric aircraft and lowest for internal combustion engine aircraft. The takeoff mass of hybrid-electric aircraft is in between. The mass fractions do not significantly change for varying payloads. This leads to uniform mass gain of all components with payload increase. The propulsion system mass fraction increases with flight time, whereas the payload fraction decreases. The propulsion mass fraction gradient over flight time increases with EFTR. For all aircraft using electric propulsion, the battery is the biggest contributor to propulsion system mass. Its fraction rises with flight time and electric flight time ratio. The fuel mass fraction falls below 5 % of propulsion system mass in the hybrid-electric aircraft. The aircraft growth factor and the component growth factors increase with flight time and quantify the rising contribution of the energy storages and generally the propulsion system to takeoff mass.

Hybrid-electric aircraft optimized for an electric flight time ratio of 0.25 are more fuel efficient than internal combustion engine aircraft for flight times below 5 h 30 min. This threshold flight time is reduced when increasing electric flight time ratios to 0.50 and 0.75. For the 10 kg payload case, the EFTR sensitivity study shows that fuel economy is best if one of the two integrated power units is only used as a booster for climb. Below 3 h flight time the internal combustion engine should be used as a booster. For longer mission the use of the electric motor as booster provides for minimum fuel consumption. The partially lower fuel consumption of hybrid-electric aircraft has three drivers. The dual-use of electric motor and internal combustion engine at the maximum power demand has two impacts: First, the lower torque demand allows a downsizing of the power units compared to a conventional use, which makes them lighter. Second, the torque demand in the climb and cruise phase is better balanced. This allows a more efficient use of the internal combustion engine, which works most efficient at full load. In conventional use, full load is demanded during the short maximum power phase, whereas the engine works less efficient at a lower torque operating point in the long cruise phase. The degree of hybridization defines the interaction of both power units during climb as ratio of electric motor shaft power to total shaft power. It takes values from 0.5 to 0.7. The third contributor to fuel

economy is the shorter use of the internal combustion engine, as during the portion of cruise defined by the EFTR the aircraft is powered only by the electric motor. All contributors to fuel economy are also advantageous for energy economy. The differences in the fuel and energy consumption characteristics result from the additional electric energy consumption in hybrid-electric aircraft. It reduces the flight times, below which hybrid-electric aircraft are more energy efficient than internal combustion engine aircraft, to lower values than for fuel consumption. An electric motor is more efficient than an internal combustion engine, so that the ratio of electric energy to total energy consumption is lower than the electric flight time ratio. In the 10 kg payload case, a battery-electric aircraft is most energy efficient for a 1 h mission. For longer flight times the lowest energy consumption is obtained with a use of the electric motor only as booster for climb. In all comparisons with the internal combustion engine, it has to be kept in mind that an engine does not have the capability to operate as silent as battery-electric or hybrid-electric systems. An ICE aircraft can therefore not accomplish the surveillance mission as desired.

Hybrid-electric aircraft offer advantages in two fields. First, they allow the combination of high-speed or long-enduring, energy-intensive mission phases with the capability to operate more silent in electric flight phases. This makes them highly suitable for surveillance missions. Second, for certain requirements discussed above, they allow to carry out missions more fuel and energy efficient than with conventional propulsion systems.

An outlook for the hybrid-electric propulsion system may be based on the analysis of increasing battery specific energy for the 10 kg case. At the maximum specific energy of 1000 Wh/kg the hybrid-electric aircraft are more fuel and energy efficient than ICE aircraft for all considered flight times. The difference in takeoff mass is reduced to 12 % for a 12 h mission. The battery-electric aircraft, characterized by the highest overall propulsion efficiency, are even more energetically favorable at this technology level. For the 1 h mission also its takeoff mass is below that of the corresponding hybrid-electric aircraft. The battery-electric takeoff mass however shows a steeper increase with flight time than the hybrid-electric takeoff mass. The longevity of hybrid-electric propulsion systems as a transition technology between internal combustion engine propulsion and battery-electric propulsion is strongly dependent on future improvements in battery technology. A further increase of specific energy will lead to an applicability of the identified advantages of the battery-electric propulsion systems to a wider requirement space.

REFERENCES

ADKINS C.N. & LIEBECK R.H., 1994. Design of Optimum Propellers. *Journal of Propulsion and Power*, 10 (5), pp. 676-682

ANDERSON, J.D., 1999. *Aircraft Performance and Design*, Boston: WCB/McGraw-Hill

AUSSERER, J.K. & HARMON, F.G., 2012. Integration, Validation, and Testing of a Hybrid-Electric Propulsion System for a Small Remotely-Piloted Aircraft. In: *10th AIAA International Energy Conversion Engineering Conference*, Atlanta, USA, 29 July – 1 August 2012

BAGASSI, S., BERTINI, B., FRANCIA, D. & PERSIANI, F. Design Analysis for Hybrid Propulsion, *28th International Congress of the Aeronautical Sciences*, Brisbane, Australia, 23-28 September 2012

BALLHAUS, 1954. *Clear Design Thinking Using the Aircraft Growth Factor*, SAE Technical Paper 540148

BETZ, A., 1919. Schraubenpropeller mit geringstem Energieverlust. *Nachrichten der Königlichen Gesellschaft der Wissenschaften zu Göttingen*. Mathematisch-physikalische Klasse 1919, pp. 198-217

CADOU, C. & MENON, S., Scaling of Losses in Small IC Aero Engines with Engine Size, *42nd AIAA Aerospace Sciences Meeting and Exhibit*, Reno, USA, 5-8 January 2004

CHRISTENSEN. J. ET AL., 2012. A Critical Review if Li/air Batteries. *Journal of the Electrochemical Society*, 159 (2), pp. R1-R30

DESCHENES, A., BROWN, K., SOBIN, A. & WEST, G., 2011. Design, Construction, and Testing of RC Aircraft for a Hybrid Propulsion System, *49th AIAA Aerospace Sciences Meeting including the New Horizons Forum and Aerospace Exhibition*, Orlando, USA, 4-7 January 2011

DEUTSCHER BUNDESTAG, 2011. *Entwurf eines Vierzehnten Gesetzes zur Änderung des Luftverkehrsgesetzes*, Drucksache 17/8098

DRELA, M., 2006a. Second-Order DC Electric Motor Model. [online] Cambridge, MA: MIT Aero & Astro. Available at: <http://web.mit.edu/drela/Public/web/qprop/motor2_theory.pdf> [Accessed 30 September 2013]

DRELA, M., 2006b Qprop Formulation. [online] Cambridge, MA: MIT Aero & Astro. Available at: < http://web.mit.edu/drela/Public/web/qprop/qprop_theory.pdf> [Accessed 30 September 2013]

DRELA, M., 2007. First-Order DC Electric Motor Model. [online] Cambridge, MA: MIT Aero & Astro, 2007. Available at: <http://web.mit.edu/drela/Public/web/qprop/motor1_theory.pdf> [Accessed 30 September 2013]

EAGLE FLIGHT RESEARCH CENTER, 2011. The Eco-Eagle [online] Available at: <http://embryriddle.wix.com/greenflight3#!__eagle-flight-research-center/the-eco-eagle> [Accessed 21 January 2013]

EHSANI, M., GAO, Y., GAY, S.E. & EMADI, A., 2005. *Modern Electric, Hybrid Electric, and Fuel Cell Vehicles*. Boca Raton: CRC Press

FILIPI, Z.S. & ASSANIS, D.N., 2000. The effect of the stroke-to-bore ratio on combustion, heat transfer and efficiency of a homogeneous charge spark ignition engine of given displacement. *International Journal of Engine Research*, 1 (2), pp. 191-208.

FLIGHT DESIGN, 2010. Viable Innovation – Hybrid Drive Propels Light Aircraft. Press release, 09 April 2010

GLASSOCK, R., HUNG, J.Y., GONZALEZ, L.F. & WALKER, R.A., 2007. Design, Modelling and Measurement of Hybrid Powerplant for Unmanned Aerial Systems (UAS), *5th Australasian Congress on Applied Mechanics*, Brisbane, Australia, 10-12 December 2007.

GLASSOCK, R., HUNG, J.Y., GONZALEZ, L.F. & WALKER, R.A., 2009. Multimodal Hybrid Powerplant for Unmanned Aerial Systems (UAS) Robotics, *24th Bristol International Unmanned Air Vehicle Systems Conference*, Bristol, United Kingdom, 30 March – 1 April 2009.

GOLDSTEIN, S., 1929. On the vortex theory of screw propellers. Proceedings of the Royal Society London, 123 (792): pp. 440-465

GREISER, C.M., MENGISTU, I.H., ROTRAMEL, T.A. & HARMON, F.G., 2011. Testing of a Parallel Hybrid-Electric Propulsion System for use in a Small Remotely-Piloted Aircraft, *9th AIAA Annual International Energy Conversion Engineering Conference*, San Diego, USA, 1-3 August 2011.

GUNDLACH, J., 2012. *Designing Unmanned Aircraft Systems – A comprehensive approach*. Reston, VA: American Institute of Aeronautics and Astronautics

GUR, O., & ROSEN, A., 2009a. Optimization of Propeller Based Propulsion System. *Journal of Aircraft*, 46 (1), pp. 95-106.

GUR, O. & ROSEN, A., 2009b. Optimization of Electric Propulsion Systems for Unmanned Aerial Vehicles. *Journal of Aircraft*, 46 (4), pp. 1340-1353.

GUZZELLA L. & ONDER C., 2010. *Introduction to Modeling and Control of Internal Combustion Engine Systems*. 2nd ed. Berlin: Springer Verlag

HANSELMANN, D., 2006. *Brushless Permanent Magnet Motor Design*. 2nd ed. Lebanon, OH: Magna Physics Publishing

HARMATS, M. & WEIHS, D., 1999. Hybrid-Propulsion High-Altitude Long-Endurance Remotely Piloted Vehicle. *Journal of Aircraft*, 36 (2), pp. 321-331

HARMON, F.G., 2005. *Neural Network Control of a Parallel Hybrid-Electric Propulsion System for a Small Unmanned Aerial Vehicle*. Ph. D. University of California Davis

HARMON, F.G., FRANK, A.A. & CHATTOT, J.-J., 2006. Conceptual Design and Simulation of a Small Hybrid-Electric Unmanned Aerial Vehicle. *Journal of Aircraft*, 43 (5), pp. 1490-1498.

HARMON, F.G., FRANK, A.A. & JOSHI, S.S., 2005. The control of a parallel hybrid-electric propulsion system for a small unmanned aerial vehicle using CMAC neural network, *Neural Networks*, Vol. 18, pp. 772-780.

HEMIGHAUS ET AL, 2006. Aviation Fuel Technical Review. Houston: Chevron Global Aviation

HENDRICKSON, S. P., MCGEER, T. 1999. *A Miniature Powerplant for Very Small, Very Long Range Autonomous Aircraft*. Final Report to the United States Department of Energy under contract number DE-FG03-96ER82187, Bingen, WA

HEYWOOD, J.B., 1988. *Internal Combustion Engine Fundamentals*, New York: McGraw-Hill Book Company

HIRLING O. & HOLZAPFEL, F., 2012. State of the Art UAS Airworthiness Regulations in Contrast to Alternative Certification Methods. *6th UAV World*. Frankfurt am Main, Germany, 6-8 November 2012

HISEROTE, R.M., 2010. *Analysis of hybrid-electric propulsion system designs for small unmanned aircraft systems*. Master Thesis. Air Force Institute of Technology

HISEROTE, R.M. & HARMON, F.G., 2010. Analysis of Hybrid-Electric Propulsion System Design for Small Unmanned Aircraft Systems. *8th AIAA Annual International Energy Conversion Engineering Conference*, Nashville, USA, 25-28 July 2010.

HUNG, J.Y. & GONZALEZ L.F., 2012a. Design, Simulation and Analysis of a Parallel Hybrid Electric Propulsion System for Unmanned Aerial Vehicles, *28th International Congress of the Aeronautical Sciences*, Brisbane, Australia, 23-28 September 2012

HUNG, J.Y. & GONZALEZ, L.F., 2012b. On parallel hybrid-electric propulsion system for unmanned aerial vehicles, *Progress in Aerospace Sciences*, 51 (2012), pp. 1-17

HÜNERSDORFF GMBH, n.d. Products [online] Available at: <http://www.huenersdorff.de/en/products.html> [Accessed 07 September 2013]

HUß, M., HÜBNER, W. & WACHTMEISTER, G., 2010. Scaling Functions for the Simulation of Different SI-Engine Concepts in Conventional and Electrified Power Trains. *GT-Suite Users Conference*, Frankfurt, Germany, 25 October 2010

KEIDEL, B., 2000. *Auslegung und Simulation von hochfliegenden, dauerhaft stationierbaren Solardrohnen*. Ph. D. Technische Universität München

KÖHLER, U., 2008. Battery System for Smart Electric Vehicles, Presented at: *EPoSS Seminar Brussels*, Brussels, Belgium, 26 June 2008

KOSTER, J. ET AL., 2011. Hybrid Electric Integrated Optimized System (HELIOS) – Design of a Hybrid Propulsion System for Aircraft. *49th AIAA Aerospace Sciences Meeting including the New Horizons Forum and Aerospace Exhibition*, Orlando, USA, 4-7 January 2011

KUHN, H., SIZMANN, A., 2012. Fundamental Prerequisites for Electric Flying. *Deutscher Luft- und Raumfahrtkongress 2012*, Berlin, Germany, 10 – 12 September 2012

LARRABEE E.E. & FRENCH S.E., 1983. Minimum induced loss windmills and propellers. *Journal of Wind Engineering and Industrial Aerodynamics*, 15 (1-3), pp. 317-327.

LIEH, J., SPAHR, E., BEHBAHANI, A. & HOYING, J., Design of Hybrid Propulsion Systems for Unamnned Aerial Vehicles. *47th AIAA/ASME/SAE/ASEE Joint Propulsion Conference & Exhibit*, San Diego, USA, 1-3 August 2011

LINDEN, D., 2011. *Handbook of Batteries*. 3rd ed. New York: McGraw-Hill Professional

LUNDSTRÖM, D., AMADORI, K. & KRUS, P., 2010. Validation of Models for Small Scale Electric Propulsion Systems. *48th AIAA Aerospace Sciences Meeting*

including the New Horizons Forum and Aerospace Exhibition, Orlando, USA, 4-7 January 2010

MCELROY, T. & LANDRUM, D.B., 2012. Simulated High-Altitude Testing of a COTS Electric UAV Motor. *50th AIAA Aerospace Sciences Meeting including the New Horizons Forum and Aerospace Exhibition*, Nashville, USA, 9-12 January 2012

MENON, S. & CADOU, C., 2007. Experimental and computational investigations of small internal combustion engine performance. *5th US Combustion Meeting*, San Diego, USA, 25-28 March 2007

MENON, S., MOULTON, N. & CADOU, C., 2007. Development of a Dynamometer for Measuring Small Internal Engine Combustion Engine Performance. *Journal of Propulsion and Power*, 23 (1), pp. 194-202.

MOFFIT, B.A., 2010. *A methodology for the validated design space exploration of fuel cell powered unmanned aerial vehicles*. Ph. D. Georgia Institute of Technology

NOTH, A. 2008. *Design of Solar Powered Airplanes for Continuous Flight*. Ph.D. Eidgenössische Technische Hochschule Zürich

PAULUS, D., RÖßLER C., SCHÖMANN, J., SCHWARZE M. & SPECK, S. 2010. *FAT Flying UAV SW Demonstrator – A/V Design Description*. Technical Report LS-TB-11/04, München: Lehrstuhl für Luftfahrtsysteme der Technischen Universität München

PHILIPS, W.F., 2009. *Mechanics of Flight*. 2nd ed. Hoboken, NJ: John Wiley & Sons, Inc.

QINETIQ, n.d. QinetiQ's Zephyr UAV exceeds official world record for longest duration unmanned flight [online] Available at: http://www.qinetiq.com/news/pressreleases/Pages/qinetiqs-zephyr-exceeds-world-record.aspx [Accessed 08 August 2013]

REILLY, D., ANDERSEN, R., CASPARIAN, R. & DUGDALE P., 1991. *Saturn DOHC and SOHC Four Cylinder Engines*. SAE Technical Paper 910676

RETZBACH, L., 2008. *Akkus und Ladetechniken*. Poing: Franzis Verlag GmbH

RETZBACH, L., n.d. *Brushless-Fibel – Funktion, Eigenschaften, Bauformen und Einsatzbeispiele von bürstenlosen Elektromotoren*. Bonn: Deutscher Modellflieger Verband

RIZZONI, G., GUZZELLA, L. & BAUMANN, B.M., 1999. Unified Modeling of Hybrid Electric Vehicle Drivetrains. *IEEE/ASME Transaction on Mechatronics*, 4 (3), pp. 246-256.

RÖßLER, C.O., 2011. *Conceptual Design of Unmanned Aircraft with Fuel Cell Propulsion System*. Ph.D. Technische Universität München

SAHA B. & GOEBEL K., 2009. Modelling Li-ion Battery Capacity Depletion in a Particle Filtering Framework. *Annual Conference of the Prognostics and Health Management Society 2009*, San Diego, USA, 27 September – 1 October 2009

SEITZ, A., SCHMITZ, O., ISIKVEREN, A.T., & HORNUNG, M., 2012. Electrically Powered Propulsion: Comparison and Contrast to Gas Turbines. *Deutscher Luft- und Raumfahrtkongress 2012*, Berlin, Germany, 10 – 12 September 2012

SCHOEMANN, J., 2011. *DemUEB Phase 3 Statusbericht zu WP3911: State-of-the-art hybrider Antriebssysteme für UAVs*, Technical Report LS-TB-11/04, München: Lehrstuhl für Luftfahrtsysteme der Technischen Universität München

SCHOEMANN, J., 2012. *DemUEB Phase 3 Abschlussbericht zu WP3911*, Technical Report LS-TB-12/07, München: Lehrstuhl für Luftfahrtsysteme der Technischen Universität München

SCHOEMANN, J. & HORNUNG, M., 2012. Modeling of Hybrid-Electric Propulsion Systems for Small Unmanned Aerial Vehicles. *12th AIAA Aviation Technology, Integration and Operations and 14th AIAA/ISSMO Multidisciplinary Analysis and Optimization Conference*, Indianapolis, USA, 17-19 September 2012

SCHOEMANN, J. & HORNUNG, M., 2013. Design of hybrid-electric propulsion systems for small unmanned aerial vehicles. *5th European Conference for Aeronautics and Space Sciences*, Munich, Germany, 1-5 July 2013

SIEMENS, 2011. World's first serial hybrid electric aircraft to fly at Le Bourget [press release], 20 June 2011, Available at: <http://www.siemens.com/press/en/pressrelease/?press=/en/pressrelease/2011/corporate_communication/axx20110666.htm> [Accessed 30 September 2013]

SIEMENS, 2013. Le Bourget: Electric Hybrid Drives for Aircraft [press release] n.d., Available at: <http://www.siemens.com/innovation/en/news/2013/e_inno_1318_1.htm> [Accessed 30 September 2013]

SION POWER, n.d. Technology Overview [online] Available at: <http://www.sionpower.com/technology.html> [Accessed 30 September 2013]

SPECK, S., WILBERG, J. & HORNUNG, M., 2013. An Approach for Aeroacoustic Footprint-Modeling of Low Altitude Platforms by Means of Time Domain System Identification, *12th AIAA Aviation Technology, Integration and Operations Conference*, Los Angeles, USA, 12-14 August 2013

SPECK, S., PFEFFERKORN, J., KICKER, K. & HORNUNG, M., 2013. Methoden zur Bewertung und Minimierung der Signatur von unbemannten Flugzeugen. *Deutscher Luft- und Raumfahrtkongress 2013*, Stuttgart, Germany, 10-12 September 2013

THEODORSEN, T., 1948. *Theory of propellers.* New York: McGraw-Hill Book Company

THIELMANN, A., SAUER, A., ISENMANN, R., WIETSCHEL, M., PLÖTZ, P., 2012. Produkt-*Roadmap Lithium-Ionen-Batterien 2030*. Karlsruhe: Fraunhofer-Institut für System- und Innovationsforschung ISI

UVS INTERNATIONAL, n.d. Remotely Piloted Aircraft Systems – The Global Perspective 2012/2013 [online] Available at: <http://www.uvs-info.com/> [Accessed 13 November 2012]

VOLKSWAGEN AG, 2013. *The Audi A1 e-tron in "Electromobility Showcase" projects*. [Press release] 10 June 2013, Available at: http://www.volkswagenag.com/content/vwcorp/info_center/en/news/2013/06/Electromobility_Showcase.html [Accessed 12 September 2013]

VOLTAVOLARÉ, 2012. Volta Volaré GT4 The world's most efficient high-performance aircraft. [online] Available at: <http://www.voltavolare.com/> [Accessed 21 January 2013]

WALD, Q.R., 2006. The aerodynamics of propellers. *Progress in Aerospace Sciences*, 42 (2006), pp. 85-128

WEINOWSKI, R. ET AL, Future downsizing of SI engines – potentials and limits of 2- and 3-cylinder concepts. *30. Internationales Wiener Motorensymposium*, Vienna, Austria, 7-8 May 2009.

PUBLICATIONS WITHIN THIS STUDY

SCHOEMANN, J., 2011. *DemUEB Phase 3 Statusbericht zu WP3911: State-of-the-art hybrider Antriebssysteme für UAVs*, Technical Report LS-TB-11/04, München: Lehrstuhl für Luftfahrtsysteme der Technischen Universität München

SCHOEMANN, J., 2012. *DemUEB Phase 3 Abschlussbericht zu WP3911*, Technical Report LS-TB-12/07, München: Lehrstuhl für Luftfahrtsysteme der Technischen Universität München

SCHOEMANN, J. & HORNUNG, M., 2012. Modeling of Hybrid-Electric Propulsion Systems for Small Unmanned Aerial Vehicles. *12th AIAA Aviation Technology, Integration and Operations and 14th AIAA/ISSMO Multidisciplinary Analysis and Optimization Conference*, Indianapolis, USA, 17-19 September 2012

SCHOEMANN, J. & HORNUNG, M., 2013. Design of hybrid-electric propulsion systems for small unmanned aerial vehicles. *5th European Conference for Aeronautics and Space Sciences*, Munich, Germany, 1-5 July 2013

ABBREVIATIONS AND SYMBOLS

Abbreviations

BC	Bottom Center
BE	Battery-Electric
BLDC	Brushless Direct-Current
CC	Charging Cruise
CFRP	Carbon Fiber Reinforced Plastics
CI	Compression-Ignited
COTS	Commercial Off-The-Shelf
DC	Direct-Current
DoH	Degree of Hybridization
EF	Electric Flight
EFTR	Electric Flight Time Ratio
EM	Electric Motor
EMC	Electromagnetic Compatibility
EMF	Electromagnetic Force
ESC	Electronic Speed Controller
GB	Gigabyte
HE	Hybrid-Electric
HTS	High-Temperature Superconductors
ICE	Internal Combustion Engine
LHV	Lower Heating Value
MEP	Mean Effective Pressure
MP	Maximum Power
MTOM	Maximum Takeoff Mass
MTOW	Maximum Takeoff Weight
OCV	Open-Circuit Voltage
RAM	Random-Access Memory
RC	Regular Cruise
RoC	Rate of Climb
SI	Spark-Ignited
TC	Top-Center
UAV	Unmanned Aerial Vehicle
WOT	Wide-Open Throttle

Greek Symbols

ε	Convergence Criterion
η	Efficiency
ρ	Density
ρ_{wire}	Electric Resistivity
ω	Rotational Velocity (in radians per second)

Symbols

A_{wire}	Wire Gauge
B	Cylinder Bore
C	Electric Capacity
c_{I0}	No-Load Current Coefficient
c_L	Lift Coefficient
c_m	Mean Piston Speed
c_Q	Torque Coefficient
c_{Ri}	Internal Resistance Coefficient
c_T	Thrust Coefficient
d	Electric Motor Diameter
$d_{propller}$	Propeller Diameter
E	Lift-to-Drag Ratio
e	Thermal efficiency of the ICE
E_{cell}	Cell Energy
g	Gravity Constant
H_{LV}	Lower Heating Value
I	Current
I_0	No-Load Current
I_{mot}	Motor Current
J	Advance Ratio
K_v	Specific Rotational Velocity
l	Electric motor length
l_{wire}	Wire Length
m	Mass
m_{PL}	Payload
$\dot{m}_{fuel}$	Fuel Mass Flow
m_{TO}	Takeoff Mass
N	Rotational Velocity (in revolutions per minute)
n_{blades}	Number of Propeller Blades

n_{cyl}	Number of engine Cylinders
n_P	Number of Battery Cells in Parallel
n_S	Number of Battery Cells in Series
P	Power
p_{ma}	Mean Available Pressure
p_{me}	Mean Efficient Pressure
p_{mloss}	Mean Pressure Loss
Q	Torque
R	Resistance
r_c	Battery C-Rate
R_i	Internal Resistance
RoC	Rate of Climb
S	Cylinder Stroke
T	Thrust
t	Time
v	Velocity
V	Voltage
V_{fuel}	Fuel Volume
V_d	Displacement Volume
V_{emf}	Electromagnetic Force

Indices (additional to abbreviations)

2S	Two-Stroke
4S	Four-Stroke
chem	Chemical
cont	Continuous
in	Input
max	Maximum
min	Minimum
out	Output
ref	Reference Aircraft

LIST OF FIGURES

LIST OF TABLES

APPENDICES

A. Propeller Off-Design Polynomial Functions

$$\eta_{\text{off-design}} = -0.0847J^2 + 0.0282Jc_T + 0.0762J\frac{v_{\text{off-design}}}{v_{\text{design}}} + 0.0156J\frac{T_{\text{off-design}}}{T_{\text{design}}}$$
$$+ 0.2531J - 0.2258c_T^2 + 0.5614c_T\frac{v_{\text{off-design}}}{v_{\text{design}}} - 0.0933c_T\frac{T_{\text{off-design}}}{T_{\text{design}}}$$
$$- 1.3508c_T - 0.0873\left(\frac{v_{\text{off-design}}}{v_{\text{design}}}\right)^2 + 0.0239\frac{v_{\text{off-design}}}{v_{\text{design}}}\frac{T_{\text{off-design}}}{T_{\text{design}}}$$
$$+ 0.1731\frac{v_{\text{off-design}}}{v_{\text{design}}} + 0.0011\left(\frac{T_{\text{off-design}}}{T_{\text{design}}}\right)^2 - 0.0809\frac{T_{\text{off-design}}}{T_{\text{design}}} + 0.6067$$

$$c_{Q,\text{off-design}} = -0.0022J^2 + 0.1870Jc_T - 0.0027J\frac{v_{\text{off-design}}}{v_{\text{design}}} - 0.0007J\frac{T_{\text{off-design}}}{T_{\text{design}}}$$
$$+ 0.0105J + 0.4636c_T^2 - 0.0724c_T\frac{v_{\text{off-design}}}{v_{\text{design}}} + 0.0182_T\frac{T_{\text{off-design}}}{T_{\text{design}}}$$
$$- 0.0264c_T + 0.0014\left(\frac{v_{\text{off-design}}}{v_{\text{design}}}\right)^2 + 0.0009\frac{v_{\text{off-design}}}{v_{\text{design}}}\frac{T_{\text{off-design}}}{T_{\text{design}}}$$
$$- 0.0028\frac{v_{\text{off-design}}}{v_{\text{design}}} + 0.0003\left(\frac{T_{\text{off-design}}}{T_{\text{design}}}\right)^2 + 0.0030\frac{T_{\text{off-design}}}{T_{\text{design}}} - 0.0038$$

$$\frac{\omega_{\text{off-design}}}{\omega_{\text{design}}} = 0.0466J^2 - 0.1835Jc_T + 0.1050J\frac{v_{\text{off-design}}}{v_{\text{design}}} - 0.0095J\frac{T_{\text{off-design}}}{T_{\text{design}}}$$
$$- 0.1784J + 0.3324c_T^2 - 0.7736c_T\frac{v_{\text{off-design}}}{v_{\text{design}}} + 0.2294c_T\frac{T_{\text{off-design}}}{T_{\text{design}}}$$
$$+ 0.7270c_T + 0.0288\left(\frac{v_{\text{off-design}}}{v_{\text{design}}}\right)^2 - 0.0240\frac{v_{\text{off-design}}}{v_{\text{design}}}\frac{T_{\text{off-design}}}{T_{\text{design}}}$$
$$+ 0.4186\frac{v_{\text{off-design}}}{v_{\text{design}}} - 0.0058\left(\frac{T_{\text{off-design}}}{T_{\text{design}}}\right)^2 + 0.2144\frac{T_{\text{off-design}}}{T_{\text{design}}} + 0.3794$$

B. Commercial Component Databases

B.1 Electric Motors

Only the motors used for the creation of models are included in the table. Models by manufacturer Scorpion are outrunnner motors, models by manufacturer Lehner are inrunner motors.

Model	K_v [rpm/V]	R_i [Ω]	I_0 [A]	I_{max} [A]	d [mm]	l [mm]	M [g]
Scorpion HK-2206-3900KV	3900	0.064	0.83	14	27.9	22.6	31.6
Scorpion HK-2206-5300KV	5300	0.031	2.12	18	27.9	22.6	34
Scorpion HKII-2268-24	3590	0.061	1.21	21	27.9	25.3	39
Scorpion HKll-2208-28	3125	0.081	1.15	18	27.9	25.3	39
Scorpion HKII.2208-34	2600	0.126	0.85	15	27.9	25.3	39
Scorpion HKII-2213-14	3585	0.038	1.74	32	27.9	30.3	54
Scorpion HKII-2213-16	3200	0.04	1.6	30	27.9	30.3	54
Scorpion HKII-2213-20	2640	0.063	1.1	26	27.9	30.3	54
Scorpion HKII-2216-12	3350	0.033	1.87	35	27.9	33.3	64
Scorpion HKII-2216-14	2920	0.04	1.35	32	27.9	33.3	64
Scorpion HKII-2216-16	2608	0.048	1.19	30	27.9	33.3	64
Scorpion HKII-2221-6	4400	0.016	2.89	52	27.9	38.3	79
Scorpion HKII-2221-8	3595	0.024	2.31	45	27.9	38.3	79
Scorpion HKII-2221-10	3000	0.031	1.79	42	27.9	38.3	79
Scorpion HKII-2221-12	2580	0.038	1.5	38	27.9	38.3	79
Scorpion HK-2221-1630KV	1630	0.079	0.71	25	27.9	38.3	79
Scorpion HK-2221-20I0KV	2010	0.052	1.01	28	27.9	38.3	79
Scorpion S-220S-32	1980	0.168	0.76	12	27.9	21.9	32
Scorpion S-220S-36	1670	0.164	0.52	10	27.9	21.9	32
Scorpion S-220S-40	1551	0.217	0.56	10	27.9	21.9	32
Scorpion S-2206-30	1293	0.185	0.55	14	27.9	24.9	40.2
Scorpion S-2206-34	1150	0.191	0.45	12	27.9	24.9	40
Scorpion S-2212-1920KV	1920	0.034	1.15	22	27.9	28.9	55
Scorpion S-2212-22	1157	0.119	0.6	15	27.9	28.9	52.3
Scorpion S-2212-26	939	0.161	0.52	13	27.9	28.9	50.7
Scorpion S-221S-1860KV	1860	0.03	1.26	25	27.9	31.9	64
Scorpion S-221S-18	1131	0.097	0.68	20	27.9	31.9	61.9
Scorpion S-221S-22	940	0.13	0.5	16	27.9	31.9	61.3
Scorpion l-lK-4015-1450KV	1450	0.009	3.16	80	48.9	41.5	244
Scorpion HK-4020-910KV	910	0.015	1.95	65	48.9	48.5	284
Scorpion HK-4020-1100KV	1100	0.01	2.45	78	48.9	46.5	286
Scorpion hK-4020-1390KV	1390	0.007	3.45	90	48.9	46.5	284
Scorpion HK-4025-630KV	630	0.024	1.1	65	48.9	51.5	326
Scorpion HK-4025-740KV	740	0.017	1.33	75	48.9	51.5	326
Scorpion HK-4025-890KV	890	0.013	1.8	95	48.9	51.5	326
Scorpion HK.4025-1100KV	1100	0.008	2.4	100	48.9	51.5	326
Scorpion HK-4035-400KV	400	0.038	1.38	78	48.9	61.5	435
Scorpion HK-4035-500KV	500	0.02	1.77	84	48.9	61.5	431
Scorpion HK-4035-530KV	530	0.022	1.38	80	48.9	61.5	444
Scorpion HK-4035-560KV	560	0.012	2.1	100	48.9	61.5	444
Scorpion HK.4035-630KV	630	0.014	1.6	95	48.9	61.5	421
Scorpion HK.4035-800KV	800	0.01	2.5	100	48.9	61.5	435

Scorpion S-4020-8	790	0.011	1.92	80	48.9	41.2	304
Scorpion S4020-10	630	0.016	1.6	95	48.9	41.2	304
Scorpion S-4020-12	542	0.02	1.32	85	48.9	46.2	304
Scorpion S-4020-14	484	0.024	1.19	80	48.9	46.2	297
Scorpion S-4020-16	415	0.03	0.94	70	45.9	46.2	304
Scorpion S-4025-10	515	0.016	1.48	100	48.9	51.2	354
Scorpion S-4025-12	440	0.022	1.23	85	48.9	51.2	347
Scorpion S-4025-16	332	0.034	0.83	75	48.9	51.2	353
Scorpion S-4035-250KV	250	0.037	0.69	65	48.9	63.3	465
Scorpion 3-4035-330KV	330	0.031	1.41	65	48.9	63.3	442
Scorpion S-4035-380KV	380	0.025	1.52	70	48.9	63.3	430
Scorpion S-4035-460KV	460	0.02	1.7	75	48.9	63.3	435
Scorpion S-5525-170KV	170	0.04	0.19	65	65.4	67.75	636.6
Scorpion S-5525-195KV	195	0.03	1.11	75	65.4	67.75	634.8
Scorpion S-5525-225KV	225	0.025	1.43	85	65.4	67.75	637.6
Scorpion S-5535-160KV	160	0.032	1.18	85	65.4	79.25	859.9
Scorpion S-5535-190KV	190	0.024	1.56	90	65.4	79.25	855.6
Scorpion S-5545-150KV	150	0.03	1.31	90	65.4	89.25	1025.9
Scorpion S-5545-180KV	160	0.018	1.92	105	65.4	89.25	1052.7
Scorpion SII-3008-1090KV	1090	0.058	0.79	26	37.5	33.75	95
Scorpion SII-3008-1220KV	1220	0.042	0.97	32	37.5	33.75	95
Scorpion SII-3014-830KV	830	0.042	1.06	30	37.5	39.75	129
Scorpion SII-3014-1040KV	1040	0.026	1.35	40	37.5	39.75	129
Scorpion SII-3014-1220KV	1220	0.018	1.64	46	37.5	39.75	129
Scorpion SII-3020-780KV	780	0.03	1.21	40	37.5	45.75	166
Scorpion SII-3020-890KV	890	0.02	1.42	45	37.5	45.75	166
Scorpion SII-3020-1100KV	1100	0.016	2.08	60	37.5	45.75	166
Scorpion SII-3026-710KV	710	0.022	1.56	60	37.5	51.75	205
Scorpion SII-3026-890KV	890	0.014	1.9	70	37.5	51.75	205
Scorpion SII-3026-1190KV	1190	0.008	3.26	80	37.5	51.75	205
Scorpion SII-3032-690KV	690	0.022	2.71	60	37.5	62.5	275
Scorpion SII-3032-880KV	880	0.012	3.12	70	37.5	62.5	275
Scorpion SII-3032-990KV	990	0.01	4.25	80	37.5	62.5	275
Scorpion HK-3026-880KV	880	0.026	1.93	52	37.5	48.4	199
Scorpion HK-3026-1000KV	1000	0.028	1.17	62	37.5	48.4	199
Scorpion HK-3026-1210KV	1210	0.018	1.63	65	37.5	48.4	193
Scorpion HK-3026-1400KV	1400	0.01	3.33	80	37.5	48.4	199
Scorpion HK-3026-1600KV	1600	0.016	1.9	70	37.5	48.4	196
Scorpion HK-3026-1900KV	1900	0.012	3.02	80	37.5	48.4	193
Lehner 1515/22	2617	0.056	1.12	21	29.3	36	90
Lehner 1515/24	2399	0.067	0.95	19	29.3	36	90
Lehner 1515/26	2217	0.078	0.86	17	29.3	36	90
Lehner 1515/28	2054	0.091	0.75	16	29.3	36	90
Lehner 1515/30	1919	0.104	0.67	15	29.3	36	90
Lehner 1515/32	1799	0.118	0.6	13	29.3	36	90
Lehner 1515/34	1695	0.134	0.55	13	29.3	36	90
Lehner 1515/36	1599	0.15	0.5	12	29.3	36	90
Lehner 1515/38	1517	0.167	0.46	11	29.3	36	90
Lehner 1515/40	1441	0.185	0.42	10	29.3	36	90
Lehner 1520/16	2691	0.034	1.37	30	29.3	41	115
Lehner 1520/18	2395	0.043	1.13	26	29.3	41	115

Lehner 1520/20	2155	0.053	0.94	23	29.3	41	115
Lehner 1520/22	1959	0.064	0.82	20	29.3	41	115
Lehner 1520/24	1796	0.076	0.71	18	29.3	41	115
Lehner 1520/26	1658	0.089	0.63	17	29.3	41	115
Lehner 1520/28	1541	0.103	0.55	15	29.3	41	115
Lehner 1520/30	1437	0.118	0.5	14	29.3	41	115
Lehner 1520/32	1349	0.134	0.44	13	29.3	41	115
Lehner 1520/34	1268	0.152	0.4	12	29.3	41	115
Lehner 1520/36	1199	0.17	0.36	11	29.3	41	115
Lehner 1520/38	1136	0.19	0.33	11	29.3	41	115
Lehner 1520/40	1078	0.21	0.31	10	29.3	41	115
Lehner 1525/14	2458	0.026	1.58	31	29.3	46	135
Lehner 1525/16	2153	0.034	1.27	27	29.3	46	135
Lehner 1525/18	1914	0.043	1.06	23	29.3	46	135
Lehner 1525/20	1724	0.053	0.89	21	29.3	46	135
Lehner 1525/22	1565	0.064	0.76	19	29.3	46	135
Lehner 1525/24	1437	0.076	0.66	17	29.3	46	135
Lehner 1525/26	1326	0.09	0.57	15	29.3	46	135
Lehner 1525/28	1231	0.104	0.51	14	29.3	46	135
Lehner 1525/30	1150	0.119	0.45	13	29.3	46	135
Lehner 1525/32	1078	0.136	0.41	12	29.3	46	135
Lehner 1525/34	1015	0.153	0.37	11	29.3	46	135
Lehner 1525/36	959	0.172	0.34	10	29.3	46	135
Lehner 1525/38	907	0.191	0.31	10	29.3	46	135
Lehner 1525/40	862	0.212	0.29	9	29.3	46	135
Lehner 1530/12	2391	0.021	1.81	35	29.3	51	155
Lehner 1530/14	2049	0.029	1.41	29	29.3	51	155
Lehner 1530/16	1795	0.038	1.13	25	29.3	51	155
Lehner 1530/18	1596	0.048	0.93	22	29.3	51	155
Lehner 1530/20	1435	0.06	0.78	19	29.3	51	155
Lehner 1530/22	1305	0.072	0.66	17	29.3	51	155
Lehner 1530/24	1197	0.086	0.58	16	29.3	51	155
Lehner 1530/26	1105	0.101	0.51	14	29.3	51	155
Lehner 1530/28	1026	0.117	0.45	13	29.3	51	155
Lehner 1530/30	958	0.134	0.41	12	29.3	51	155
Lehner 1530/32	898	0.152	0.37	11	29.3	51	155
Lehner 1530/34	846	0.172	0.33	10	29.3	51	155
Lehner 1530/36	798	0.193	0.3	9	29.3	51	155
Lehner 1530/38	756	0.215	0.27	9	29.3	51	155
Lehner 1530/40	719	0.238	0.26	8	29.3	51	155
Lehner 1535/10	2458	0.016	2.16	44	29.3	56	175
Lehner 1535/12	2047	0.023	1.6	35	29.3	56	175
Lehner 1535/14	1757	0.032	1.24	29	29.3	56	175
Lehner 1535/16	1538	0.042	1.09	25	29.3	56	175
Lehner 1535/18	1369	0.053	0.83	22	29.3	56	175

Lehner 1535/20	1230	0.065	0.7	19	29.3	56	175
Lehner 1535/22	1119	0.079	0.63	17	29.3	56	175
Lehner 1535/24	1025	0.094	0.52	16	29.3	56	175
Lehner 1535/26	947	0.11	0.46	14	29.3	56	175
Lehner 1535/28	879	0.128	0.41	13	29.3	56	175
Lehner 1535/30	821	0.147	0.36	12	29.3	56	175
Lehner 1535/32	769	0.167	0.33	11	29.3	56	175
Lehner 1535/34	724	0.189	0.29	10	29.3	56	175
Lehner 1535/36	684	0.211	0.27	10	29.3	56	175
Lehner 1535/38	649	0.236	0.24	9	29.3	56	175
Lehner 1535/40	616	0.261	0.23	9	29.3	56	175
Lehner 1920/10	3143	0.011	3.15	61	36	44	170
Lehner 1920/12	2621	0.015	2.32	49	36	44	170
Lehner 1920/14	2248	0.021	1.8	41	36	44	170
Lehner 1920/16	1967	0.028	1.44	35	36	44	170
Lehner 1920/18	1750	0.035	1.19	30	36	44	170
Lehner 1920/20	1575	0.043	1	27	36	44	170
Lehner 1920/22	1433	0.052	0.86	24	36	44	170
Lehner 1920/24	1311	0.062	0.74	22	36	44	170
Lehner 1920/26	1212	0.073	0.66	20	36	44	170
Lehner 1920/28	1125	0.084	0.58	18	36	44	170
Lehner 1920/30	1050	0.097	0.52	17	36	44	170
Lehner 1920/31	1016	0.103	0.43	16	36	44	170
Lehner 1920/32	1017	0.103	0.49	16	36	44	170
Lehner 1920/34	985	0.11	0.47	15	36	44	170
Lehner 1920/36	928	0.124	0.42	15	36	44	170
Lehner 1920/38	876	0.139	0.39	13	36	44	170
Lehner 1920/40	830	0.155	0.35	13	36	44	170
Lehner 1920/42	788	0.172	0.33	12	36	44	170
Lehner 1930/8	2617	0.008	2.89	66	36	54	230
Lehner 1930/10	2095	0.012	2	51	36	54	230
Lehner 1930/12	1746	0.018	1.49	41	36	54	230
Lehner 1930/14	1498	0.024	1.16	34	36	54	230
Lehner 1930/16	1311	0.031	0.93	29	36	54	230
Lehner 1930/18	1164	0.04	0.77	25	36	54	230
Lehner 1930/20	1048	0.049	0.65	22	36	54	230
Lehner 1930/22	954	0.059	0.55	20	36	54	230
Lehner 1930/24	874	0.071	0.48	18	36	54	230
Lehner 1930/26	807	0.083	0.42	16	36	54	230
Lehner 1930/28	749	0.096	0.38	15	36	54	230
Lehner 1930/30	700	0.11	0.33	14	36	54	230
Lehner 1930/32	656	0.125	0.3	13	36	54	230
Lehner 1930/34	617	0.142	0.27	12	36	54	230
Lehner 1930/36	583	0.159	0.25	11	36	54	230
Lehner 1930/38	553	0.177	0.23	11	36	54	230

Lehner 1930/40	525	0.196	0.21	10	36	54	230
Lehner 1940/6	2616	0.005	4.43	94	36	64	290
Lehner 1940/8	1963	0.008	2.77	67	36	64	290
Lehner 1940/10	1572	0.013	1.93	51	36	64	290
Lehner 1940/12	1310	0.019	1.43	41	36	64	290
Lehner 1940/14	1124	0.026	1.11	35	36	64	290
Lehner 1940/16	983	0.033	0.89	30	36	64	290
Lehner 1940/18	873	0.042	0.74	26	36	64	290
Lehner 1940/20	786	0.052	0.63	23	36	64	290
Lehner 1940/22	715	0.063	0.53	20	36	64	290
Lehner 1940/24	656	0.075	0.47	18	36	64	290
Lehner 1940/26	605	0.088	0.4	16	36	64	290
Lehner 1940/28	562	0.102	0.36	14	36	64	290
Lehner 1940/30	524	0.118	0.32	13	36	64	290
Lehner 1940/32	492	0.134	0.29	12	36	64	290
Lehner 1940/34	463	0.151	0.26	11	36	64	290
Lehner 1940/36	438	0.169	0.24	10	36	64	290
Lehner 1940/38	415	0.189	0.22	11	36	64	290
Lehner 1940/40	394	0.209	0.2	10	36	64	290
Lehner 1950/6	2093	0.005	3.35	102	36	74	350
Lehner 1950/8	1570	0.009	2.11	72	36	74	350
Lehner 1950/10	1256	0.015	1.46	57	36	74	350
Lehner 1950/12	1048	0.021	1.08	47	36	74	350
Lehner 1950/14	899	0.029	0.84	39	36	74	350
Lehner 1950/16	786	0.038	0.68	33	36	74	350
Lehner 1950/18	699	0.048	0.56	29	36	74	350
Lehner 1950/20	629	0.059	0.47	26	36	74	350
Lehner 1950/22	572	0.071	0.4	23	36	74	350
Lehner 1950/24	524	0.085	0.35	20	36	74	350
Lehner 1950/26	484	0.099	0.31	18	36	74	350
Lehner 1950/28	449	0.115	0.27	17	36	74	350
Lehner 1950/30	420	0.132	0.24	15	36	74	350
Lehner 1950/32	393	0.15	0.22	14	36	74	350
Lehner 1950/34	370	0.17	0.2	13	36	74	350
Lehner 1950/36	350	0.19	0.18	12	36	74	350
Lehner 1950/38	332	0.212	0.16	11	36	74	350
Lehner 1950/40	315	0.235	0.15	10	36	74	350
Lehner 2230/12	1648	0.012	2.55	77	44	61	345
Lehner 2230/14	1413	0.016	1.98	64	44	61	345
Lehner 2230/16	1236	0.02	1.6	55	44	61	345
Lehner 2230/18	1100	0.026	1.32	48	44	61	345
Lehner 2230/20	991	0.032	1.11	42	44	61	345
Lehner 2230/22	901	0.039	0.95	37	44	61	345
Lehner 2230/24	826	0.046	0.83	34	44	61	345
Lehner 2230/26	761	0.054	0.73	31	44	61	345

Lehner 2230/28	707	0.063	0.64	28	44	61	345
Lehner 2230/30	661	0.072	0.57	26	44	61	345
Lehner 2230/32	619	0.082	0.52	24	44	61	345
Lehner 2230/34	583	0.092	0.47	22	44	61	345
Lehner 2230/36	551	0.104	0.42	21	44	61	345
Lehner 2230/38	521	0.116	0.39	19	44	61	345
Lehner 2230/40	496	0.128	0.36	19	44	61	345
Lehner 2240/10	1482	0.008	2.58	99	44	71	450
Lehner 2240/12	1236	0.012	1.92	80	44	71	450
Lehner 2240/14	1059	0.016	1.49	68	44	71	450
Lehner 2240/16	927	0.021	1.2	59	44	71	450
Lehner 2240/18	824	0.027	0.99	51	44	71	450
Lehner 2240/20	742	0.033	0.84	45	44	71	450
Lehner 2240/22	674	0.04	0.71	41	44	71	450
Lehner 2240/24	618	0.048	0.62	37	44	71	450
Lehner 2240/26	571	0.056	0.54	33	44	71	450
Lehner 2240/28	530	0.065	0.48	30	44	71	450
Lehner 2240/30	495	0.075	0.43	27	44	71	450
Lehner 2240/32	464	0.085	0.39	25	44	71	450
Lehner 2240/34	437	0.096	0.35	23	44	71	450
Lehner 2240/36	412	0.108	0.32	22	44	71	450
Lehner 2240/38	391	0.12	0.29	21	44	71	450
Lehner 2240/40	371	0.133	0.27	19	44	71	450
Lehner 2250/8	1482	0.006	3.28	134	44	81	560
Lehner 2250/10	1186	0.009	2.28	103	44	81	560
Lehner 2250/12	989	0.013	1.68	83	44	81	560
Lehner 2250/14	848	0.018	1.32	72	44	81	560
Lehner 2250/16	742	0.023	1.06	62	44	81	560
Lehner 2250/18	660	0.029	0.87	54	44	81	560
Lehner 2250/20	593	0.036	0.73	48	44	81	560
Lehner 2250/22	540	0.044	0.63	42	44	81	560
Lehner 2250/24	495	0.052	0.54	38	44	81	560
Lehner 2250/26	457	0.061	0.48	35	44	81	560
Lehner 2250/28	424	0.071	0.42	31	44	81	560
Lehner 2250/30	396	0.081	0.38	29	44	81	560
Lehner 2250/32	371	0.092	0.34	26	44	81	560
Lehner 2250/34	349	0.104	0.31	24	44	81	560
Lehner 2250/36	330	0.117	0.28	23	44	81	560
Lehner 2250/38	313	0.13	0.26	21	44	81	560
Lehner 2250/40	297	0.144	0.24	20	44	81	560
Lehner 2260/6	1646	0.004	4.49	186	44	91	660
Lehner 2260/8	1235	0.007	2.8	132	44	91	660
Lehner 2260/10	988	0.011	1.95	102	44	91	660
Lehner 2260/12	824	0.016	1.45	86	44	91	660
Lehner 2260/14	707	0.021	1.13	72	44	91	660

Lehner 2260/16	618	0.028	0.9	62	44	91	660
Lehner 2260/18	549	0.035	0.75	54	44	91	660
Lehner 2260/20	495	0.044	0.63	47	44	91	660
Lehner 2260/22	450	0.053	0.54	42	44	91	660
Lehner 2260/24	412	0.063	0.47	38	44	91	660
Lehner 2260/26	381	0.074	0.41	34	44	91	660
Lehner 2260/28	353	0.086	0.36	31	44	91	660
Lehner 2260/30	330	0.098	0.33	28	44	91	660
Lehner 2260/32	309	0.112	0.29	25	44	91	660
Lehner 2260/34	291	0.126	0.27	24	44	91	660
Lehner 2260/36	275	0.142	0.24	22	44	91	660
Lehner 2260/38	261	0.158	0.22	21	44	91	660
Lehner 2260/40	248	0.175	0.2	18	44	91	660
Lehner 2280/6	1235	0.005	5.22	166	44	111	880
Lehner 2280/8	927	0.008	3.27	119	44	111	880
Lehner 2280/10	742	0.013	2.27	94	44	111	880
Lehner 2280/12	619	0.018	1.69	77	44	111	880
Lehner 2280/14	530	0.025	1.31	65	44	111	880
Lehner 2280/16	464	0.032	1.06	55	44	111	880
Lehner 2280/18	413	0.041	0.87	48	44	111	880
Lehner 2280/20	371	0.05	0.73	40	44	111	880
Lehner 2280/22	338	0.061	0.63	38	44	111	880
Lehner 2280/24	310	0.072	0.54	34	44	111	880
Lehner 2280/26	286	0.085	0.48	30	44	111	880
Lehner 2280/28	266	0.098	0.43	28	44	111	880
Lehner 2280/30	248	0.113	0.38	25	44	111	880
Lehner 2280/32	232	0.128	0.34	23	44	111	880
Lehner 2280/34	218	0.145	0.31	22	44	111	880
Lehner 2280/36	206	0.162	0.28	20	44	111	880
Lehner 2280/38	196	0.181	0.26	19	44	111	880
Lehner 2280/40	186	0.2	0.24	18	44	111	880
Lehner 3040/8	1314	0.003	6.3	240	60	80	1050
Lehner 3040/10	1052	0.005	4.37	184	60	80	1050
Lehner 3040/12	877	0.007	3.25	153	60	80	1050
Lehner 3040/14	752	0.01	2.53	129	60	80	1050
Lehner 3040/16	658	0.013	2.04	111	60	80	1050
Lehner 3040/18	585	0.017	1.68	97	60	80	1050
Lehner 3040/20	526	0.021	1.41	86	60	80	1050
Lehner 3040/22	479	0.025	1.21	76	60	80	1050
Lehner 3040/24	439	0.03	1.05	69	60	80	1050
Lehner 3040/26	405	0.035	0.92	62	60	80	1050
Lehner 3040/28	376	0.04	0.82	57	60	80	1050
Lehner 3040/30	351	0.046	0.73	52	60	80	1050
Lehner 3040/32	329	0.052	0.66	48	60	80	1050
Lehner 3040/34	310	0.059	0.59	44	60	80	1050

Lehner 3040/36	293	0.066	0.54	41	60	80	1050
Lehner 3040/38	277	0.074	0.49	38	60	80	1050
Lehner 3040/40	264	0.082	0.46	36	60	80	1050
Lehner 3060/6	1168	0.002	5.64	250	60	100	1250
Lehner 3060/8	876	0.004	3.53	179	60	100	1250
Lehner 3060/10	701	0.006	2.45	143	60	100	1250
Lehner 3060/12	584	0.008	1.82	117	60	100	1250
Lehner 3060/14	501	0.011	1.42	98	60	100	1250
Lehner 3060/16	438	0.015	1.14	85	60	100	1250
Lehner 3060/18	390	0.019	0.94	74	60	100	1250
Lehner 3060/20	350	0.023	0.79	65	60	100	1250
Lehner 3060/22	319	0.028	0.68	58	60	100	1250
Lehner 3060/24	292	0.033	0.59	52	60	100	1250
Lehner 3060/26	270	0.039	0.52	47	60	100	1250
Lehner 3060/28	251	0.046	0.46	43	60	100	1250
Lehner 3060/30	234	0.052	0.41	39	60	100	1250
Lehner 3060/32	219	0.06	0.37	36	60	100	1250
Lehner 3060/34	206	0.067	0.33	33	60	100	1250
Lehner 3060/36	195	0.075	0.3	30	60	100	1250
Lehner 3060/38	185	0.084	0.28	28	60	100	1250
Lehner 3060/40	175	0.093	0.26	27	60	100	1250
Lehner 3080/6	876	0.002	6.78	238	60	140	1650
Lehner 3080/8	657	0.004	4.24	170	60	140	1600
Lehner 3080/10	526	0.007	2.95	136	60	140	1600
Lehner 3080/12	438	0.009	2.19	111	60	140	1600
Lehner 3080/14	376	0.013	1.7	94	60	140	1600
Lehner 3080/16	329	0.017	1.37	81	60	140	1600
Lehner 3080/18	293	0.021	1.13	71	60	140	1600
Lehner 3080/20	263	0.026	0.95	62	60	140	1600
Lehner 3080/22	239	0.031	0.81	56	60	140	1600
Lehner 3080/24	219	0.037	0.71	50	60	140	1600
Lehner 3080/26	203	0.044	0.62	45	60	140	1600
Lehner 3080/28	188	0.051	0.55	41	60	140	1600
Lehner 3080/30	176	0.059	0.49	38	60	140	1600
Lehner 3080/32	165	0.067	0.44	35	60	140	1600
Lehner 3080/34	146	0.084	0.37	29	60	140	1600
Lehner 3080/36	139	0.094	0.33	29	60	140	1600
Lehner 3080/38	132	0.104	0.31	25	60	140	1600

B.2 Internal Combustion Engines

Manufacturer	Model	n_{cyl}	Cycle	V_d [cm³]	P_{max} [kW]	m [kg]	B [mm]	S [mm]	Ignition method
3W	3W-28i	1	2	28.5	2.5	1,211			SI

3W	3W-28i CS	1	2	28.5	2.6	1,211			SI
3W	3W-55Xi	1	2	54.9	4.0	1,787			SI
3W	3W-55Xi CS	1	2	28.5	4.4	1,787			SI
3W	3W-55i CS	1	2	52.9	4.0	1,932			SI
3W	3W-55i	1	2	54.9	3.9	1,937			SI
3W	3W-55i US	1	2	54.9	3.9	1,937			SI
3W	3W-55i US CS	1	2	53.3	4.3	1,937			SI
3W	3W-80Xi	1	2	78.0	6.3	2,359			SI
3W	3W-80Xi CS	1	2	78.0	6.7	2,359			SI
3W	3W-85Xi	1	2	83.7	6.9	2,395			SI
3W	3W-85Xi TS	1	2	83.7	7.0	2,395			SI
3W	3W-85Xi CS	1	2	83.7	7.3	2,395			SI
3W	3W-85Xi TS CS	1	2	83.7	7.8	2,395			SI
3W	3W-80Xi TS	1	2	78.0	6.5	2,495			SI
3W	3W-80Xi TS CS	1	2	78.0	7.1	2,495			SI
3W	3W-56iB2	2	2	57.0	3.8	1,846			SI
3W	3W-56iB2 CS	2	2	57.0	4.0	1,846			SI
3W	3W-110 iB2 CS	2	2	108.3	9.0	3,044			SI
3W	3W-110 iB2	2	2	108.3	8.8	3,048			SI
3W	3W-110 iR2 CS	2	2	108.3	8.1	3,484			SI
3W	3W-110 iR2	2	2	108.3	7.8	3,488			SI
3W	3W-157 XiB2	2	2	157.0	12.7	4,105			SI
3W	3W-157 XiB2 TS	2	2	157.0	13.0	4,105			SI
3W	3W-157 XiB2 CS	2	2	157.0	13.4	4,105			SI
3W	3W-170 XiB2	2	2	169.9	13.5	4,105			SI
3W	3W-157 XiB2 TS CS	2	2	157.0	13.8	4,105			SI
3W	3W-170 XiB2 CS	2	2	169.9	14.0	4,105			SI
3W	3W-170 XiB2 TS	2	2	169.9	14.2	4,105			SI
3W	3W-170 XiB2 TS CS	2	2	169.9	14.7	4,105			SI
3W	3W 150iR2	2	2	150.6	11.2	4,695			SI
3W	3W-210 XiB2 TS CS	2	2	209.9	13.5	4,994			SI
3W	3W-210Xi B2 F TS	2	2	209.9	13.2	4,999			SI
3W	3W-275 XiB2 TS	2	2	273.7	19.4	7,031			SI
3W	3W-275 XiB2 TS CS	2	2	273.7	20.5	7,031			SI
3W	3W-342iB2F	2	2	341.8	23.5	8,577			SI
3W	3W-342iB2F TS	2	2	341.8	23.9	8,827			SI
3W	3W-112 iB4	4	2	114.1	9.1	3,869			SI
3W	3W-112 iB4 CS	4	2	114.1	9.7	3,869			SI
3W	3W-220 iB4	4	2	216.6	16.3	6,192			SI
3W	3W-220 iB4 CS	4	2	216.6	16.9	6,192			SI
BME	58 Extreme	1	2	58.2	4.5	1,216			SI
BME	50 Classic	1	2	50.1	4.1	1,474			SI

BME	116 Extreme	2	2	116.3	8.9	2,068			SI
BME	150 LT	2	2	149.0	12.3	2,835			SI
Desert Aircraft	DA-50R	1	2	55.0	3.7	1,330	42.6	35	SI
Desert Aircraft	DA-60	1	2	60.5	0.0	1,410			SI
Desert Aircraft	DA-85	1	2	85.9	6.3	1,950	52	40.49	SI
Desert Aircraft	DA-120	2	2	121.0	0.0	2,250			SI
Desert Aircraft	DA-100L	2	2	100.0	7.3	2,530	42.6	35	SI
Desert Aircraft	DA-170	2	2	171.8	13.4	3,560	52	40.49	SI
Desert Aircraft	DA-150	2	2	150.0	12.3	3,610	49	40	SI
Desert Aircraft	DA-200	4	2	200.0	14.2	4,950	42.6	35	SI
Enya	SS15DBB S	1	2	2.5	0.4	180	15	14	CI
Enya	ULTRA11CXD	1	2	2.1	0.4	190	14.3	13	CI
Enya	ULTRA11CXD S	1	2	2.1	0.4	190	14.3	13	CI
Enya	SS15DBB TN	1	2	2.5	0.4	200	15	14	CI
Enya	SS25D AL-CHRO TN	1	2	4.1	0.6	210	17.8	16.4	CI
Enya	SS25DBB S	1	2	4.1	0.5	230	17.8	16.4	CI
Enya	SS25DBB TN	1	2	4.1	0.6	250	17.8	16.4	CI
Enya	09-IV TV W/SNV	1	2	1.6	0.1	112	13	12.2	SI
Enya	Quicky 09 TV W/SNV	1	2	1.6	0.1	128	13	12.2	SI
Enya	20TV W/SNV	1	2	3.3	0.3	173	17.2	14	SI
Enya	15-V TV W/SNV	1	2	2.5	0.2	180	15	14	SI
Enya	SS15	1	2	2.5	0.3	180	15	14	SI
Enya	SS15BB	1	2	2.5	0.4	185	15	14	SI
Enya	ULTRA11CX TN	1	2	2.1	0.4	190	14.3	13	SI
Enya	SS25 W/SNV	1	2	4.1	0.5	210	17.8	16.4	SI
Enya	SS30 W/SNV	1	2	4.8	0.6	210	19	17	SI
Enya	SS25 AL-CHRO TN	1	2	4.1	0.6	210	17.8	16.4	SI
Enya	SS25BB TN	1	2	4.1	0.5	225	17.8	16.4	SI
Enya	SS30BB TN	1	2	4.8	0.6	225	19	17	SI
Enya	35X TN	1	2	5.7	0.8	265	20	18	SI
Enya	40XZ TN	1	2	6.5	0.9	268	21.4	18	SI
Enya	SS40 W/SNV	1	2	6.5	0.8	300	20.9	18.9	SI
Enya	SS45 Ring TN	1	2	7.4	0.9	315	22.3	18.9	SI
Enya	SS50 Ring TN	1	2	8.0	1.0	315	22.3	20.4	SI
Enya	SS40BB TN	1	2	6.5	0.9	330	20.9	18.9	SI
Enya	61 CXR TN	1	2	10.0	1.3	377	25	20.4	SI
Enya	50CX TN	1	2	8.4	1.0	395	22.9	20.4	SI
Enya	180X TN	1	2	29.1	2.8	1,290	34	32	SI
Hirth	F36	1	2	208.0	11.0	9,400	54	70	SI
Hirth	F33	1	2	313.0	20.6	12,700	69	76	SI
Jamara Engines	Power Pro 26	1	2	25.4	1.8	735	34	28	SI
Jamara Engines	Power Pro DL-50	1	2	50.0	3.7	1,380	44	35	SI
Jamara Engines	P-45	1	2	45.0	3.1	1,600	43	31	SI

Jamara Engines	Power Pro B 48	2	2	47.9	3.4	1,450	33	28	SI
Jamara Engines	Power Pro B-100	2	2	100.0	7.2	2,350	44	35	SI
Lightning Aircraft	108D2	2	2	108.0	7.5	3,175	45	34.03	SI
Lightning Aircraft	150D2-B	2	2	105.0	11.2	4,196	50	36.16	SI
Lightning Aircraft	250D2	2	2	250.0	17.9	5,670	60	44.2	SI
Lightning Aircraft	302D2-FI	2	2	302.0	20.9	14,969	66	44.2	SI
Magnum	XL-15S	1	2	2.5	0.7	165			SI
Magnum	XL-25 AII ABC	1	2	4.1	0.8	196			SI
Magnum	XL-32 AIIS ABC	1	2	5.3	0.9	336			SI
Magnum	XL-46 S ABC	1	2	7.5	1.4	377			SI
MVVS	2,5 DFS/R	1	2	2.5	0.5	198	15	14	CI
MVVS	2,5 DFS/R-RC	1	2	2.5	0.5	213	15	14	CI
MVVS	2,5 DFS/R-ABC-RC	1	2	10.0	1.1	580	23	24	CI
MVVS	26 SP	1	2	25.7	2.8	936	33	30.1	SI
MVVS	40 SP	1	2	40.0	0.0	1,451	38	35.2	SI
MVVS	50 SP	1	2	50.0	0.0	1,560	40	38	SI
MVVS	58 IRS	1	2	58.0	6.3	1,820	42	42	SI
MVVS	80 SP	1	2	79.6	7.5	2,220	48	44	SI
MVVS	116 IRS	2	2	116.0	10.4	3,100	42	42	SI
MVVS	152 IRS	2	2	152.0	0.0	3,530	48	42	SI
MVVS	2,0 GFS-ABC-RC	1	2	2.0	0.4	155	13.5	14	SI
MVVS	2,5 GFS/R-ABC	1	2	2.5	0.5	188	15	14	SI
MVVS	2,5 GFS/R-ABC-RC	1	2	2.5	0.5	207	15	14	SI
MVVS	4,6 GFS/R-ABC-RC	1	2	4.6	0.8	280	18	18	SI
MVVS	10,0 GFS/R-ABC-RC	1	2	10.0	1.3	549	23	24	SI
MVVS	15 GFS/R-ABC-RC	1	2	14.9	1.8	552	27	26	SI
MVVS	12,7 GFS/R-ABC-RC	1	2	12.8	1.7	560	25	26	SI
MVVS	26 GFS-RC	1	2	25.7	2.9	900	33	30.1	SI
MVVS	26 GFS-RC-W	1	2	25.7	2.9	950	33	30.1	SI
NW UAV	Heavy Fuel Engine	1	2	34.0	1.5	771			CI
OS	10LA	1	2	1.8	0.1	112	13.4	12.4	SI
OS	15LA	1	2	2.5	0.3	128	15.2	13.7	SI
OS	15CV-A	1	2		0.4	170	15.2	13.7	SI
OS	25LA	1	2	4.0	0.4	197	18	16	SI
OS	25FX	1	2	4.1	0.6	248	18	15.3	SI
OS	46LA	1	2	7.5	0.9	272	23	18.4	SI
OS	25AX	1	2	4.1	0.6	275	18	16	SI
OS	35AX	1	2		1.0	363	20.2	18	SI
OS	46AX	1	2	7.5	1.2	375	22	19.6	SI

OS	55AX	1	2	9.0	1.3	404	23	21.5	SI
OS	65AX	1	2	10.6	1.5	497	24	23.5	SI
OS	65LA	1	2	10.9	1.3	535	24	23.5	SI
OS	61FX	1	2	9.9	1.4	550	24	22	SI
OS	91FX	1	2		2.1	550			SI
OS	95AX	1	2	15.6	2.2	567	27.7	25.8	SI
OS	75AX	1	2	12.3	1.8	578	25.8	23.5	SI
OS	120AX	1	2	20.0	2.3	647	30.4	27.5	SI
OS	140RX-P	1	2	23.0	2.6	830	32	28.6	SI
OS	160FX	1	2	26.0	2.8	925	33.6	29.6	SI
OS	BGX-1	1	2	35	3.1	1,340	37.3	32	SI
OS	25LA-S	1	2	4.1	0.4	186	18	16	SI
OS	46LA-S	1	2	7.6	0.9	264	13	18.4	SI
Sauer	S33A/B	1	2	312	20.6	12,700	69	76	SI
Thundertiger	GP-07	1	2	1.13	0.1	94	12.0	10.0	SI
Thundertiger	GP-10	1	2	1.75	0.2	162	13.4	12.4	SI
Thundertiger	GP-18	1	2	2.93	0.3	162	16.2	14.2	SI
Thundertiger	GP-15	1	2	2.49	0.3	180	15.2	13.7	SI
Thundertiger	GP-28	1	2	4.53	0.6	221	18.7	16.5	SI
Thundertiger	GP-25	1	2	4.07	0.4	242	18.0	16.0	SI
Thundertiger	PRO-25	1	2	4.07	0.6	286	18.0	16.0	SI
Thundertiger	PRO-36	1	2	5.98	0.8	314	20.8	17.6	SI
Thundertiger	GP-42	1	2	6.90	0.8	357	21.5	19.0	SI
Thundertiger	PRO-46	1	2	7.47	1.2	449	21.8	20.0	SI
Thundertiger	PRO-40	1	2	6.52	1.0	455	20.9	19.0	SI
Thundertiger	PRO-91	1	2	14.96	2.1	562	28.0	24.3	SI
Thundertiger	GP-61	1	2	10.58	1.5	693	24.2	23.0	SI
Thundertiger	PRO-61	1	2	9.98	1.4	758	23.5	23.0	SI
Thundertiger	PRO-120-RP	1	2	20.76	2.6	780	31.0	27.5	SI
Thundertiger	PRO-120	1	2	20.76	2.4	975	31.0	27.5	SI
Wolverine 3	Ricardo	2	2	88	2.3				CI
ZDZ	40RV	1	2	39.69		1,300	38	35	SI
ZDZ	40RE	1	2	39.69		1,300	38	35	SI
ZDZ	50NG	1	2	48.5		1,400	42	35	SI
ZDZ	60RV	1	2	48.5		1,400	42	35	SI
ZDZ	80RV	1	2	80		1,870	52	38	SI
ZDZ	80RV-J	1	2	80		1,870	52	38	SI
ZDZ	80B2 RV	2	2	79.38		1,750	38	35	SI
ZDZ	80R2 NG	2	2	79.38		2,600	38	35	SI
ZDZ	100B2 NG	2	2	97		2,190	42	35	SI
ZDZ	100R2 NG	2	2	97		2,800	42	35	SI
ZDZ	120B2 RV	2	2	120		2,950	45	38	SI
ZDZ	160B2 RV-CH	2	2	160		3,000	52	38	SI
ZDZ	160B2 RV-J	2	2	159.6		3,250	47	46	SI
ZDZ	210B2 RV	2	2	210		4,400	52	50	SI

ZDZ	420B4	4	2	420		9,500	52	50	SI
Zenoah	G200PU	1	2	20.1	1.7	1,100	32	25	SI
Zenoah	Titan ZG 20	1	2	20.1	2.4	1,185	32	25	SI
Zenoah	G260PU-EI	1	2	25.4	2.2	1,400	34	28	SI
Zenoah	Titan ZG 26EI	1	2	25.4	3.0	1,590	34	28	SI
Zenoah	G260PU	1	2	25.4	2.2	1,700	34	28	SI
Zenoah	Titan ZG 38SC	1	2	38	2.6	1,800			SI
Zenoah	Titan ZG 45SL	1	2	45	3.9	1,850	43	31	SI
Zenoah	G380PU	1	2	37.4	1.9	2,000	38	33	SI
Zenoah	Titan ZG 62SL	1	2	62	5.0	2,040	62	47.5	SI
Zenoah	G450PU	1	2	45	3.0	2,100	43	31	SI
Zenoah	G620PU	1	2	62	4.2	2,300	47.5	35	SI
Zenoah	Titan ZG 80 B	2	2	80	6.0	2,870	40.5	31	SI
Zenoah	G800BPU	2	2	79.9	5.8	3,500	40.5	31	SI
Enya	41-4CD TN	1	4	6.6	0.7	420	22.3	17	CI
Enya	41-4C	1	4	6.6	0.7	370	22.3	17	SI
Enya	53-4C	1	4	8.7	0.8	415	24	19.2	SI
Enya	R155-4C	1	4	25.4	2.5	960	34	28	SI
Kolm	EZ50	1	4	50.0	4.5	1,950			SI
Kolm	IL100	2	4	100.0	5.6	2,950			SI
Kolm	BX100	2	4	100.0	6.6	3,450			SI
Kolm	IL130	2	4	135.0	8.8	3,670			SI
Kolm	BX130	2	4	135.0	8.8	3,850			SI
Magnum	XL-30 AR FS	1	4	5.00	0.5	282			SI
Magnum	XL-52 AR FS	1	4	8.56	1.2	399			SI
Magnum	XL-61 AR FS	1	4	9.95	1.2	418			SI
Magnum	XL -70 AR FS	1	4	11.50	1.2	599			SI
OS	FS-30S	1	4	4.9	0.5	279	19.5	16.5	SI
OS	FS-40S	1	4	6.5	0.5	355	21.2	18.4	SI
OS	56FS-a	1	4	9.3	1.0	461	24	20.6	SI
OS	72FS-a	1	4	11.8	1.2	530	27	20.6	SI
OS	81FS-a-P	1	4	13.3	1.3	570	27.7	22	SI
OS	81FS-a	1	4	13.3	1.3	570	27.7	22	SI
OS	FS-95V	1	4	15.6	1.7	592	29	23.8	SI
OS	110FS-a-P	1	4	18.0	1.8	610	30.4	24.8	SI
OS	FS-91SII	1	4	14.9	1.6	640	27.7	24.8	SI
OS	FS-91SII-P	1	4	15.0	1.6	650	27.7	24.8	SI
OS	110FS-a	1	4	18.0	1.8	672	30.4	24.8	SI
OS	155FS-a	1	4	25.6	2.6	805	33.6	28.6	SI
OS	FS-200S	1	4	32.4	2.9	853	38	28.6	SI
OS	FS-120S-E	1	4	20.0	1.9	864	30.4	27.6	SI
OS	FS-200S-P	1	4	32.4	3.0	876	38	28.6	SI
OS	FS-120 III-P	1	4	19.7	2.1	920	30.4	27.5	SI
OS	FT-160	2	4	13.3	2.0	1,100			SI
OS	FT-300	2	4	48.8	4.0	1,828	33.6	27.5	SI

OS	FF-320	4	4	53.2	4.0	2,190	28	22	SI
RCV	58-CD	1	4	9.5	0.6	500			SI
RCV	60-SP	1	4	10.0	0.7	570			SI
RCV	91-CD	1	4	15.0	1.1	715			SI
RCV	90-SP	1	4	15.0	1.1	785			SI
RCV	130-CD	1	4	21.3	1.5	995			SI
RCV	120-SP	1	4	20.0	1.3	1,000			SI
Thundertiger	F-54S 4-Takt	1	4	8.87	0.8	420	24.0	19.6	SI
Thundertiger	F-91S 4-Takt	1	4	14.97	1.6	743	28.3	23.8	SI
XRDi	150 cc	1	4	150	15.0	7,257	49	40	CI
XRDi	200 cc	1	4	200	17.0	9,072	65.15	60	CI
XRDi	400 cc	2	4	400	35.0	14,969	65.15	60	CI
OS	49-PI Wankel			4.97	1.3	335			SI
UAV Engines	AR731 Wankel			208	38.0	9,900			SI
UAV Engines	AR741 Wankel			208	38.0	10,700			SI
Limbach	L 275 E	2	2	274.00	20.0	7,200	66	40	SI
Limbach	L 550 E	4	2	548	50.0	16,000	66	40	SI
Honda	GX100	1	4	98		10,600	56	40	SI
Honda	GX120	1	4	118		13,000	60	42	SI
Honda	GX160	1	4	163		15,100	68	45	SI
Honda	GX200	1	4	196		16,100	68	54	SI
Honda	GX240	1	4	270		25,000	77	58	SI
Honda	GX270	1	4	270		25,000	77	58	SI
Honda	GX340	1	4	389		31,500	88	64	SI
Honda	GX390	1	4	389		31,500	88	64	SI
Honda	GXH50	1	4	49		5,500	41.8	36	SI
Honda	GX25	1	4	25		2,900	35	26	SI
Honda	GX35	1	4	35.8		3,460	39	30	SI
Honda	GC160	1	4	160		11,500	64	50	SI
Honda	GC190	1	4	187		13,200	69	50	SI

B.3 Electronic Speed Controllers

Model	**Imax,in [A]**	**m [g]**	**Vmax,in [V]**	**Pmax,in [W]**
Jive 80+ LV	80	84	22.2	1776
Jive 100+ LV	100	92	22.2	2220
FAI Jive 150+ LV	150	140	18.5	2775
Jive 60+ HV	60	84	44.4	2664
Jive 80+ HV	80	84	44.4	3552
Powerkive 120+ HV	120	140	44.4	5328
Kosmik 160+ HV	160	200	51.8	8288
Kosmik 200+ HV	200	200	51.8	10360
YGE 7 S	7	0.7	7.4	52
YGE 8 S	8	4.9	11.1	89

YGE 12 S	12	6	11.1	133
YGE 18	18	14	14.8	266
YGE 30	30	21	14.8	444
YGE 40	40	35	22.2	888
YGE 60	60	35	22.2	1332
YGE 80	80	55	22.2	1776
YGE 100	100	69	22.2	2220
YGE 120	120	71	22.2	2664
YGE 160 FAI	160	79	22.2	3552
YGE 60 HV	60	49	44.4	2664
YGE 90 HV	90	79	44.4	3996
YGE 150 HV FAI	150	89	44.4	6660
YGE 200 HV FAI	200	119	44.4	8880
YGE 120 HV	120	119	51.8	6216
YGE 160 HV	160	156	51.8	8288
MasterSPIN 11	11	12	14.8	163
MasterSPIN 22	22	18	14.8	326
MasterSPIN 33	33	30	18.5	611
MasterSPIN 44	44	40	22.2	977
MasterSPIN 55	55	56	25.9	1425
MasterSPIN 66	66	50	22.2	1465
MasterSPIN 70 Opto	70	50	22.2	1554
MasterSPIN 48 Opto	48	45	37	1776
MasterSPIN 75 0pto	75	55	37	2775
MasterSPIN 77 0pto	77	105	44.4	3419
MasterSPIN 99 0pto	99	105	44.4	4396
MasterSPIN 125 Opto	125	160	44.4	5550
MasterSPIN 170 Opto	170	270	51.8	8806
MasterSPIN 220 Opto	220	460	51.8	11396
SPIN 11	11	12	14.8	163
SPIN 22	22	26	14.8	326
SPIN 33	33	32	18.5	611
SPIN 44	44	44	22.2	977
SPIN 55	55	60	29.6	1628
SPIN 66	70	56	22.2	1554
SPIN 44 OPTO	44	35	22.2	977
SPIN 66 OPTO	70	45	22.2	1554
SPIN 48 OPTO	48	45	37	1776
SPIN 75 OPTO	75	55	37	2775
SPIN 77 OPTO	77	110	44.4	3419
SPIN 99 OPTO	90	110	44.4	3996
SPIN 125 OPTO	125	120	44.4	5550
SPIN 200 OPTO	170	326	51.8	8806
SPIN 300 OPTO	220	360	51.8	11396
Turnigy Fatboy	300	1150	55.5	16650
Turnigy Monster 2000	200	335	44.4	8880

Turnigy K-Force	150	169	22.2	3330
Turnigy K-Force	120	169	44.4	5328
Turnigy dlux 80HV	80	153	44.4	3552
Turnigy Superbrain	100	109	44.4	4440
Turnigy Superbrain	60	69	22.2	1332
Turnigy Superbrain	80	69	22.2	1776
Turnigy Superbrain	45	68	22.2	999
Turnigy K_Force 70HV	70	115	44.4	3108
Turnigy K-Force 100	100	115	22.2	2220
Turnigy K-Force 40	40	38	22.2	888
Turnigy dlux 55	55	110	22.2	1221
Turnigy dlux 70	70	110	22.2	1554
Turnigy Plush 80	80	120	22.2	1776
Turnigy Plush 40	40	79	22.2	888
Turnigy Plush 60	60	75	22.2	1332
Turnigy Plush 30	30	55	14.8	444
Turnigy Trust 70	70	79	22.2	1554
Turnigy Trust 55	55	79	22.2	1221
Turnigy Trust 45	45	69	22.2	999

B.4 Lithium-Polymer Batteries

Manufacturer	**Model**	**Capacity [mAh]**	**n_S**	**I_{max} [A]**	**m [g]**
PolyQuest	1320LP	1320	2	23	70
PolyQuest	2100LP	2100	2	37	107
PolyQuest	2500XP	2500	2	62.5	140
PolyQuest	3300XP	3300	2	82.5	188
PolyQuest	700XQ	700	2	21	52
PolyQuest	1200XQ	1200	2	36	78
PolyQuest	2000XQ	2000	2	60	118
PolyQuest	3200XQ	3200	2	96	185
PolyQuest	4500XQ	4500	2	135	278
PolyQuest	1320LP	1320	3	23	105
PolyQuest	2100LP	2100	3	37	154
PolyQuest	2500XP	2500	3	62.5	209
PolyQuest	3300XP	3300	3	82.5	275
PolyQuest	3700XP	3700	3	92.5	299
PolyQuest	700XQ	700	3	21	71
PolyQuest	1200XQ	1200	3	36	114
PolyQuest	2000XQ	2000	3	60	173
PolyQuest	3200XQ	3200	3	96	275
PolyQuest	4500XQ	4500	3	135	414
PolyQuest	2100LP	2100	4	37	207
PolyQuest	2500XP	3300	4	62.5	261

PolyQuest	3300XP	3300	4	82.5	347
PolyQuest	3700XP	3700	4	92.5	375
PolyQuest	2000XQ	2000	4	60	220
PolyQuest	3200XQ	3200	4	96	343
PolyQuest	4500XQ	4500	4	135	503
PolyQuest	3300XP	3300	5	82.5	434
PolyQuest	3700XP	3700	5	92.5	472
PolyQuest	3200XQ	3200	5	96	433
PolyQuest	4500XQ	4500	5	135	645
PolyQuest	3200XQ	3200	6	96	500
PolyQuest	4500XQ	4500	6	135	720
Rockamp	zero.G	120	1	2.4	3.1
Rockamp	zero.G	150	1	3	4.1
Rockamp	zero.G	250	2	5	16
Rockamp	zero.G	1000	2	20	55
Rockamp	zero.G	1600	2	32	87
Rockamp	zero.G	2200	2	44	117
Rockamp	zero.G	5000	2	100	251
Rockamp	zero.G	5800	2	116	294
Rockamp	hi.Q	800	2	32	52
Rockamp	hi.Q	1200	2	48	82
Rockamp	hi.Q	2200	2	88	134
Rockamp	hi.Q	2600	2	104	153
Rockamp	hi.Q	3700	2	148	236
Rockamp	hi.Q	4400	2	176	265
Rockamp	Heliperformance	3700	2	81.4	208
Rockamp	Heliperformance	4500	2	99	249
Rockamp	Heliperformance	5000	2	110	267
Rockamp	classic	350	2	10.5	24
Rockamp	classic	850	2	25.5	52
Rockamp	classic	1000	2	30	58
Rockamp	classic	1300	2	39	75
Rockamp	classic	1800	2	54	103
Rockamp	classic	2200	2	66	127
Rockamp	classic	2600	2	78	140
Rockamp	classic	3300	2	99	183
Rockamp	classic	3700	2	111	204
Rockamp	classic	4500	2	135	253
Rockamp	classic	5000	2	150	274
Rockamp	zero.G	250	3	5	24
Rockamp	zero.G	1000	3	20	80
Rockamp	zero.G	1600	3	32	127
Rockamp	zero.G	2200	3	44	171
Rockamp	zero.G	5000	3	100	364
Rockamp	zero.G	5800	3	116	439
Rockamp	hi.Q	800	3	32	77

Rockamp	hi.Q	1200	3	48	106
Rockamp	hi.Q	2200	3	88	194
Rockamp	hi.Q	2600	3	104	221
Rockamp	hi.Q	3700	3	148	347
Rockamp	hi.Q	4400	3	176	394
Rockamp	classic	350	3	10.5	34
Rockamp	classic	850	3	25.5	74
Rockamp	classic	1000	3	30	86
Rockamp	classic	1300	3	39	109
Rockamp	classic	1800	3	54	149
Rockamp	classic	2200	3	66	184
Rockamp	classic	2600	3	78	205
Rockamp	classic	3300	3	99	270
Rockamp	classic	3700	3	111	296
Rockamp	classic	4500	3	135	379
Rockamp	classic	5000	3	150	404
Rockamp	zero.G	5000	4	100	480
Rockamp	zero.G	5800	4	116	561
Rockamp	hi.Q	2200	4	88	255
Rockamp	hi.Q	2600	4	104	291
Rockamp	hi.Q	3700	4	148	434
Rockamp	hi.Q	4400	4	176	494
Rockamp	hi.Q	5000	4	200	550
Rockamp	Classic	2200	4	66	242
Rockamp	Classic	2600	4	78	264
Rockamp	Classic	3300	4	99	343
Rockamp	Classic	3700	4	111	387
Rockamp	Classic	4500	4	135	484
Rockamp	Classic	5000	4	150	520
Rockamp	zero.G	5000	5	100	597
Rockamp	zero.G	5800	5	116	708
Rockamp	hi.Q	2600	5	104	362
Rockamp	hi.Q	3700	5	148	545
Rockamp	hi.Q	4400	5	176	621
Rockamp	hi.Q	5000	5	200	710
Rockamp	Heliperformance	3700	5	81.4	505
Rockamp	Heliperformance	5000	5	110	658
Rockamp	Classic	2600	5	78	328
Rockamp	Classic	3300	5	99	426
Rockamp	Classic	3700	5	111	480
Rockamp	Classic	4500	5	135	608
Rockamp	Classic	5000	5	150	657
Rockamp	zero.G	5000	6	100	704
Rockamp	zero.G	5800	6	116	828
Rockamp	hi.Q	2600	6	104	432
Rockamp	hi.Q	3700	6	148	633

Rockamp	hi.Q	4400	6	176	721
Rockamp	hi.Q	5000	6	200	825
Rockamp	Heliperformance	4500	6	99	708
Rockamp	Classic	2600	6	78	395
Rockamp	Classic	3300	6	99	506
Rockamp	Classic	3700	6	111	872
Rockamp	Classic	4500	6	135	715
Rockamp	Classic	5000	6	150	763
Thunder Power	TP125-1SPL25UM	125	1	3.1	3.40
Thunder Power	TP160-1SPL25UM	160	1	4	4.40
Thunder Power	TP250-1SPL25J	250	1	6.2	9
Thunder Power	TP350-1SPL25J	350	1	8.7	11
Thunder Power	TP325-1SPP45J	325	1	14.6	12
Thunder Power	TP325-1SPP65J	325	1	21.1	12
Thunder Power	TP5400-1SPR65B	5400	1	351	147
Thunder Power	TP5400-1SPR65	5400	1	351	156
Thunder Power	TP250-2SPL25J	250	2	6.2	17
Thunder Power	TP350-2SPL25J	350	2	8.7	22
Thunder Power	TP480-2SPL25J	480	2	12	29
Thunder Power	TP730-2SPL25J	730	2	18.2	39
Thunder Power	TP910-2SPL25J	910	2	22.7	49
Thunder Power	TP1350-2SPL25J	1350	2	33.7	64
Thunder Power	TP1350-2SPL25	1350	2	33.7	66
Thunder Power	TP2100-2SPL25	2100	2	52.5	98
Thunder Power	TP2700-2SPL25	2700	2	67.5	122
Thunder Power	TP3300-2SPL25	3300	2	82.5	168
Thunder Power	TP3900-2SPL25	3900	2	97.5	188
Thunder Power	TP4400-2SPL25	4400	2	110	206
Thunder Power	TP5000-2SPL25	5000	2	125	240
Thunder Power	TP5400-2SPL25	5400	2	135	246
Thunder Power	TP6600-2SPL25	6600	2	165	331
Thunder Power	TP7800-2SPL25	7800	2	195	368
Thunder Power	TP325-2SPP45J	325	2	14.6	21
Thunder Power	TP850-2SPP45J	850	2	38.2	50
Thunder Power	TP850-2SPP45	850	2	38.2	52
Thunder Power	TP1300-2SPP45	1300	2	58	73
Thunder Power	TP1800-2SPP45	1800	2	81	101
Thunder Power	TP2250-2SPP45	2250	2	101	123
Thunder Power	TP2700-2SPP45	2700	2	121	153
Thunder Power	TP3300-2SPP45	3300	2	148	186
Thunder Power	TP3850-2SPP45	3850	2	173	217
Thunder Power	TP4400-2SPP45	4400	2	198	246
Thunder Power	TP5000-2SPP45	5000	2	225	278
Thunder Power	TP6600-2SPP45	6600	2	297	363
Thunder Power	TP7700-2SPP45	7700	2	297	426
Thunder Power	TP325-2SPP65J	325	2	21.1	22

Thunder Power	TP850-2SPP65J	850	2	55.2	52
Thunder Power	TP850-2SPP65	850	2	55.2	52
Thunder Power	TP1300-2SPP65	1300	2	84.5	77
Thunder Power	TP1800-2SPP65	1800	2	117	105
Thunder Power	TP2250-2SPP65	2250	2	146	133
Thunder Power	TP2700-2SPP65	2700	2	175	156
Thunder Power	TP3300-2SPP65	3300	2	214	192
Thunder Power	TP3850-2SPP65	3850	2	250	221
Thunder Power	TP4400-2SPP65	4400	2	286	249
Thunder Power	TP5000-2SPP65	5000	2	325	280
Thunder Power	TP6600-2SPP65	6600	2	429	367
Thunder Power	TP7700-2SPP65	7700	2	500	430
Thunder Power	TP1320-2SJPL	1320	2	17	58
Thunder Power	TP1320-2SPL	1320	2	17	59
Thunder Power	TP2000-2SPL	2000	2	32	85
Thunder Power	TP2100-2SPL	2100	2	31.5	95
Thunder Power	TP2600-2SPL	2600	2	52	122
Thunder Power	TP4000-2S2PL	4000	2	64	173
Thunder Power	TP6000-2S3PL	6000	2	96	255
Thunder Power	TP8000-2S4PL	8000	2	128	320
Thunder Power	TP2700-2SSR35	2700	2	94	168
Thunder Power	TP3300-2SSR35	3300	2	115	204
Thunder Power	TP4300-2SSR35	4300	2	150	233
Thunder Power	TP5400-2SSR35	5400	2	189	276
Thunder Power	TP6600-2SSR35	6600	2	231	341
Thunder Power	TP8000-2SSR35	8000	2	280	376
Thunder Power	TP5300-2SPR65B	5300	2	344	298
Thunder Power	TP5300-2SPR65	5300	2	344	309
Thunder Power	TP250-3SPL25J	250	3	6.2	24
Thunder Power	TP350-3SPL25J	350	3	8.7	32
Thunder Power	TP480-3SPL25J	480	3	12	42
Thunder Power	TP730-3SPL25J	730	3	18.2	57
Thunder Power	TP910-3SPL25J	910	3	22.7	72
Thunder Power	TP1350-3SPL25J	1350	3	33.7	92
Thunder Power	TP1350-3SPL25	1350	3	33.7	94
Thunder Power	TP2100-3SPL25	2100	3	52.5	147
Thunder Power	TP2700-3SPL25	2700	3	67.5	182
Thunder Power	TP3300-3SPL25	3300	3	82.5	243
Thunder Power	TP3900-3SPL25	3900	3	97.5	275
Thunder Power	TP4400-3SPL25	4400	3	110	310
Thunder Power	TP5000-3SPL25	5000	3	125	357
Thunder Power	TP5400-3SPL25	5400	3	135	367
Thunder Power	TP6600-3SPL25	6600	3	165	480
Thunder Power	TP7800-3SPL25	7800	3	195	542
Thunder Power	TP325-3SPP45J	325	3	14.6	31
Thunder Power	TP850-3SPP45J	850	3	38.2	72

Thunder Power	TP850-3SPP45	850	3	38.2	74
Thunder Power	TP1300-3SPP45	1300	3	58	109
Thunder Power	TP1800-3SPP45	1800	3	81	148
Thunder Power	TP2250-3SPP45	2250	3	101	179
Thunder Power	TP2700-3SPP45	2700	3	121	218
Thunder Power	TP3300-3SPP45	3300	3	148	268
Thunder Power	TP3850-3SPP45	3850	3	173	316
Thunder Power	TP4400-3SPP45	4400	3	198	360
Thunder Power	TP5000-3SPP45	5000	3	225	396
Thunder Power	TP6600-3SPP45	6600	3	297	531
Thunder Power	TP7700-3SPP45	7700	3	297	620
Thunder Power	TP325-3SPP65J	325	3	21.1	33
Thunder Power	TP850-3SPP65J	850	3	55.2	74
Thunder Power	TP850-3SPP65	850	3	55.2	74
Thunder Power	TP1300-3SPP65	1300	3	84.5	112
Thunder Power	TP1800-3SPP65	1800	3	117	151
Thunder Power	TP2250-3SPP65	2250	3	146	189
Thunder Power	TP2700-3SPP65	2700	3	175	223
Thunder Power	TP3300-3SPP65	3300	3	214	274
Thunder Power	TP3850-3SPP65	3850	3	250	319
Thunder Power	TP4400-3SPP65	4400	3	286	364
Thunder Power	TP5000-3SPP65	5000	3	325	399
Thunder Power	TP6600-3SPP65	6600	3	429	537
Thunder Power	TP7700-3SPP65	7700	3	500	626
Thunder Power	TP1320-3SJPL	1320	3	17	84
Thunder Power	TP1320-3SPL	1320	3	17	86
Thunder Power	TP2000-3SPL	2000	3	32	122
Thunder Power	TP2100-3SPL	2100	3	31.5	142
Thunder Power	TP2600-3SPL	2600	3	52	182
Thunder Power	TP4000-3S2PL	4000	3	64	255
Thunder Power	TP6000-3S3PL	6000	3	96	381
Thunder Power	TP8000-3S4PL	8000	3	128	474
Thunder Power	TP2700-3SSR35	2700	3	94	232
Thunder Power	TP3300-3SSR35	3300	3	115	262
Thunder Power	TP4300-3SSR35	4300	3	150	339
Thunder Power	TP5400-3SSR35	5400	3	189	432
Thunder Power	TP6600-3SSR35	6600	3	231	495
Thunder Power	TP8000-3SSR35	8000	3	280	531
Thunder Power	TP5300-3SPR65	5300	3	344	447
Thunder Power	TP1350-4SPL25	1350	4	33.7	122
Thunder Power	TP2100-4SPL25	2100	4	52.5	192
Thunder Power	TP2700-4SPL25	2700	4	67.5	238
Thunder Power	TP3300-4SPL25	3300	4	82.5	315
Thunder Power	TP3900-4SPL25	3900	4	97.5	362
Thunder Power	TP4400-4SPL25	4400	4	110	414
Thunder Power	TP5000-4SPL25	5000	4	125	471

Thunder Power	TP5400-4SPL25	5400	4	135	480
Thunder Power	TP6600-4SPL25	6600	4	165	623
Thunder Power	TP7800-4SPL25	7800	4	195	714
Thunder Power	TP1300-4SPP45	1300	4	58	140
Thunder Power	TP1800-4SPP45	1800	4	81	191
Thunder Power	TP2250-4SPP45	2250	4	101	238
Thunder Power	TP2700-4SPP45	2700	4	121	285
Thunder Power	TP3300-4SPP45	3300	4	148	352
Thunder Power	TP3850-4SPP45	3850	4	173	413
Thunder Power	TP4400-4SPP45	4400	4	198	473
Thunder Power	TP5000-4SPP45	5000	4	225	525
Thunder Power	TP6600-4SPP45	6600	4	297	700
Thunder Power	TP7700-4SPP45	7700	4	297	810
Thunder Power	TP850-4SPP65	850	4	55.2	97
Thunder Power	TP1300-4SPP65	1300	4	84.5	144
Thunder Power	TP1800-4SPP65	1800	4	117	199
Thunder Power	TP2250-4SPP65	2250	4	146	251
Thunder Power	TP2700-4SPP65	2700	4	175	292
Thunder Power	TP3300-4SPP65	3300	4	214	367
Thunder Power	TP3850-4SPP65	3850	4	250	416
Thunder Power	TP4400-4SPP65	4400	4	286	478
Thunder Power	TP5000-4SPP65	5000	4	325	529
Thunder Power	TP6600-4SPP65	6600	4	429	708
Thunder Power	TP7700-4SPP65	7700	4	500	818
Thunder Power	TP2000-4SPL	2000	4	32	160
Thunder Power	TP2100-4SPL	2100	4	31.5	188
Thunder Power	TP2600-4SPL	2600	4	52	238
Thunder Power	TP4000-4S2PL	4000	4	64	338
Thunder Power	TP6000-4S3PL	6000	4	96	488
Thunder Power	TP8000-4S4PL	8000	4	128	633
Thunder Power	TP2700-4SSR35	2700	4	94	293
Thunder Power	TP3300-4SSR35	3300	4	115	341
Thunder Power	TP4300-4SSR35	4300	4	150	435
Thunder Power	TP5400-4SSR35	5400	4	189	558
Thunder Power	TP5300-4SPR65	5300	4	344	583
Thunder Power	TP2700-5SPL25	2700	5	67.5	292
Thunder Power	TP3300-5SPL25	3300	5	82.5	392
Thunder Power	TP3900-5SPL25	3900	5	97.5	448
Thunder Power	TP4400-5SPL25	4400	5	110	518
Thunder Power	TP5000-5SPL25	5000	5	125	588
Thunder Power	TP5400-5SPL25	5400	5	135	589
Thunder Power	TP6600-5SPL25	6600	5	165	776
Thunder Power	TP7800-5SPL25	7800	5	195	884
Thunder Power	TP2250-5SPP45	2250	5	101	292
Thunder Power	TP2700-5SPP45	2700	5	121	352
Thunder Power	TP3300-5SPP45	3300	5	148	434

Thunder Power	TP3850-5SPP45	3850	5	173	510
Thunder Power	TP4400-5SPP45	4400	5	198	585
Thunder Power	TP5000-5SPP45	5000	5	225	655
Thunder Power	TP6600-5SPP45	6600	5	297	868
Thunder Power	TP7700-5SPP45	7700	5	297	1005
Thunder Power	TP2250-5SPP65	2250	5	146	315
Thunder Power	TP2700-5SPP65	2700	5	175	360
Thunder Power	TP3300-5SPP65	3300	5	214	451
Thunder Power	TP3850-5SPP65	3850	5	250	514
Thunder Power	TP4400-5SPP65	4400	5	286	591
Thunder Power	TP5000-5SPP65	5000	5	325	660
Thunder Power	TP6600-5SPP65	6600	5	429	878
Thunder Power	TP7700-5SPP65	7700	5	500	1015
Thunder Power	TP2000-5SPL	2000	5	32	197
Thunder Power	TP2100-5SPL	2100	5	31.5	234
Thunder Power	TP2600-5SPL	2600	5	52	292
Thunder Power	TP4000-5S2PL	4000	5	64	416
Thunder Power	TP6000-5S3PL	6000	5	96	627
Thunder Power	TP8000-5S4PL	8000	5	128	790
Thunder Power	TP2700-6SPL25	2700	6	67.5	352
Thunder Power	TP3300-6SPL25	3300	6	82.5	468
Thunder Power	TP3300-6SPL25L	3300	6	82.5	478
Thunder Power	TP3900-6SPL25	3900	6	97.5	534
Thunder Power	TP3900-6SPL25L	3900	6	97.5	544
Thunder Power	TP4400-6SPL25	4400	6	110	623
Thunder Power	TP4400-6SPL25L	4400	6	110	633
Thunder Power	TP5000-6SPL25	5000	6	125	708
Thunder Power	TP5000-6SPL25L	5000	6	125	718
Thunder Power	TP5400-6SPL25	5400	6	135	710
Thunder Power	TP6600-6SPL25	6600	6	165	925
Thunder Power	TP7800-6SPL25	7800	6	195	1053
Thunder Power	TP2250-6SPP45	2250	6	101	351
Thunder Power	TP2700-6SPP45	2700	6	121	419
Thunder Power	TP3300-6SPP45	3300	6	148	516
Thunder Power	TP3300-6SPP45L	3300	6	148	526
Thunder Power	TP3850-6SPP45	3850	6	173	607
Thunder Power	TP3850-6SPP45L	3850	6	173	617
Thunder Power	TP4400-6SPP45	4400	6	198	698
Thunder Power	TP4400-6SPP45L	4400	6	198	708
Thunder Power	TP5000-6SPP45	5000	6	225	798
Thunder Power	TP5000-6SPP45L	5000	6	225	808
Thunder Power	TP6600-6SPP45	6600	6	297	1035
Thunder Power	TP7700-6SPP45	7700	6	297	1199
Thunder Power	TP2250-6SPP65	2250	6	146	372
Thunder Power	TP2700-6SPP65	2700	6	175	428
Thunder Power	TP3300-6SPP65	3300	6	214	537

Thunder Power	TP3300-6SPP65L	3300	6	214	547
Thunder Power	TP3850-6SPP65	3850	6	250	620
Thunder Power	TP3850-6SPP65L	3850	6	250	630
Thunder Power	TP4400-6SPP65	4400	6	286	705
Thunder Power	TP4400-6SPP65L	4400	6	286	715
Thunder Power	TP5000-6SPP65	5000	6	325	804
Thunder Power	TP5000-6SPP65L	5000	6	325	814
Thunder Power	TP6600-6SPP65	6600	6	429	1048
Thunder Power	TP7700-6SPP65	7700	6	500	1211
Thunder Power	TP2600-6SPL	2600	6	52	352
Thunder Power	TP4000-6S2PL	4000	6	64	496
Thunder Power	TP6000-6S3PL	6000	6	96	750
Thunder Power	TP8000-6S4PL	8000	6	128	932
Thunder Power	TP3300-7SPL25	3300	7	82.5	543
Thunder Power	TP3900-7SPL25	3900	7	97.5	620
Thunder Power	TP4400-7SPL25	4400	7	110	727
Thunder Power	TP5000-7SPL25	5000	7	125	825
Thunder Power	TP3300-7SPP45	3300	7	148	598
Thunder Power	TP3850-7SPP45	3850	7	173	704
Thunder Power	TP4400-7SPP45	4400	7	198	812
Thunder Power	TP5000-7SPP45	5000	7	225	922
Thunder Power	TP3300-7SPP65	3300	7	214	623
Thunder Power	TP3850-7SPP65	3850	7	250	717
Thunder Power	TP4400-7SPP65	4400	7	286	820
Thunder Power	TP5000-7SPP65	5000	7	325	929
Thunder Power	TP3300-8SPL25	3300	8	82.5	618
Thunder Power	TP3300-8SPL25L	3300	8	82.5	628
Thunder Power	TP3900-8SPL25	3900	8	97.5	704
Thunder Power	TP3900-8SPL25L	3900	8	97.5	714
Thunder Power	TP4400-8SPL25	4400	8	110	831
Thunder Power	TP4400-8SPL25L	4400	8	110	841
Thunder Power	TP5000-8SPL25	5000	8	125	940
Thunder Power	TP5000-8SPL25L	5000	8	125	950
Thunder Power	TP3300-8SPP45	3300	8	148	675
Thunder Power	TP3300-8SPP45L	3300	8	148	685
Thunder Power	TP3850-8SPP45	3850	8	173	802
Thunder Power	TP3850-8SPP45L	3850	8	173	812
Thunder Power	TP4400-8SPP45	4400	8	198	926
Thunder Power	TP4400-8SPP45L	4400	8	198	936
Thunder Power	TP5000-8SPP45	5000	8	225	1046
Thunder Power	TP5000-8SPP45L	5000	8	225	1056
Thunder Power	TP3300-8SPP65	3300	8	214	708
Thunder Power	TP3300-8SPP65L	3300	8	214	718
Thunder Power	TP3850-8SPP65	3850	8	250	815
Thunder Power	TP3850-8SPP65L	3850	8	250	825
Thunder Power	TP4400-8SPP65	4400	8	286	935

Thunder Power	TP4400-8SPP65L	4400	8	286	945
Thunder Power	TP5000-8SPP65	5000	8	325	1054
Thunder Power	TP5000-8SPP65L	5000	8	325	1065
Thunder Power	TP3900-9SPL25	3900	9	97.5	790
Thunder Power	TP4400-9SPL25	4400	9	110	935
Thunder Power	TP5000-9SPL25	5000	9	125	1054
Thunder Power	TP3300-9SPP45	3300	9	148	758
Thunder Power	TP3850-9SPP45	3850	9	173	899
Thunder Power	TP4400-9SPP45	4400	9	198	1039
Thunder Power	TP5000-9SPP45	5000	9	225	1172
Thunder Power	TP3300-9SPP65	3300	9	214	793
Thunder Power	TP3850-9SPP65	3850	9	250	913
Thunder Power	TP4400-9SPP65	4400	9	286	1050
Thunder Power	TP5000-9SPP65	5000	9	325	1181
Thunder Power	TP3900-10SPL25	3900	10	97.5	875
Thunder Power	TP3900-10SPL25L	3900	10	97.5	885
Thunder Power	TP4400-10SPL25	4400	10	110	1040
Thunder Power	TP4400-10SPL25L	4400	10	110	1050
Thunder Power	TP5000-10SPL25	5000	10	125	1168
Thunder Power	TP5000-10SPL25L	5000	10	125	1178
Thunder Power	TP3300-10SPP45	3300	10	148	841
Thunder Power	TP3300-10SPP45L	3300	10	148	851
Thunder Power	TP3850-10SPP45	3850	10	173	998
Thunder Power	TP3850-10SPP45L	3850	10	173	1008
Thunder Power	TP4400-10SPP45	4400	10	198	1151
Thunder Power	TP4400-10SPP45L	4400	10	198	1161
Thunder Power	TP5000-10SPP45	5000	10	225	1298
Thunder Power	TP5000-10SPP45L	5000	10	225	1308
Thunder Power	TP3300-10SPP65	3300	10	214	878
Thunder Power	TP3300-10SPP65L	3300	10	214	889
Thunder Power	TP3850-10SPP65	3850	10	250	1011
Thunder Power	TP3850-10SPP65L	3850	10	250	1021
Thunder Power	TP4400-10SPP65	4400	10	286	1164
Thunder Power	TP4400-10SPP65L	4400	10	286	1175
Thunder Power	TP5000-10SPP65	5000	10	325	1308
Thunder Power	TP5000-10SPP65L	5000	10	325	1319

B.5 Fuel Tanks

Manufacturer / Type	**Mass [g]**	**Volume [L]**
DuBro	34	0.12
DuBro	163	1.2
DuBro	178	1.5
DuBro	48	0.18
DuBro	57	0.24

DuBro	60	0.3
DuBro	61	0.36
DuBro	62	0.42
DuBro	63	0.48
DuBro	25	0.06
DuBro	75	0.6
DuBro	80	0.71
DuBro	155	0.95
Hünersdorff Weithalskanister	620	5
Hünersdorff Weithalskanister	910	10
Hünersdorff Weithalskanister	1390	22
Hünersdorff Weithalskanister	1500	31
Hünersdorff Fuel Friend	100	0.5
Hünersdorff Fuel Friend	240	1
Hünersdorff Fuel Friend	250	1.5
Hünersdorff Fuel Friend	380	2
Hünersdorff Industrie-Kanister	110	2
Hünersdorff Industrie-Kanister	130	2.5
Hünersdorff Industrie-Kanister	140	3
Hünersdorff Industrie-Kanister	250	5
Hünersdorff Industrie-Kanister	390	10
Hünersdorff Industrie-Kanister	900	20
Hünersdorff Industrie-Kanister	1300	30
Hünersdorff Industrie-Kanister	270	6
Hünersdorff Industrie-Kanister	320	8
Hünersdorff Industrie-Kanister	1150	25
Hünersdorff Kraftstoff-Kanister	210	2
Hünersdorff Kraftstoff-Kanister	380	3
Hünersdorff Kraftstoff-Kanister	400	5
Hünersdorff Kraftstoff-Kanister	800	10
Hünersdorff Kraftstoff-Kanister	1300	20